Attenuation and Fate of Harmful Waste Contaminants using Clay Minerals and Bio-Polymerized Clays for Containment Applications

Thesis

as a requirements for degree of

DOCTOR OF PHILOSOPHY

By

Himanshu Yadav

(Roll No. 186104015)

Under the guidance of

Dr. T.V. Bharat

(Professor, Department of Civil Engineering)

and

Dr. Sachin Kumar

(Professor, Department of Biosciences and Bioengineering)

DEPARTMENT OF CIVIL ENGINEERING

INDIAN INSTITUTE OF TECHNOLOGY GUWAHATI

July, 2024

भारतीय प्रौद्योगिकी संस्थान गुवाहाटी
Indian Institute of Technology Guwahati

Candidate's Declaration

The work reported in this thesis is original and was carried out by me during my tenure as a Ph.D. student at the Department of Civil Engineering, Indian Institute of Technology Guwahati. I hereby declare that this thesis has not been submitted for the award of any degree, diploma, membership, or similar title in any university or academic institution.

Date: 29th July, 2024

Himanshu Yadav

Ph.D. Candidate, (186104015)

Department of Civil Engineering,
Indian Institute of Technology
Guwahati

भारतीय प्रौद्योगिकी संस्थान गुवाहाटी
Indian Institute of Technology Guwahati

Certificate

It is certified that the thesis entitled **"Attenuation and Fate of Harmful Waste Contaminants using Clay Minerals and Bio-Polymerized Clays for Containment Applications"**, is submitted by Himanshu Yadav (186104015), a research scholar in the Civil Engineering Department, Indian Institute of Technology Guwahati, for the award of the degree of Doctor of Philosophy, is a record of original research work carried out by him under our supervision. The thesis has fulfilled all requirements as per the regulations of the institute and in our opinion, has reached the standard needed for submission. The results presented in this thesis have not been submitted elsewhere for the award of any other degree or diploma.

Prof. T.V. Bharat

Professor, Department of Civil Engineering,

Indian Institute of Technology, Guwahati

Prof. Sachin Kumar

Professor, Department of Biosciences and Bioengineering,

Indian Institute of Technology, Guwahati

भारतीय प्रौद्योगिकी संस्थान गुवाहाटी
Indian Institute of Technology Guwahati

ABSTRACT

The amount and rate of waste production have significantly increased across the globe due to an increase in population, increased standard of living, urbanization, and industrialization. An increased pathogenic waste post-COVID-19 pandemic forced the policy-makers to treat biomedical waste (BMW) also similar to municipal solid waste (MSW) to dispose into dumpsites and MSW landfills across the globe. Thus, several emerging contaminants are also increasing in the containment facilities. A momentous change in the engineering designs of containment facilities is seen over the years with a huge effort from the Geo-environmental engineering community to account for the emerging and increased amount of contaminants.

The geosynthetic clay liners (GCLs) completely replaced the compacted clay liners (CCLs) in municipal solid waste (MSW) landfills and mine waste containment applications due to ease in transportation, installation, and less dust pollution. The presence of inorganic salts influences the osmotic potential of the granular bentonite to perform as a liner in the landfill application. The presence of heavy metals in mine tailing ponds and biomedical waste along with the MSW in landfills is thus threatening due to the easy escape of these harmful contaminants into the environment under reduced osmotic conditions. Further, the liner system is also exposed to vertical stresses due to the self-weight of the waste. An understanding of the role of grain sizes on the hydraulic and volume changes for GB under critical chemo-mechanical loadings is not available. Non-conventional GCLs have been explored very recently and contain polymer-amended granular bentonite. The hydrophilic polymers have received good attention for modifying the GCLs in landfill applications. The efficacy of various commercial polymers for liner application in high ionic strength environment is required to be studied. However, the biopolymers for amendment of GCLs are not significantly

explored. In this study, hydraulic and volume change characteristics of granular bentonite amended with the biopolymers such as xanthan gum, guar gum, agar-agar gum, and acacia gum were studied under mechanical loading while exposed to different high ionic strength pore-fluids. An effort was made to understand the volume change and hydraulic behavior of biopolymer-amended GB, under thermo-chemo-mechanical loading conditions.

The kaolin was also accessed for application as a compacted liner system after amending with the polymers. The amendment of kaolin with xanthan gum improved the hydraulic and diffusive characteristics under high concentrations of inorganic salt solutions under low mechanical stresses. The biopolymer-amended kaolin also improved its hydraulic and diffusive characteristics with heavy metals from the mine tailing facilities.

Further, the fate and attenuation ability of different viral pathogens with different clay minerals, their mechanisms, and the role of granulation and salt environment are not explored. The present work evaluated the role of clay minerals, interaction time, and solid-to-liquid ratio on clay-virus interaction. The mechanism governing the attachment of the virus to the bentonite clay was also understood based on changing exchangeable cation types in two bentonite clays. Further, the role of grain sizes of the granules of GB was also understood in the sorption and hydraulic characteristics of the viral pathogens from Japanese encephalitis and H1N1 influenza viruses. Biomedical waste disposal protocols were proposed for the design of an exclusive BMW containment facility.

Acknowledgments

First and foremost, I thank MHRD and IIT Guwahati for the financial support, without support research work would not have been possible. Further, I would like to express the acknowledgement to the **Department of Science and Technology**, and the **National Jute Board**, Government of India, for financial support. I express my sincere gratitude to my PhD supervisor, **Prof. T.V. Bharat,** for his constant support, guidance, encouragement, advice, and valuable discussions throughout. He has motivated me to explore all the possible domains and areas. I am thankful for his belief in me. I also express my sincere gratitude to my PhD Co-supervisor, **Prof. Sachin Kumar,** for his constant support, guidance, encouragement, advice, and valuable discussions throughout.

I extend my heartfelt gratitude to **Prof. Sai K. Vanapalli**, from the University of Ottawa, Canada, **Foreign Examiner** of the thesis for his valuable suggestions and comments for improving its quality. I extend my sincere gratitude to **Prof. N.K. Samadhiya**, from I.I.T. Roorkee, **Indian Examiner** of the thesis for his valuable suggestions and comments for improving its quality.

I am highly thankful to my doctoral committee members, **Prof. Rajan Choudhary** (Chairman), and **Dr. Arindam Dey** from the Department of Civil Engineering, and **Prof. Nitin Chaudhary** from the Department of Biosciences and Bioengineering, for their constant support, guidance, and suggestions during my work progress seminars. I am also thankful to the Viva-Voice committee members for their valuable suggestions during the Viva-Voice seminar.

I would also like to acknowledge the support received from the **Clay Mineral Society, U.S.A.** as a student research grant and travel grant to attend the 17th International Clay Conference. Further, I would like to acknowledge the support received from the **International Society of Soil Mechanics and Geotechnical Engineering (ISSMGE)** to attend the 9th International Congress on Environmental Geotechnics in Chania, Greece.

I also acknowledge the support and technical assistance received from the staff namely **P. Pathak**, and **C. Medhi** from Environmental Engineering, and **Hariram Upadhayay** from Geotech lab, Department of Civil Engineering, IIT Guwahati. I am thankful to **Dr. Bula Choudhary** from Biotech Park, IIT Guwahati for providing the lab facility for

Freeze-drying the soil samples. I must acknowledge **Bijay Chaudhury** from Workshop, IIT Guwahati for the fabrication of various set-ups.

I also acknowledge the support received from FESEM, TGA, EDX, BET, AFM and XRD facilities Central Instrument Facility, IIT Guwahati. I acknowledge Dr. Prabhat Patel from Centre for Environment, IIT Guwahati for his help in FTIR analysis; I am thankful to Dr. Chandi Patra and Ajit from BSBE for their help in Freeze drying of Samples. I acknowledge the support from Christy from Environmental Lab. for the Kjeldahl Method of ammonia.

I am grateful to Deepa, and Shubham from BSBE, and Sahil Kumar and Ajeet Sharma from CED for their kind help in conducting various experiments during my PhD work. I am also grateful to my lab. seniors – Dr. Dhanesh Sing Das, Mr. Bedabrata Ghosh, Dr. Partha Das, and Dr. Ankit Srivastava for sharing their knowledge and useful discussions along with a healthy working environment.

I am thankful to my friends Lalit, Surender, Sahil, Ashok, Deepa, Akhila, Vishnu, Riya, Niranjan, Aman, and Manish for always being there and made my PhD journey easier. Finally, I would like to express my deepest gratitude to my parents Mr. Ram Vilas Yadav and Mrs. Usha Yadav, and my sister (Ms. Shivangi Yadav) who gave me blessings, moral support, and continuous encouragement to pursue my dreams.

Himanshu Yadav

Table of Contents

Chapter 1: Introduction

Chapter 2: Background and Literature Review

Chapter 3: Materials and Methodology

Chapter 4: Influence of Grain Size and Plasticity of Granular Bentonite under Chemo-Mechanical Loadings with Salt Solutions

Chapter 5: Influence of Polymer and Biopolymer Amended Granular Bentonite under Thermo-Chemo-Mechanical Loadings

LIST OF FIGURES

भारतीय प्रौद्योगिकी संस्थान गुवाहाटी
Indian Institute of Technology Guwahati

LIST OF TABLES

भारतीय प्रौद्योगिकी संस्थान गुवाहाटी
Indian Institute of Technology Guwahati

LIST OF ABBREVIATIONS

MSW	Municipal solid waste
BMW	Biomedical waste
GCL	Geosynthetic clay liner
GB	Granular bentonite
PB	Powdered bentonite
XG	Xanthan Gum
GBXG2	Xanthan gum amended granular bentonite with 2 % XG
K	Kaolin
XGK	Xanthan gum amended kaolin
GGK	Guar gum amended kaolin
GG	Guar Gum
AG	Acacia Gum
AA	Agar Gum

Chapter – 1
Introduction

1.1 General

Industrialization and urbanization have increased the standard of living, and migration of people from rural to urban areas led to the increased generation rate and quantity of municipal solid waste (MSW). Landfills are engineered containment facilities to prevent the migration of harmful leachate from the MSW to the groundwater. Landfill liner is the main component of landfills, which prevents the migration of harmful contaminants to the groundwater and surrounding environment (Daniel, 1993; Hornsey et al. 2010; Kong et al., 2017). A leachate collection system containing a network of perforated pipes is provided at the bottom of the landfill and above the liner system to collect the leachate before reaching to the liner system. Further, gas collection systems, groundwater monitoring systems, daily cover, intermediate cover, and final cover systems are also provided in engineered landfills. Environmental protection agencies recommend hydraulic conductivity of landfill liners to be lower than 10^{-9} m/sec (EPA, 2015). There are well-defined guidelines for handling and containing MSW.

The waste generated during diagnosis, treatment, or immunization of humans, animals, or avian species, testing of biologicals, etc. is known as biomedical waste (BMW). The BMW includes general waste, infectious waste, pathological waste, sharps, pharmaceutical waste, genotoxic waste, chemical waste, and radioactive waste. Around 75 – 90 % of waste generated from healthcare facilities is non-hazardous and falls under the category of general waste, and it can be treated like municipal solid waste. Moreover, exposure to the hazardous biomedical waste can

cause infection, injuries, chemical toxicity, radioactive hazards, genotoxicity, and cytotoxicity. The BMW is categorized into 10 categories in Biomedical Waste Management and Handling Rules, (1998) as shown in Table 1.1.

Table 1.1 Categories of Biomedical Waste as given in BMW Rules, (1998)

S. No.	Option	Waste Category	Treatment and Disposal
1.	Category No. 1	Human Anatomical Waste (ex. Human tissues, organs, body parts)	Incineration/ deep burial
2.	Category No. 2	Animal Waste (ex. Animal tissues, organs, body parts carcasses, blood, discharge from hospital and animal houses	Incineration/ deep burial
3.	Category No. 3	Microbiology and Biotechnology Waste	Local autoclaving/ microwaving/ incineration
4.	Category No. 4	Waste Sharps (ex. Needles, syringes, blades, glass etc.)	Disinfection/ autoclaving/ microwaving/ shredding
5.	Category No. 5	Discarded Medicines and Cytotoxic Drugs	Incinerations/ Disposal in Landfills
6.	Category No. 6	Solid Waste (ex.; Items contaminated with blood, body fluid, dressing, plastic casts, lines, etc.	Incineration/ microwaving
7.	Category No. 7	Solid Waste (ex.; waste from disposable items other than sharps)	Disinfection by chemical treatment, autoclaving/ microwaving/ shredding

8.	Category No. 8	Liquid Waste (ex.; waste from lab. and washing cleaning, housekeeping, and disinfection activities)	Disinfection by chemical treatment and discharge into drains
9	Category No. 9	Incineration Ash (ex.; ash from incineration of any biomedical waste)	Disposal to landfills
10.	Category No. 10	Chemical Waste (ex.; Chemicals used in biologicals, chemicals used in disinfections, insecticides, etc.	Chemical Treatments and discharge into drains for liquid and landfills for solids

The BMW must be considered hazardous as a small quantity of waste can cause infections. Biomedical waste can pose a threat to the lives of patients, healthcare workers, staff, and the community as improper management of this waste can lead to a risk of infection. Several studies have confirmed the open dumping (Israel et al., 2011; Debalkie and Kumie 2017; Derso et al., 2018); open burning of medical waste (Abebe, et al., 2017); illegal recycling and reselling of hazardous hospital waste (Gupta and Boojh, 2006), due to the non-availability of a proper disposal facility for medical waste. Such activities can be a serious threat to the environment and the waste handlers. Incineration of biomedical waste is generally followed practice for the management of BMW. The incineration process is very costly due to the requirement of high energy. Biomedical waste emits harmful gases like dioxins, furans, carbon monoxide, sulfur dioxide, fine dust particles, etc. Apart from these gases incineration facilities also emits heavy metals like lead, mercury, and cadmium to the surrounding environment. (Lee and Huffman, 1996; Gautam et al., 2010; Singh and Kaur, 2012). Incineration ash also contains harmful contaminants which also include heavy metals (Emmanuel et al., 2004). There is a lack of proper understanding and

availability of the BMW containment facilities, which might be a good option for BMW waste disposal.

Augmented demand for the metals and minerals for leather, electroplating, metallurgy, batteries, electrodes, solar panels, electronics, and galvanizing industries is addressed by expanding the mining activity. The extraction process of these important raw minerals during the mining generates large quantities of waste. On an annual basis, 5-14 billion tons of tailings, pulverized material after extraction of the metal-bearing minerals (Mäkinen et al. 2020), are generated and its disposal is difficult (Lottermoser 2010). Tailings containing high moisture contents are disposed in engineering disposal facilities behind tailing dams (Vasudev and Bharat 2022; Yin et al. 2020). Several million tonnes of chromate residue is also generated from the mining of chromate ore and stored in the form of slurry in tailing ponds (Chrysochoou, et al., 2009; Du, & Chrysochoou; 2020). The process of extraction of zinc from the mineral involves the generation of jarosite as waste material in slurry form. This jarosite is also stored in tailing storage facilities. The presence of heavy metals like mercury, chromium, arsenic, lead, zinc, copper, cadmium, and iron are hazardous and require to be contained (Asokan et al. 2006; Peng et al., 2021; Bishop et al., 2023). Leachate released from these tailings has detrimental effects on the surroundings due to the escape of these toxic metals (Parviainen 2009; García et al. 2017; Abreu et al. 2016). Recent studies show soil contamination by heavy metals near the tailing disposal facilities (Li et al., 2014; Silva et al., 2022), and water of nearby rivers (Hatje et al. 2017). The leachability of the harmful heavy metals with rainwater also contributes to water pollution (Heo et al., 2016; Costa et al., 2021). There are recent reports of possible health risks resulting from the accumulation of heavy metals in the food chain near the mine tailing facilities (Lim et al., 2008).

Improper disposal of household, industrial, biomedical, and mining waste can cause serious consequences to the environment as well as human health. Engineered barrier systems are utilized to contain the migration of these harmful contaminants into the environment. The bentonite clays with high percentages of montmorillonite mineral are used as engineered barriers in landfills (Benson et al., 1994; Lee et al., 2005; Bharat et al., 2009; Das and Bharat, 2017), and tailing disposal facilities (Fall et al., 2009). Earlier, 0.75m to 1m thick layers of compacted bentonites were used as liners, known as compacted clay liners (CCLs). These liners got completely replaced by 5-7 mm thick geosynthetic clay liners (GCLs), in recent times, that contain granulated form of bentonites. The GCLs are preferred over CCLs due to their limited thickness, which saves space for waste, ease in transportation, and less dust production during manufacturing and installation (Bouazza, 2002; Das & Bharat, 2021). Bentonites are subjected to hydraulic, chemical, mechanical, and thermal loadings under field conditions. Even with the low hydraulic conductivity, the migration of contaminants takes place through the diffusion process. Moreover, the adsorption of the contaminants onto the clay surface also becomes important in the design of landfill liner systems. Thus, the evaluation of the diffusion and retardation characteristics (D_e and R_d) is important. Kaolin clay rich in kaolinite mineral has recently been explored as a potential material for landfill liner application (Das and Bharat, 2021; Das, 2021), due to their availability around the world and improved osmotic efficiency under high compaction density.

1.2 Motivation and Scope

The grain size of the granular bentonite (GB) used in GCLs varies based on the manufacturers, and different batches. The GCLs are provided as liner materials in waste containment facilities based on the plasticity of the bentonite and assumed that the granule size does not play any role in the permeation behavior of GCLs. However, the behavior of GB gets altered due to exposure to

the chemical loadings and the poorly developed repulsive pressures. The role of granule size in GB on permeation rates and volume change in the presence of high ionic strength salt concentrations and mechanical loadings is yet to be studied. Several polymers and biopolymers are explored for the amendment of bentonite to improve the chemical compatibility of bentonites (Emidio et al., 2010; Scalia et al., 2014; Tian et al., 2016; Fu et al., 2021; Wang et al., 2022). Amendment of GB in GCLs is to be explored under the critical chemo-mechanical loading conditions. Further, the temperatures in GCLs can rise up to 55˚C physical, biological, and chemical processes associated with waste degradation (Barclay and Rayhani, 2013). Moreover, GCLs are also exposed to sunlight in case of prior placement of GCLs before waste placement. So, the hydraulic and volume change of GCLs under elevated temperatures is important. The hydraulic and volume change characteristics of biopolymer-amended GB under extreme thermo-chemo-mechanical loadings are yet to be explored.

The leachate generated from coal combustion products (CCPs) contains high concentrations of Na^+, K^+, Ca^{2+}, and Mg^{2+} (Chen et al. 2019). The leachate generated from red mud/bauxite tailings also contains high concentrations of inorganic cations along with sulfates, and chlorides (Li and Rowe 2020). Similarly, the leachate of dolomite tailings and limestone tailings contains high concentrations of calcium ions (Farmaki et al. 2018; Harwood and Koirtyohann 1987), and potash mining leads to the generation of tailings having high concentrations of sodium and potassium ions (Tallin et al. 1990). Mining waste contains heavy metals as well, existing bentonite-based barriers show high cracking due to changes in the moisture contents, while kaolin clays exhibit minimum crack formation (Mishra et al., 2019). Kaolin clays need to be compacted at very high density to achieve fluid permeation rates lower than the permissible limits. Several biopolymers might help in reducing the permeation rates of the kaolin. Fluid permeation rates of biopolymer-amended

kaolin thus need to be explored with different salts and heavy metals. Moreover, diffusion characteristics of biopolymer-amended kaolin thus need to be studied.

The COVID-19 crisis has pushed for BMW management solutions which have led to investigations of natural materials with high sorption capacities. Clay minerals, e.g. bentonite, kaolin, illite, halloysite, and sepiolite are also favorable candidates for use as engineered barriers in BMW confinement based on their wide distribution over the earth's crust and inherit properties. Here we investigated a viral pathogen sorption study through the perspective of clay minerals, specifically focusing on bentonite. These may also be involved in sorption through the type of clay mineral, isoelectric point (IEP) of the virus, nature of the viruses, pH of the medium, SSA, and exchangeable cations types are some key factors that have an impact on it (Yu et al., 2013; Das and Bharat, 2021; Das, 2021). Although there is still a substantial knowledge gap in the basic details of virus-clay mineral interactions, the field has made much progress. We highlight the importance of further examining control mechanisms behind these virus-bentonite interactions, with an emphasis on understanding the influence that cation type and valence play in regulating them. Further, the modification of the DLVO theory for clay-virus interaction was improved by incorporating the diffused double layer theory in it.

Similarly, Japanese encephalitis and H1N1 viruses have created a pandemic in the recent past among humans. Most of the biomedical waste generated from these pandemics is disposed of in the MSW landfills in the absence of an exclusive BMW facility. The knowledge of the fate of these viruses through GCLs in landfills is not available. The role of grain sizes of GB on the attenuation ability of these viruses is to be understood. Moreover, the role of the presence of salts from landfill leachate on the sorption ability of viruses with GBs required to be studied. To design an exclusive biomedical waste facility or disposal of viral pathogenic waste in the existing MSW

landfills, the knowledge of the diffusion and hydraulic characteristics becomes important apart from the sorption studies. The diffusion coefficient of different viruses through compacted clays needs to be studied.

Overall work evaluated the role of the granulation process on hydraulic and volume change characteristics of GB in various salt environments. Further, five biopolymers were explored to improve the hydraulic performance of GB. The influence of temperatures on biopolymer-amended GB was done to evaluate its performance in extreme thermo-chemo-mechanical loading conditions. Further, various clay minerals were assessed to understand the sorption ability of viral pathogens. The mechanism for the interaction of bentonite clays with the virus is understood by experiments and theoretical modelling. The role of grain sizes of the GB on its interaction with JEV and H1N1 is also studied. Further, the diffusion and hydraulic characteristics of these viruses through compacted clays are presented. Finally, the utilization of biopolymer-amended kaolin as a liner to the mine tailing facilities is also studied for containment of salts and heavy metals.

1.3 Objectives

Based on the above discussion, the objectives of the work were listed as follows:

- To study the influence of the mechanical granulation process and plasticity of granular bentonite on sealing and volume change characteristics under extreme chemo-mechanical loadings.
- To study the sealing, volume change, and diffusion characteristics of biopolymer-amended GB under thermo-chemo-mechanical loading conditions.
- To study the sorption, hydraulic, and diffusion characteristics of viral pathogens with different clay minerals.

- To study biopolymers amended kaolin as an engineered barrier for tailing disposal facilities.

1.4 Organization of the Thesis

The thesis consists of eleven chapters including seven contributing chapters. The **Chapter 1** consists of the general introduction to the problem, motivation, scope of the work, and objectives of the present study. **Chapter 2** contains the theoretical background and literature review, which includes different clay minerals, diffused double layer theory, sorption models, diffusion theory, DLVO interaction energy evaluations, the role of grain sizes of GB, polymer or biopolymer amended GB under hydro-chemo-mechanical loadings or thermo-hydro-chemo-mechanical loadings, pathogens causing pandemic or epidemic, characteristics of pathogens, sorption of virus to clay minerals, diffusion of viruses through clays, and biopolymer amended kaolin as liner for tailing disposal facilities. **Chapter 3** contains the details of the clays used in the study. The basic characterization of studied soils was presented in detail. The details of inorganic salts, heavy metals, viruses, polymers, and biopolymers were also presented in this chapter. Further, the experimental methodologies adopted to understand the behavior of clays under chemical, hydraulic, mechanical, and thermal stresses are also discussed in this chapter. **Chapter 4** contains the influence of the grain size and plasticity of the granular bentonites on the hydraulic and volume change under chemical, hydraulic, and mechanical loading conditions. **Chapter 5** contains the hydraulic and volume change of polymer and biopolymer-amended granular bentonite under chemical, hydraulic, and mechanical loading conditions. The study considers sodium polyacrylate polymer and four different biopolymers, namely, guar gum, xanthan gum, acacia gum, and agar-agar gum. Further, the role of temperature on the hydraulic and volume change behavior of xanthan gum-amended granular bentonites is also presented in this chapter. **Chapter 6** contains the role of

the mineralogy on the sorption ability of the Newcastle disease virus. The study considered kaolinite, montmorillonite, illite, halloysite, and sepiolite for sorption studies with the virus. **Chapter 7** contains the mechanism governing the sorption of NDV to the bentonites. **Chapter 8** contains the role of the grain sizes of the granular bentonite on the sorption ability of the Japanese encephalitis virus, and PR8 strain of H1N1 influenza virus. **Chapter 9** contains the hydraulic, and diffusion characteristics of the viruses through different clays. **Chapter 10** contains the hydraulic, volume change, and diffusion behavior of biopolymer-amended kaolin under hydro-chemo-mechanical loading for containment of mine tailing waste. Further, the hydraulic and diffusion characteristics of the biopolymer-amended kaolin under constant volume conditions were studied for the containment of heavy metals from the mine tailing facilities. **Chapter 11** discusses the important conclusion from the work and the scope of future research work based on the findings in the present work.

Chapter – 2

Background and Literature Review

2.1 Background

This chapter discusses commonly available clay minerals, i.e., kaolinite, montmorillonite, and illite. Further, there is a discussion on additional clays, which have limited availability in some places worldwide. These additional clays like halloysites and sepiolite have some specific applications. The discussion then proceeds to the diffused double layer (DDL) theory to understand the behavior of clays in distilled water and salt environments. Further, sorption kinetic models, equilibrium sorption models, and diffusion theory for migration of the contaminants through compacted clays are discussed. A brief discussion on (Derjaguin–Landau–Verwey–Overbeek) DLVO theory for clay virus interaction energy has been covered. The literature review has been done at the end of this chapter.

2.1.1 Clay Minerals

Specific combinations of tetrahedral and octahedral sheets led to the formation of different clay minerals. Tetrahedral is made up of a silicon atom as a central cation and is attached to four oxygen or hydroxyl groups. Different tetrahedral silica units join by sharing corner oxygen atoms and forming a hexagonal network of these units. The corner oxygen is shared between two tetrahedral units of oxygen and the formation of a hexagonal in two dimensions is continued to form a tetrahedral sheet. The octahedral unit has an aluminum, iron, or magnesium atom at the center of six oxygen or hydroxyl groups. Aluminum is present in only 2/3rd of all the possible positions, moreover, divalent cations like magnesium are present in all possible positions to valence the

structure (Grim, 1968). The octahedral sheet is known as gibbsite when aluminum is present as the central atom and it is known as brucite in the presence of magnesium as the central atom. One or more than one silica sheets combine with alumina sheets to form clay minerals. The clay minerals are classified based on the arrangement of these silica layers and alumina layers. Different clay minerals are further discussed in detail in subsequent sections.

2.1.1.1 Kaolinite

The kaolinite mineral consists of a 1:1 layer of alumina and silica stacked together as shown in Figure 2.1. The octahedral sheet has aluminum as a central cation. The oxygen of the silica unit present at the corner of the silica unit is shared with the alumina sheet. 2/3rd of the total oxygen present in the plane of the alumina unit attached to the silica unit is shared, and the other 1/3rd oxygens are hydroxyl groups. The charges on the basal silica sheet are permanently negative due to the isomorphous substitution of Si^{4+} with Al^{3+} (Palomino and Santamaria, 2005; Das, 2022). The charge on the alumina face is pH-dependent and can be either positive or negative. The overall charge of both faces is negative with pH-dependent magnitude. Further, the edge of both sheets might contain both positive and negative charges depending on the pH (Celik, 2004; Chaudhury and Bharat, 2018). Exchangeable cations are only present at the external sheet as there is no interlayer separation between the two layers due to strong interaction between octahedral and tetrahedral layers.

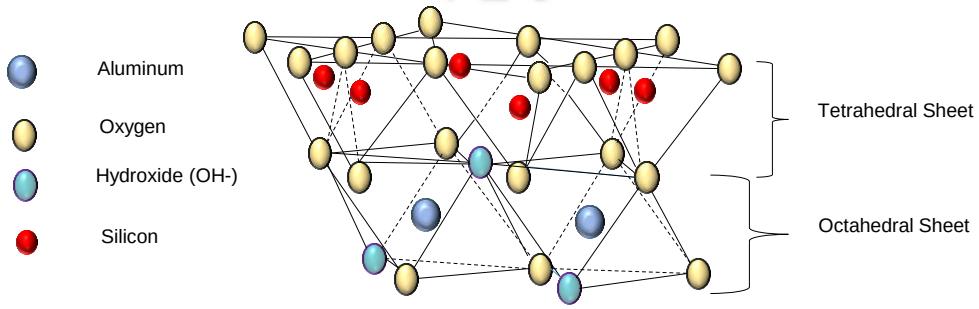

Figure 2.1: Representation of one unit of kaolinite mineral with 1:1 Alumina and silica sheets

2.1.1.2 Montmorillonite

Montmorillonite mineral is a hydrous aluminum silicate clay mineral with a dioctahedral structural configuration. They consist of repeating a 2:1 layer involving a central alumina sheet sandwiched by two silica sheets (Grim, 1968) (Figure 2.2). Both the faces of montmorillonite are similar to each other with oxygens from the silica sheets. The bonding between two adjacent montmorillonites is relatively weak. The mineral surface consists of a strong negative charge due to the isomorphous substitution of silicon with lower positive valence atoms in the silica sheet. The excess negative layer charge is compensated by the exchangeable cations (van Olphen, 1963). The interlayer space between two particles can be accessed by polar fluids like water leading to high expansion in these minerals.

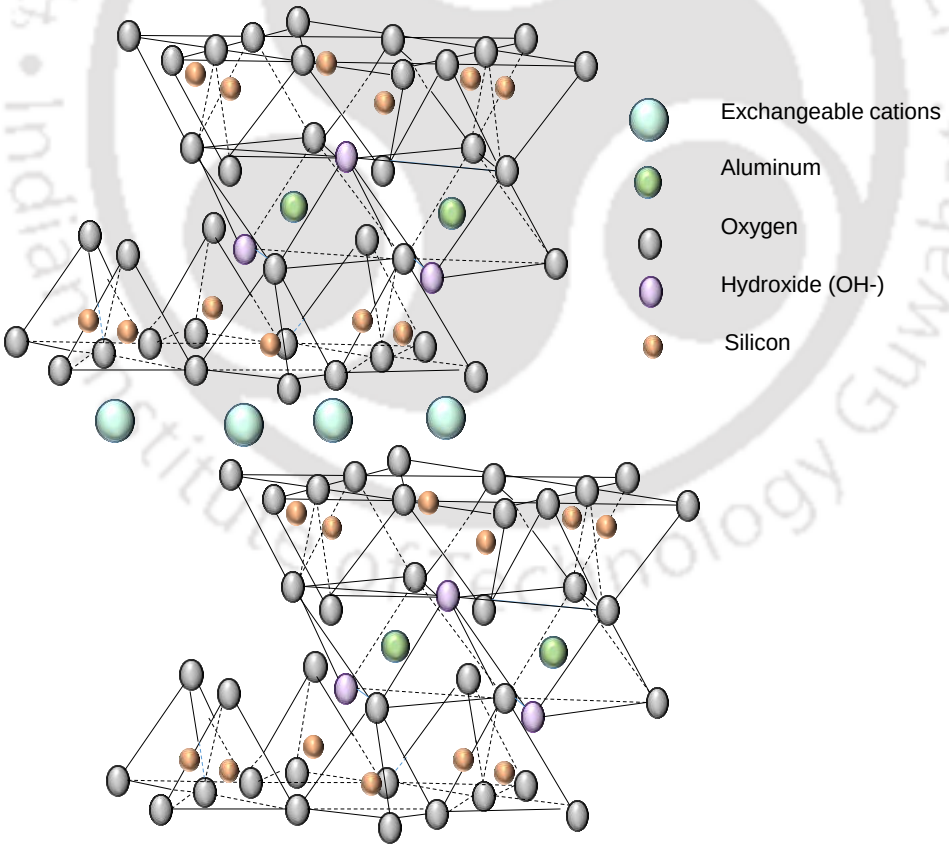

Figure 2.2: Representation of one unit of montmorillonite mineral with 2:1 Alumina and silica sheets along with exchangeable cations

2.1.1.3 Illite

Illite has a similar structure to montmorillonite with a 2:1 silica-to-alumina arrangement. The charge deficiency of these layers is balanced by potassium and this potassium is not easily exchangeable as compared to the montmorillonite. The charge deficiency in illite minerals is due to the isomorphous substitution of silica sheets, whereas the charge deficiency in montmorillonite minerals is due to substitution in inner octahedral sheets. The potassium in the structural unit of illite is relatively fixed leading to low swelling of the mineral as compared to montmorillonite and polar molecule does not interlayers.

2.1.1.4 Halloysite

Halloysite is also a 1:1 clay mineral belonging to the kaolinite group. It has a multilayer wrapped tubular structure due to geological conditions and structural mismatch in sharing oxygen between the silica and alumina sheets (Bates 1950; Singh 1996). Halloysite is chemically similar to kaolinite, except two adjacent layers in halloysite are separated by a monolayer of water molecules. Halloysite has an alumina layer as the internal layer and a silica layer as an outer layer, which led to the complete exposure of the silica sheet (Yuan et al., 2015). The internal gibbsite surface of the halloysite led to positive zeta potential for the internal surface and negative zeta potential for the outer surface (Veerabadran et al., 2007). The outer negative charges of the halloysite are balanced with exchangeable cations. Further, the termination sites of the halloysite have pH-dependent charges like kaolinite leading to the agglomeration and blockage of halloysite nanotubes at lower pH. Moreover, the switch in nature of the charge of termination sites from positive to negative upon changes in pH from lower to higher led to the dispersion of halloysite nanotube (Joo et al., 2013; Yuan et al., 2015).

2.1.1.5 Sepiolite

Sepiolite is a hydrated magnesium silicate of fibrous morphology. It has an alternate structure of blocks and tunnels, which grows in the direction of the fiber. The structural unit of the sepiolite consists of a 2:1 layer of silica and magnesium sheets. The blocks consist of a magnesium octahedral layer sandwiched between two layers of silica. The discontinuous silica layer led to the formation of many hydroxyl groups (-OH) at the corners of channels at the outer surface of sepiolite. Discontinuation in the octahedral layer also led to charge imbalance for the last magnesium in the layer, which led to the attachment of water molecules to these terminating magnesium ions, and these water molecules are known as coordinated water. Further, the water attached to other sites like tunnel oxygen from the silica layer with hydrogen bonding is known as zeolite water (Castro-Smirnov et al., 2016). The sepiolite particles cannot swell due to the edge conjugation, moreover, the specific surface area prediction of these minerals is difficult as probe molecules might not enter completely into the tunnels of sepiolite mineral (Tadiello et al., 2022). The presence of the magnesium ion in the octahedral layer makes it a negatively charged structure, which will be compensated by the presence of exchangeable cations.

2.1.2 Diffused double layer theory

The interactions of clay with the pore-fluid are important aspects for understanding the hydraulic characteristics, volume change, and sorption characteristics. The clay particles have strong negative charges, which create a high concentration of cations near the clay surface. The lower concentration of cations towards the pore-fluid creates a concentration gradient leading to the diffusion of cations to the pore-fluid. This diffusive of cations is compensated or prevented by the electrostatic forces of attraction towards the clay surface. Hence, water molecules move toward the clay surface to reduce the concentration gradient and form a water film around the clay particle

known as a diffused double layer (DDL). The DDL plays an important role in clay particle interaction. The electrostatic potential distribution in DDL is given by (van Olphen, 1963; Bharat & Sridharan, 2015; Das 2022).

$$y = 2\ln\left(\frac{\exp(\kappa x)+\exp\left(\frac{y_0}{4}\right)}{\exp(\kappa x)-\exp\left(\frac{y_0}{4}\right)}\right) \qquad (2.1)$$

where, y = normalized electrostatic potential (= vqϕ / RT); at x distance from the clay surface; y_0 is the normalized electrostatic potential at clay surface (y_0 = vqϕ$_0$ / RT = vFϕ$_0$ / RT); 1/ κ is the characteristics length, $\kappa = \sqrt{\frac{8\pi e^2 v^2 n}{\in k_B T}}$*, ∈ is the dielectric constant; n is the ion concentration (ion/cm^3); e is the elementary charge; k_B is the Boltzmann's constant; and T is the absolute temperature.*

The DDL thickness governs the engineering behavior of clays, and it depends on the electrolyte concentration; cation valence; dielectric of the media; etc. The leachate in the leachate contains salt concentration, which influences the DDL thickness of the liner material and hence it governs the performance of landfill liners as well.

2.1.3 Diffusion theory

The governing advection-diffusion equation for studying contaminant transport through saturated soils is given by (Bharat et al., 2009):

$$\frac{\partial C}{\partial t} = \left(\frac{D_e}{R_d}\right)\frac{\partial^2 C}{\partial x^2} - \left(\frac{V_s}{R_d}\right)\frac{\partial C}{\partial x} \qquad (2.2)$$

The transport of contaminants is governed by Fick's diffusion equation (eq. 2.3) in the absence of advection (Shackelford et al., 1989; Bharat, 2013; Shackelford, 1991):

$$\frac{\partial C}{\partial t} = \left(\frac{D_e}{R_d} \right) \frac{\partial^2 C}{\partial x^2} \tag{2.3}$$

Where C is the concentration of contaminant (salt) at time t (s) and spatial location x (cm); V_s is the seepage velocity; and R_d is the dimensionless retardation factor, is given by (eq. 2.4).

$$R_d = 1 + \frac{K_d \rho_d}{n} \tag{2.4}$$

Where K_d is the partition coefficient, ρ_d is the dry bulk density of soil, and n is the porosity of the soil.

The initial conditions for the laboratory diffusion test are given by (Bharat et al., 2009).

$$C(x = 0, t = 0) = C_0 \tag{2.5a}$$

$$C(x, t = 0) = 0 \tag{2.5b}$$

$$C(x = L, t = 0) = 0 \tag{2.5c}$$

Eq. 2.5 represents the concentration of salts in the source, concentration along the sample, and collector reservoir. The boundary conditions at the source and collector reservoir are given by (Bharat et al., 2009; Das & Bharat, 2017).

$$C(x = 0, t) = C_0 + \frac{nD_e}{H_s} \int_0^t \left(\frac{\partial C}{\partial x} \right)_{x=0} dt \tag{2.6}$$

$$C(x = L, t) = -\frac{nD_e}{H_c} \int_0^t \left(\frac{\partial C}{\partial x} \right)_{x=L} dt \tag{2.7}$$

Where C_0 is the initial concentration of contaminants at t = 0, H_s and H_C are equivalent heights of source and collector reservoirs, respectively.

Estimation of diffusion coefficient, D_e, and retardation factor, R_d, is important for engineered barrier design. The diffusion equation (Eq. 2.3) was solved along with initial and boundary conditions (eq. 2.5-2.7) to obtain a closed-form analytical solution (Bharat, 2013). The barrier design parameters were estimated by minimizing the errors between experimental and theoretical concentrations by solving forward analysis using the modified particle swarm optimization technique (Bharat et al., 2009).

The values of diffusion coefficient, retardation factor, and seepage velocity were evaluated experimentally for soil samples and were used for numerical analysis. The movement of contaminants through soil can be considered using the combined advection-diffusion equation. To obtain the concentration profiles with time for different cations, the partial differential equation (eq. 2.2) was solved using the forward time central space (FTCS) scheme of finite difference method using MATLAB, the discretized form of eq. 2.2 is presented as follows:

$$\frac{C_i^{j+1} - C_i^t}{\Delta t} = \frac{D_e}{R_d}\left(\frac{C_{i+1}^j - 2C_i^j + C_{i-1}^j}{\Delta x^2}\right) - \frac{V_s}{R_d}\left(\frac{C_i^j - C_{i-1}^j}{\Delta x}\right) \tag{2.8}$$

which can be presented as:

$$C_i^{j+1} = C_i^t + \frac{D_e \Delta t}{R_d \Delta x^2}\left(C_{i+1}^j - 2C_i^j + C_{i-1}^j\right) - \frac{V_s \Delta t}{R_d \Delta x}\left(C_i^j - C_{i-1}^j\right) \tag{2.9}$$

Finally, concentration profiles for 500 mm thick barrier material were obtained and design life with different cations was estimated.

2.1.4 Adsorption of Viral Pathogens

2.1.4.1 Sorption kinetics

The mechanism of virus adsorption by the clays was explored with the help of kinetic models. Commonly used adsorption kinetics models are (a) pseudo-first-order kinetic model; and (b) pseudo-second-order kinetic model (Xue & Caryn 2014; Patra et al. 2020) based on the solid-phase sorption. The equations of pseudo-first-order and pseudo-second-order kinetic models are given by:

$$\ln\left(q_e - q_t\right) = \ln q_e - k_1 t \tag{2.10}$$

and

$$\frac{t}{q_t} = \frac{1}{2k_2 q_e^2} + \frac{1}{q_e} t \tag{2.11}$$

where, q_t (PFU mg^{-1}) is the amount of virus adsorbed at time t (minutes), q_e (PFU mg^{-1}) is the equilibrium adsorption capacity, k_1 (min^{-1}) is the pseudo-first-order adsorption rate constant, k_2 (mg.PFU^{-1}.min^{-1}) is the pseudo-second-order rate constant.

2.1.4.2 Percentage removal (%)

The amount of the virus sorbed on the bentonite and kaolin surface was determined by:

$$q_e = \left[\left(C_i - C_e\right) \times \frac{V_l}{M_s}\right] \tag{2.12}$$

where q_e (PFU mg^{-1}) is the amount of the virus sorbed per unit mass of sorbent; V_l (mL) is the volume of solution used in batch test; M_s (mg) is the mass of adsorbent solid used in test; C_i

(PFU mL^{-1}) is the initial concentration of virus stock used in experiments and C_e *(PFU mL^{-1}) is the equilibrium concentration of solution.* The percentage removal of plaque was determined by

$$\left(\frac{C_i - C_e}{C_i}\right) \times 100$$

The distribution factor is a standard parameter, which is generally used to express the affinity of sorbate to sorb on solid and it is calculated using

$$(K_d)_{Sorption} = \left(\frac{C_i - C_e}{C_e}\right) \times \left(\frac{V_l}{M_s}\right) \quad (2.13)$$

2.1.4.3 Equilibrium sorption isotherms

Linear, Langmuir, and Freundlich sorption isotherm models were used in this study to understand the equilibrium sorption behavior of virus particles on clay. The linear sorption model for sorption is given in equation (2.14):

$$q_e = (K_d)_{Linear} C_e \quad (2.14)$$

Where the slope of linear isotherm provides the value of the distribution coefficient, $(K_d)_{Linear}$.

Langmuir isotherm model is a widely used isotherm model and assumes that monolayer adsorption of adsorbate (virus) over uniform adsorbent (Langmuir, 1918; Kumar et al. 2022). The linear form of the Langmuir isotherm model is as presented below in equation (2.15):

$$\frac{C_e}{q_e} = \frac{1}{bq_{\max}} + \frac{C_e}{q_{\max}} \quad (2.15)$$

Where C_e *(PFU mL^{-1}) is the equilibrium virus concentration remaining in the solution;* q_e *(PFU.mg^{-1}) is the adsorbed amount of virus per unit mass of adsorbent after attaining equilibrium;*

b (mL. PFU^{-1}) is Langmuir isotherm constant which represents adsorption energy and q_{max} *represents maximum adsorption capacity.* The Langmuir isotherm constant, b is related to another dimensionless coefficient known as the separation factor, $R_{L,}$ to determine whether the adsorption process is favourable or not. The separation factor is related to the parameter as shown in equation (16) (Langmuir, 1918; Patra et al., 2019):

$$R_L = \frac{1}{1+bC_i} \tag{2.16}$$

where, C_i *is the initial virus concentration and b is the Langmuir isotherm constant.* The value of the separation factor represents the favourability of adsorption ($R_L > 1$ for unfavourable adsorption; $R_L = 1$ for linear adsorption; $0 < R_L < 1$ for favourable adsorption; and $R_L = 0$ for irreversible adsorption).

The Freundlich adsorption isotherm is considered a multi-layer of virus adsorption on the clay surface. This adsorption model considers the uneven distribution of adsorption over non-uniform surfaces (Freundlich & Heller, 1939). The linearized form of the model is as given below in equation (2.17):

$$\ln q_e = \ln K_f + n \ln C_e \tag{2.17}$$

Where, q_e *(PFU.mg^{-1}) is the sorbed concentration;* K_f *(PFU^{1-n}.mL^n.mg^{-1}) is the Freundlich coefficient and n is the exponent and it determines the degree of sorption linearity.*

The sorption potential of clay liners (i.e., retardation factor) based on the batch sorption assuming linear and Freundlich isotherm is given by following equations:

$$(R_d)_{Linear} = 1 + \frac{\rho_d (K_d)_{Linear}}{\eta} \quad (2.18)$$

$$(R_d)_{Fruendlich} = 1 + \frac{\rho_d K_f C_0^{(n-1)}}{\eta} \quad (2.19)$$

where, η *is the porosity of the clay;* ρ_d *is the dry density of the clay;* $(K_d)_{Linear}$ *is the linear sorption parameter (mL/mg); n and* K_f *(PFU^{1-n}.mL^n.mg^{-1}) are the Freundlich isotherm constants.*

2.1.5 DLVO Theory

The Derjaguin–Landau–Verwey–Overbeek (DLVO) theory is utilized to evaluate the interaction energy between two smooth homogeneous surfaces with ideal geometries. The sum of attractive energy due to van der Waal forces, repulsive energy due to overlap of electric double layers, and Born repulsion energy at very close separation distance. So, the total energy between two surfaces is arithmetic sum of diffused layer potential energy, ϕ_{dl}, van der Waal, ϕ, and Born potential energy:

$$\phi_{DLVO}(x) = \phi_{vdW}(x) + \phi_{dl}(x) + \phi_{Born}(x) \quad (2.20)$$

Since the clays are much larger surfaces than the virus, so the interaction between the clay particle and virus can be assumed as sphere – plate type of interaction. For sphere – plate like geometries the van der Waal interactions can be evaluated using following expression (Gregory; 1981):

$$\phi_{vdW}(x) = -\frac{A_{123} r_P}{6x}\left(1 + \left(\frac{14x}{\lambda}\right)\right)^{-1} \quad (2.21)$$

where, h is the separation distance between the approaching particles; r_p *is the radius of the particles (virus);* A_{123} *is the combined Hamaker constant for colloid (virus), medium 1, and clay*

plate, medium 3 in medium 2 (i.e., water). λ is the characteristic wavelength for sphere–particle interactions.

The diffused layer interaction energy for the sphere–plate system can be evaluated based on the following expression:

$$\phi_{dl}(x) = \pi \in_r \in_0 \left[2\psi_P \psi_S \ln\left(\frac{1+e^{-kx}}{1-e^{-kx}}\right) + \left(\psi_P^2 + \psi_S^2\right) \ln\left(1-e^{-2\kappa x}\right) \right] \tag{2.22}$$

where, $\in_r = \in/\in_0$ is the relative dielectric constant of liquid; $\in$ is the dielectric constant of suspending liquid; and $\in_0$ is the permittivity of free space; ψ_p is the surface potential of colloid particle (virus); ψ_s is the surface potential of clay platelet; and κ is the inverse of diffused layer thickness and can be evaluated using following expression:

$$\kappa = \left[\frac{2nN_A 1000.e^2}{\in_r \in_0 k_B T} \right]^{1/2} \tag{2.23}$$

where, I_s is the ionic strength, N_A is the Avogadro's number, e is the elementary charge; k_B is the Boltzmann's constant; and T is the absolute temperature.

The Born energy for sphere–plate can be evaluated using the following relationship (Ruckenstein and Prieve, 1976):

$$\phi_{Born} = \frac{A_{123}\sigma_{Born}^6}{7560} \left[\frac{8r_P + x}{\left(2r_P + x\right)^7} + \frac{6r_P - x}{x^7} \right] \tag{2.24}$$

where, σ_{Born} is the born collision parameter; The ϕ_{Born} can easily neglected for h > 1nm, and the presence of hydrated ions in the aqueous system will prevent separation distance to achieve 0.3 nm.

2.2 Literature Review

2.2.1 Role of Grain Sizes of Granular Bentonites

A granulated form of bentonite is preferred in most of the GCLs due to its workability. The bentonite in its natural state is obtained by quarrying in solid form, which contains about 30% moisture content. The material is dried and crushed. The final crushing, grinding, or milling operation led to different grain sizes of bentonites as per the requirement (Kutlić et al., 2012). The final grain sizes of the granular bentonite (GB) depend on the mining source, the initial moisture content in natural form, the preparation method, mechanical processing, and plasticity. Therefore, the average granule size of the GBs also varies with the batch from the same manufacturer. Granular bentonite in the natural state in GCL contains several macro voids. The granules of GB swell by hydration and seals these voids and the process of sealing of voids in granular bentonite is called self-sealing ability. The self-sealing is also important for the sealing of technological gaps created between the bentonite blocks in nuclear waste repositories and sealing of the puncture in GCL during the placement in the field (Rowe and Li, 2020; Li and Rowe, 2020; Parastar et al., 2017; Rowe, & AbdelRazek, 2020). In this study, the term self-sealing of granular bentonite was used for the sealing of macro voids present between the granules of the GB.

The initial degree of hydration of GB influences the hydraulic conductivity as well as the diffusion characteristics of the GCL. Insufficient hydration of GCLs is, however, reported due to high thermal exposure of GCLs in the field (Rowe et al., 2011; Benson 2013; Acikel et al., 2018a). The

temperatures near the liner reach up to 55ºC due to physical, biological, and chemical processes of waste decomposition in municipal solid waste landfills (Barclay and Rayhani, 2013). Therefore, the GCLs remain unhydrated in the landfill before exposure to the leachate. The hydraulic behavior of GCLs with chemical loads under initial unhydrated conditions is important (Acikel et al., 2018a).

Granule size distribution (GSD) or mean grain size of GB is found to play an important role in the hydration characteristics of bentonite. The mean effective grain size (D50) of granules of GB varied in a range of 0.25 mm to 1.0 mm as reported in various studies (Seiphoori et al. 2016; Anderson et al., 2012; Jo et al., 2001; Lee and Shackelford, 2005; Chen et al., 2018). A significant difference in the hydration rates in granular and powder bentonite is observed (Vangpaisal and Bouazza, 2004; Bouazza et al., 2006). Effective gel formation of powdered bentonite was observed over granular bentonite due to the larger exposed surface area in powdered bentonites with water (Vangpaisal and Bouazza, 2004). In granular bentonite, water permeates across the soil before sealing is achieved by swelling of grains due to the availability of easier flow paths in comparison to powder bentonite. Moreover, the soil water characteristics are different from the GSDs (Acikel et al., 2018b; Rouf et al., 2016). However, the influence of the initial gradation of the granular bentonite in GCL on the hydraulic and sealing behavior is not available.

The role of grain sizes of GBs on hydraulic and volume change behavior under chemo-mechanical loading conditions is to be established. Further, the role of the quality of the GB on hydraulic and volume change under chemo-mechanical loadings is also not understood properly and is to be evaluated.

2.2.2 Polymers and Biopolymer amended GB as Engineered Barrier

The GCLs act as a barrier to the contaminant's migration from waste disposal facilities to the groundwater (Bouazza and Bowders, 2009; Tian et al., 2016; Rowe and Li, 2020; Das and Bharat 2021). The granular form of bentonite is generally preferred in GCLs due to its workability, and pouring ability, and it is the primary product during the manufacturing process of bentonite (Seiphoori et al, 2016; Kutlić et al. 2012). The granular bentonite (GB) present in GCLs contains large macro-voids, which seal upon the hydration of bentonite. The hydration of GB leads to the disintegration of granules into individual particles due to the formation of diffused double layers (DDLs) (Das and Bharat, 2021). The process of disintegration of GB into individual particles and sealing of macro-voids is known as the sealing ability of GB (Das and Bharat, 2021). The effectiveness of the GCLs depends on their hydration with moisture before encountering contaminants (Petrov and Rowe, 1997; Rayhani et al. 2011; Anderson et al., 2012).

Landfill leachate contains a high concentration of sodium, potassium, and calcium due to waste from the rubber industry, and construction & demolition waste (Boopathy et al., 2013; Das and Bharat, 2021). Further, the waste from pharmaceutical industries during the production process and improper disposal of pharmaceuticals from households also lead to their accumulation in landfills (Kusturica et al., 2020; Daughton, 2003). Pathogenic waste from the recent COVID pandemic also reached landfills (WHO, Interim Guidelines, 2020; Zand and Heir, 2020; Anand et al., 2022). Moreover, industrial landfill leachate contains harmful dyes, pigments, pesticides, and potentially carcinogenic compounds (Góralczyk-Bińkowska, et al., 2021; Benkhaya, et al., 2020; Haarstad and T. Mæhlum; 2008). Leachate from coal combustion products (CCPs) also contains high concentrations of these cations along with heavy metals (Chen et al., 2019). Leachate from bauxite, dolomite, potash, and limestone tailings contain sodium, potassium, and calcium salts

along with other harmful contaminants (Li and Rowe, 2020; Farmaki et al., 2018; Harwood & Koirtyohann, 1987; Tallin et al., 1990). In the presence of high-concentration salt solutions, the GB loses its sealing ability due to poorly developed osmotic potential. The van-der-Waal forces of attraction among the bentonites in granules are dominant and lead to poor disintegration of GB. The non-sealing ability of GB in such an environment leads to advection-controlled migration of leachate. Different contaminants like heavy metals, dyes, pigments, pesticides, pharmaceuticals, phenol, etc. can easily pass through the macro-voids present in GB and can severely contaminate the groundwater.

Several researchers are exploring the second generation GCLs, which contain the polymer-amended GB to overcome the non-sealing ability of GBs under extreme chemical loadings. Propylene carbonate enhanced the swelling of bentonite by enhancing the osmotic swelling (Onikata et al., 1996 & 1999; Lin et al., 2000; Katsumi et al., 2008; Mazzieri et al., 2010). Hyper clay GCLs produced after the amendment of bentonite with sodium-carboxymethyl cellulose (Na-CMC), and glycerol carbonate also enhanced the swelling (Di Emidio et al. 2010; 2011; and 2015). Several mechanisms governing the hydraulic performance were hypothesized as enhanced osmotic swelling of the intercalated bentonite particles; pore-clogging among the particles; and prevention of cation exchange (Scalia et al., 2018). These polymers are either linear or crosslinked in nature. The interactions of clay particles and polymers are governed by electrostatic forces of attraction, hydrogen bonding, ion-dipole interaction, and cation bridging. Although polymerized clays have been explored for more than 10 years, still there is a lack of understanding of the mechanism controlling the hydraulic, volume-change, and diffusion behavior.

A new cross-linked polymer, sodium polyacrylate, and novel linear biopolymers, guar gum (GG), acacia gum (AG), agar-agar gum (AA), and xanthan gum (XG) are explored for improvement in

the sealing-ability of GB under adverse chemical and mechanical loadings. The GB was amended with either polymer or biopolymer using dry mixing before the permeation experiment. Polymers and Biopolymers contain large amounts of carboxyl groups ($-COO^-$) and hydroxyl groups. These carboxyl or hydroxyl groups attract water due to a high negative charge and start swelling upon hydration with water and form hydrogels.

The GCLs are subjected to mechanical loading due to the presence of weight of the waste in landfills or mine tailing facilities. Moreover, the GCLs are also subjected to hydraulic loading due to the presence of leachate and chemical loadings due to the presence of contaminants in leachate. The hydraulic and volume change of the liner material is important under hydro-chemo-mechanical (HCM) loading conditions. The GCLs in landfills or tailing facilities are also subjected to elevated temperatures before the placement of waste or due to the decomposition of MSW in landfills. However, the performance of liners or biopolymer-amended GBs under Thermo-hydro-chemo-mechanical loadings is not available. The current study evaluates the hydraulic and volume change behavior of polymer and XG-amended GB under HCM loadings. Further, the hydraulic and volume change behavior of XG-amended GB under THCM loadings is also to be established. The through-diffusion experiments were conducted on the samples attaining the sealing to evaluate the diffusion and retardation characteristics. The mechanisms governing the behavior were discussed in detail.

2.2.3 Introduction to the Viral Pathogens

Millions of viruses are present in the world, and some of them can cause outbreaks of epidemics or pandemics. Some viruses have already created pandemic situations in the past including the recent COVID-19 pandemic. Enveloped viruses contain protein covering over the inner DNA or RNA, these outer protein covering can also have the presence of one or more than one type of

spike proteins. Some examples of enveloped viruses are coronavirus, influenza virus, flavivirus, African swine flu virus, Newcastle disease virus, Japanese encephalitis virus, and simplex virus. Moreover, non-enveloped viruses do not contain outer protein covering. Norovirus, calicivirus, astrovirus, rotavirus, adenovirus, and enterovirus are examples of non-enveloped viruses. Due to the presence of the protein covering and spike proteins, the size of enveloped viruses is larger than non-enveloped viruses (Kumar et al., 2021).

2.2.4 Methods for quantification of viruses

Quantification and rapid detection of the viral become very crucial during the spread of the pandemic. It is required for accurate diagnosis, understanding of disease dynamics, vaccine development, and minimizing the impacts of outbreaks on public health. Polymerase chain reaction (PCR) is widely used for the detection of the genetic material of the virus by amplifying the viral ribonucleic acid (RNA) to detect its presence (Corman et al., 2020; Tahamtan and Ardebili, 2020; Liu et al., 2020). The antigen testing based on specific surface proteins are also used to detect the coronavirus although this technique is quite faster but a slightly less accurate method than the PCR testing (Ogata et al., 2020). As antibody testing detects the presence of antibodies due to infection, this method is utilized to detect previous exposure to the virus rather than active infection (Petherick, 2020; Tang et al., 2011; Noda et al., 2021). Polymerase chain reaction (PCR), reverse transcription – PCR (Vabret et al., 2001; Matoba et. al., 2014), real-time quantitative PCR (qPCR) (Colombo et al., 2019), loop mediation isothermal amplification (LAMP) (Huang et al., 2020), recombinase polymerase amplification (RPA) (Xi et al., 2019), helicase – dependent amplification (HDA) (Toe et al., 2015), rolling circle amplification (RCA) (Na et al., 2018), Enzyme-linked immunosorbent assay (ELISA) (Chen et al., 2019), lateral flow immunoassay (LFIA) (Rong et al., 2019), and blotting technique (Zhang et al., 2014) are frequently

used. Moreover, the techniques like Haemagglutination (HA) test as per OIE terrestrial manual (OIE, 2012), Tissue culture infective dose 50 ($TCID_{50}$) (Ahamed et al., 2004), plaque-forming unit (PFU) calculations (Jang et al. 2011). Techniques like qPCR require specialized equipment and have relatively longer runtime, while LAMP requires a high run temperature of up to 65˚C and multiple primers, which is generally challenging. The ELISA has a long run time and often reports false negatives in early infection. Blotting and LFIA techniques show qualitative or semi-qualitative results with limited sensitivity.

2.2.5 Biological Decay of Pathogens

The spread of a viral pandemic depends on several factors including temperature, relative humidity (RH), and ultraviolet (UV) radiations from the sunlight. The reason behind the changes in infection rates of viral pathogens is the decay of these pathogens with time. The viral pathogens decay faster at higher temperatures, and more exposure to UV radiations (Beggs & Avital, 2021). The rate of the decay or decay coefficient can be evaluated by considering the first-order decay of viral pathogens as given in Equation 2.25:

$$N_t = N_0 \times e^{-\lambda t} \tag{2.25}$$

where, N_0 and N_t are the number of viral particles at time zero and t minutes, respectively λ (min^{-1}) is the decay coefficient and t is time in minutes.

The decay coefficient of different viral pathogens under different temperature and relative humidity conditions are summarized in Table 2.1

Table 2.1: Half-life and decay coefficient of different viral pathogens

S. No.	Pathogens	Half-Life (hrs)	Decay coefficient (hrs^{-1})	Method Used	Media	Temperature (°C)	RH	Reference
1.	MERS-CoV	0.9545	0.726	TCID50	Plastic	20	40	van Doremalen et al., 2013
		0.4418	1.569			30	30	
		0.9040	0.767			30	80	
		0.9401	0.737		Steel	20	40	
		0.9736	0.712			30	30	
		0.6412	1.081			30	80	
2.	SARS-CoV2	1.09	0.636	TCID50	Aerosols	22	65	van Doremalen et al., 2020
		0.774	0.895		Copper			
		3.46	0.200		Cardboard			
		5.63	0.123		Steel			
		6.81	0.102		Plastic			
3.	SARS-CoV-1	1.18	0.587		Aerosols			
		1.5	0.462		Copper			
		0.587	1.181		Cardboard			
		4.16	0.167		Steel			
		7.55	0.092		Plastic			
4.	Bacteriophage, ϕ6	81.5	8.5×10^{-3}	Plaque assay	Toy	22	60	Bearden and Casanova, 2016
		35.5	0.0195			22	40	
5.	Transmissible gastroenteritis Virus (TGEV)	1825	3.798×10^{-4}	Plaque Assay	Steel	4	20	Casanova et al., 2010
		359	1.932×10^{-3}				50	
		287	2.412×10^{-3}				80	
		473.5	1.464×10^{-3}			20	20	
		42.79	0.0162				50	
		180.8	3.83×10^{-3}				80	
		25.17	0.0275			40	20	
		3.4	0.204				50	
		3.89	0.178				80	
6.	Mouse Hepatitis Virus (MHV)	1242	5.58×10^{-4}	Plaque Assay	Steel	4	20	
		252	2.75×10^{-3}				50	
		412.9	1.679×10^{-3}				80	
		627.8	1.104×10^{-3}			20	20	
		56.02	0.0124				50	
		72.66	9.54×10^{-3}				80	

	38.76	0.0178			20
	4.55	0.1524		40	50
	2.402	0.2885			80

2.2.6 Isoelectric Point of Viruses

Viruses have pH-dependent surface charges in polar media like water. This surface charge of the virus plays an important role in its adsorption on charged clay particles. Electrostatic forces between the virus and clay are responsible for interactions. The pH of the media at which electrostatic charge switches its nature is known as the Isoelectric point (IEP) of the virus. The IEP of the virus is a unique property of any type of virus and governs its behavior. The IEP of several viral strains was presented in tabular form along with the method used.

Table 2.2: Isoelectric point of different viral strains along with the method used

S. No.	Virus	Strain	IEP	Method Used	Reference
1	Cowpox	Brighton	4.3	EM-LM	Douglas et al. (1969)
		Kampen	5.4	IEF-DA	Mouillot and Netter (1977)
2.	Hepatitis A virus	Hepatitis A virus	2.8	IEF-DA	Nasser et al. (1992)
3.	Human Adenovirus C	Human adenovirus 5	4.5	EM-LS	Trilisky and Lenhoff (2007)
4.	Human enterovirus B	Human echovirus 1 (4CH-1)	5.5	IEF-A	Zerda and Gerba (1984)
		Human echovirus 1 (R115)	6.2		
		Human echovirus 1 (V212)	6.4		
		Human echovirus 1 (V239)	5.3		
		Human echovirus 1 (V248)	5.0		

5.	Human rhinovirus A	Human rhinovirus 2	6.8	CIEF	Schnabel et al. (1996)
			6.4	IEF-DA	Korant et al. (1975)
6.	Influenza A virus	H1N1 (Leningrad)	4 – 4.5	EM-LM	Molodkina et al. (1986)
		H3N1	6.5 – 6.8	IEF-PA	Brydak (1993)
		H3N2 (Leningrad)	5.0	EM-LM	Molodkina et al. (1986)
		PR8	5.3	EM-LM	Miller et al. (1944)
		Influenza A virus	6.5 - 7	EDN-FET	Patolsky et al. (2004)
7.	Monkeypox	Chimpanzee Paris	6.2	IEF-DA	Mouillot and Netter (1977)
		Copenhague	6.5		
		Denmark	3.4	EM-LM	Douglas et al. (1969)
8.	Poliovirus	PV-1	7.4 and 4	IEF-DA	Nasser et al. (1992)
			6.9	IEF	Brioen et al. (1985)
		PV-1 Brunender	7.4 and 3.8	IEF-DA	La Colla et al. (1972)
		PV-1 Brunhilde	7.1	IEF-A	Zerda and Gerba (1984)
			7.1 and 4.5	IEF-DA	Mandel (1971)
		PV-1 Chat	7.5 and 4.5	IEF-PA	Ward (1978)
		PV-1 LSc2ab	6.6	IEF-A	Zerda and Gerba (1984)
			6.75 and 4.1	IEF-DA	Butler et al. (1985)
		PV-1 Mahoney	8.3	IEF-DA	Floyd and Sharp (1978)
		PV-2 Sabin T2	6.5 and 4.5	IEF	Murray and Parks (1980)
9.	Rotavirus A	Simian rotavirus A／SA11	8.0	IEF_DA	Butler et al. (1985)
10.	Smallpox	Harvey	3.4	EM-LM	Douglas et al. (1969)
		Moloya, Teheran,	5.6	IEF-DA	Mouillot and Netter (1977)

		Vannes, Djibouti			
		Sidi Amock, Harvey	5.9		
		Butler	5.7		
11.	Enterobacteria phage MS2	Enterobacteria phage MS2	3.9	IEF-A	Zerda and Gerba (1984)
			3.5	EM-LS	Penrod et al. (1995)
			3.9	IEF-DA	Nasser et al. (1992)
12	Enterobacteria phage T4	Enterobacteria phage T4	2.0	EM-LS	Aronino et al. (2009)
			4.0 - 5.0	IEF-PA	Childs and Birnboim (1975)
13.	Enterobacteria phage uX174	Enterobacteria phage S13	7.0	-	Aach (1963)
		Mutants	7.4		
		Wild type	6.6		
		Enterobacteria phage uX174	2.6	EM-LS	Aronino et al. (2009)
			6.6	-	Horka´ et al. (2007)

2.2.7 Containment of Pathogenic Waste from Coronavirus or NDV using Clay Minerals

Pathogenic wastes are hazardous due to the virulent nature of the pathogens involved.-Pathogenic waste significantly risks animal health, food safety, the national economy, human health, and the environment. Thus, proper management of pathogen waste is necessary. COVID-19, a highly contagious viral infection due to SARS-CoV-2, has created a global health emergency across the globe. Several variants of coronavirus, such as B.1.1.7 from the UK, B.1.351 from South Africa, P.1 from Brazil, and B.1.617.2 from India after mutations are observed (Kumar et al., 2021). A large amount of pathogenic waste has been generated from isolation facilities, and hospitals in the form of personal protective equipment (PPE) kits, needles, syringes, masks, etc., from the SARS-CoV-2 (Chawdhury et al., 2022). A sudden increase in massive pathogenic waste has created a

disposal problem. Open disposal of pathogenic waste, virus-containing faeces, and sanitary waste are the potential reasons for secondary transmissions of virus. The World Health Organization (WHO) recommends disposing of healthcare waste containing human viral pathogens into municipal solid waste (MSW) landfills (WHO Interim Guidelines, 2020). Most of the nations have been disposing of this waste in the existing landfills due to the absence of exclusive biomedical waste disposal facilities. Due to the inability to seal macro-voids in granular bentonite of geosynthetic clay liners (GCLs), there are possibilities of advection dominant virus migration through GCLs under a leachate environment. However, limited theoretical studies (Das & Bharat, 2022), and molecular dynamic simulations (Tiwari et al., 2022) on the fate and transport of viral pathogens through clays are recently available, and experimental studies on virus transport are lacking to provide scientific rationale in accepting pathogenic waste into MSW landfills. Such studies are also useful for developing pathogenic waste disposal protocols for future epidemics or pandemics.

The present study considers the Newcastle disease virus (NDV) as a surrogate virus for coronavirus to study its fate and transport. Several studies on the virucidal efficiency of disinfectants, and heat inactivation were conducted on surrogate viruses to study the test virus (Steinmann, 2004; Slomka & Appleton, 1998). For example, the Duck hepatitis B virus is used as a surrogate to the hepatitis B virus for inactivation study (Tsiquaye & Barnard, 1993), the Bovine viral diarrhea virus as a surrogate to the hepatitis C virus, and the Feline calicivirus is used as a surrogate to the Norovirus (Slomka & Appleton, 1998). Moreover, recent studies on vaccine development have successfully used the NDV as a surrogate for the coronavirus (Sun et al., 2020a, b; 2021). The phenomenon of vaccine development is much more complex due to the involvement of biological processes, NDV still is found to be a good surrogate for vaccine studies. Thus, NDV

was chosen for the barrier applications. NDV is a single-stranded enveloped RNA virus like-coronavirus. NDV belongs to the family of *Paramyxoviridae*. The NDV is used as a vaccine vector for SARS-CoV2 due to the presence of similar spike protein and is easier to handle in the laboratory, the handling of SARS-CoV2 requires biosafety level 3 (BS3) labs. Moreover, Newcastle disease is an infectious and contagious viral infection that affects more than 250 different bird species worldwide with various degrees of vulnerability (Miller & Torchetti, 2014; Kaleta & Baldauf, 1998). A large amount of pathogenic waste gets generated from the NDV outbreaks in the form of carcasses, potentially contaminated feces, litter, farm bedding, and fomites.

The sorption characteristics of the coronavirus or NDV with different clay minerals like montmorillonite, kaolinite, illite, halloysite, and sepiolite are not available and need to be established to understand the role of the mineralogy. Some of these clay minerals can be utilized as the exclusive liner material for biomedical waste disposal facilities depending on their sorption characteristics.

2.2.8 Mechanisms for bentonite-virus sorption

Bentonite clays based on montmorillonite minerals have a high sorption ability for proteins and viral pathogens. The understanding of the sorption ability of the virus to these clays still lacking or not properly understood due to variations in viral characteristics. The mechanism governing the sorption of NDV to the bentonite clay would be understood. The role of type and valence of the exchangeable cations of the bentonite on the sorption characteristics of the NDV will be understood to check whether the virus is directly attaching to the negatively charged clay surface or the presence of cation is playing the role.

2.2.9 Role of grain sizes of GBs in GCLs for Pathogenic Waste from JEV and H1N1 Influenza Virus

Japanese encephalitis (JE) is caused by the Japanese encephalitis virus (JEV), mosquitos act as carriers of this virus. JEV is predominant in East, Southeast, and South Asia, including some parts of Australia (Mackenzie et al., 2004; Campbell et al. 2011). Despite being a low fatality rate, the JE is the cause of concern due to the permanent neurological damage to more than half of the symptomatic survivors (Nath et al., 2020). Recent studies estimated more than 65,000 cases annually along with 20,400 deaths due to JE (Campbell et al. 2011). In India, JE has become common in the Northern parts and UP has become the epicenter for this disease, about 1000 kids die every year from UP each year and it has been declared a national emergency since 2007 (Ghosh and Basu, 2009). Apart from the humans, JE also infects cattle, sheep, dogs, cats, poultry, and reptiles. The outbreak among these species also creates potentially pathogenic contaminated faeces and carcasses.

The extremely contagious airborne disease known as influenza is caused by the influenza virus, which affects populations of birds, people, and mammals. The only influenza viruses that have been linked to pandemics are Influenza A type viruses (IAV). A pandemic can happen when a novel and extremely distinct IAV subtype spreads from poultry to wild aquatic birds and is capable of infecting humans. IAV subtypes that had caused significant human pandemic mortality included the H1N1 variations that produced the "Spanish flu" in 1918 and the swine flu pandemic in 2009 (Johnson and Mueller, 2002; Kilbourne, 2006). Such pandemics due to human viral pathogens can create an emergency. The pandemic situation also leads to the generation of huge waste containing pathogens in the form of gloves, masks, syringes, kits, etc. Moreover, the outbreak in the avian species can cause the generation of large waste in the form of carcasses, and potentially

contaminated faeces. The safe disposal of such waste is a challenging task for the waste managing authorities due to the involvement of the virulent nature of the pathogens. Several viral outbreaks in the recent past made us think about the proper way of disposal of pathogenic waste.

Moreover, a large quantity of pathogenic waste is generated during the treatment from the hospitals and isolation facilities in the form of gloves, needles, syringes, and masks. Due to the lack of knowledge and treatment facilities, the pathogenic waste is directly disposed of the dumpsites or landfills without knowing the fate of the pathogens. The GCLs contain of granular bentonite (GB), the GB granules swell and disintegrate into the individual clay particles. The GB particle disintegration leads to a fluid permeation rate lower than the limiting value. The bentonite has different sizes of granules depending on the batch, and site of excavation. The granules having any size can achieve the sealing of the macro-voids when distilled water is permeation. The extent of the breaking of GB into individual particles governs its behavior. The role of pore-fluid becomes very important in such a situation. The bentonite clays, dominant with montmorillonite mineral have an excellent adsorption ability to the heavy metals, inorganic salts, proteins, DNAs, RNAs, bacteriophages, and viruses due to negatively charged clay particles. JEV has a positive sense, single-stranded, RNA genome. The envelope protein of the JEV is capable of receptor binding (Nath et al., 2020). JEV has the ability for sorption on clay particles, but there is no study on the JEV-clay interactions. Only a few sorption studies on clay-bacteriophages are available (Aguzzi et al. 2007; Slowing et al. 2008; Park et al., 2016), but the bacteriophages might not represent the true behaviour of the clay-JEV interactions. The role of grain sizes of GB on the sorption ability of the JEV is to be established.

The influenza type A (H1N1 virus) contains hemagglutinin (HA) and neuraminidase (NA) as surface proteins. Due to the presence of the charges in these proteins, they potentially get attached

to the negatively charged bentonite particles. There are few studies on clay-pathogen interactions are available for drug delivery purposes. However, studies on the sorption of the H1N1 with bentonite clays are lacking. The sorption performance of the GB is most important before disposal of such waste to landfills. The influence of the granule size on the performance of the virus-containing waste is not studied in a salt environment. The objective of the present study is to understand the influence of the granule size on the sorption characteristics of the H1N1 influenza virus with and without a salt environment.

2.2.10 Diffusion of Viral Pathogens through Clay Minerals

Diffusion is the process of migration of viral pathogens from regions of higher concentration to low concentration. Diffusive flux according to Fick's first law through any compacted clay barrier can be presented as:

$$F = nD_e \frac{\partial C}{\partial x} \qquad (2.26)$$

where F is the flux through a unit area in a unit time interval; C is the concentration of the virus in liquid solution; x is the distance in the direction of transport; n is the effective porosity; and D_e *is the effective diffusion coefficient. The effective diffusion coefficient,* $D_e = \tau D_0$, *where* D_0 *is the free solution diffusion coefficient and* τ *is the tortuosity factor, accounts for the tortuous path in compacted bentonite.* The tortuosity factor is defined as the ratio of straight length to the actual path traveled by virus particles. There is no study reporting the effective diffusion coefficient of the virus through compacted bentonite or compacted kaolin. But few studies reported the free solution diffusion coefficient of some viruses as shown in Table 2.3. The previous study (Das & Bharat, 2022) on the transport of viral pathogens assumed a range of 0.11 – 0.64 for value τ, to evaluate the effective diffusion coefficients of the viral pathogens.

Table 2.3: Free solution diffusion coefficient of different viral pathogens and bacteriophages

S. No.	Virus	Conditions	D_0 (m^2/sec)	Method	Reference
1	Tobacco Mosaic Virus (TMV)	pH – 5	4×10^{-12}	Dynamic light scattering	Santos et al., 1996
		pH – 7.2	3.9×10^{-12}		
		pH – 10	4.2×10^{-12}		
2.	SARS-CoV-2	Medium - Water	3.10×10^{-12}	Stokes – Einstein Equation	Bavi et al., 2022
3.	Influenza Virus	-	3.18×10^{-12}	Stokes – Einstein Equation	Beauchemin et al., 2006
4.	MS2	-	1.97×10^{-11}	Stokes – Einstein Equation	Anders and Chrysikopoulos, 2009
	PRD1		7.78×10^{-12}		
5.	TMV	T-20℃ and pH 7.5	4.25×10^{-10}	Light Scattering	Moller, 1964
	MS2	T-20℃ and pH 7.3	1.16×10^{-11}		
6.	Reo-Virus	pH 7 and T-32 ℃	8.3×10^{-12}	Light Scattering	Gomatos and Tamm, 1963
7.	Qβ	d – 29 nm	16.6×10^{-12}	Membrane flux	Baltus et al., 2017
			15.2×10^{-12}	Light Scattering	
	ϕX-174	d – 26 nm	14.8×10^{-12}	Membrane flux	
			15.4×10^{-12}	Light Scattering	
	MS2	d – 28 nm	16.3×10^{-12}	Membrane flux	
			15.7×10^{-12}	Light Scattering	
	PRD1	d – 70 nm	6.1×10^{-12}	Membrane flux	
			5.1×10^{-12}	Light Scattering	
	T4	120×86 nm capsid; 140×50 nm tail	4.9×10^{-12}	Membrane flux	
			4.2×10^{-12}	Light Scattering	
	P1	65 nm capsid; 220×20 nm tail	4.1×10^{-12}	Membrane flux	
			4.5×10^{-12}	Light Scattering	
	P22	65 nm capsid; 27×3.8 nm center tail hub; 6× (18×8) nm tail spike	3.8×10^{-12}	Membrane flux	
			3.7×10^{-12}	Light Scattering	
	Mu1	60 nm capsid; 100×18 nm tail	4.9×10^{-12}	Membrane flux	
			4.3×10^{-12}	Light Scattering	

The values present in Table 2.3, are evaluated either based on light scattering in virus samples and do not involve compacted clays during experiments or based on empirical relations. So, even after the availability of these diffusion parameters in the literature, the applicability of these parameters for compacted clay barriers is debatable. Further, there is no diffusion study is conducted on compacted clays with viral pathogens. So, diffusion characteristics of viral pathogens through compacted clays should be evaluated through experiments for reliable design of BMW facilities.

2.2.11 Biopolymer-Amended-Kaolin Clays as Engineered Barrier System

When utilizing a material as an engineered barrier, hydraulic and diffusion performance are crucial. To stop advective flows, the material's hydraulic infiltration rate is crucial. The diffusion and retardation parameters of engineered barrier material play an essential role in inhibiting the transport of contaminants and sorbing them on its surface. Active clays, like bentonites, frequently serve as engineered barriers because of their excellent self-sealing ability, restricted diffusion ability, significant sorption, and exceptionally low saturated hydraulic conductivity. (Benson et al. 1994; Kaufhold et al. 2015). Lower than 1×10^{-9} m/s is the desired saturated hydraulic conductivity value to reduce the advective flow of contaminants. (Yu et al. 2020; Das and Bharat 2021; Darde et al. 2021). Further, diffusion becomes the most common form of contaminant movement through the barrier. The geosynthetic clay liners (GCLs) are an engineered barrier consisting of two geotextiles positioned on both sides of granular bentonite (GB) (Guan et al. 2014; Devarangadi and U. 2020). Self-sealing ability is the capacity of bentonite to fill macro-voids after being hydrated. The bentonite-containing geosynthetic clay liners (GCLs) were utilized in the containment of zinc and copper mine tailings (Shackelford et al., 2010). The GB are not able to seal under the influence of strong salt solutions because of a reduction in osmotic potential, and generated repulsive pressures are not sufficient to break GB granules into individual particles (Setz

et al. 2017; Li and Rowe 2020; Das and Bharat 2021; Christian and Tarek 2021). To safely store all types of waste, barrier effectiveness with extreme salt conditions is essential (Das and Bharat 2021). According to Acikel et al. (2018), the GBs in GCLs are often subjected to hydration from the soil below it, which causes crack formation upon exposure to higher temperatures before ponding the tailings. The presence of shrinkage cracks in bentonite material makes advection dominant flows through it (Rayhani et al. 2007), and causes the barrier to collapse. Further, the sorption ability of the most common form of chromium i.e., chromate ions on negatively charged bentonite clays is very low due to negative charges of chromate ions. For long-term containment applications, a composite barrier using high-density polyethylene (HDPE) geomembranes formed from polymeric materials was also utilized in conjunction with the GCL (Rowe 2001; Rowe et al. 2007; Bouazza et al. 2008). However, because HDPE geomembranes are not a sustainable choice, they degrade over time and contribute to pollution (Rowe 1998; 2012; 2020; Giroud & Bonaparte 1989; Sun et al. 2019). In several recent investigations on second-generation GCLs, polymers were also employed in the GCLs in addition to bentonite (Di Emidio et al. 2010; Scalia et al. 2014; Tian et al. 2016; Fu et al. 2021; Wang et al. 2022). The use of second-generation GCLs is constrained by the elution of polymers (Tian et al. 2019; Chen et al., 2023) and the inability of polymer-modified GB to seal.

Kaolin clay having kaolinite as a dominant mineral has pH-dependent electrostatic charges on termination sites and permanent electrostatic charges on alumina basal surfaces (Celik 2004; Choudhury and Bharat, 2018). Kaolin clay has a consistence appearance and exhibits minimal shrinkage cracks upon drying in the presence of several pore-fluids (Mishra et al., 2019). Although kaolin clay is widely available across the globe, it has not been explored as an engineered barrier for tailing disposal facilities with heavy metals. Due to crack resistance and the large availability

of kaolin clays, they should be explored as engineered barriers after amendment to improve their sealing ability.

Due to the fast depletion of non-renewable resources, the use of traditional, polymers has created sustainability and environmental concerns. Recently, biopolymers like xanthan gum (XG) and guar gum (GG) have gained recognition as environmentally friendly and low-carbon polymers to enhance soil characteristics (Amulya et al. 2021). It was found that adding xanthan gum significantly improved the natural soil's shear strength and lowered hydraulic conductivity by several orders of magnitude (Dehghan et al. 2019; Chang et al. 2015). The biopolymer kaolin composite materials can act as a suitable material for the containment of salt solutions and heavy metals. The hydraulic and diffusion behavior of XG-amended kaolin (XGK) and guar gum-amended kaolin (GGK) are not available. However, such studies are important for controlling the escape of salt leachates and heavy metals, into the surroundings. The hydraulic, and diffusion characteristics of the biopolymer amended kaolin under salt and heavy metal environment is to be establish.

भारतीय प्रौद्योगिकी संस्थान गुवाहाटी
Indian Institute of Technology Guwahati

Chapter – 3

Materials and Methodology

3.1 General

The chapter presents the various clays used in the study and their properties. The index, surface, and mineralogical properties of clays were also discussed in this chapter. Further, the details of the various other materials including polymers, biopolymers, and chemicals used in the study are also discussed in this chapter. A detailed description of experimental setups and methodology used in the study also provided in this chapter.

3.2 Materials

3.2.1 General

The study primarily utilized commercial powdered bentonite labeled as B3 in Gapak et al., (2017), granular bentonite (GB) from the commercial geosynthetic clay liner (GCL), and a commercial kaolin (K). The powdered bentonite was procured from the Kutch region of Gujarat. The GBs used in Chapter 4, GB1-GB4 have the same index properties, and mineralogical properties corresponding to GB, because the GB only went through the mechanical grinding process. The GB5 used in Chapter 4 was taken from the literature (Das & Bharat, 2021). Further, GB-A to GB-D used in Chapter 7 also have the same properties as GB, except GBs of different grain sizes. The discussion on grain sizes of GB is given in chapters 4 and 7. Further, other powdered bentonites B1 – B4 were also used in Chapter 6 to consider the influence of specific surface area of bentonite. Chapter 6 also considered kaolin (K) along with three different additional clay minerals Illite (I), Halloysite (H), and Sepiolite (S) were used in Chapter 6 to understand the role of mineralogy on

the sorption of viral strain. Different homo-ionic bentonites were prepared from different quality bentonites labeled as B1 and B3, as mentioned in Gapak et al., (2017) by replacing the exchangeable cations with either sodium, potassium, or calcium. So, six different bentonites namely Na-B1, K-B1, Ca-B1, Na-B3, K-B3, and Ca-B3 were prepared after homo-ionization process. These bentonites bentonite B1 and B3 along with their homo-ionic forms were used in Chapter 7. The procedure for the preparation of homo-ionic clay is discussed in subsequent sections. The kaolin (K) was also used in Chapter 10.

3.2.2 Granular Bentonite

Granular bentonite, designated as GB used in this study, was exhumed from the commercially available geosynthetic clay liner. The index and physical properties of GB were determined using the standard test procedures and presented in Table 3.1. Further, the chemical composition of studied GB was performed by pallet method using a Panalytical Zetium X-ray Fluorescence Spectrometer (XRF). The results from the XRF analysis are summarized in Table 3.2.

3.2.3 Powdered Bentonites

Indian powdered bentonites (B1 and B3) were procured from the Kutch region of Gujarat and Barmer district of Rajasthan, India. The index and surface properties of the studied bentonites were reproduced from the literature (Gapak et al., 2017; Das and Bharat, 2021) and presented in Table 3.1. Further, the chemical composition of the studied B1 and B3 were also reproduced from the earlier works and presented in Table 3.2

3.1.3 Kaolin

The commercial kaolin (K) was directly used without any pretreatment. Further, the portion of soil passing through a 425-micron sieve was used in the study. The basic index and surface properties of kaolin were reported from earlier works (Choudhury and Bharat, 2018), and were

reproduced in Table 3.1. The chemical composition of kaolin clay was performed by pallet method using a Panalytical Zetium X-ray Fluorescence Spectrometer (XRF). The results from the XRF analysis are summarized in Table 3.2.

Table 3.1: Index properties of Bentonite and Kaolin

Property	Bentonite B1	Bentonite B3	Granular Bentonite (GB)	Kaolin (K)
Specific gravity	2.76	2.77	2.78	2.62
Liquid limit	175	393	658	40
Plastic limit	27	50	48	32
Specific surface area (m^2/gm)	380	530	648	12*
Cation Exchange Capacity (meq/100gm)	35.2	71.7	152.67	5
Mg^{2+}	8.30	6.2	23.5	-
Ca^{2+}	15.21	29.4	42.2	-
K^+	1.40	1.3	0.9	-
Na^+	10.31	34.8	86.1	-

*BET Surface Area Method

3.1.4 Special Clay Minerals

Three different clay minerals illite(I), Halloysite (H), and sepiolite (S) were commercially procured to understand the role of mineralogy in the sorption of viruses to these minerals.

Table 3.2: Chemical composition of GB, bentonites, and Kaolin used in the study

Oxides	GB	B1	B3	Kaolin
SiO_2	50.89	59.72	59.55	51.60
Al_2O_3	13.20	23.21	22.53	46.58
Fe_2O_3 or FeO	21.17	4.72	4.47	0.32

MnO	0.196	0.124	0.154	0.00
MgO	3.46	1.57	1.97	0.00
CaO	4.67	1.09	1.11	0.02
Na_2O	3.89	2.83	2.97	0.30
K_2O	0.24	1.54	1.66	0.17
TiO_2	1.30	3.54	3.60	0.42
P_2O_5	0.24	0.45	0.48	0.31

3.1.4 Xanthan Gum

Xanthan gum (XG) is a natural polysaccharide obtained from the fermentation of the gram-negative bacterium *Xanthomonas campestris* (Patel et al., 2020). XG forms a thick and viscous gel upon hydration. Due to the presence of several carboxyl and hydroxyl groups, it has the capability of making intermolecular and intramolecular hydrogen bonding upon hydration. The XG shows high viscosity at lower concentrations, and its properties are not significantly influenced by temperature, pH, or the presence of salt concentrations.

3.1.5 Guar Gum

Guar Gum is a polysaccharide, taken out of guar beans, which are scientifically referred to as *Cyamopsis Tetragonolba*. It may dissolve in both hot and cold water and form a thick viscous gel (Soldo et al., 2020).

3.1.6 Other Biopolymers

The other two biopolymers, acacia gum (Gum Arabic), and agar-agar gum were procured from Sigma-Aldrich. Acacia gum is a polysaccharide obtained from *Acacia senegal* trees, it is a negatively charged linear biopolymer. It contains a large amount of carboxyl and hydroxyl groups, which makes it a suitable material to arrest the contaminants. Moreover, agar-agar gum is a linear biopolymer, extracted from the red algae. Agar-agar gum also forms a gel upon hydration, which

makes it a suitable material for food stabilizer and medication purposes. The required amount of biopolymer was mixed with air-dried GB or kaolin before use in experiments.

3.1.7 Inorganic Salts

Analytical-grade chemicals with 99% purity were procured from Spectrochem (India) and supplied by a local vendor. The chloride salts of sodium, potassium, and calcium were used to make the salt solutions of 0.5 M concentration. A required amount of salt was measured and mixed in distilled water to make salt solutions.

3.1.8 Heavy Metals

Heavy metal solutions of 1000 ppm of Cr^{6+}, Zn^{2+}, and Pb^{2+} were made from $K_2Cr_2O_7$, $Zn(NO_3)_2.6H_2O$, and $Pb(NO_3)_2$. The required amount of the heavy metal's salts were taken and dissolved in 1L in the volumetric flask to make a 1000 ppm concentration of each heavy metal. The concentrations of the Zn^{2+} and Pb^{2+} samples for diffusion were measured with Atomic absorption spectroscopy (AAS). The concentration of hexavalent chromium was measured by taking absorbance from a UV-visible spectrophotometer at 540 nm.

3.1.9 Cells and Viruses

Baby Hamster Kidney 21 (BHK-21) cell lines used in this study were procured from the National Centre for Cell Science (NCCS), Pune, India. BHK-21 cells were maintained in Dulbecco's Modified Eagle's Medium (DMEM) with 10% Fetal Bovine Serum (FBS) at 37° C under 5% CO_2. The NDV R2B strain and Bareilly used in this study were obtained from the College of Veterinary Sciences, Khanapara, Assam, India. Viruses were propagated in the allantoic cavity of 9-day-old embryonated chicken eggs and stored at -80°C for further use. The virus stock used for all the experiments in this study was titrated by plaque assay and had a concentration of 1.4×10^8 PFU/ml (plaque-forming units per ml).

A vaccine strain of Japanese encephalitis virus (JEV) propagated and maintained in the laboratory of Viral Immunology Lab, IIT Guwahati, BSBE department was used in this study. The virus stock used for the experiments was titrated by a plaque assay and had a concentration of 8×10^6 PFU/mL.

PR8 strain H1N1 influenza virus used in this study was obtained from the National Institute of High-Security Animal Diseases, Bhopal, India. Viruses were propagated in the allantoic cavity of 9-day-old embryonated chicken eggs and stored at −80 °C until further use. The virus stock used for the experiments was titrated as 2^8 by Hemagglutination assay (HA).

3.3 Experimental Methods

3.3.1 Preparation of Homo-ionic Clays

To understand the mechanism of interaction of NDV sorption to the bentonite, six different homo-ionic bentonites were prepared from two powdered bentonites. The procedure for the homo-ionization of clays was as follows (Bharat and Das, 2017):

i. Take 90 mL of 1M ammonium acetate solution in a conical flask and pour 2 gm of oven-dried clayey soil sample passing through a 425 µm size sieve, avoid sticking soil particles onto the flask surface near the neck.
ii. Place a conical flask containing soil–ammonium acetate solution on a mechanical orbital shaker for 2 hours at 195 – 205 rpm and after mixing allow to stand overnight.
iii. Next day, the sample is to be transferred to a centrifuge tube of 250 ml capacity. If any soil particles are left in a conical flask, then it need to be washed using 10 ml of the same 1M ammonium acetate solution. Two samples are to be made simultaneously and weighed and made equal if there is any variation in the weight of the samples. Then both samples are centrifuged at 1000 rpm for 1 minute to remove supernatant solution.

iv. Soil sample is mixed with 80 ml water and transferred to a conical flask and the centrifuge tube is rinse of with 10 mL distilled water and added to the conical flask. Then conical flask is kept on a mechanical orbital shaker for 30 minutes for mixing.

v. After mixing, soil – water solution is again placed in a centrifuge tube, the conical flask is again rinsed off with 10 mL distilled water and added to the solution and after balancing two centrifuge tubes they are centrifuged for 1 minute at 1000 rpm.

vi. Electrical conductivity of the supernatant is monitored and the same process of washing soil is repeated until electrical conductivity approaches zero.

vii. Then soil sample is to be mixed for 2 hours with 90 mL 1M electrolyte solution of required cations (i.e., Na, K, or Ca) on the mechanical shaker and allowed to stand overnight.

viii. Next day, the sample is centrifuged to remove the supernatant solution and washed using the above procedure until the electrical conductivity of the supernatant approaches zero.

ix. Once the supernatant has approached the electrical conductivity to zero, the soil sample is taken out for lyophilization, and the lyophilized clay is used for further sorption experiments.

3.3.2 Pore-Fluid Permeation Rates

The fluid permeation rate through the studied clays was undertaken under constant volume conditions. The fluid permeation experimental set-up was developed from the solid acrylic rod, which holds a soil sample of diameter 24 mm and 10 mm thickness as shown in Figure 3.1. The dry density of clay samples was taken as 1.2 Mg/m^3. One end of the soil specimen was attached to the burette having the chosen pore-fluids. The burette's valve was loosened to enable the pore-fluid to enter through at the start of the experiment. The permeation rates of different samples were estimated continuously by monitoring the head level of the pore-fluid in the burette. The

permeation rate was measured until the equilibrium. The equilibrium was ensured by a constant rate of permeation rate over 24 hours. This experiment was conducted for kaolin and biopolymer-amended kaolin. The decrease in fluid penetration rate below 1×10^{-9} m/sec indicates the clogging of the voids in kaolin with biopolymer. The time involved in accomplishing the closure of voids with biopolymer gel is called sealing time (ST).

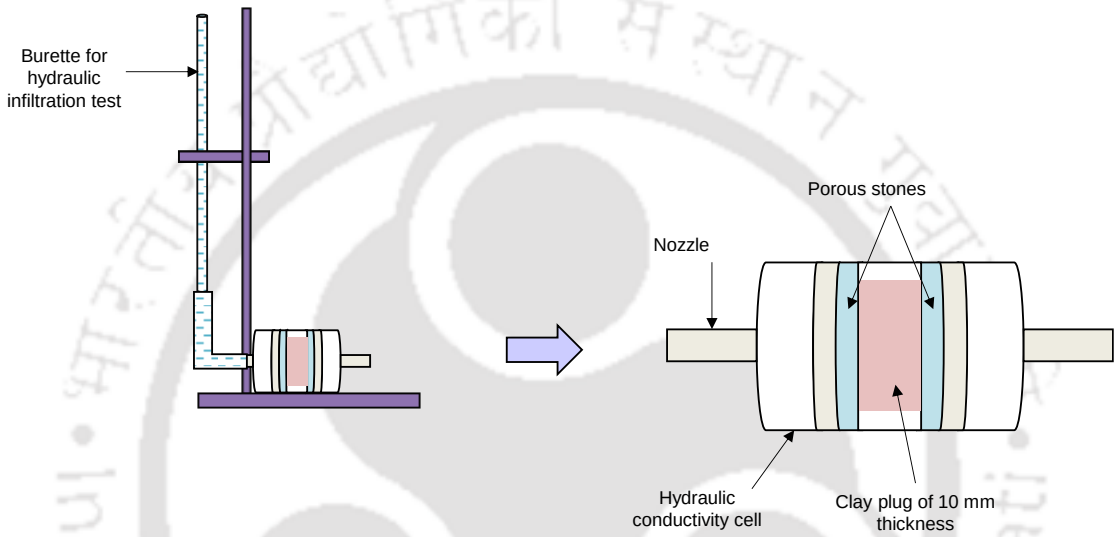

Figure 3.1: Experimental set-up for fluid permeation under constant volume condition

The same experimental set-up with a smaller burette was also utilized to evaluate the fluid permeation rate of GBs with the H1N1 virus in the KCl environment. The GB samples were saturated using 0.5M KCl salt solution to simulate the existing condition in the landfill, as the liner will be saturated with the leachate before receiving the pathogenic waste. Further, the pore-fluid containing H1N1 virus and 0.5M KCl salt solution was filled in the burette. The new pore-fluid-containing virus and salt solution were passed through the compacted GB samples. The rate of change in the head of the burette was measured with time to evaluate the fluid permeation rates of different GBs. Moreover, the samples after permeations were also collected to measure the presence of the virus on the other side. A separate container containing pore-fluid (H1N1 virus

with 0.5M salt solution) was kept to measure the biological decay of the virus in a high KCl environment.

3.3.2 Hydro-Chemo-Mechanical Behavior

The modified odeometer setup, as depicted in Figure 3.2, was used to study the hydraulic and volume change behavior of GB, polymer-amended GB, and biopolymer-amended GB. The required amount of dry sodium polyacrylate (polymer) and biopolymer was weighed and mixed with air-dried GB. The perspex setup was fabricated to accommodate 10 mm thick and 53 mm diameter soil sample. The porous stones were placed on either end of the compacted bentonite sample. A filter paper was placed in between the porous stone and the GB sample to avoid clogging the soil sample. An average dry density of 1.2 Mg/m^3 was used to compact the bentonite sample with the same density of GB in GCLs (Das and Bharat, 2021). The modified odeometer setup was placed on the loading assembly and connected to the burette with desired pore fluid from the bottom of the sample. The dial gauge with the least count of 0.002 mm was attached at the top of the compacted sample to measure the vertical deformations of the sample. The required load (i.e., 20 kPa and 50 kPa) was applied to the compacted bentonite to simulate the waste load. The experiment was started by starting the flow of pore fluid across the soil sample by opening the valve of the burette. Replacement of pore-fluid with fresh pore-fluid was done to maintain the constant concentration and head. The permeation rate was estimated continuously with time and continued till the reading in the dial gauge and permeation rate were constant over 24 hours. The volume change of bentonite samples was presented in terms of normalized thickness (h/h_0).

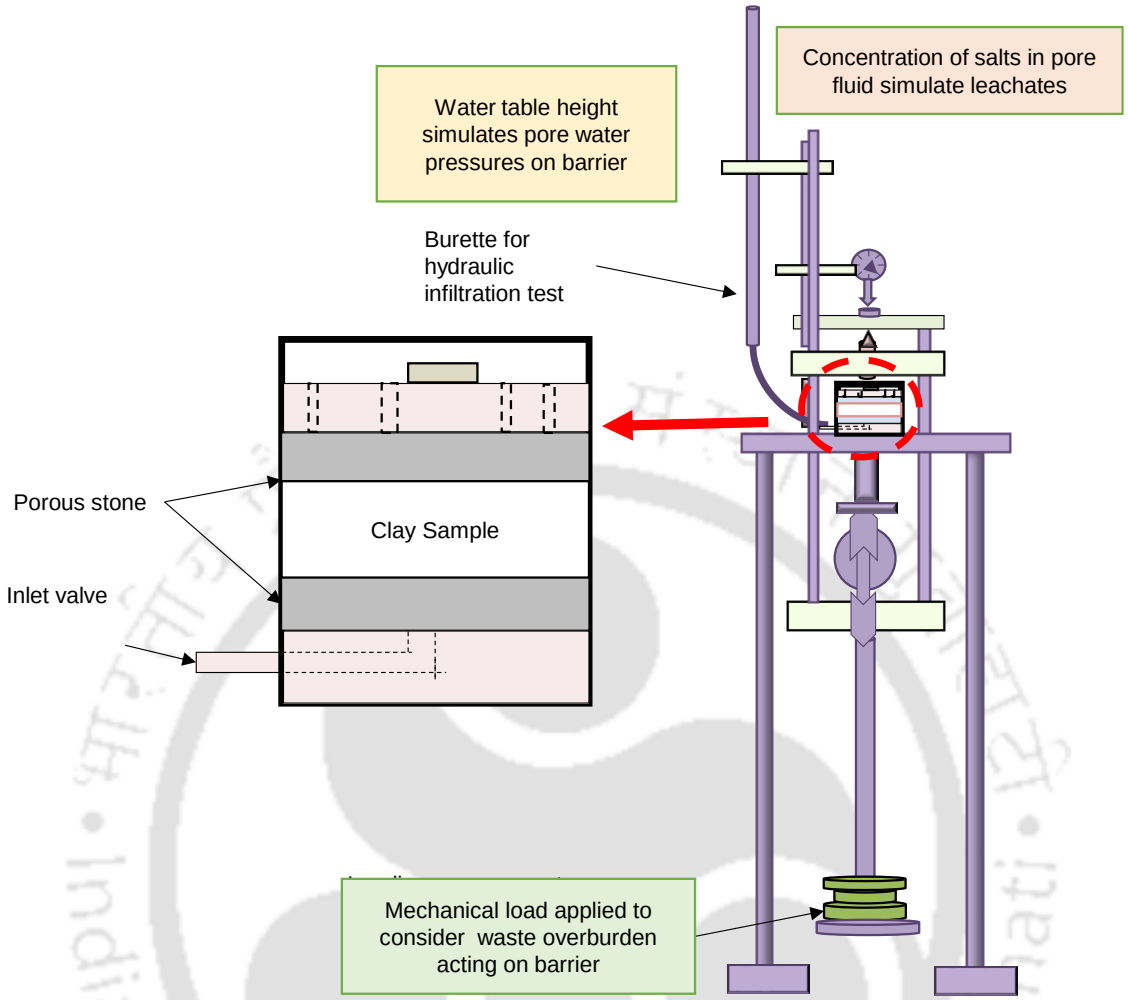

Figure 3.2. Experimental setup for the hydro-chemo-mechanical performance of soil samples

3.3.3 Thermo-Hydro-Chemo-Mechanical Behavior

The odeometer setup discussed previously was further modified to evaluate the fluid-permeation rate and volume change under thermos-hydro-chemo-mechanical loading conditions as depicted in Figure 3.3. Due to the requirement of heating the soil sample, the set-up was fabricated using two chambers. The inner chamber was fabricated using solid aluminum rod to accommodate a soil sample of 53 mm diameter and 10 mm thickness. Further, the base plate as well as the outer chamber was fabricated using the solid Teflon rod. The base plate has a pedestal along with a groove so that the inner cylindrical aluminum chamber can be fitted to the base plate. The soil sample was compacted in the inner aluminum chamber and porous stone was provided on either

side of the soil sample. A grade 42 filter paper was provided between the soil sample and the porous stone to prevent the clogging of the porous stone. The outer chamber, made up of Teflon, was placed and tightened with the help of an O-ring to prevent the leakage of oil from the outer chamber. The set-up was placed on the loading assembly. The oil was filled in the outer chamber. The vehicle mobile engine oil was used in the study, due to its capacity to maintain the same temperature for longer duration and higher ignition point. Further, the heating coil was placed inside the oil and the coil was connected to the temperature controller. The thermometer was also connected to the temperature controller to stop heating once the targeted temperature was achieved. Further, the coil heats the oil if temperature drops the 0.5℃ lower than the targeted temperature. But during the heating process, the temperature of oil rises quickly and reaches 3℃ more than the targeted temperature before the temperature controller stops the coil. Further, the set-up has an inlet valve at the base plate open to the inner chamber. The inlet valve is connected to the burette containing pore-fluid. The dial gauge with the least count of 0.002mm is connected at the top of the setup to measure the volume change of the soil sample. The heating arrangement of the sample was started and continued until the target temperature was achieved in the soil sample. One experiment was initially, conducted to measure the time required to reach the targeted temperature in soil sample. The GB sample took around 30 hours to reach the targeted temperature at the middle of the soil sample. Further, the mechanical loading and permeation were started after 30 hours of equilibrium time from exposure to temperatures for all other samples. Mechanical loading was applied to the sample to simulate the self-weight of the waste. Further, the experiment was started by the flow of pore-fluid through the soil sample. The variations in the readings of the burette and dial gauge were measured to evaluate fluid permeation rates and volume change of the

samples. The experiments were continued until there was no volume change and a constant permeation rate for over 24 hours.

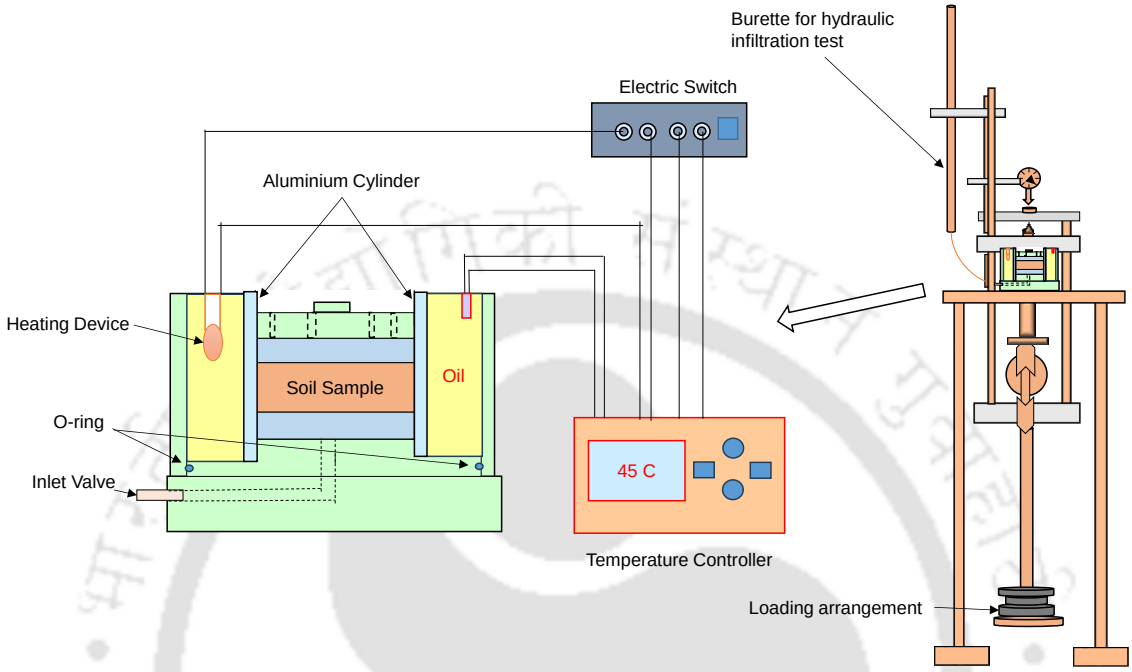

Figure 3.3: Experimental set-up for thermo-hydro-chemo-mechanical behavior

3.3.4 Through-Diffusion Experiment

Laboratory through-diffusion tests were performed as this technique does not require the concentration profile along the soil sample. The diffusion cell was fabricated using the solid acrylic rod to accommodate the 10 mm thick and 24 mm diameter bentonite sample. A 5 mm thick porous stone was used on either end of the soil sample as shown in Figure 3.4. A 42-grade filter paper was used in between the soil sample and the porous stone. The soil samples were compacted at a dry density of 1.2 Mg/m^3. The diffusion cell was attached to the reservoirs on either end and a rubber gasket was used at each threading to prevent the leakage. Both the reservoirs were filled with distilled water to saturate the samples. The weight of the diffusion cell was monitored at some intervals. The samples took around 45 days for complete saturation and the weight of diffusion cells was constant after saturation.

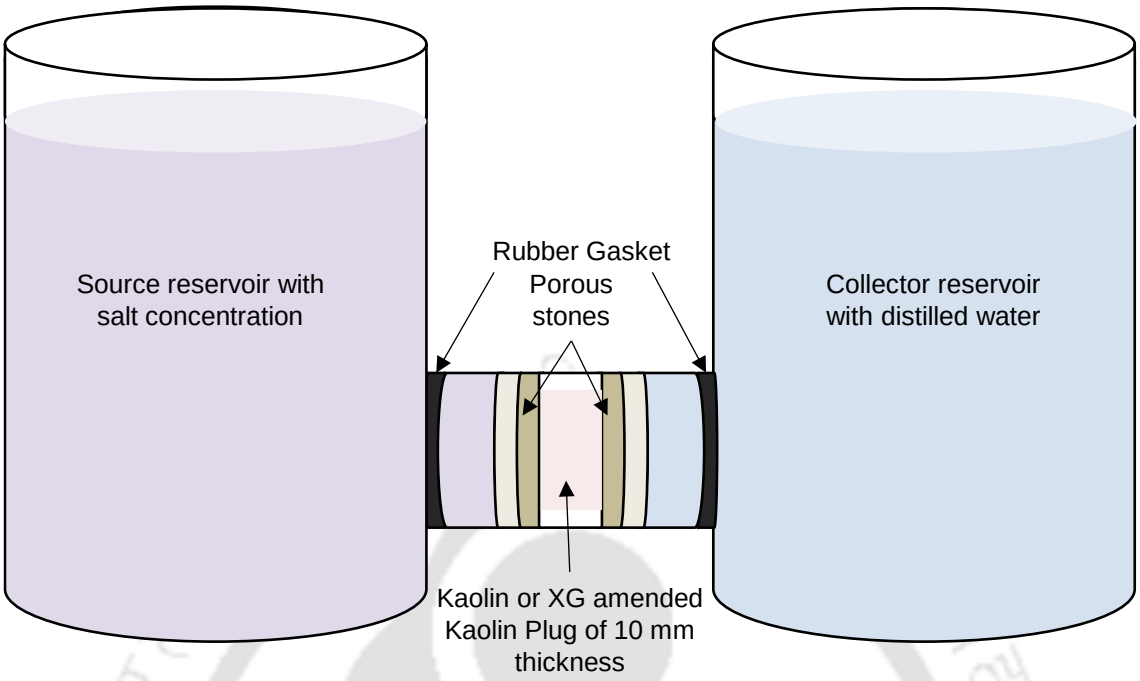

Figure 3.4. Experimental setup for Through diffusion experimental setup.

The diffusion experiment was started with the replacement of the source reservoir with 0.5 M salt solution. The collector reservoir was also replaced with fresh distilled water to avoid the influence of excess salts on diffusion characteristics. 10 ml of solution samples were collected from both source and collector reservoirs to evaluate the concentration with some intervals. The source and collector reservoirs were also stirred with a clean stirrer to maintain uniform concentration throughout the reservoirs. The concentrations of serially diluted samples were measured with the help of a flame photometer (Systronics, India). The measured concentrations were used for diffusion analysis.

3.3.5 Through-Diffusion Experiment for Viruses

A through-diffusion testing methodology was adopted for virus transport in this study across the clay plug as it is a non-destructive technique and the slicing of the sample is not required. Further, both retardation factor and diffusion coefficients can be estimated from the single experiment. The

diffusion cell was fabricated from solid Perspex material to accommodate a 10 mm thick and 24 mm diameter clay sample as shown in Figure 3.5.

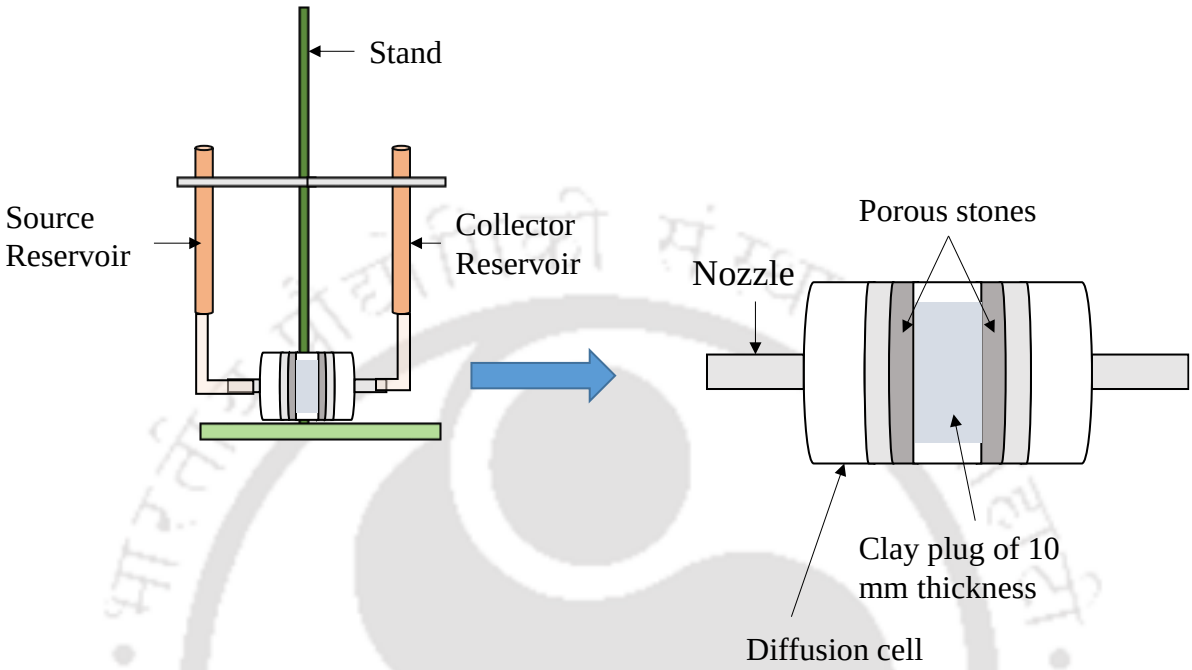

Figure 3.5: Experimental setup used for through-diffusion experiment

The clay samples were statically compacted to a dry density of 1.2 Mg/m^3 in the diffusion cell. Porous stones were placed on either end of the clay sample, and a grade 42 filter paper was placed in between the porous stone and clay sample to avoid the clogging of porous stones. The diffusion cell was attached with reservoirs on either end with connecting pipes. The rubber gasket was used around the threading to prevent any leakage. The samples were kept for saturation with the solution containing the egg allantoic fluid at the same concentration at which the virus will be introduced in the source reservoir after saturation. The saturation of the clay sample was ensured by the constant weight of the diffusion cell with time; thus, the weight of the cell was regularly monitored to check the saturation of the sample. The saturation of the bentonite sample took about 45 days and the kaolin sample took around 10 days. The diffusion experiment was started by replacing the source reservoir with fresh 10000 pfu/mL concentration of NDV along with the egg allantoic fluid.

The initial virus concentration in the kaolin sample's source reservoir was 2500 pfu/mL. The egg allantoic fluid in the collector reservoirs was also replaced with a fresh solution to avoid the influence of any excess cations in the egg allantoic fluid. The solution in the source and collector was regularly stirred and samples of 500µL were collected from the source and collector reservoir at regular intervals. A separate virus sample with the egg allantoic fluid at the same concentration was also kept to monitor the biological decay of the virus sample with time. The concentrations of the virus were measured with the plaque assay for source, collector, and control samples.

3.3.6 Virus Sorption Experiment

Samples of air-dry bentonite clays were weighed and placed in 1.5 mL Eppendorf tubes before suspending in 350µL of virus dilutions made in DMEM containing 2% FBS. This mixture was incubated at room temperature for 2 hrs with continuous and gentle mixing. After incubation, tubes were centrifuged, and supernatants were collected in separate tubes. Virus concentration was titrated via plaque assay as explained below.

3.3.7 Plaque Assay

The BHK-21 cells were seeded in DMEM containing 10% FBS on 12 well plates (5×10^5 cells/ well) twelve hours before the assay. Media was removed from the wells, and 200 µL of supernatant from the bentonite-virus mixture was added into their respective wells. The plates were incubated at 37° C under 5% CO_2 for 1 hr with gentle mixing every 15 minutes. After incubation, the supernatant was removed from the wells, and 1 mL of overlaying medium (DMEM with 2% FBS and 0.8% methylcellulose) was added.

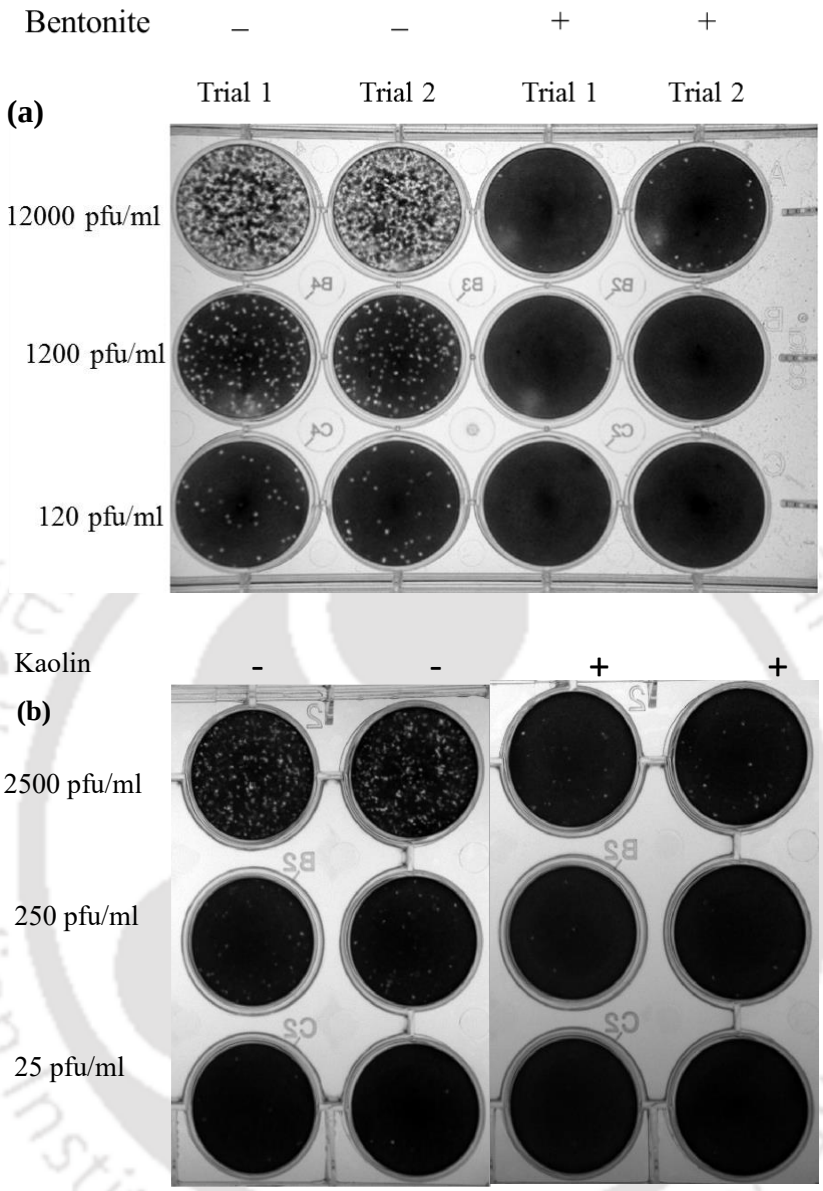

Figure 3.6: Wells for counting the plaque for sorption of NDV samples with (a) bentonite B3 and control NDV samples with three different concentrations of virus (b) kaolin and control NDV samples with three different concentrations of virus

The plates were then incubated at 37° C under 5% CO_2 for 72 hrs. The medium was then removed from the wells, and methanol was added before incubating it for 30 minutes at room temperature. Methanol was then removed from the wells and washed with distilled water before adding 0.5% crystal violet and incubated at room temperature for 1 hr. The wells were then washed with distilled water to count visible plaques in each well, as shown in Figure 3.6.

3.3.8 SYBR Green-based Real-Time PCR titer for quantification of H1N1 Influenza virus

PR8 strain H1N1 used in this study was obtained from the National Institute of High Security Animal Disease, Bhopal, India. Viruses were propagated in the allantoic cavity of 9-day-old embryonated chicken eggs and stored at −80 °C until further use. The virus stock used for the experiments was titrated as 2^8 by Hemagglutination assay (HA). The H1N1 virus concentrations were measured in supernatant from the sorption experiment, the source and collector from the diffusion experiment, sample was collected after the permeation experiment using the SYBR Green-based Real-time PCR method. RNA was extracted from the viral suspension of allantoic-fluid and virus diluted in DMEM with different samples using RNAiso plus (Takara, Japan) reagent as per manufacturer instructions. The RNA was reverse-transcribed into cDNA using a High-capacity cDNA Reverse transcription kit (applied biosystem, US). The SYBR Green real-time PCR assay was performed with previously published primers (Kim et al., 2019). The reaction was set up with 5 µl of mastermix (Applied Biosystem, US), 100 ng of cDNA, primer mix (100 nM to 500 nM) and volume makeup with nuclease-free water till 10 µl, with the following thermal conditions: 50°C for 2 min, 95°C for 10 min and 40 cycles of 95°C for 15 sec and 60°C for 1 min, 95°C for 15 sec, 60°C for 1 min. Positive control and No Template Control (NTC) in duplicates were included to rule out any false positives.

The standard curve approach with SYBR green-based Real-time PCR was used to quantify the copy number of H1N1 viral RNA. RNA concentration of positive H1N1 propagated in the allantoic fluid was determined spectrophotometrically in µDrop (Thermo Scientific, US). Molecular copy number was calculated using the given formula.

$$Y \text{ (molecular copies/µl)} = X \text{ ng} \times 6.0221 \times 10^{23} \text{ molecules/mole} / \text{Transcript length(bp)} \times 340 \text{ g/mole} \quad (3.1)$$

RNA was reverse transcribed into complementary DNA (cDNA), which served as the template for subsequent PCR amplification. The cDNA was serially diluted to create a range of concentrations covering the expected copy number range in our experimental samples. The real-time PCR was then performed with a thermal cycler, and the fluorescence emitted by the SYBR Green dye was monitored during each cycle. The threshold cycle (Ct) values for each dilution of the standard curve were recorded. By plotting the Ct values against the logarithm of the corresponding RNA copy numbers, we generated a linear standard curve. A regression equation **y= mx + c** is used to determine y-intercept and slope of the standard curve to calculate the copy number (Adams, 2006). Finally, the copy number of H1N1 viral RNA in our experimental samples was determined by comparing their Ct values to the standard curve. A test result was considered positive if a sigmoid amplification curve crossed the threshold before 40 cycles.

Chapter – 4

Influence of Grain Size and Plasticity of Granular Bentonite under Chemo-Mechanical Loadings with Salt Solutions

---

4.1 General

This chapter discusses the role of grain sizes and plasticity of granular bentonite (GB) on the hydraulic and volume change characteristics under extreme chemical loads for long term stability. The average granule size of the GBs varies depending on the manufacturer and with the batch from the same manufacturer. Further, the GCLs are subjected to mechanical loading from the landfill waste. The influence of different GSDs of the same granular bentonite was assessed for self-sealing ability, hydraulic infiltration, and volume change behavior under extreme chemical loadings at 50 kPa mechanical load. The plasticity of the GB also influenced the sealing and swelling ability under chemo-mechanical loading. The underlying mechanism explaining the influence of plasticity and granulation size on the self-sealing behavior and equilibrium hydraulic conductivity was presented. The finely granulated bentonite was recommended to be used in the GCL for containment applications.

4.2 Hydro-Chemo-Mechanical (HCM) Behavior

Different sizes of the GB, mean effective grain sizes (D50) from 0.25 mm to 1 mm are present in GCLs. Significant variations in hydration process leads to different behaviour of GB with different sizes. Present work considered the influence of granule size by keeping the mineralogy of the

material same. Granular bentonites in GCLs are exposed to coupled hydraulic, chemical, and mechanical loading due to presence of leachate, presence of salts in leachate, and weight of waste. The study was conducted under critical conditions, i.e., high chemical and lower mechanical loading. The influence of plasticity was also considered on HCM behaviour of the GB from the same manufacture.

4.2.1 Processing of GB

An exhumed GB from the commercial, needle-punched GCL was used in this study. The commercial GB was milled in the laboratory to obtain three different grain size distributions with the varying fineness of the granules for studying the influence of GSD on the self-sealing ability and hydraulic behavior under the studied HCM loading. The laboratory-processed bentonites were named GB2, GB3, and GB4 while the commercial GB was named GB1. To study the influence of plasticity, the properties of GB from another batch from the same manufacturer were taken from the literature (Das and Bharat, 2021a) and named as GB5.

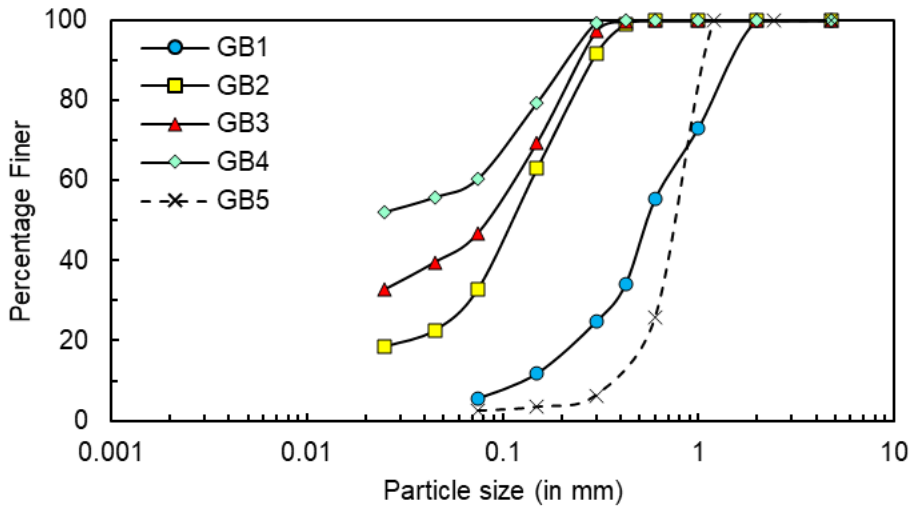

Figure 4.1 Grain size distribution curve for all GBs and comparison with grain size of GB used in literature (G.S.D. of GB5 obtained by personal communication from Dr. Partha Das)

The grain size distribution of all the studied GBs was obtained by sieve analysis (IS 2720 – 4; 1985) using size greater than 75 µm. Generally, the hydrometer analysis is used for the particles smaller than 75 µm. However, the hydrometer analysis using water is not useful to estimate the granules size as water disintegrates the individual granules into particles. The hydrometer analysis with water will not represent true granulation of GBs and with water the GSD will be same for all GBs (GB2-GB4). Therefore, the wet sieve analysis with kerosene was performed for grain size lower than 75 µm size. The kerosene allowed to retain the individual grain size due to non-polar nature. The kerosene on the bentonite was allowed to evaporate by oven drying. The grain size distribution curves for all the GBs were presented in Figure 4.1.

4.2.2 Influence of Grain Size Distribution on HCM Behavior

Fluid permeation rates of distilled water through the studied GBs under 50 kPa mechanical load were presented in Figure 4.2 (a). The permeation rates were found to be similar and were not influenced by the grain sizes significantly before 70 min. The fluid permeation rates changed slightly beyond 70 minutes and were sealed to reach the limiting hydraulic conductivity in between 200 – 600 minutes for all the studied GBs. The fluid permeation rate varied with the mean particle size or GSD and was highest for GB1 and lowest for GB3 and GB4. The permeation rates were higher for GB1 due to the presence of larger macro-voids during the initial hydration stage. Further, the variations of volume change with time for GBs in terms of normalized thicknesses with distilled water were presented in Figure 4.2(b). The normalized thickness decreased immediately after the inundation indicating a collapse of the sample under the applied vertical load. The repulsive pressure develops between the particles with time due to the formation of diffused double layers (DDLs) upon hydration, which compensates the mechanical load, to increase the overall volume of the sample. The thickness thus increased steadily indicating

macroscopic swelling between 4 – 30 minutes for all studied GBs. The equilibrium normalized thicknesses varied in a small range of 1.31 to 1.36 for the studied GBs, indicating a marginal influence on the initial granule (or voids) size of the GBs in the presence of water. Further, out of all experiments, 25 percentage of experiments were repeated to see the repeatability of the experiments and results were found to be repetitive.

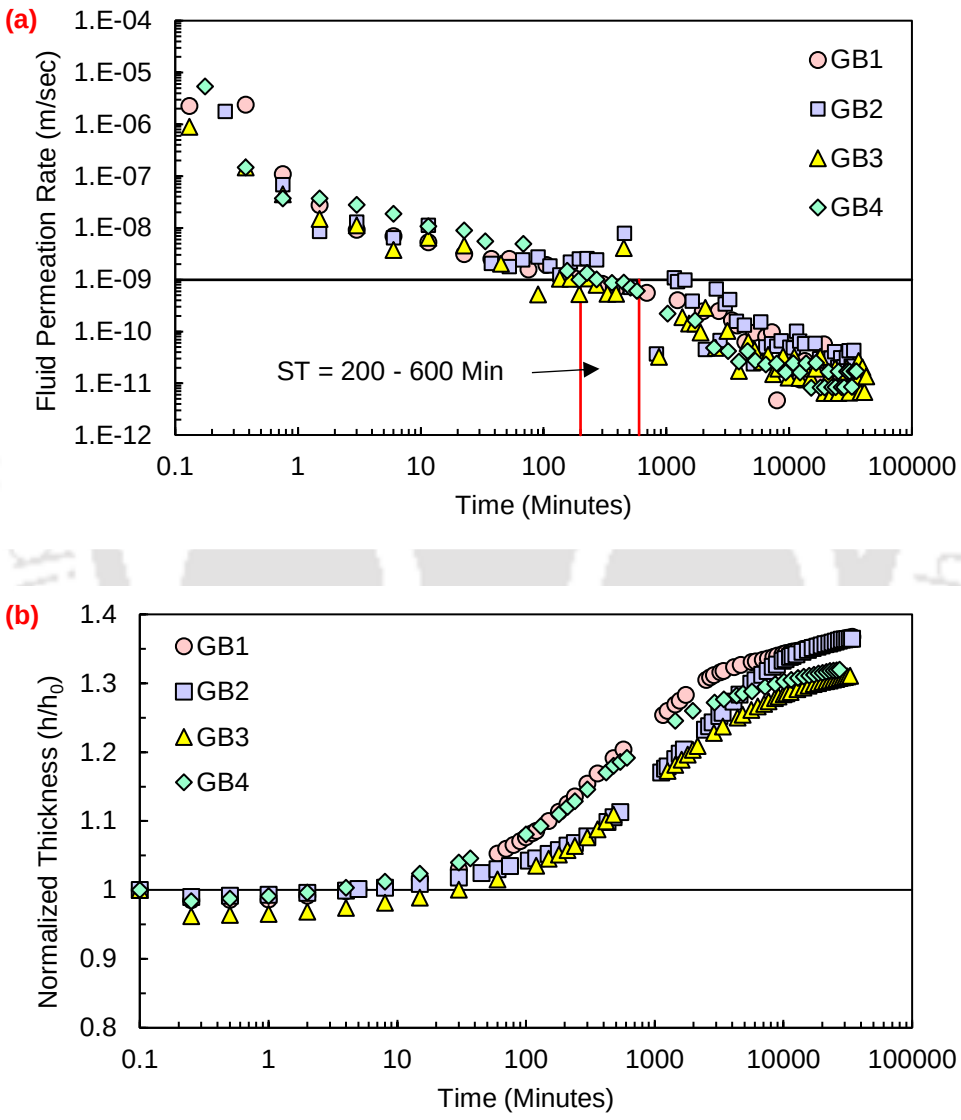

Figure 4.2: Variations of (a) fluid permeation rates; and (b) normalized thickness of GBs with time for distilled water.

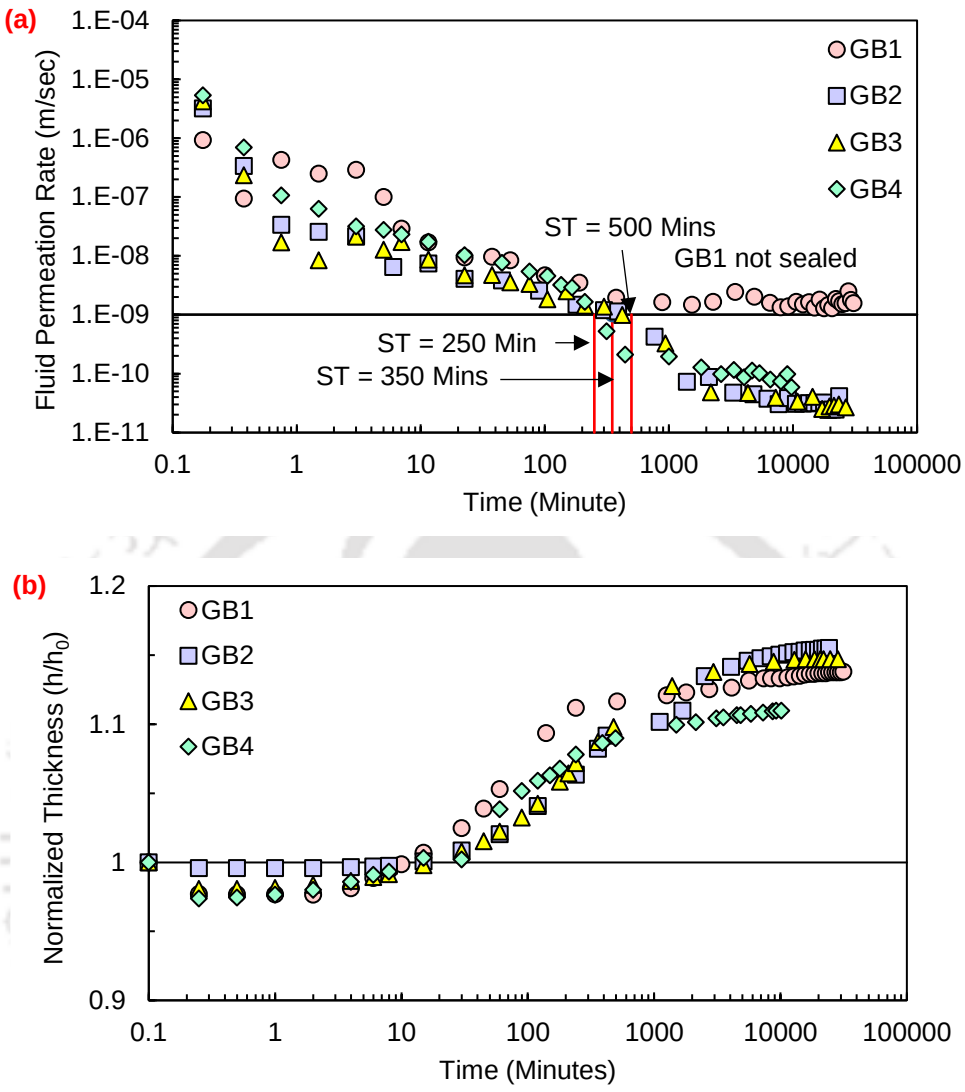

Figure 4.3: Variations of (a) fluid permeation rates, and (b) normalized thickness of GBs with time for 0.5 M NaCl.

Fluid permeation rates of 0.5 M NaCl solution through the studied GBs under the applied mechanical load of 50 kPa were presented in Figure 4.3(a). The fluid permeation rate in GB1 was highest throughout the test and GB1 did not achieve limiting hydraulic conductivity even at equilibrium due to the inability of macro-voids to seal in the presence of 0.5M NaCl solution. The fluid permeation rates of other GBs were similar to GB1 initially up to 200 minutes and then slightly changed to record different sealing times of 250, 350, and 500 minutes for GB4, GB3, and

GB2, respectively. The order of sealing time varied according to the grain size distribution of the GBs. The GB with the highest fineness fraction (GB4) attained the sealing in the lowest time, while GB2, which was coarser as compared to GB3 and GB4, attained the sealing at a larger time.

Further, variations of the normalized thickness (h/h_0) with time for different GBs with 0.5 M NaCl as pore fluid were presented in Figure 4.3(b). The normalized thickness decreased initially, due to the dominance of mechanical load in comparison to the developed repulsive pressure in the presence of 0.5 M NaCl solution. An initial collapse of 0.5 – 3 % was observed in GBs after starting the test. The normalized thickness increased with permeation time and exhibited swelling after 8 – 30 minutes for all GBs. The increase in repulsive pressure due to the development of DDLs in bentonite particles increased the final volume of the sample and led to swelling. The equilibrium normalized thicknesses varied only between 1.11 to 1.15 for all the studied GBs, which indicated similar volume change behavior of GBs with 0.5 M NaCl as pore fluid.

Fluid permeation rates for 0.5 M KCl solution through the studied GBs under the applied stress of 50 kPa were presented in Figure 4.4 (a). The fluid permeation rates through different GBs were nearly the same at the beginning of the testing, but the rates changed drastically beyond 50 minutes. The fluid permeation rate was highest in GB1 and did not achieve the limiting hydraulic conductivity even at equilibrium due to the inability of macro-voids to seal in the presence of 0.5 M KCl solution. In contrary, the macro voids in the other GBs got sealed and the permeation rate decreased to limiting hydraulic conductivity at 8000, 250, and 200 minutes, respectively. The sealing time decreased with the fineness of the granules in the studied GBs. A significantly high sealing time of 8000 minutes was observed for GB2 due to the presence of coarser granules in GB2 as compared to GB3 and GB4.

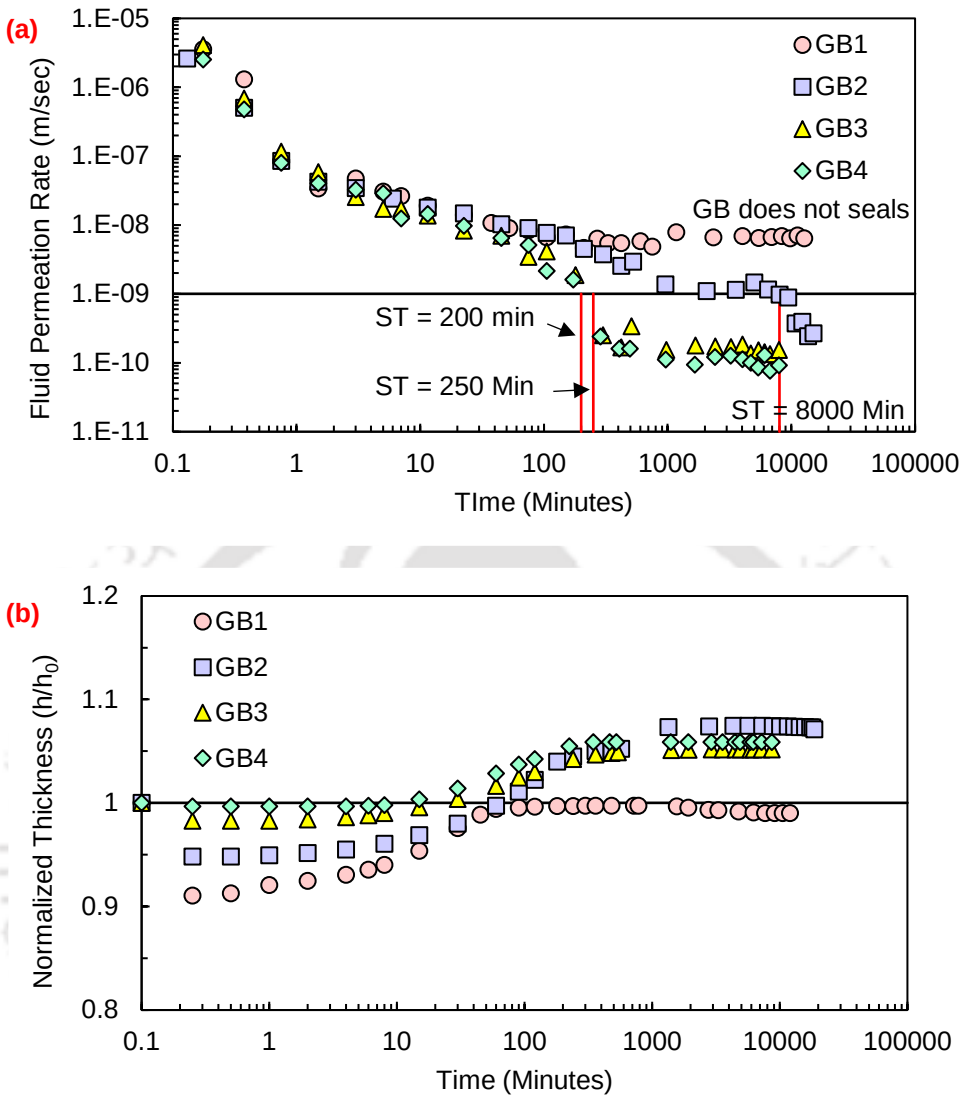

Figure 4.4: Variations of (a) fluid permeation rates; and (b) normalized thickness of GBs with time for 0.5 M KCl

Further, variations of the normalized thickness with time for different GBs with 0.5 M KCl were presented in Figure 4.4(b). The normalized thickness decreased immediately after the inundation, due to the dominant mechanical load in comparison to the developed swelling pressure from the electrostatic repulsion at the beginning. The repulsive pressure increased with time due to the formation of the DDLs and compensated the mechanical load, which increased the overall volume of the sample. A significant collapse with a normalized thickness of 0.91 was observed for GB1

immediately after the fluid inundation. The thickness increased with time to reach the initial height after 100 minutes but decreased further at equilibrium. The initial collapse decreased with an increase in the fineness of the GBs. The volume change behavior was distinctly altered with different GSDs of the GBs throughout the permeation. The normalized height increased with permeation and exhibited swelling after 50, 20, and 8 minutes. An equilibrium normalized thickness of 0.99 was observed for GB1, which indicated a slight collapse at equilibrium. The equilibrium normalized thicknesses varied in the range of 1.05-1.07 for the other GBs, which indicated swelling by these GBs at equilibrium.

The fluid permeation rates of 0.5M $CaCl_2$ through the studied GBs under the applied mechanical load were presented in Figure 4.5(a). The fluid permeation rates through different GBs were nearly the same at the beginning of the testing, but the rates change drastically similar to the previous study with KCl, beyond 70 minutes. The fluid permeation rate was highest in GB1 and did not achieve limiting hydraulic conductivity even at the equilibrium due to the inability of sealing of macro-voids present in GB1 in the high $CaCl_2$ salt environment. On the other hand, other GBs got sealed with a sealing time of 350 minutes for both GB2 and GB3, while GB4 has a sealing time of 200 minutes. The fluid permeation rates varied inversely with the fineness of GBs, which means GB4 has the lowest sealing time and GB2 has the higher sealing time.

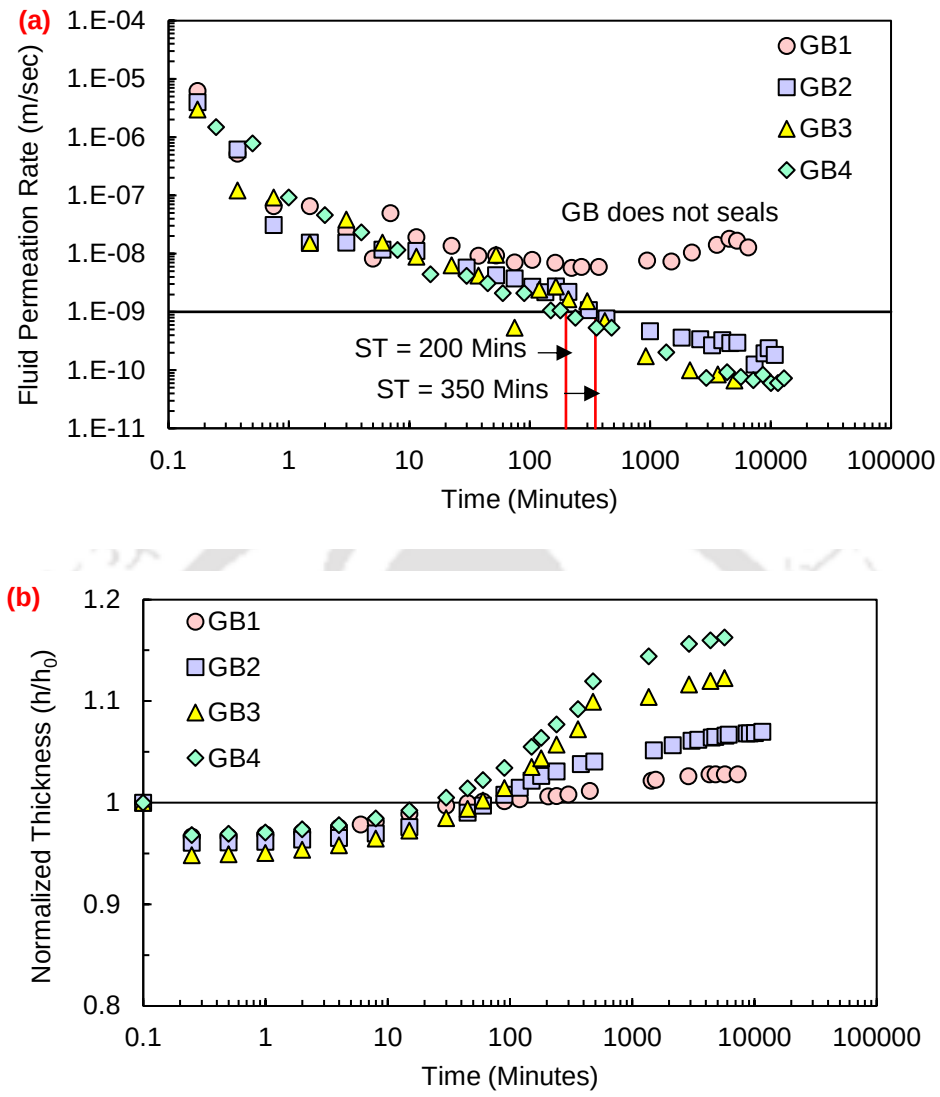

Figure 4.5: Variations of (a) fluid permeation rates, and (b) normalized thickness of GBs with time for 0.5 M $CaCl_2$.

The variations of volume change behavior with time in terms of normalized thicknesses of compacted GBs with 0.5 M $CaCl_2$ as pore fluid under 50 kPa mechanical loading were presented in Figure 4.5(b). The normalized thickness decreased immediately after the inundation and showed an initial collapse of 4 -5 % for all studied GBs. The mechanical load dominated initially but was compensated by the repulsive pressure with time due to the development of thin DDLs. The normalized thickness increased with time and exhibited swelling in 15 – 50 minutes starting the

experiments for studied GBs. The equilibrium normalized thicknesses of GB varied in the range of 1.03 – 1.16. The equilibrium normalized thickness was found to be lowest for GB1 and found to be increasing with an increase in the fineness of GB.

The influence of pore-fluid cation on the fluid permeation rates was presented in Figure 4.6(a) and 4.6(b) for GB1 and GB4, respectively. The fluid permeation rates achieved limiting hydraulic conductivity for both GB1 and GB4 with the distilled water. The fluid permeation rates increased several orders of magnitude with high ionic salt concentration for GB1. The fluid permeation rate was highest for $CaCl_2$, which was followed by KCl and NaCl. The divalent cations (Ca^{2+}) suppressed the formation of DDLs significantly (Bharat et al. 2019), which resulted in the formation of lower osmotic repulsive pressure between the particles associated at the surface of the granules. Similarly, the smallest monovalent hydrated cations (K^{+}) would easily replace the surface cations to form thin DDLs around the particles (Bharat and Shridharan, 2015; Bharat and Das, 2017; Bharat et al. 2019) that are in contact with the pore-solutions in the soil matrix. Thus, the developed osmotic repulsion force is marginal to disintegrate the granules into individual particles that are associated by the van der Waals' attraction forces in the presence of high ionic strength calcium and potassium salts. In contrary, the equilibrium hydraulic conductivity was marginally influenced with different cations for GB4 (Fig. 4.6b) due to the availability of only micro-voids between the particles by the mechanical granulation process. And, the developed osmotic pressure from the thin DDLs sealed the micro voids and restricted the flow of various cations. The GB4 achieved sealing, therefore, under all the studied high ionic strength salts. Further, the volume change in terms of normalized thickness with different pore fluids for GB1 and GB4 were presented in Figures 4.6(c) and 4.6(d), respectively. The initial collapse was found to be highest with KCl for GB1 and the collapse reduced significantly with the other salts. The

GB1 showed collapse at equilibrium also although the volume increased slightly with permeation time. On the other hand, the initial collapse magnitude was marginal for GB4 with all the studied pore fluids. The equilibrium volume with NaCl was higher than KCl for both GB1 and GB4, which was due to the larger DDL thickness with the sodium ions (Das and Bharat, 2017). The normalized thickness for calcium was found to be in the order of potassium with GB1 due to divalent and smallest hydrated ionic size as explained earlier.

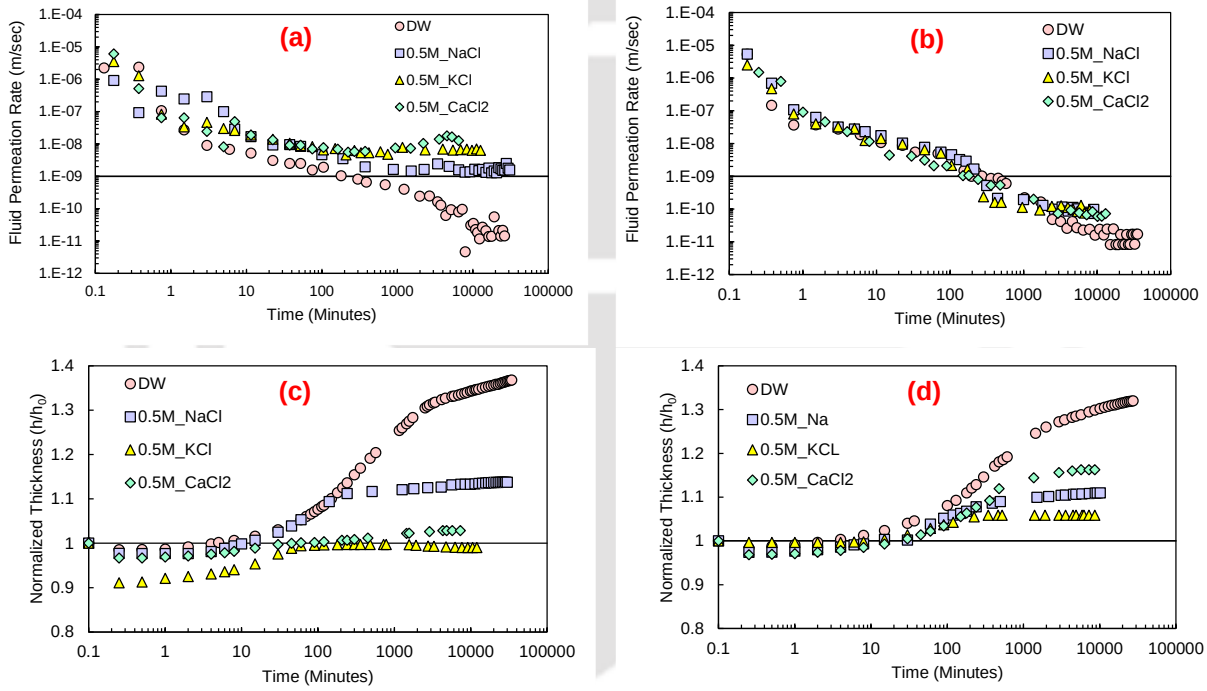

Figure 4.6: Variations of (a) hydraulic permeation rates for GB1; and (b) hydraulic permeation rates with time for GB4; and (c) normalized thickness for GB1; (d) normalized thickness for GB4; under 50 kPa mechanical load with different pore fluids

The van der Waal forces of attraction tightly holds the individual particles of bentonite in GB. The observation from the experiments that the granules remains granules in high concentration salt solutions is only due to insufficient development of repulsive forces (osmotic). The repulsive forces developed in GB under high concentration salt solution are not able to overcome the van der Waal force of attraction. The estimation of surface forces such as van der Waals', Columbic attraction, and osmotic repulsion forces at different particle interactions is highly complex and is

not available in the literature for the GB. The influence of different surface forces at different particle (weak and strong) interactions are studied by discrete element methods and molecular dynamic simulations at present. The (extremely strong) particle interaction in GB under the chemical and mechanical loading conditions are not available and are mathematically a challenging problem. Thus, disintegration of GB into individual particles are only qualitatively related to the developed osmotic pressures under the chemical environment.

In summary, the surface forces between the particles govern the hydro – chemo – mechanical behavior of compacted GBs. The number of particles associated with each other in a granule by van – der – Waals attraction forces is less with the increase in the fineness in the GSD. Thus, more repulsive pressure is generated with the decrease in the granules size or increase in the fineness. An initial collapse is observed after the inundation due to dominant mechanical pressure in compared to the developed repulsive pressures from the DDL formation. The volume increases with time due to improved formation of the DDLs and dominance in the repulsive pressures. A macroscopic swelling is observed when the developed DDLs completely occupy the macro void space. The swelling of individual clay particles will lead to the disintegration of the granules due to the development of sufficient repulsive pressure against the van der Waals attraction and influences the permeation rate. The filling of macro voids by the diffused double layers may decrease the hydraulic conductivity to a limiting value ($< 10^{-9}$ m/sec). The thickness of the DDL reduces in the presence of high ionic strength salt solutions, which increases the equilibrium hydraulic conductivity and decreases the swelling ability. The presence of high ionic strength potassium and calcium salts is more critical to the sealing and stability of the liner due to smaller hydrated cationic size and higher valence, respectively. As the presence of these salts in the leachate depends on the waste source, the decrease in the average size of the bentonite granules in

the liner by the mechanical granulation process might effectively help in the self-sealing of the macro-voids. The individual particles can swell and achieve the limiting hydraulic conductivity (< 10^{-9} m/sec) as the repulsive pressure is generated easily in the finer form of GB.

4.2.3 Influence of Plasticity on Hydraulic and Volume change Behaviour

The variations in the volume change and permeation of GB1 and GB5 with time were compared to understand the influence of plasticity. The GB1 was higher quality bentonite while the GB5 was lower quality bentonite based on their plasticity (Gapak et al. 2017, Bharat and Gapak, 2018). The hydro – chemo – mechanical behaviour of both the studied GBs were presented in Figures 4.7 and 4.8 under the applied load of 50 kPa. The variations in volume change behavior with time were plotted in terms of normalized thickness as shown in Figure 4.7(a), 4.7(b), 4.7(c), and 4.7(d) with different pore fluids such as distilled water, 0.5 M NaCl, 0.5 M KCl, and 0.5 M $CaCl_2$, respectively. As the plasticity of GB1 was higher than the GB5, a higher normalized thickness was observed with all the studied pore fluids. The lower quality bentonite showed 8-9 % equilibrium collapse with high ionic strength calcium and potassium salt environment, while higher quality bentonite showed an equilibrium collapse of only 1 % with 0.5 M KCl, and showed a marginal swelling with high ionic sodium and potassium environment. The higher swelling in GB1 was attributed to both the higher plasticity and finer grain sizes. Similar observations on volume change were also reported by (Lee and Shackelford, 2005), which shows higher volume for high-quality bentonite and supported a similar trend.

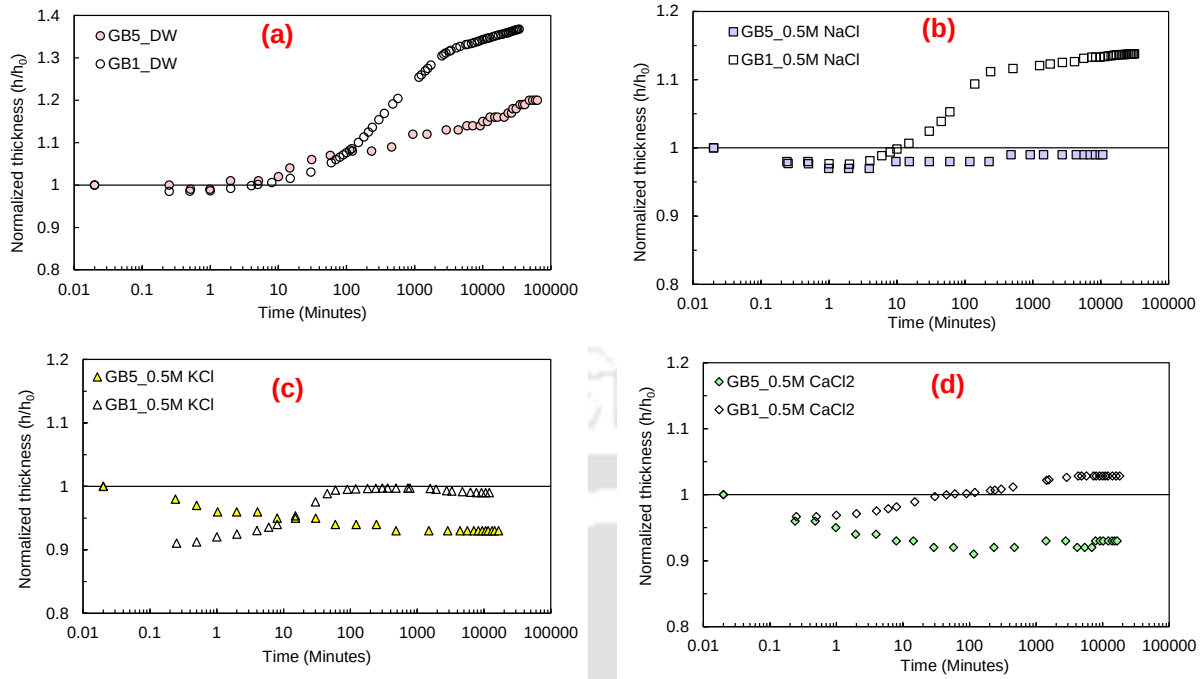

Figure 4.7: Variations of normalized thickness of GB with time for different plasticity under 50 kPa mechanical stress with (a) distilled water; (b) 0.5 M NaCl; (c) 0.5 M KCl; and (d) 0.5 M $CaCl_2$ as pore fluid

The variations of permeation rates with time for both the GB were presented in Figure 4.8. Both the GBs showed nearly similar fluid permeation rates with distilled water as shown in Figure 4.8(a). Plasticity did not have much influence on the hydraulic behavior of GB with distilled water. The hydraulic performance of GB5 with equilibrium hydraulic conductivity of 4×10^{-10} m/sec was found to be satisfactory with 0.5 M NaCl as a pore fluid; while the hydraulic performance of GB1 was not found to be satisfactory or it does not seal with equilibrium hydraulic conductivity of 1.5×10^{-9} m/sec as shown in Figure 4.8(b). Hydraulic behavior of GB with 0.5 M KCl and $CaCl_2$ were found to be unsatisfactory for both the GB as shown in Figures 4.8(c) and 4.8(d) respectively. The equilibrium hydraulic conductivity was found to be 6.5×10^{-9} m/sec and 1.9×10^{-9} m/sec for GB1 and GB5, respectively with 0.5 M KCl as pore fluid. While the equilibrium hydraulic conductivity was found to be 1.3×10^{-8} m/sec and 5×10^{-8} m/sec with high $CaCl_2$ solution for GB1 and GB5, respectively. The final hydraulic permeation rate of higher quality bentonite (GB1) was found to

be higher than low-quality bentonite (GB5) under a 0.5 M KCl environment. Similar observation on higher hydraulic conductivity for high-quality bentonite with high salt concentration was also reported by (Lee and Shackelford, 2005). This increase in hydraulic conductivity with an increase in bentonite quality is attributed to the high loss in osmotic potential. The final permeation rate for GB5 was found to be higher than GB1 with calcium as pore fluid. The lower permeation rate in high-quality bentonite (GB1) was attributed to the mineralogy of GB1, the high amount of divalent cations in GB1 as compared to GB5 makes GB1 more resistant to divalent permeation fluid and hence led to a lower permeation rate with a calcium solution.

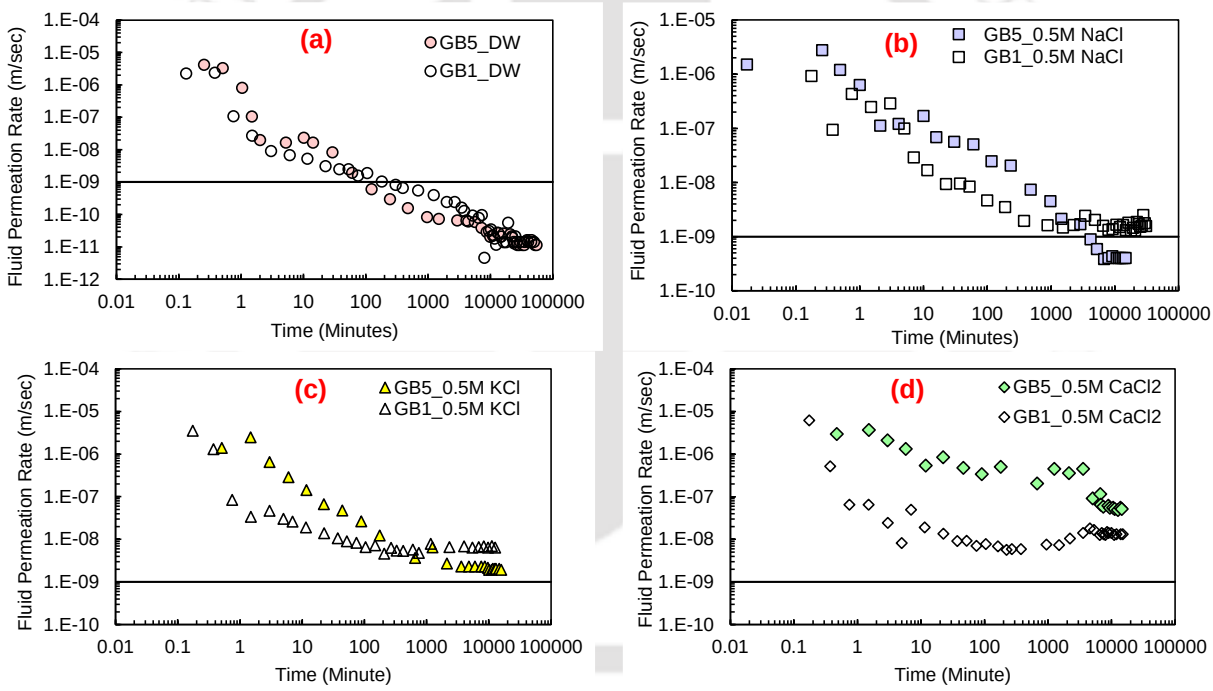

Figure 4.8: The variations of fluid permeation with time for granular bentonites with different plasticity under 50 kPa vertical stress with (a) distilled water; (b) 0.5 M NaCl; (c) 0.5 M KCl; and (d) 0.5 M $CaCl_2$ as pore fluid

4.3 Summary

Self-sealing, volume change behavior, and hydraulic permeation rates of different compacted GBs were studied with different pore fluids under 50 kPa mechanical stress. The following conclusions

were drawn based on the influence of grain size distribution and plasticity of GB on the hydro-chemo-mechanical behavior.

- The hydraulic performance of coarse granulated bentonite was not satisfactory in the presence of high ionic strength salt solutions. The equilibrium hydraulic conductivity was nearly one fold higher than the limiting value due to improper sealing of the macro voids in the presence of high ionic strength salt solutions. A poor disintegration of the GB into individual particles were noticed due to insufficiently developed osmotic repulsion between the particles.
- The presence of finer granules by the mechanical granulation process improved the sealing and hydraulic behaviour in the presence of high ionic strength salt solutions. The equilibrium hydraulic conductivity was marginally influenced by the presence of different cations in the leachate due to the availability of only micro-voids between the particles in the finer GBs.
- Initial and equilibrium collapse behaviour of GB in the presence of high ionic strength salts was circumvented by reducing the mean granule size. The sudden collapse of the liner system might negatively influence the leachate collection system and other components of the landfill. The finer GBs exhibited marginal initial collapse and macroscopic swell at equilibrium.
- The plasticity of a coarser GB further influences the self-sealing and hydraulic performance. The performance of high-quality coarse bentonite was better under the high calcium environment, while the performance of low-quality coarse bentonite was found to be better with high ionic sodium and potassium salt solutions. Therefore, the finer GBs are suitable in waste containment facilities that receive high ionic strength salt solutions.

Chapter – 5

Influence of Polymer and Biopolymer Amended Granular Bentonite under Thermo-Chemo-Mechanical Loadings

---

5.1 General

The role of granule size of the GB on sealing and volume change behavior was discussed in Chapter 4. The GB failed to attain sealing in the high-concentration salt environment. This section discusses the sealing ability, hydraulic, and volume change performance of polymer and biopolymer-amended GB. The present work utilized sodium polyacrylate and four different biopolymers, namely, guar gum, acacia gum, agar-agar gum, and xanthan gum under extreme chemo-mechanical loading conditions. The present work is divided into three sections. The hydraulic and volume change of polymer and biopolymer amended GB under critical chemo-mechanical loadings was discussed in the first section. Further, the diffusion of cations through compacted GB and xanthan gum amended GB is discussed in the second section. The sealing ability of xanthan gum amended GB under the influence of elevated temperatures was discussed in the third section. Further, the governing mechanisms for evaluating the polymer-amended GB behavior were discussed in detail in this section.

5.2 Hydro-Chemo-Mechanical Behavior

Granular bentonite is used in GCLs due to its pourability in the manufacturing process and it is the primary product during the bentonite processing (Kutlic et al., 2012; Bouazza 2002). The granules of GB disintegrate into individual particles upon hydration by the leachate due to the development

of repulsive diffused double layers (DDLs) around the clay surfaces. The granules of GB remain granule after the permeation of high-concentration salt solutions. The inability of GB to seal the macro-voids upon hydration under such an environment can lead to the migration of toxic heavy metals, organic contaminants, and other emerging contaminants to the groundwater.

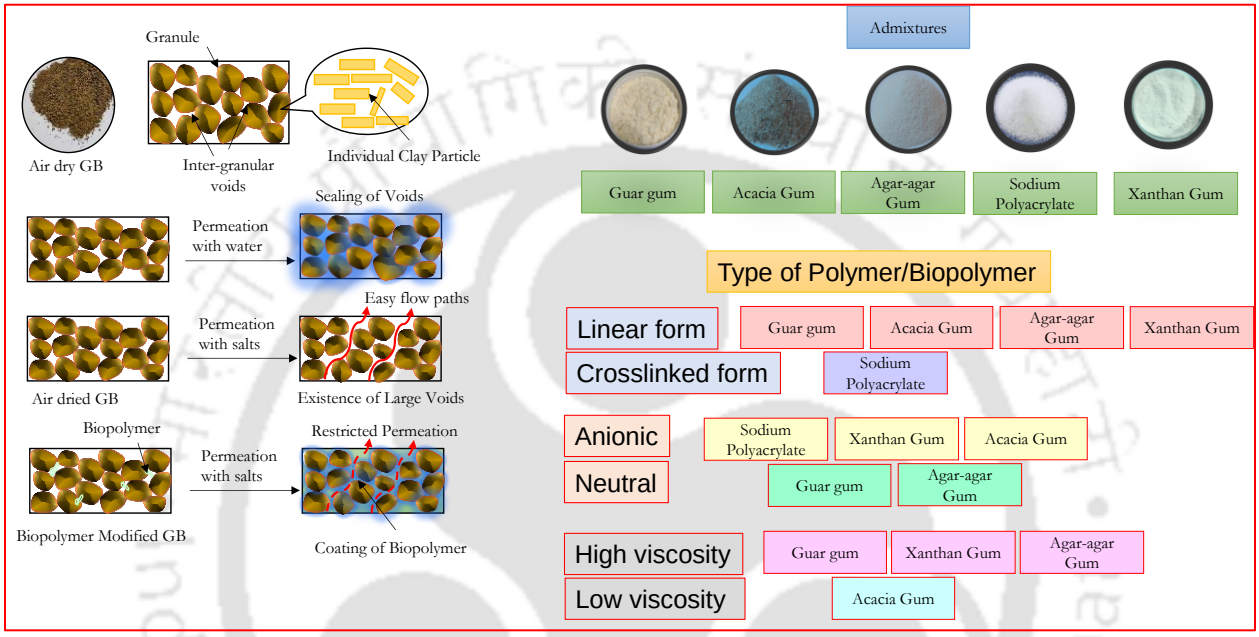

Figure 5.1 Illustration showing the applications of the polymer and biopolymers for improvement in sealing and volume change behaviour of GB

The landfill liners are subjected to a wide range of mechanical loading, the lower mechanical loadings are more critical due to the poor disintegration of GB (Peirce et al., 1986; Das and Bharat 2021). Therefore, the present study considered the higher chemical loading along with lower mechanical loading to consider worst-case scenarios. Granular bentonites in GCLs are exposed to coupled hydraulic, chemical, and mechanical loading due to the presence of leachate, salts in leachate, and weight of waste. The study was conducted under critical conditions, i.e., high chemical and lower mechanical loading. Biopolymers also improve the liquefaction resistance, bearing capacity, and erosion control, and reduce the hydraulic conductivity of the soils by several orders of magnitude (Chen et al., 2013; Latifi et al., 2016; Hataf et al., 2018; Kwon et al., 2019;

Shariatmadari et al., 2020). Gaur-gum biopolymer, xanthan gum, and agar-agar can form a thick viscous gel upon hydration. Although, acacia gum forms a slightly less viscous gel, but has the presence of various carboxyl groups which can arrest the cation of the pore-fluid. These biopolymers have the potential to act as suitable material to achieve sealing as shown in Figure 5.1.

5.2.1 Polymer Amended Granular Bentonite under HCM Loadings

A different percentage of polymer amendments was explored. A 5% (GBP5) and 10% polymer (GBP10) by weight was considered with GB for evaluating the performance. Temporal variations of fluid permeation rates under 50 kPa mechanical loads with distilled water as pore-fluid were plotted for GB and polymer-amended GB (GBP) in Figure 5.2(a). Fluid permeation rates were found in order of 10^{-6} m/sec initially, which dropped with time and achieved the sealing of macro-voids present in compacted GB and GBP samples. The sealing of these voids was achieved in 200-300 minutes from the start of the test. The reduction in the fluid permeation rates is due to the development of repulsive forces in GB upon hydration, which further leads to the disintegration of GB granules. Moreover, the lower fluid permeation rate in the case of GBP is also due to the formation of the hydrogel upon hydration of sodium polyacrylate. The GB sample achieved an equilibrium fluid permeation rate of 1.42×10^{-11} m/sec, whereas, the GBP5 and GBP10 samples achieved equilibrium fluid permeation of 5.8×10^{-11} m/sec and 2.5×10^{-10} m/sec, respectively. A slight increase in the equilibrium fluid permeation rate was observed upon an increase in polymer amendment.

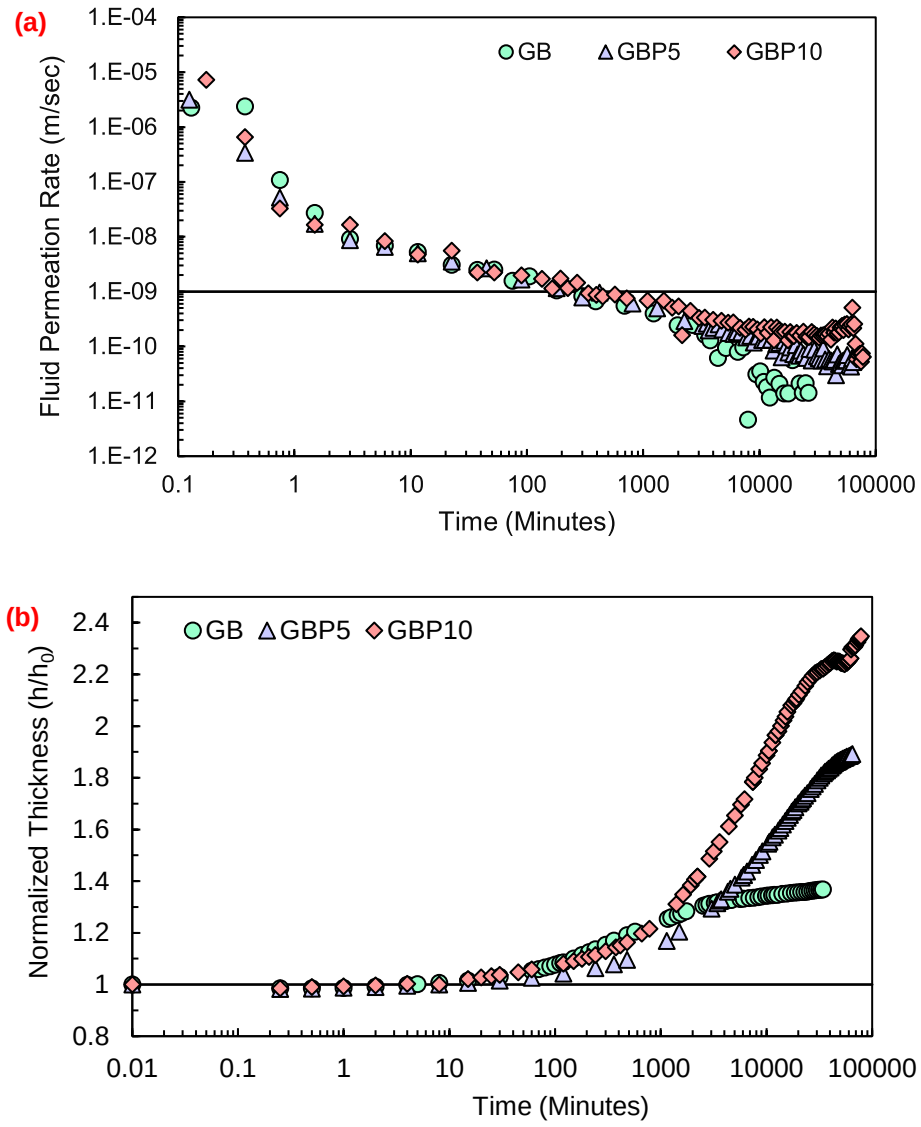

Figure 5.2: Temporal variation of (a) fluid permeation rate; (b) normalized thickness of GB and polymer amended GB with distilled water under 50 kPa mechanical loading.

The temporal variations of fluid permeation rates of GB and GBP samples under 50 kPa mechanical loading with 0.5 M KCl as pore-fluid were plotted in Figure 5.3(a). The initial fluid permeation rates of GB and GBP samples were in order of 10^{-6} m/sec, which reduced significantly upon hydration with the pore-fluid due to the development of repulsive forces. Both GB and GBP achieved an equilibrium fluid permeation rate of 4 – 8 ×10-9 m/sec, slightly higher than the limiting value. The development of repulsive forces was not sufficient to achieve the limiting values of fluid permeation rates.

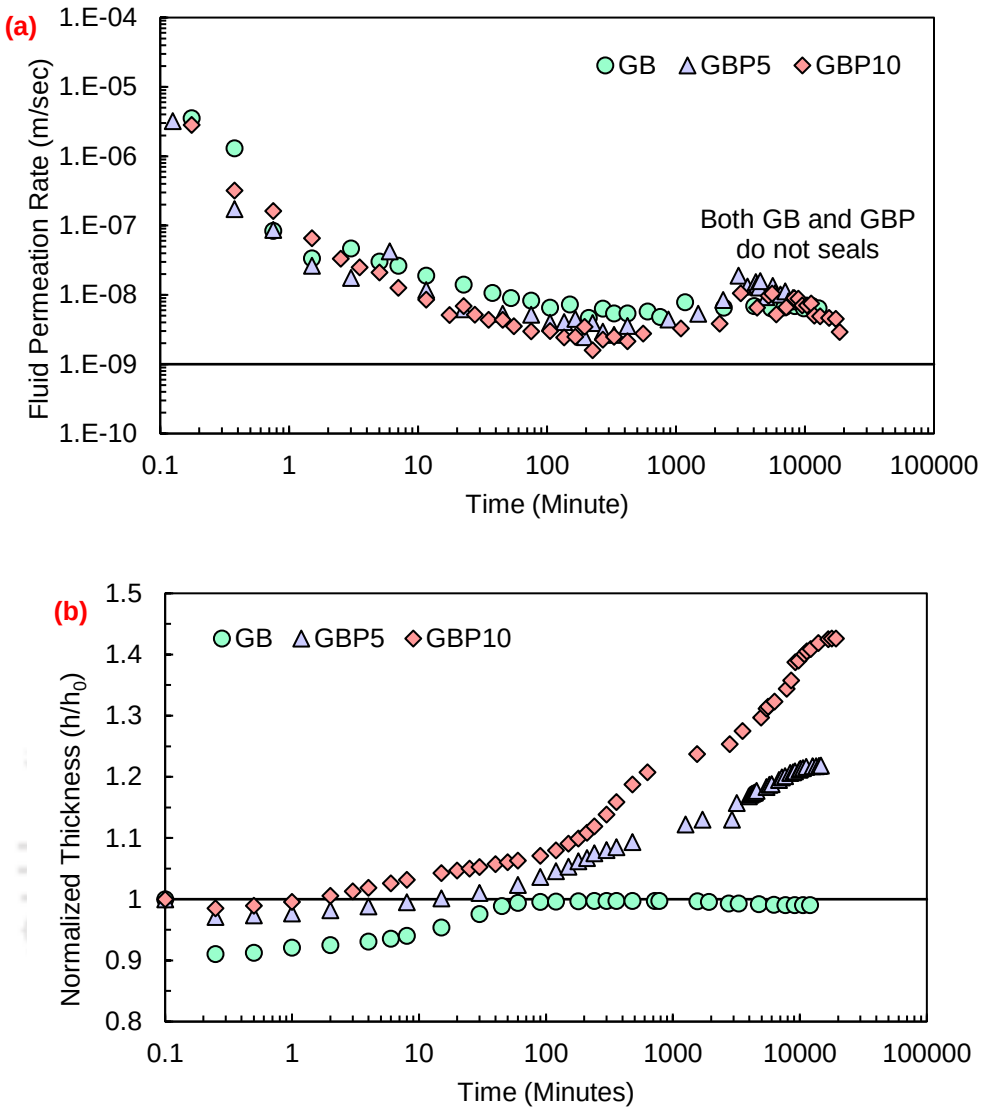

Figure 5.3: Temporal variations of (a) fluid permeation rate; (b) normalized thickness of GB and polymer amended GB with 0.5 M KCl under 50 kPa mechanical loading.

The temporal variations of volume change in terms of normalized thickness (h/h_0) with 0.5M KCl as pore-fluid under 50 kPa mechanical loading were presented in Figure 5.3(b). The samples showed a slight collapse upon application of chemo-mechanical loading. The magnitude of the collapse was found to be higher in GB as compared to GBP samples. The samples started swelling due to the development of the repulsive force, which also led to the breaking of the granules of GB upon hydration. In addition to repulsive forces, the formation of hydrogel also contributed to swelling of the GBP samples. The GB sample could not achieve the original volume even at

equilibrium, which means the swelling pressure of GB in KCl environment is lower than the applied mechanical loading. However, GBP samples achieved their original volume within 30 minutes from the start of the experiment. The swelling rate of the GBP samples were found to be faster than GB sample due to formation of hydrogel with 0.5M KCl as pore-fluid. The samples achieved equilibrium normalized thicknesses of 0.99, 1.22, and 1.43 for GB, GBP5, and GBP10 respectively, under a 0.5M KCl environment. The normalized thicknesses higher than 1 for represents that the applied mechanical loading is smaller than the swelling pressure of GBP samples. Similarly, the hydraulic and volume change variations of GBP with 0.5M NaCl and 0.5M $CaCl_2$ were presented in Appendix 1.

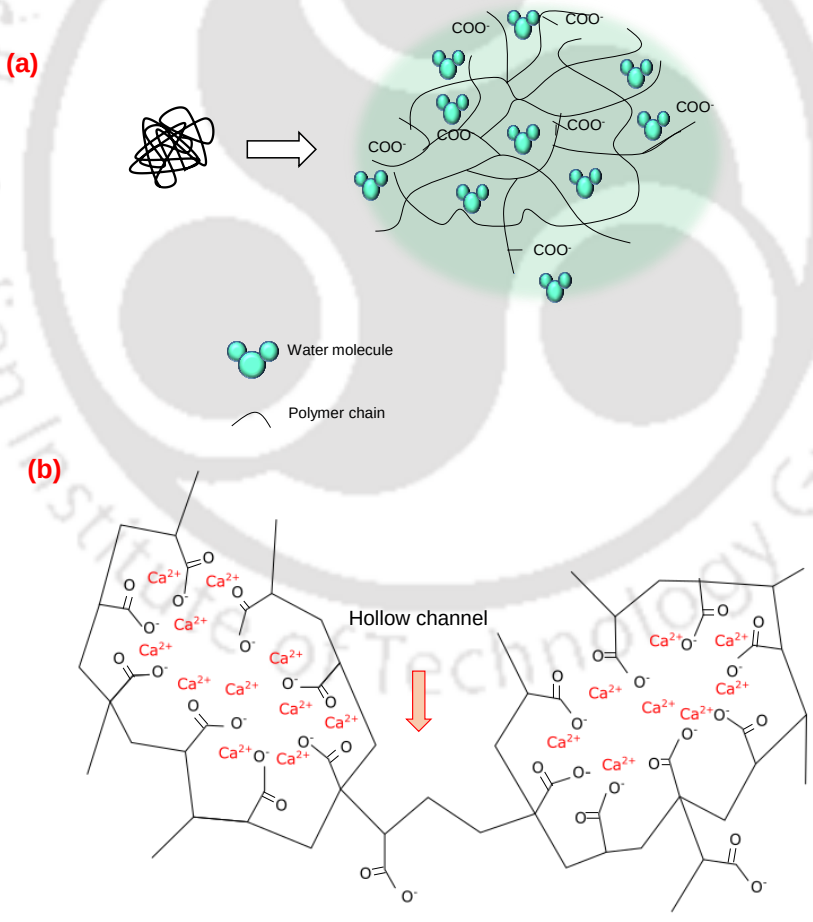

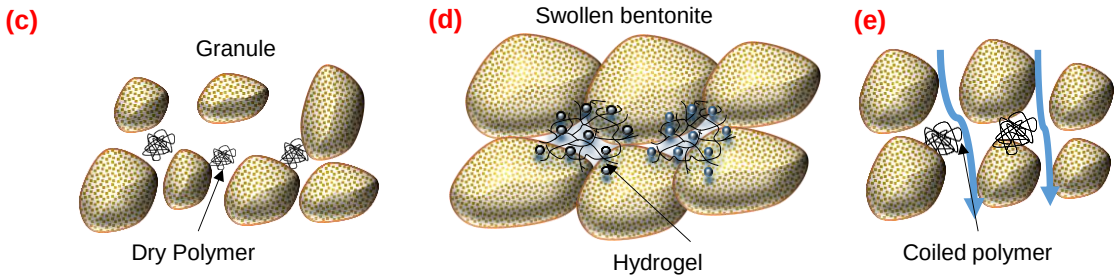

Figure 5.4: Illustration showing (a) swelling mechanism of sodium polyacrylate; (b) formation of hollow channels in sodium polyacrylate in the presence of high-concentration salt solutions. (c) polymer amended GB, (d) swollen GB and swollen polymer after permeation with distilled water; (e) permeation with high concentration pore-fluid leading to the coiling of the polymer

Polymer (Sodium polyacrylate) has high capacity of water adsorption due to the presence of a large number of carboxyl groups and high repulsion between chains leads to significant swelling of polymer as shown in Figure 5.4(a). Moreover, sodium polyacrylate has a cross-linked structure, which led to the phase separated swelling of sodium polyacrylate. The swelling of polymer structure depends on several factors including pH, ionic strength, and temperature. High ionic salt solution results in the coiled structure of polymer as shown in Figure 5.4(b) (Swann et al., 2010). With divalent cations like calcium, the structure of sodium polyacrylate forms a complex structure that prevents the formation of hydrogel. This structure also has several hollow channels Figure 5.4(b), which can easily allow the flow of contaminants and lead to higher hydraulic conductivity with polymer-amended GB.

Mechanisms controlling the fluid permeation rates of samples were also presented in Figure 5.4. The dry compacted GBP was presented in Figure 5.4(c), where coiled polymer was presented around the granules of GB. The swelling of GB and swelling of polymers in the GBP sample after permeation with distilled water has been shown in Figure 5.4(d). Further, the permeation of high-concentration pore-fluids through GBP were presented in Figure 5.4(e). Due to the coiling of polymers and loss in osmotic efficiency of GB in the presence of high ionic salts, the macro-voids of GBP samples did not seal and higher permeation was observed.

5.2.2 Guar Gum Amended GB under HCM Loadings

Temporal variations of the fluid permeation rates of GBGG samples with different pore–fluids under 20 kPa mechanical loading were presented in Figure 5.5(a). The fluid permeation rates were found to be higher initially, which decreased with time due to the hydration of GBGG samples. The GBGG samples achieved a limiting value ($<10^{-9}$ m/s) of the fluid permeation rate within 80 minutes from the start of the experiment with distilled water and 0.5M KCl as pore–fluid. The fluid permeation rate of the GBGG sample with distilled water started increasing after achieving a minimum value of 10^{-11} at 20,000 minutes. The sample showed a fluid permeation rate slightly higher than the limiting value at equilibrium. Similarly, the fluid permeation rate of 0.5 M KCl started increasing after achieving the lowest fluid permeation rate at 8000 minutes from the start of the experiment, and it reached slightly higher than the limiting value of the fluid permeation rate at equilibrium. Further, it took 1100 minutes to seal with 0.5 M NaCl solution under 20 kPa mechanical loading. The fluid permeation rate with 0.5 M NaCl also achieved the minimum value after 9000 minutes from the start of the experiment, and it reached higher than the limiting value at equilibrium. The GBGG sample with 0.5 M $CaCl_2$ as pore–fluid did not seal and achieved an equilibrium fluid permeation rate slightly higher than 10^{-9} m/s. The temporal variations of the volume change in terms of normalized thickness (h/h_0) of GBGG samples with different pore-fluids under 20 kPa mechanical loading were presented in Figure 5.5(b). An initial collapse of 2-3% was observed in GBGG samples upon application of 20 kPa mechanical loading. The GBGG samples started swelling upon hydration due to the formation of diffused double layers (DDLs). These GBGG samples under 20 kPa achieved the original volume in 10, 100, 500, and 6000 minutes from the start of the experiments for KCl, $CaCl_2$, D.W., and NaCl, respectively. Further, the swelling of the samples was continued under the applied mechanical loading of 20 kPa and

achieved the equilibrium normalized thicknesses of 1.19, 1.15, 1.2, and 1.33 for D.W., NaCl, KCl, and $CaCl_2$, respectively. Similarly, temporal variations of the fluid permeation rates and volume change of GBGG samples with different pore-fluids under 50 kPa mechanical loading were presented in Appendix-1.

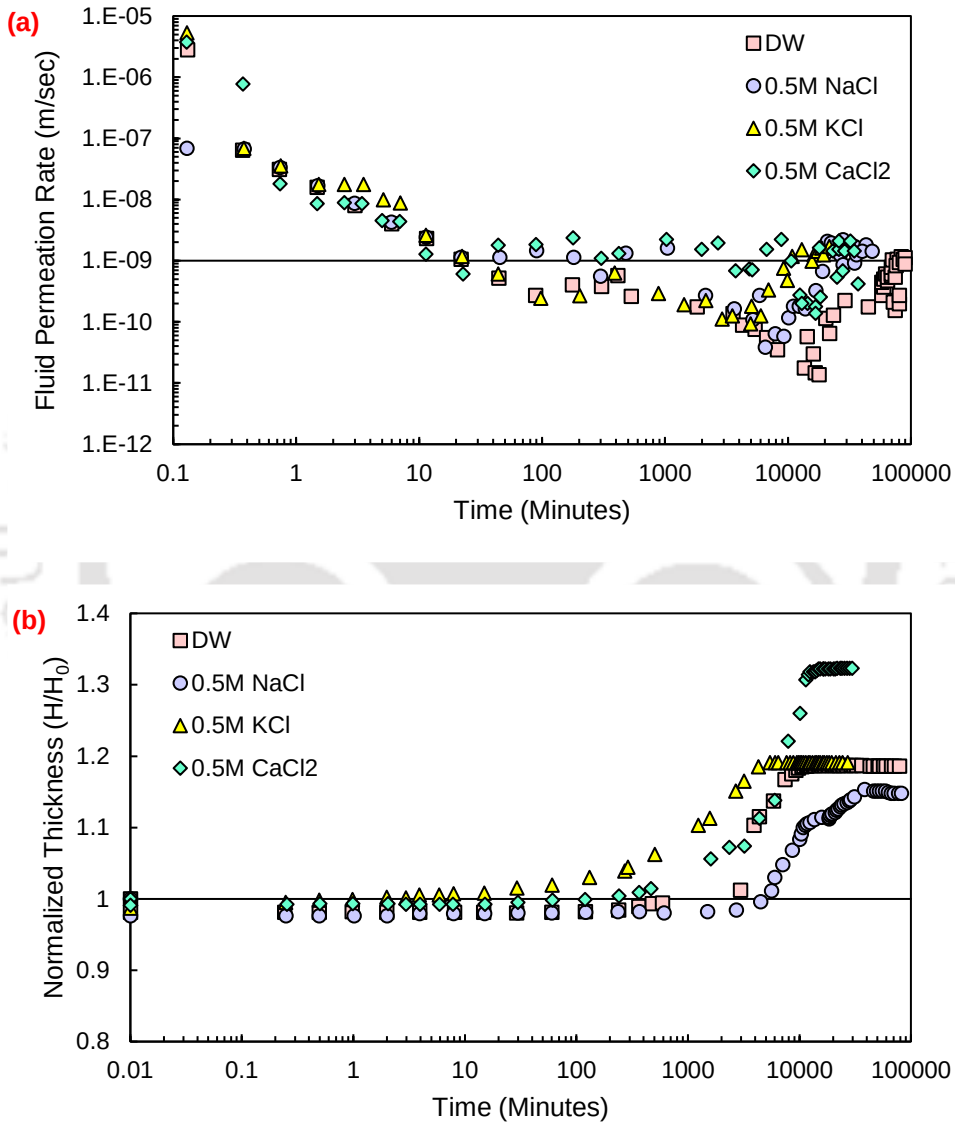

Figure 5.5: Temporal variations of (a) fluid permeation rates; (b) normalized thickness under 20 kPa mechanical loadings for GBGG samples with different pore-fluids

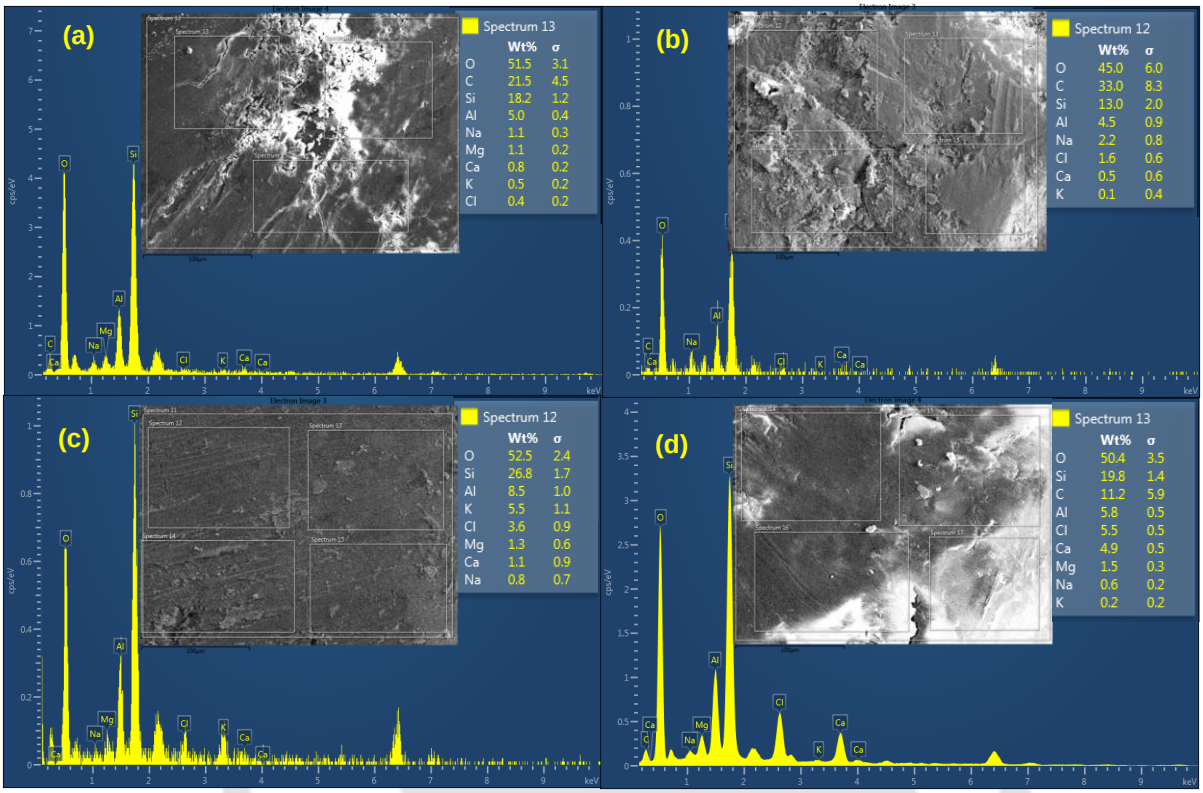

Figure 5.6: Energy dispersive X-ray spectroscopy spectra for GBGG samples after permeation with (a) D.W.; (b) 0.5 M NaCl; (c) 0.5 M KCl; and (d) 0.5 M $CaCl_2$ as pore-fluid under 20kPa mechanical loading

The elemental analysis of GBGG samples was performed using energy-dispersive X-ray spectroscopy (EDX) and presented in Figure 5.6. The EDX spectra of the GBGG sample after permeation with distilled water were presented in Figure 5.6(a). Silicon, oxygen, carbon, and aluminum were present as major elements, while traces of sodium, magnesium, calcium, and potassium were also present. The major elements were the main components of either GB or GG, while trace elements are presentative of the exchangeable cations. The EDX spectra of the GBGG sample after permeation with 0.5 M NaCl salt solution were presented in Figure 5.6(b). Apart from the presence of major elements, the percentage of sodium increased slightly, which represents the sorption of sodium on the GBGG samples after permeation. The EDX spectra of the GBGG sample after permeation with 0.5M KCl salt solution were presented in Figure 5.6(c). The percentage of potassium increased significantly, which represents the adsorption of potassium on GBGG sample

during permeation. Moreover, other elements like sodium, magnesium, calcium, etc. were also present in trace amounts in the GBGG sample. The GBGG after permeation with the 0.5 M $CaCl_2$ salt solution was presented in Figure 5.6(d). The results from EDX show the presence of calcium in a high amount; moreover, other exchangeable cations were present in trace amounts in the sample. The increased percentage of calcium represents the adsorption of calcium ions on the GBGG sample. Similarly, the EDX of GBAG and GBAA under different pore-fluid conditions has been provided in Appedix-2.

5.2.3 Acacia Gum Amended GB under HCM Loadings

5.2.3.1 Role of Pore-fluids

Temporal variations of fluid permeation rates for GBAG samples under 20 kPa with different pore–fluids were presented in Figure 5.7(a). The fluid permeation was found in the order of 10^{-5} – 10^{-6} m/s initially, which reduced with time for GBAG samples with different pore–fluids due to hydration. The GBAG sample achieved sealing in 70 minutes from the start of the experiment with distilled water under 20 kPa mechanical loading. The fluid permeation rate with distilled water achieved an equilibrium rate of 2×10^{-11} m/sec after 5000 minutes from the start of the experiment. The temporal variations of the fluid permeation rate for the GBAG sample under 20 kPa with 0.5 M NaCl as pore–fluid was also plotted in the same figure. The fluid permeation rates of GBAG samples were found to be higher initially, which decreased with time due to hydration. The process of hydration leads to the development of DDLs, which leads to the swelling of the sample along with the sealing of the macro-voids present among the GB granules. The initial fluid permeation rates of GBAG samples were in the order of 10^{-5} – 10^{-6} m/s. The sample with 20 kPa could not achieve sealing until equilibrium. The equilibrium fluid permeation for the GBAG sample with a

20 kPa mechanical loading was found to be in the order of 10^{-8} – 10^{-9} m/s, which is slightly higher than the limiting fluid permeation rate.

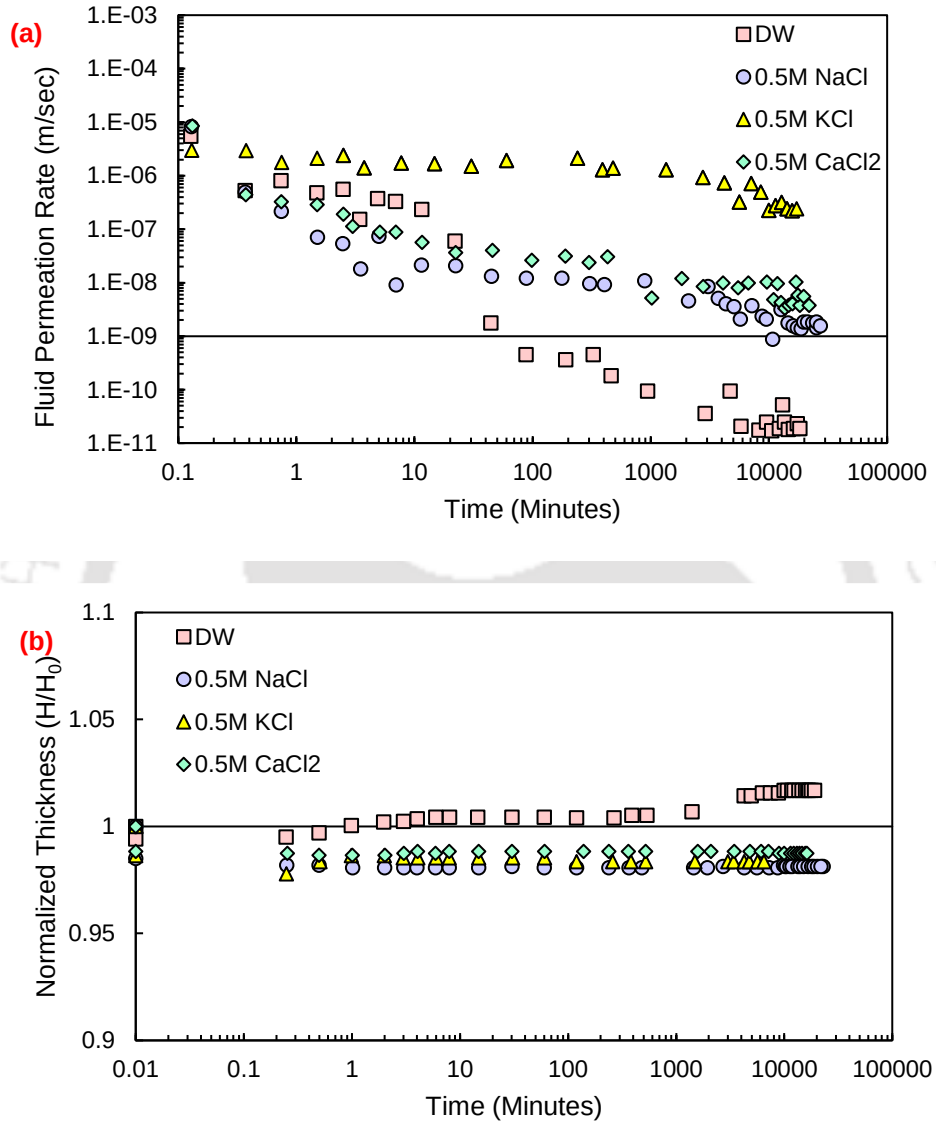

Figure 5.7: Temporal variations of (a) fluid permeation rates; (b) normalized thicknesses under 20 kPa mechanical loadings for GBAG samples with different pore-fluids

The temporal variations of the fluid permeation rates for GBAG samples with 0.5 M KCl as pore–fluid under 20 kPa mechanical loadings were also presented in Figure 5.7(a). The initial fluid permeation rates of GBAG samples were found to be in the order of 10^{-5} m/s, which decreased with time due to hydration upon permeation of pore–fluid. The GBAG sample with 20 kPa

mechanical loading achieved an equilibrium fluid permeation rate of 2×10^{-6} m/s, which is significantly higher than the limiting value. The temporal variations of fluid permeation rates for GBAG samples with 0.5 M $CaCl_2$ as pore-fluid and 20 kPa mechanical loadings were plotted in Figure 5.7(a). Initially, the fluid permeation rates of GBAG samples were found to be in the order of $10^{-5} – 10^{-6}$ m/s, which decreased with time due to the hydration of the samples. The sample with lower mechanical stress (i.e., 20 kPa) showed a fluid permeation rate in the order of 10^{-8} m/s at equilibrium, which is slightly higher than the limiting value.

Temporal variations of volume change in terms of normalized thickness (H/H_0) for the GBAG samples under 20 kPa mechanical loadings with different pore-fluids were presented in Figure 5.7(b). The GBAG sample with distilled water as pore-fluid showed an initial collapse of 1 % upon application of mechanical loading. The sample with 20 kPa mechanical loading started swelling upon hydration and achieved its original volume within a few minutes from the start of the experiment. The GBAG sample with 20 kPa achieved an equilibrium normalized thickness of 1.01 under 20 kPa, which shows the negligible volume change of GBAG samples upon application of hydro-mechanical loading conditions. The GBAG sample with 0.5 M NaCl, 0.5 M KCl, and 0.5 M $CaCl_2$ as pore-fluid under 20 kPa mechanical loading showed an initial collapse of 2%. The GBAG samples did not show any significant swelling upon hydration and continued with the same normalized thickness until equilibrium after permeation of salt solutions as pore-fluid. The observation of no swelling in GBAG samples is attributed to the poorly developed repulsive pressure among the bentonite particles. Similarly, the temporal variations of fluid permeation rates and normalized thicknesses for GBAG samples with various pore-fluids under 50 kPa mechanical loadings were plotted in Appendix 1.

5.2.3.2 Role of Salt Concentration

The temporal variations of the fluid permeation rates of GBAG samples under 20 kPa mechanical loadings with different concentrations of KCl salt solutions were presented in Figure 5.8(a). The fluid permeation rate was found to be in order of 10^{-5} m/s initially, which reduces with time upon permeation due to the hydration of samples. The samples with distilled water and a lower concentration of KCl salt solution as pore-fluid achieved the sealing of the macro-voids within 50 minutes from the start of the experiment. The equilibrium fluid permeation was found to be in the order of 10^{-11} m/s for both distilled water and low-concentration KCl as pore-fluid. Moreover, the sample with a high concentration of KCl salt solution as pore-fluid could not achieve sealing and achieved an equilibrium fluid permeation rate in the order of 2×10^{-6} m/s, which is significantly higher than the limiting value. The lower permeation with low-concentration pore-fluid and distilled water is due to the development of DDLs and the breaking of GB granules into individual particles with these pore-fluids. The GBAG sample could not achieve sealing with a high concentration of KCl due to a loss in osmotic potential.

The temporal variations of the volume change in terms of normalized thickness (H/H_0) for 20 kPa mechanical loading with different concentrations of KCl were plotted in Figure 5.8(b). GBAG samples showed an initial collapse of 1-2 % upon application of loads. Further, the samples started swelling on permeation of pore fluids due to the formation of DDLs. The sample permeated with distilled water attains its original volume within a few minutes from the start of the experiment. Moreover, the sample permeated with a lower concentration of KCl solution to achieve its original volume at equilibrium. The sample permeated with a high concentration of KCl did not show any significant swelling due to loss in the osmotic potential in a salt environment and this sample could not achieve its original volume. The GBAG samples showed equilibrium normalized thicknesses

of 1.02, 1.00, and 0.98 with distilled water, 0.1 M KCl, and 0.5 M KCl salt solution as pore-fluid, respectively. Similarly, the temporal variations of fluid permeation rates and normalized thicknesses of GBAG samples under 20 kPa mechanical loading with different concentrations of NaCl and $CaCl_2$ salt solutions were plotted in Appendix 1.

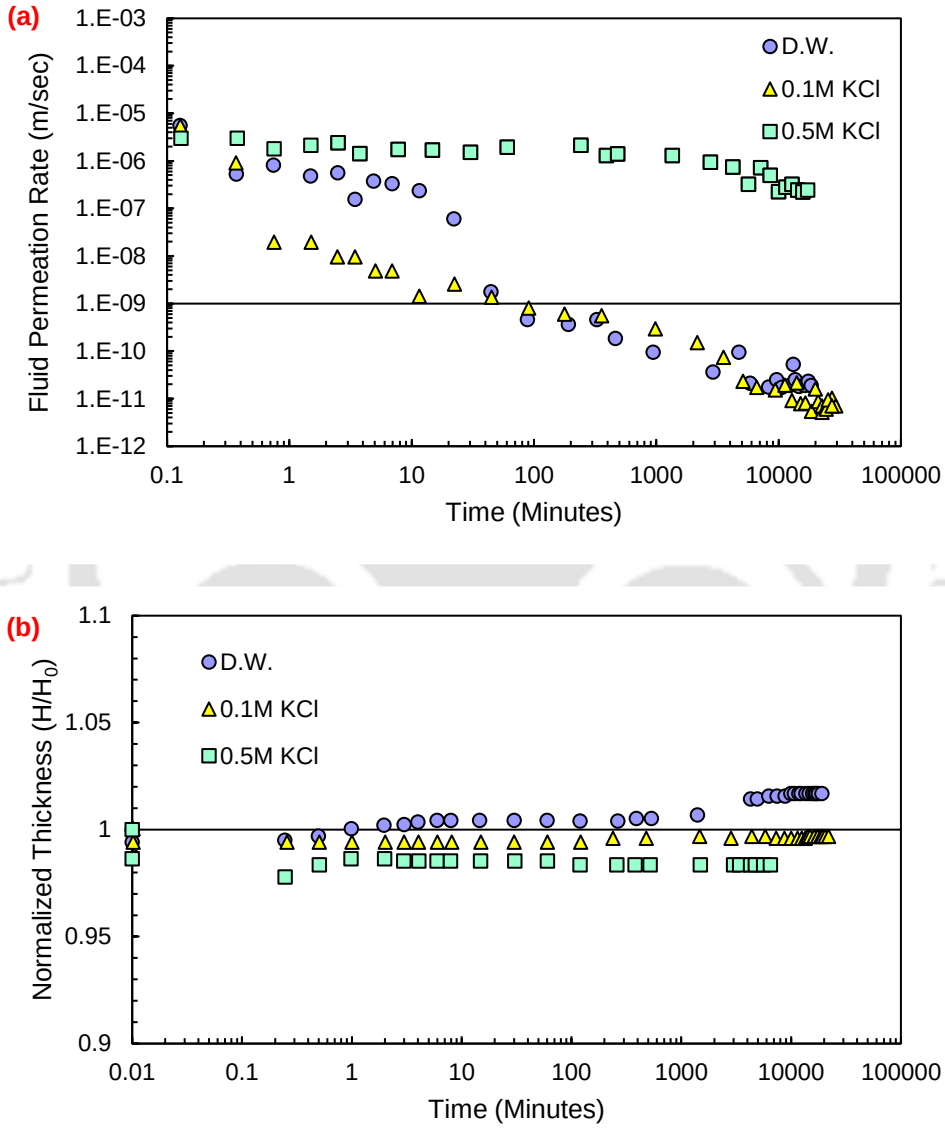

Figure 5.8: Temporal variations of (a) fluid permeation rates; (b) normalized thicknesses with different concentrations of KCl for GBAG samples under 20 kPa mechanical loading

5.2.4 Agar-Agar Gum Amended GB under HCM Loadings

Temporal variations of the fluid permeation rate of GB amended with 10 % agar-agar gum (GBAA) sample with different pore-fluids under 20 kPa mechanical loading are plotted in Figure 5.9(a). The fluid permeation rate was found to be in the order of 10^{-5} m/s, which reduces with time due to the hydration of samples. The fluid permeation of the GBAA sample with distilled water was much slower than the other pore-fluids. The GBAA sample with 20 kPa achieved the sealing of macro-voids within 50 minutes from the start of the experiment with distilled water as pore-fluid and it achieved an equilibrium fluid permeation rate in the order of 10^{-10} - 10^{-11} m/s. The sample with 0.5M NaCl as pore-fluid achieved the sealing of the macro-voids within 500 minutes from the start of the experiment. GBAA samples with 0.5M NaCl achieved an equilibrium fluid permeation in order of 10^{-10} m/s. The fluid permeation rate of the GBAA sample with 0.5 M KCl were found to be in the order of 10^{-5} -10^{-6} initially, which reduces with time upon hydration. The fluid permeation rate of GBAA samples with high concentration of KCl at equilibrium were found to be in the order of 10^{-9} m/s. The sealing of these samples took 2000 minutes from the start of the experiment for 20 kPa mechanical loadings. The fluid permeation rates of the GBAA samples with 0.5 M $CaCl_2$ were found to be higher initially, which reduced with time due to the formation of DDLs due to hydration. The fluid permeation rate of GBAA samples with 0.5 M $CaCl_2$ at equilibrium was found to be in the order of 10^{-9} m/s. The sample achieved this rate of fluid permeation after 4000 minutes from the start of the experiment. The hydration of GB led to the formation of DDLs, and the hydration of agar-agar gum led to the formation of thick viscous gel. This thick viscous biopolymer gel clogs the voids present between the granules of the GB. Moreover, agar-agar gel forms a coating over the bentonite particles, and the presence of hydroxyl

groups in agar-agar gel holds the cation from the pore-fluid, which led migration of pore-fluid with relatively lower concentration to the GB particles.

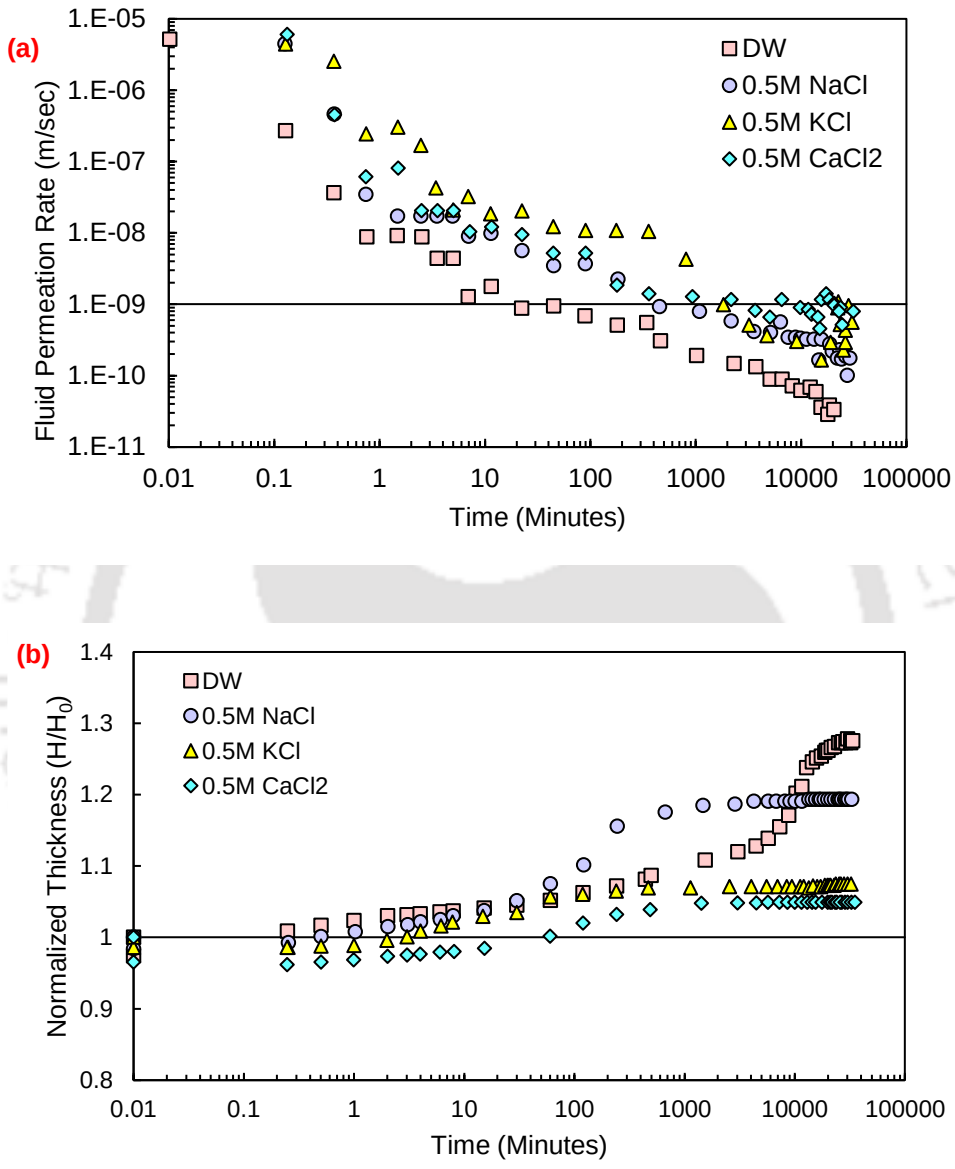

Figure 5.9: Temporal variations of (a) fluid permeation rates; (b)normalized thicknesses under 20 kPa mechanical loadings for GBAA samples with different pore-fluids

Temporal variations of volume change in terms of normalized thickness (H/H_0) for GBAA samples with different pore-fluids under 20 kPa mechanical loadings were presented in Figure 5.9(b). The GBAA samples showed an initial collapse of 2-3 % upon application of 20 kPa mechanical

loading. The samples started swelling upon hydration due to the formation of DDLs in GB. The sample with 20 kPa achieved its original volume within a few minutes from the start of the experiment with distilled water, 0.5 M NaCl, and 0.5 M KCl as pore-fluid, while the sample with 0.5 M $CaCl_2$ took 80 minutes to achieve its original volume. The samples continued to swell and achieve an equilibrium normalized thickness of 1.27, 1.2, 1.07, and 1.05 for D.W., 0.5 M NaCl, 0.5 M KCl, and 0.5 M $CaCl_2$, respectively.

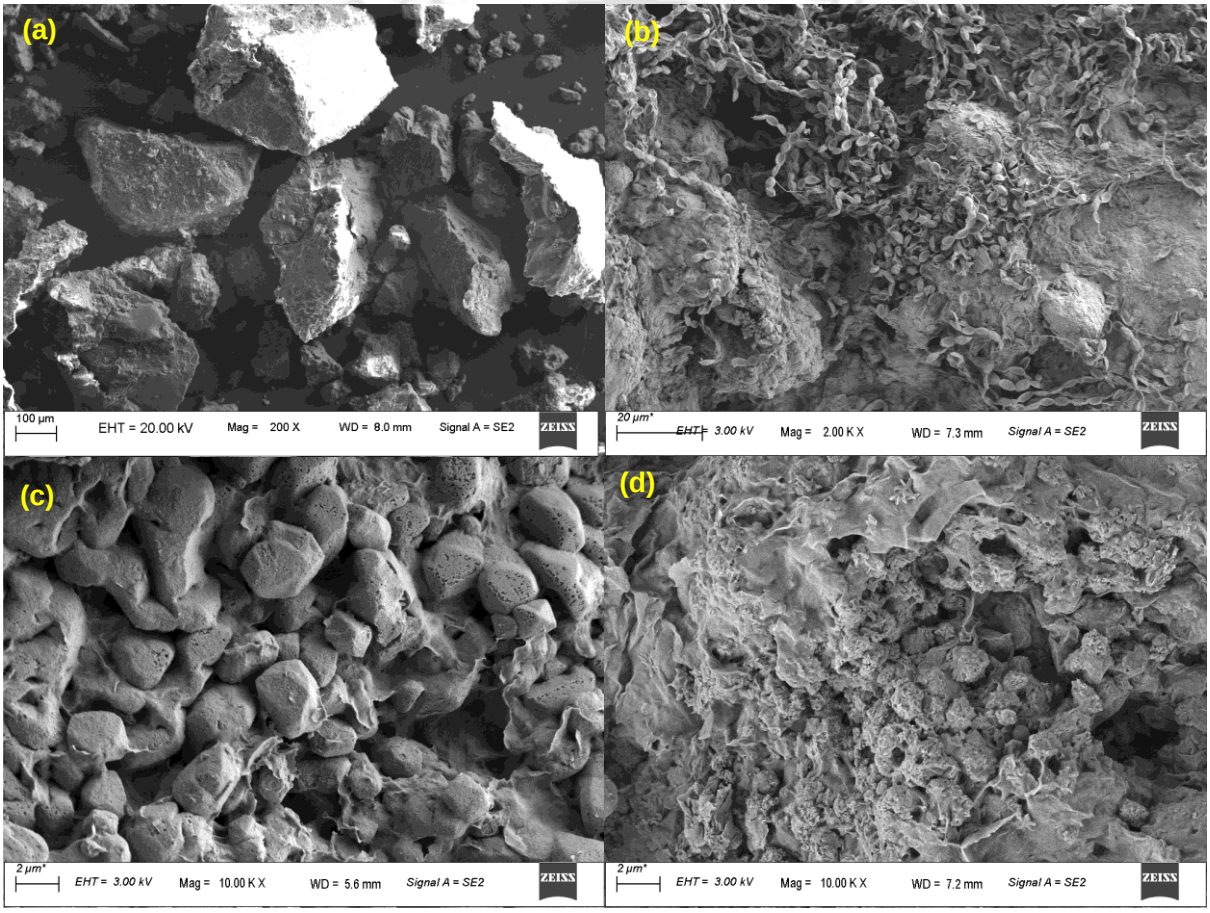

Figure 5.10: FESEM micrographs of (a) GB; (b) GBGG; (c) GBAG; and (d) GBAA samples after permeation with 0.5M KCl as pore-fluid

The FESEM micrographs of GB, GBGG, GBAG, and GBAA samples after permeation with 0.5 M KCl samples were shown in Figure 5.10. The morphology of GB after permeation with high concentration of KCl salt solution showed the presence of granules in intact form. The inability to

break GB into individual particles is clearly visible from Figure 5.10(a). The FESEM micrograph of the GBGG sample was presented in Figure 5.10(b). The linear chains of GG were also visible in the micrograph, and the attachment of the GG chains to the GB granules is also visible in the micrograph. The FESEM micrograph of the GBAG sample after permeation was presented in Figure 5.10(c). The small granules of AG are clearly visible in the figure. The incomplete dissolution of the AG granules in the KCl environment is the reason for the higher hydraulic permeation rate, which is clearly visible in Figure 5.10(c). The micrograph of the GBAA sample after permeation with high concentration of the KCl salt solution was presented in Figure 5.10(d). The formation of AA gel is clearly visible in Figure 5.10(d), which contributes to the lower fluid permeation rate of the GBAA sample.

5.2.5 XG Amended GB under HCM Loadings

5.2.5.1 Influence of Biopolymer Loading

A different percentage of xanthan gum biopolymer amendments was explored. A 2% (GBXG2) and 5% biopolymer (GBXG5) by weight was considered with GB for evaluating the performance. The variations of hydraulic infiltration rates with time were plotted for GB amended with different percentages of xanthan gum with 50 kPa mechanical stress and distilled water as pore fluid in Figure 5.11(a). The sealing time (ST) was found to be decreasing with the increase in percentage of xanthan gum. The sealing time for GB with distilled water was 300 minutes, which was reduced to 40 minutes for 5 % XG amended GB. The initial fluid permeation rates were found to be in the order of 10^{-5} – 10^{-6} m/sec, which reduced significantly upon hydration with distilled water. The observed reduction in fluid permeation rates is due to the breaking of GB granules upon development of repulsive forces in clay particles. Moreover, the formation of gel upon hydration of xanthan gum also supported the GB in reducing the fluid permeation rate for GBXG samples.

The xanthan gum gel present in the voids of GB clogs the voids and forms a coating around the clay particles, which supports reduction in fluid permeation rates. The samples achieved equilibrium fluid permeation rates in order of 10^{-11} – 10^{-12} m/sec for GB and GBXG samples with distilled water as pore-fluid.

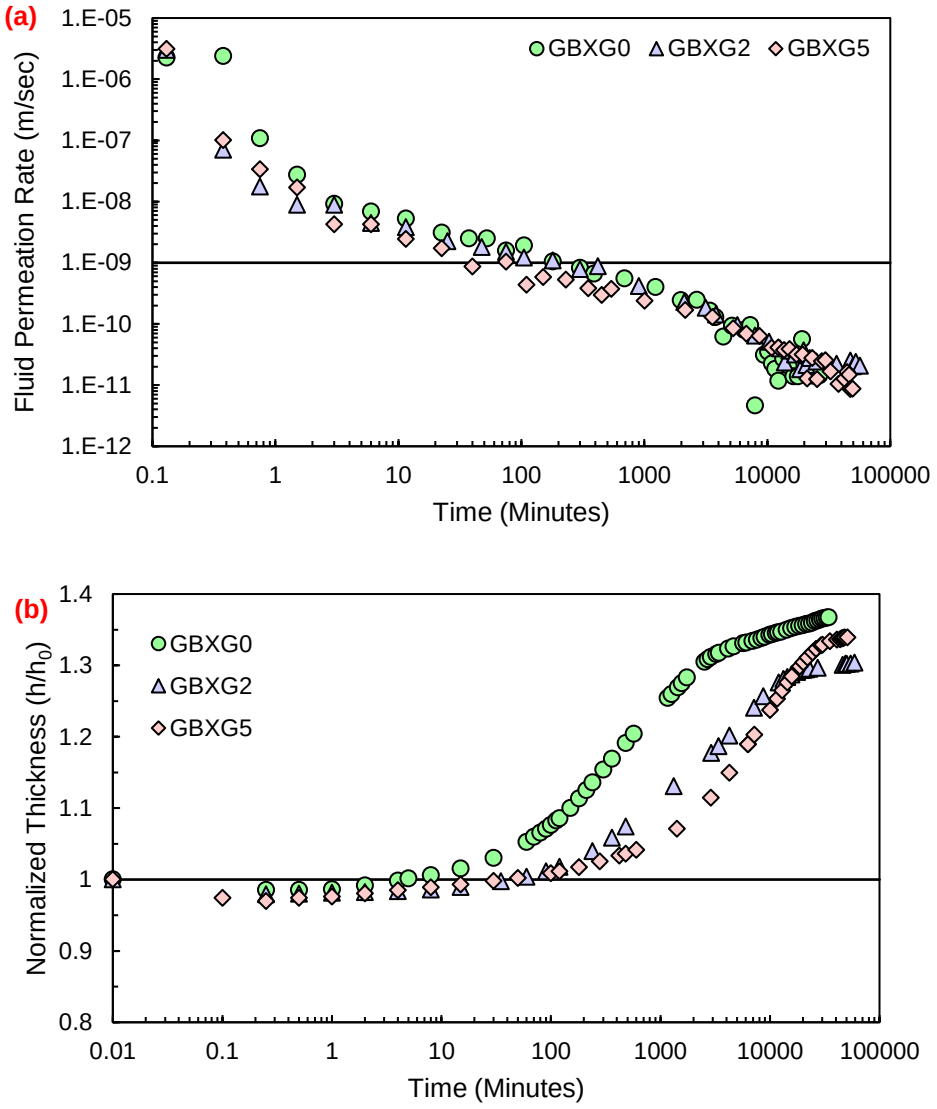

Figure 5.11: Temporal variations of (a) fluid permeation rate; (b) normalized thickness of GB and xanthan gum amended GB with distilled water under 50 kPa mechanical loading.

The temporal variations of normalized thicknesses (h/h_0), which is indicative of volume-change for GB and xanthan-gum amended GB (GBXG) samples under 50 kPa mechanical loading and

distilled water as pore-fluid were plotted in Figure 5.11(b). The slight collapse of 2 – 3 % was observed in all the samples due to the application of hydro-mechanical loading. The influence of mechanical load dominated initially which was countered by the developed repulsive forces upon hydration. The normalized thickness increased with time upon swelling of GB and GBXG samples, and achieved original volume within 5-50 minutes from start of the experiment. The time taken to achieve the normalized swelling after initial collapse also increased for the xanthan gum amended GB samples. This could be due to the low availability of water near the clay particles due to the formation of a thin membrane of XG around the clay particles upon hydration. The equilibrium values of normalized thickness varied between 1.30-1.36 for GB and GBXG samples. The higher value of equilibrium thickness was found to be for GB sample, which indicates the reduced swelling of GBXG sample. The equilibrium normalized thicknesses higher than 1 represents that the swelling pressure of the samples is higher than the applied mechanical loadings.

The temporal variations of fluid permeation rates for GB and GBXG samples under 50 kPa mechanical loading with 0.5M KCl as pore-fluid is presented in Figure 5.12(a). The initial fluid permeation rate was found to be 10^{-5} – 10^{-6} m/sec, which reduces with time due to the hydration of samples. The GB sample achieved fluid permeation rate of 6×10^{-9} m/sec at equilibrium, which is higher than liming value. The reason for non-sealing ability of GB sample in 0.5M KCl environment is due to poor disintegration of the granules of the GB. The GBXG2 and GBXG5 samples achieved sealing in ST of 1000 and 200 minutes, respectively from start of the experiment. The equilibrium fluid permeation rate of 5.5×10^{-10} and 4.4×10^{-11} m/sec for GBXG2 and GBXG5 samples with 0.5M KCl as pore-fluid. The order of magnitude of fluid permeation rate is significantly influenced by the percentage of the xanthan gum. The improved hydraulic

performance of GBXG samples is attributed to the formation of coating around the GB granules and clogging of pore of GB with formation of gel of xanthan gum upon hydration.

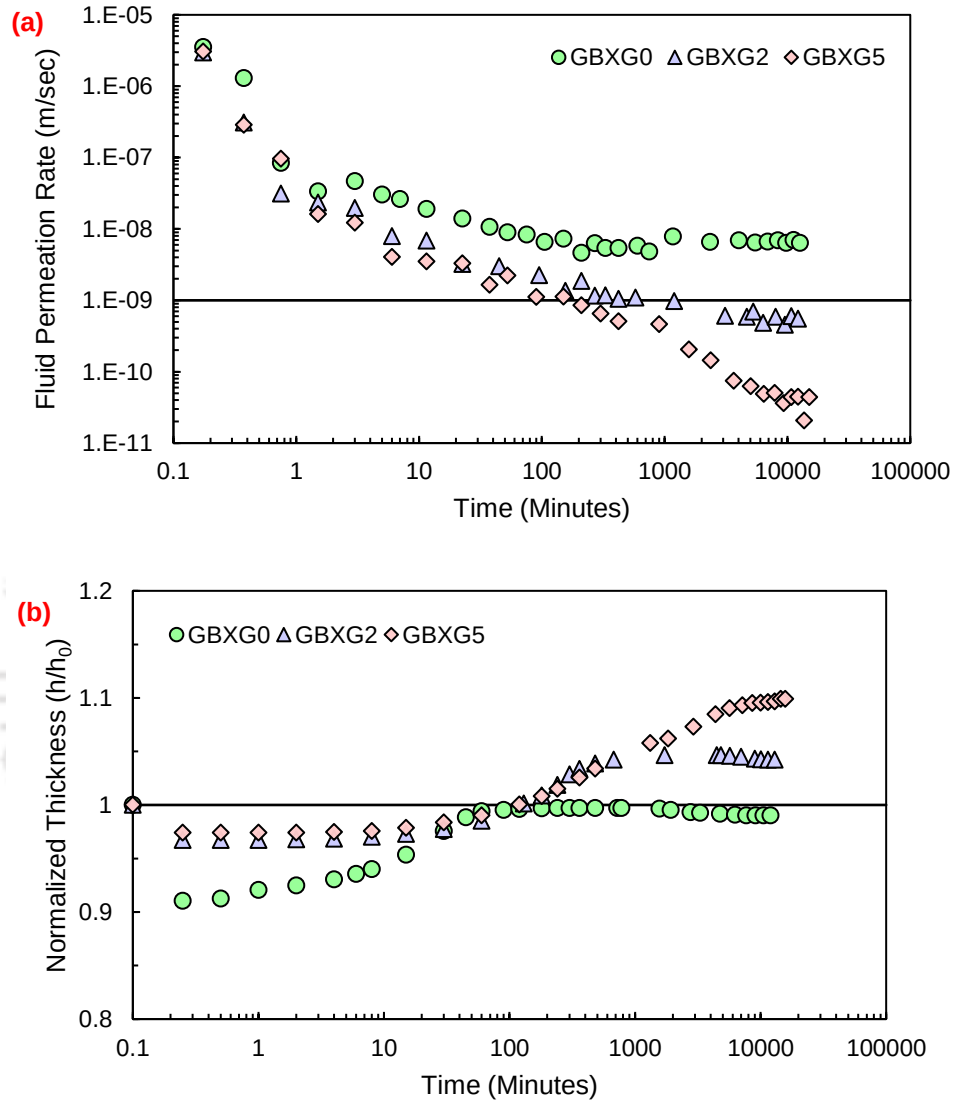

Figure 5.12: Temporal variations of (a) fluid permeation rate; (b) normalized thickness of GB and xanthan gum amended GB with 0.5 M KCl under 50 kPa mechanical loading.

The temporal variations of volume change in terms of normalized thicknesses (h/h_0) for GB and GBXG samples under 50 kPa mechanical loading and 0.5M KCl as pore-fluid were presented in Figure 5.12(b). An initial collapse of samples was observed upon application of HCM loadings. The magnitude of the collapse was 9 % for GB sample, which reduces to 3-4% after amendment

with the xanthan gum. Further, the normalized thickness increases later due to the development of the repulsive forces. The GBXG samples achieved its original volume within 200 minutes from the start of the experiment, but GB sample could not achieve its original volume even at equilibrium. The normalized thickness increases with time due to development of DDLs. The equilibrium normalized thickness was found to be increased with the percentage of xanthan gum. The equilibrium normalized thicknesses were found to be 0.99, 1.04, and 1.099 for GB, GBXG2, and GBXG5 samples with 0.5M KCl. Similarly, the variations of fluid permeation rates and normalized thicknesses of GBXG samples with 50 kPa loading for 0.5M NaCl and 0.5M $CaCl_2$ were plotted in Appedix-1.

5.2.5.2 Influence of Salt Concentration

The temporal variations of fluid permeation rates for GBXG2 under 50 kPa mechanical loading for different concentrations of KCl salt solution were plotted in Figure 5.13(a). The fluid permeation rates were found to be higher initially, which reduces with time due to the hydration of GB and the formation of xanthan gum gel. The GBXG2 samples achieved the sealing in ST of 80 – 500 minutes from the start of the experiments. The ST was found to be highest for high concentration KCl salt solution, and it reduced with low concentration KCl and distilled water. The GBXG2 sample achieved an equilibrium fluid permeation rate of 2×10^{-11}, 9.8×10^{-12}, and 5.5×10^{-10} m/sec for D.W., 0.1M KCl, and 0.5M KCl as pore-fluid. The fluid permeation rate of sample reduced significantly with lower concentration pore-fluid and D.W., which is due to more development of repulsive forces in low concentration pore-fluids.

The temporal variations of normalized thicknesses (h/h_0) for GBXG2 under 50 kPa mechanical loading with different concentrations of KCl as pore-fluids were presented in Figure 5.13(b). The initial collapse of 3-4 % was observed with all concentrations of KCl upon application of HCM

loading. The normalized thickness increases with the time for all samples and achieved its original volume in 35 – 130 minutes from the start of the experiment. The samples continued to swell and achieved equilibrium normalized thickness between 1.04 – 1.30 for different concentrations of KCl. The normalized thickness was found to be lowest for 0.5M KCl. Similarly, the variations in fluid permeation rates and normalized thicknesses for GBXG2 under 50 kPa mechanical loading with different concentrations of NaCl and CaCl2 were presented in Appendix 1.

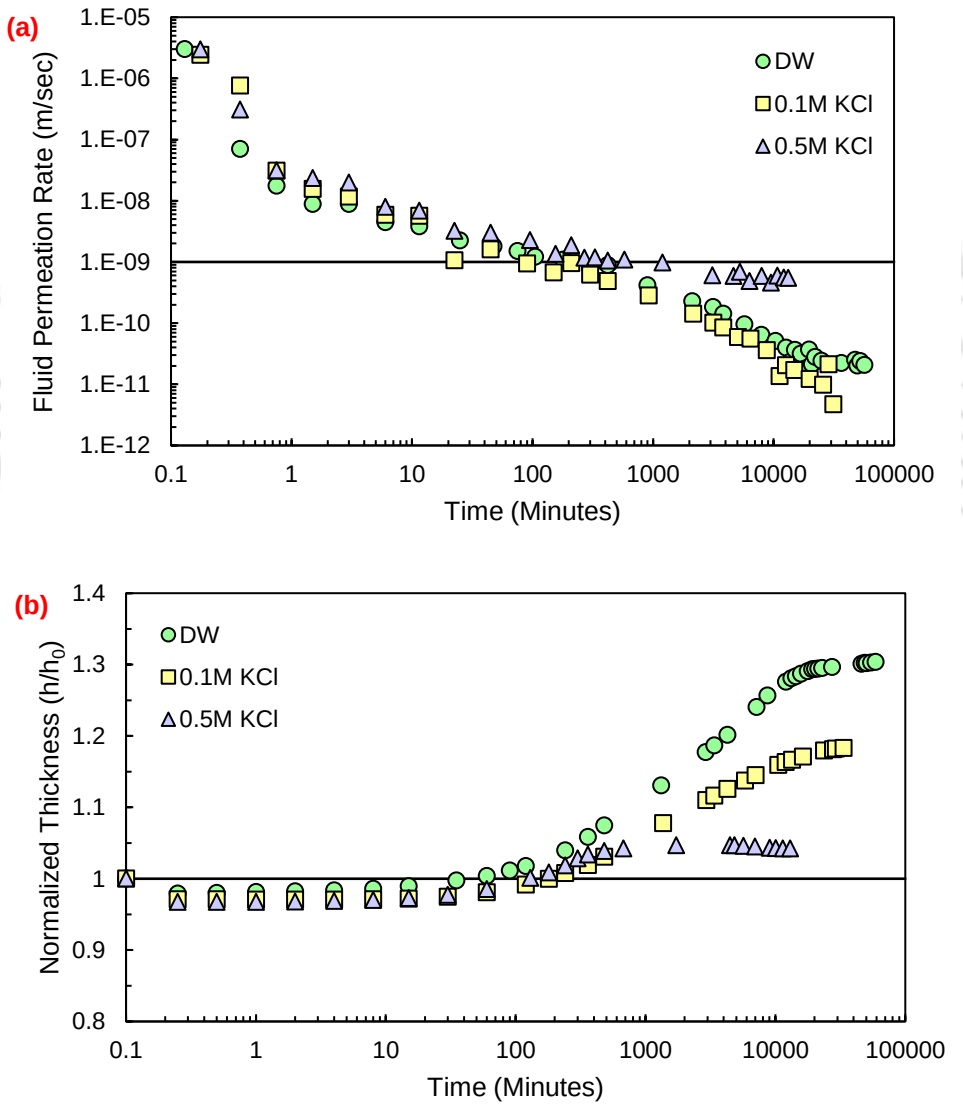

Figure 5.13: Temporal variations of (a) fluid permeation rate; (b) normalized thickness of xanthan gum amended GB (2% XG) with different concentrations of KCl under 50 kPa mechanical loading.

5.2.5.3 Influence of Mechanical Loading

Temporal variations of fluid permeation rates of GBXG2 samples under different mechanical loading conditions with 0.5M KCl as pore-fluid were presented in Figure 5.14(a). The initial fluid permeation rate of the GBXG2 sample was found to be in order of $10^{-5} – 10^{-6}$ m/sec, which reduced with time upon hydration. The sample with 50 kPa mechanical loading achieved sealing in 450 minutes from the start of the experiment, while the sample with 20 kPa mechanical loading took around 1200 minutes to achieve sealing. The GBXG2 sample with 50 kPa mechanical loading achieved an equilibrium fluid permeation rate of 5.5×10^{-10} m/sec; moreover, the GBXG2 sample with lower mechanical loading (i.e., 20 kPa) achieved a fluid permeation rate of 7.8×10^{-11} m/sec at equilibrium. Lower equilibrium fluid permeation with a lower mechanical rate is attributed to the propagation of XG gel in smaller pores under low mechanical loading.

Temporal variations of volume change in terms of normalized thicknesses (h/h_0) under different mechanical loading conditions with 0.5M KCl environment were plotted in Figure 5.14(b). The sample with 20 kPa loading showed an initial collapse of 1 %, while sample with 50 kPa mechanical loading showed an initial collapse of 4 % upon application of HCM loadings. Samples continued to swell and achieved their original volume after 4 and 130 minutes from start of the experiment for 20 kPa, and 50 kPa mechanical loading samples, respectively. Samples achieved equilibrium normalized thicknesses of 1.10 and 1.04 for 20 kPa and 50 kPa mechanical loadings with 0.5M KCl, respectively. Higher normalized thickness of sample with lower mechanical loading is attributed to the more development of diffused double layers (DDLs). Similarly, the temporal variations of fluid permeation rates and volume changes under different mechanical loading with 0.5M NaCl and 0.5M $CaCl_2$ were plotted in Appendix 1.

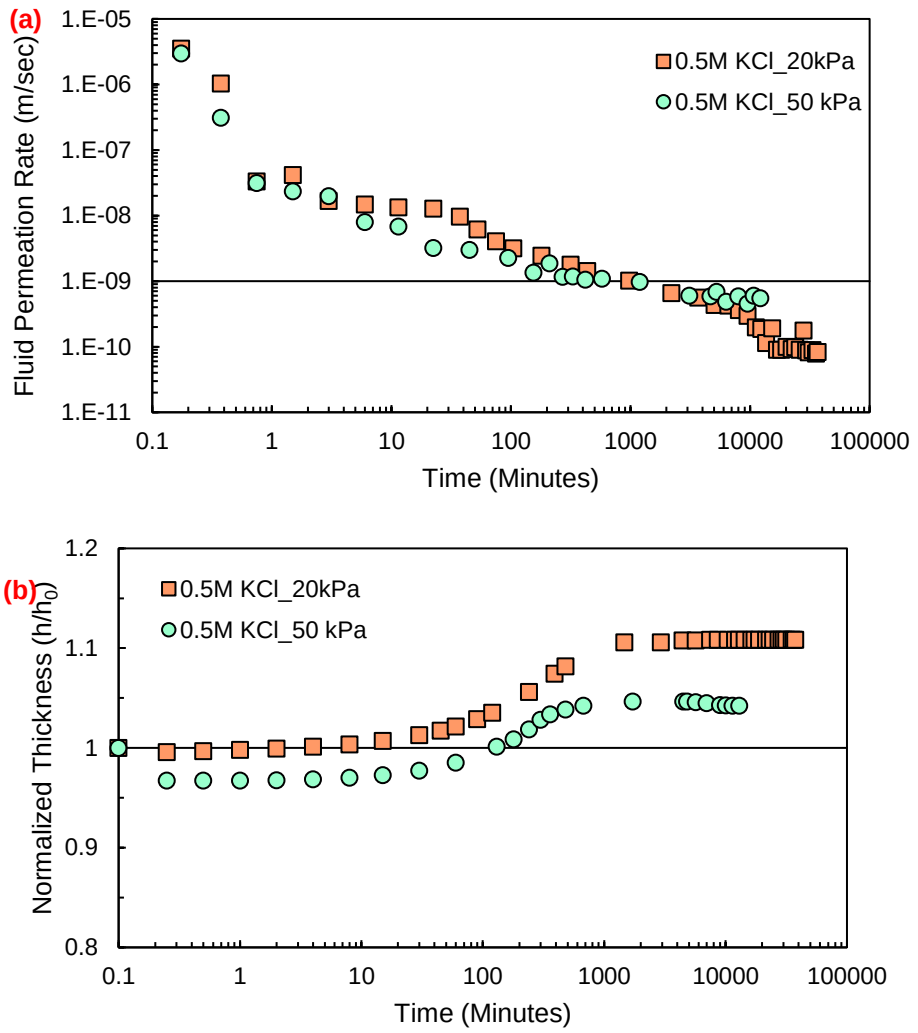

Figure 5.14: Temporal variations of (a) fluid permeation rates; (b) normalized thicknesses of GBXG2 samples under different mechanical loadings for 0.5M KCl

5.3 Diffusion of Cations through GB and XG amended GB

Through-diffusion experiments were conducted on GB and GBXG2 with 0.5M concentration of two cations (i.e., K^+ and Ca^{2+}) as initial concentration in the source reservoir. The compacted GB and GBXG2 samples were kept for saturation by keeping distilled water on both side of the diffusion set-up. The saturation of the samples was ensured by monitoring the weight of the sample, the insignificant or no changes in weight of the sample represent the complete saturation. The saturation of the samples took around 45 days. After saturation, the pore-fluid in the source

reservoir was changed with the 0.5M concentration of the pore-fluid. Further, the pore-fluid in collector reservoir was replaced with the fresh distilled water. Small amount of the samples was collected from both source and collector reservoirs and analyzed for presence of the inorganic cations up to 60 days at different time intervals using flame photometer. The temporal variations of relative concentrations (c/c_0) measured source and collector reservoir of KCl experiment with GB and GBXG2 were presented in Figure 5.15 (a) and Figure 5.15 (b), respectively. The concentration of source reservoir deceased and concentration of collector reservoir increased with time for both GB and GBXG2 samples. A relative concentration of 0.03 and 0.05 were observed in collector reservoir after 60 days for GB and GBXG2 samples, respectively, with KCl salt solution. The diffusion coefficient and retardation factors were evaluated by minimizing the error between measured and theoretical concentration profiles obtained by solving equations (2-6), and optimization (Bharat et al., 2009; Bharat, 2013). The theoretical profiles for both the reservoirs were also plotted in Figure 5.15(a) and 5.15(b) for GB and GBXG, respectively. The diffusion coefficient of GB and GBXG2 samples with KCl solution were found to be 3.73×10^{-11} m^2/sec and 5.49×10^{-11} m^2/sec, respectively. Further, retardation factor, R_d of GB and GBXG2 samples with KCl solution were found to be 5.59 and 8.49, respectively. The theoretical profiles for GB and GBXG samples with KCl salt solution showed a good theoretical estimation with root mean square error (RMSE) value of 0.007 and 0.011, respectively. Similarly, the temporal variations of relative concentrations (c/c_0) measured source and collector reservoir of $CaCl_2$ experiment with GB and GBXG2 were presented in Figure 5.16(a) and Figure 5.16 (b), respectively. A relative concentration of 0.03 was observed in the collector reservoir after 60 days for both GB and GBXG2 samples, with $CaCl_2$ salt solution.

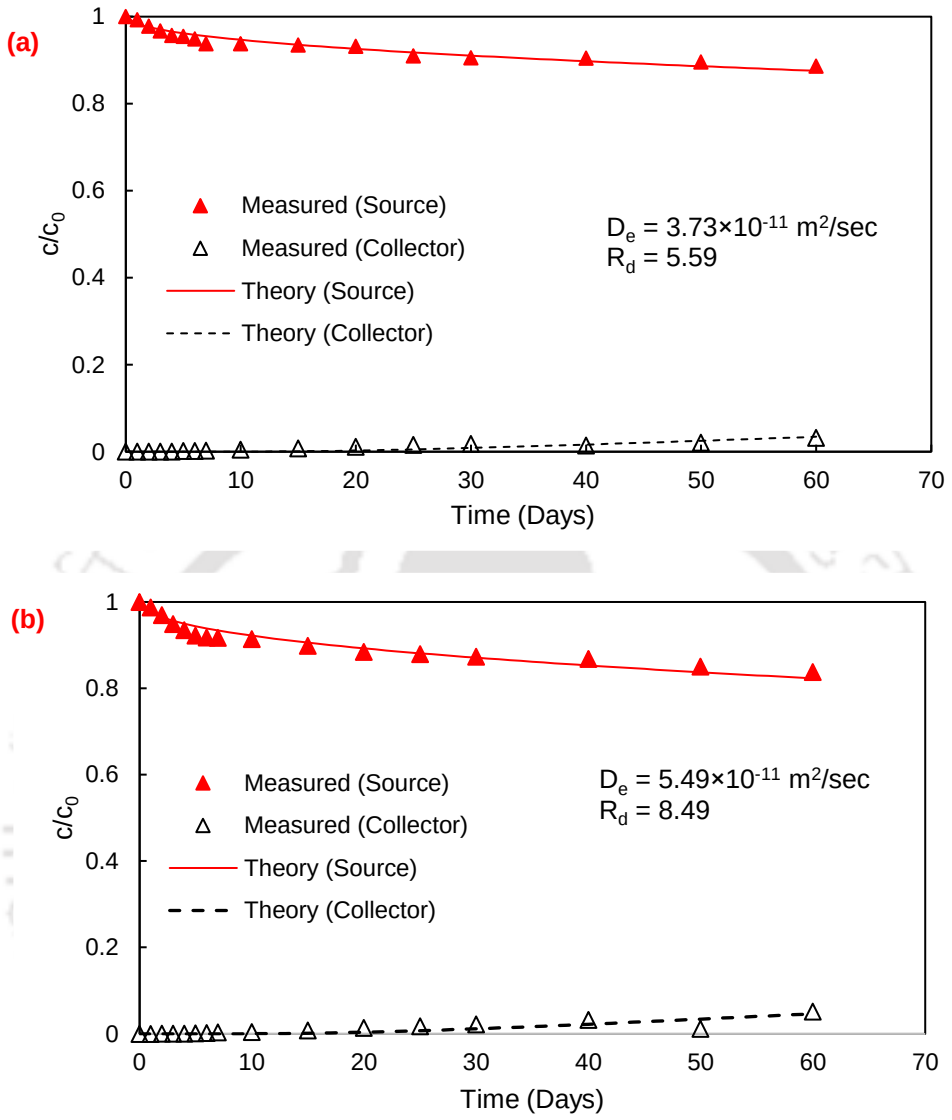

Figure 5.15: Comparison of experimental measured and theoretical profile at source and collector reservoir for (a) GB; and (b) GBXG2 with 0.5M KCl

The diffusion coefficient of GB and GBXG2 samples with $CaCl_2$ solution was found to be 4.56×10^{-11} m^2/sec and 5.37×10^{-11} m^2/sec, respectively. Further, retardation factor, R_d of GB and GBXG2 samples with $CaCl_2$ solution were found to be 8.04 and 8.84, respectively. The theoretical profiles for GB and GBXG samples with $CaCl_2$ salt solution showed a good theoretical estimation with root mean square error (RMSE) value of 0.018 and 0.017, respectively.

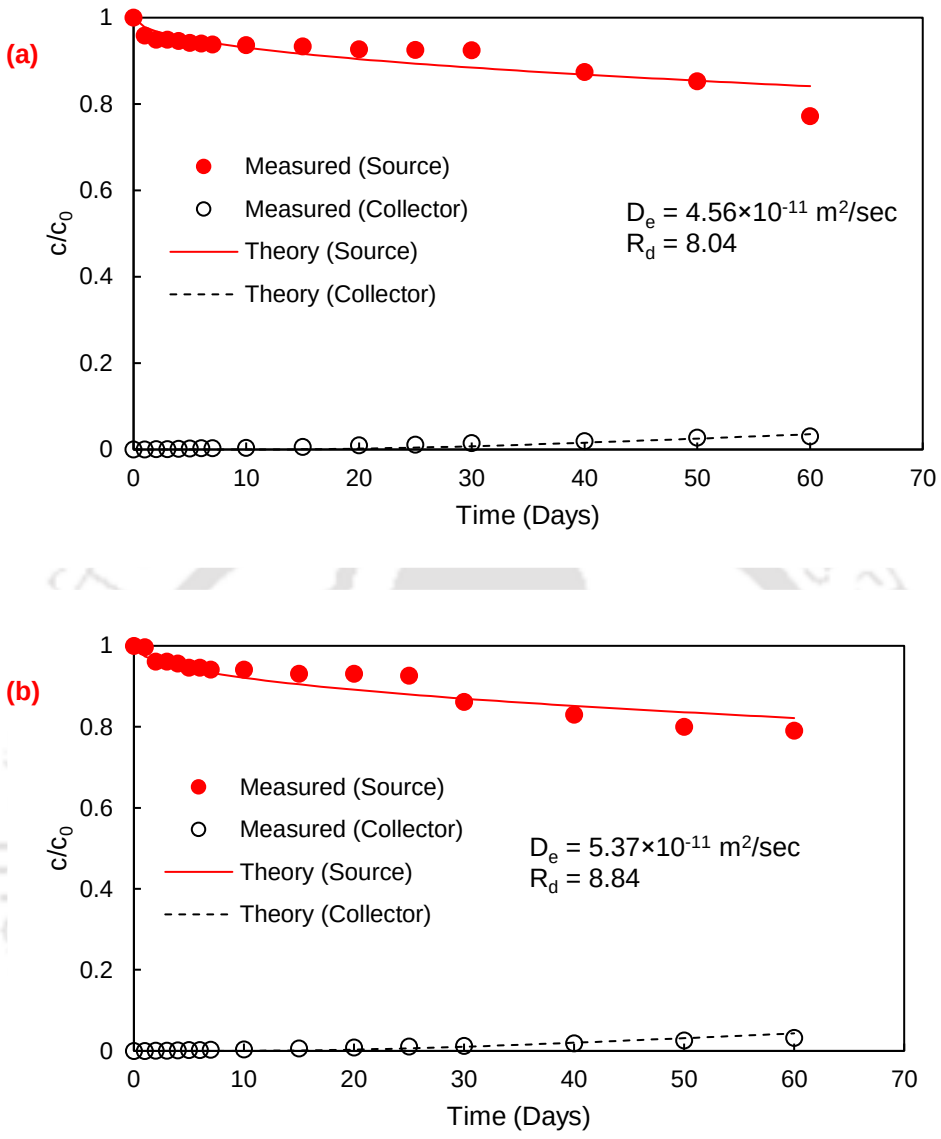

Figure 5.16: Comparison of experimental measured and theoretical profile at source and collector reservoir for (a) GB and (b) GBXG2 with 0.5M $CaCl_2$

The FESEM micrographs of samples were collected and presented after permeation with different pore-fluids in Figure 5.17. The FESEMs of GB, and GBXG5 after permeation with 0.5M NaCl were presented in Figure 5.17(a), and 5.17(b), respectively. GB sample has morphology with some voids present in it. Further, GBXG samples haves a smooth and coating like morphology as depicted in (Figure 5.17 (b, d, f)). Formation of this coating leads to the very low fluid permeation rates of the GBXG samples.

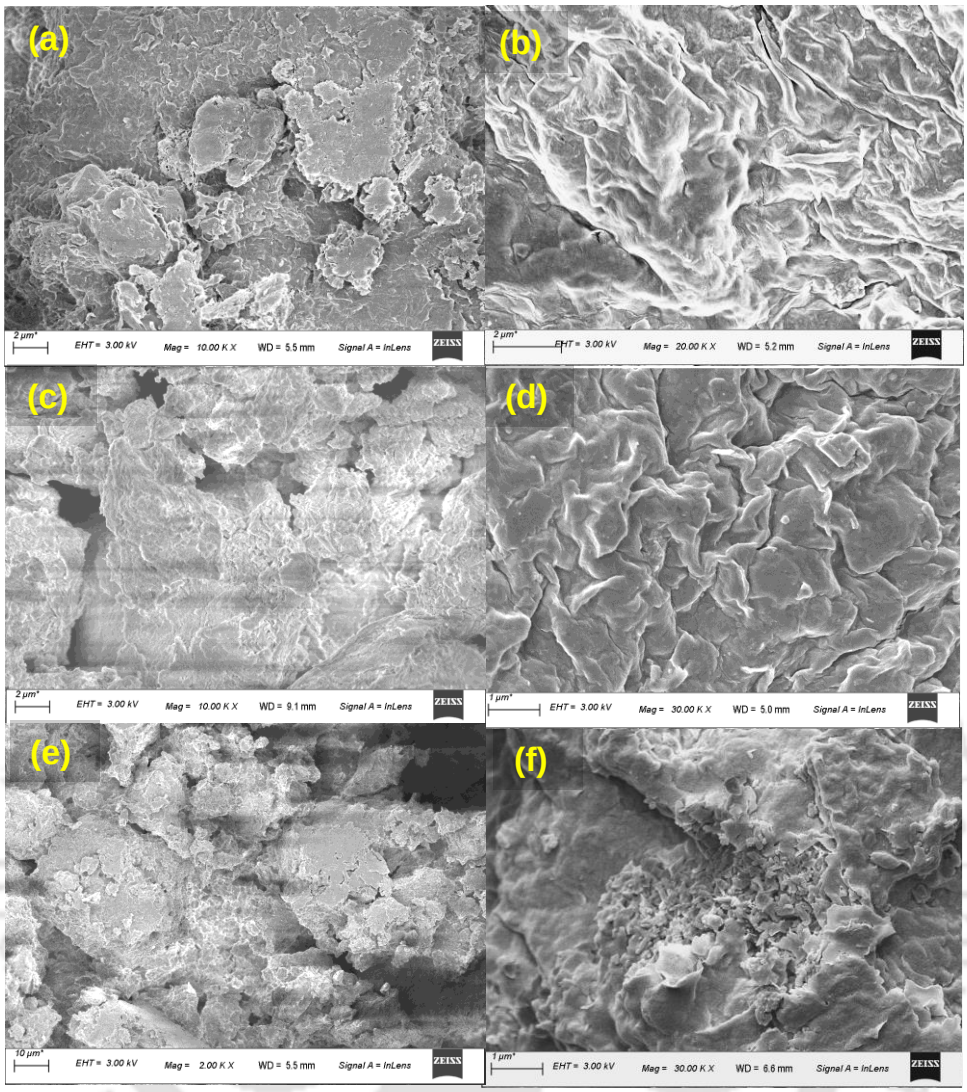

Figure 5.17: FESEM micrographs of (a) GB; (b) GBXG5; samples after permeation with 0.5M NaCl; micrographs of (c) GB; (d) GBXG5 samples after permeation with 0.5M KCl; and micrographs of (e) GB; and (f) GBXG5 after permeation with 0.5M $CaCl_2$

The dry XG biopolymer is also found in coiled structure and it swells and forms gel upon hydration due to presence of carboxyl and hydroxyl groups (Figure 5.31a). XG biopolymer has linear structure, which has possibilities for interactions with the bentonite particles and forms XG coating on bentonite surfaces. Although, both the XG and bentonite has negative charge, the possible interaction mechanism between them is through cation bridging. The swelling of polymer or biopolymer structure depends on several factors including pH, ionic strength, and temperature. Moreover, the XG coating over the GB surface entraps cations, when permeated with the high

concentration salt solutions. After the cation arrest by the XG biopolymer, the ionic concentration of pore-fluid reduced and when low concentration pore-fluid pass to the GB, it led to the breaking of the granules of GB. Moreover, the XG gel also clogs the voids present in between GB granules and hence results in lower fluid permeation rates. Mechanisms controlling the fluid permeation rates of samples were also presented in Figure 5.18. The dry compacted GBXG sample were presented in Figure 5.18(b). The biopolymer particles were present around the GB. Swelling of GBXG, formation of coating and swelling of GB particles were presented in Figure 5.18(c). Similarly, GBXG behavior under high concentration pore-fluids, were presented in Figure 5.18(d). The formation of XG gel, and its coating around the GB restricted the permeation of the GBXG samples.

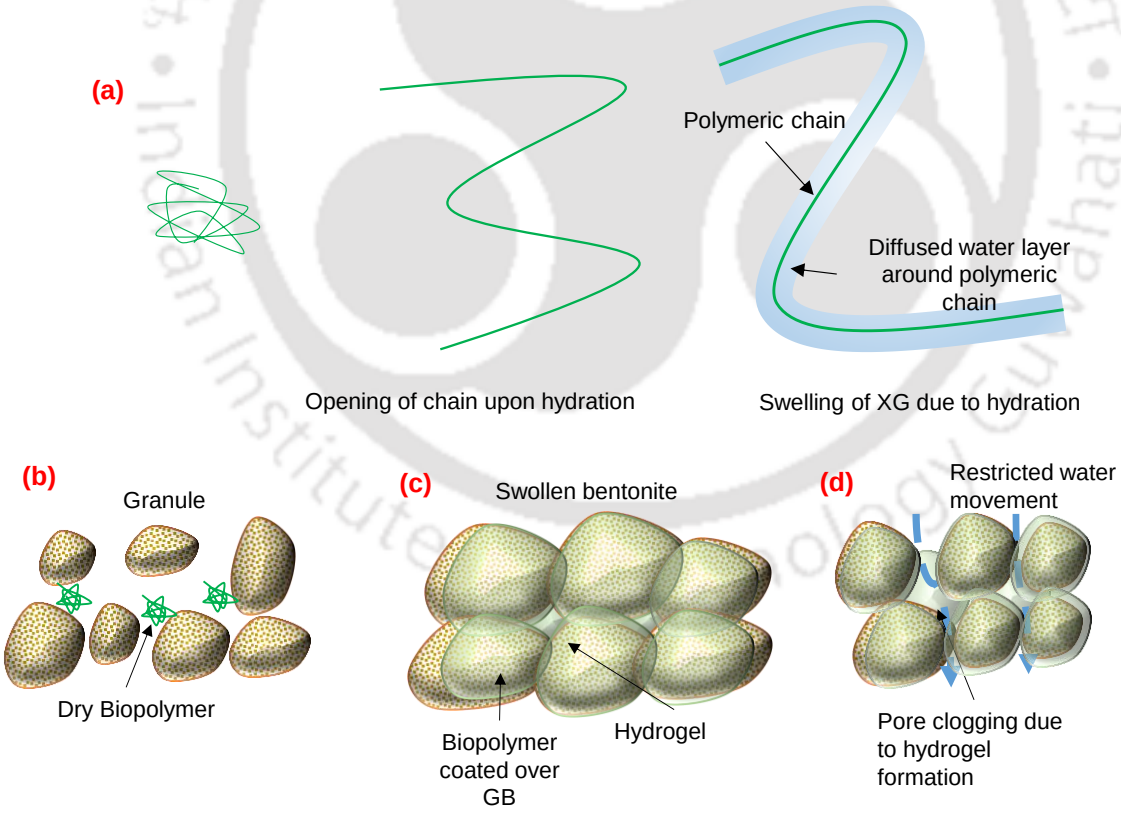

Figure 5.18: Illustration showing (a) swelling mechanism of xanthan gum; (b) XG amended GB; (c) biopolymer coated GB after permeation with distilled water; (d) Restricted permeation of pore-fluid due to the pore-clogging of the macro-voids.

5.4 Xanthan Gum Amended GB under Thermo-Hydro-Chemo-Mechanical Loadings

The temporal variations of fluid permeation rates of GB with time for distilled water pore-fluid and 20 kPa mechanical loadings were presented in Figure 5.19(a). Initial fluid permeation rates were found to be in order of 10^{-5} – 10^{-6} m/sec, which reduced with time due to the hydration of GB for all temperatures. The reduction in the fluid permeation rates is attributed to breaking of the GB granules into individual particles, due to development of repulsive forces. All three samples achieved the sealing after 200 – 1000 minutes from start of the experiments. The GB samples achieved equilibrium fluid permeation rates of 7×10^{-11}, 1×10^{-10}, and 3×10^{-10} m/sec for 27°C, 45°C and 65°C temperatures respectively. Other studies like, Pusch (1980), Cho et al., (1999) also observed increase in fluid permeation rates of bentonites at elevated temperatures. The increase in the fluid permeation rates at elevated temperatures is attributed to the decrease in the viscosity of the pore-fluid. Although, the density of the water or pore-fluid also decreases with increase in temperatures, which decreases the hydraulic conductivity. But the influence of viscosity of pore-fluid dominates the behaviour over influence of density of pore-fluid. The heating of the bentonites does not change its mineralogy and chemical composition (Villar and Lloret, 2004). But the adsorbed water on bentonite surface gets converted into the bulk pore-fluid and results into higher fluid permeation due to increase in pore space (Pusch, 1986). Such conversion of the adsorbed water into the pore-fluid also increases the aggregation of the bentonite particles, which results in lower specific surface area, and cation exchangeable capacity at elevated temperatures. Further, aggregation at elevated temperatures and higher pressures also led to the conversion of montmorillonite to illite (Powers, 1967).

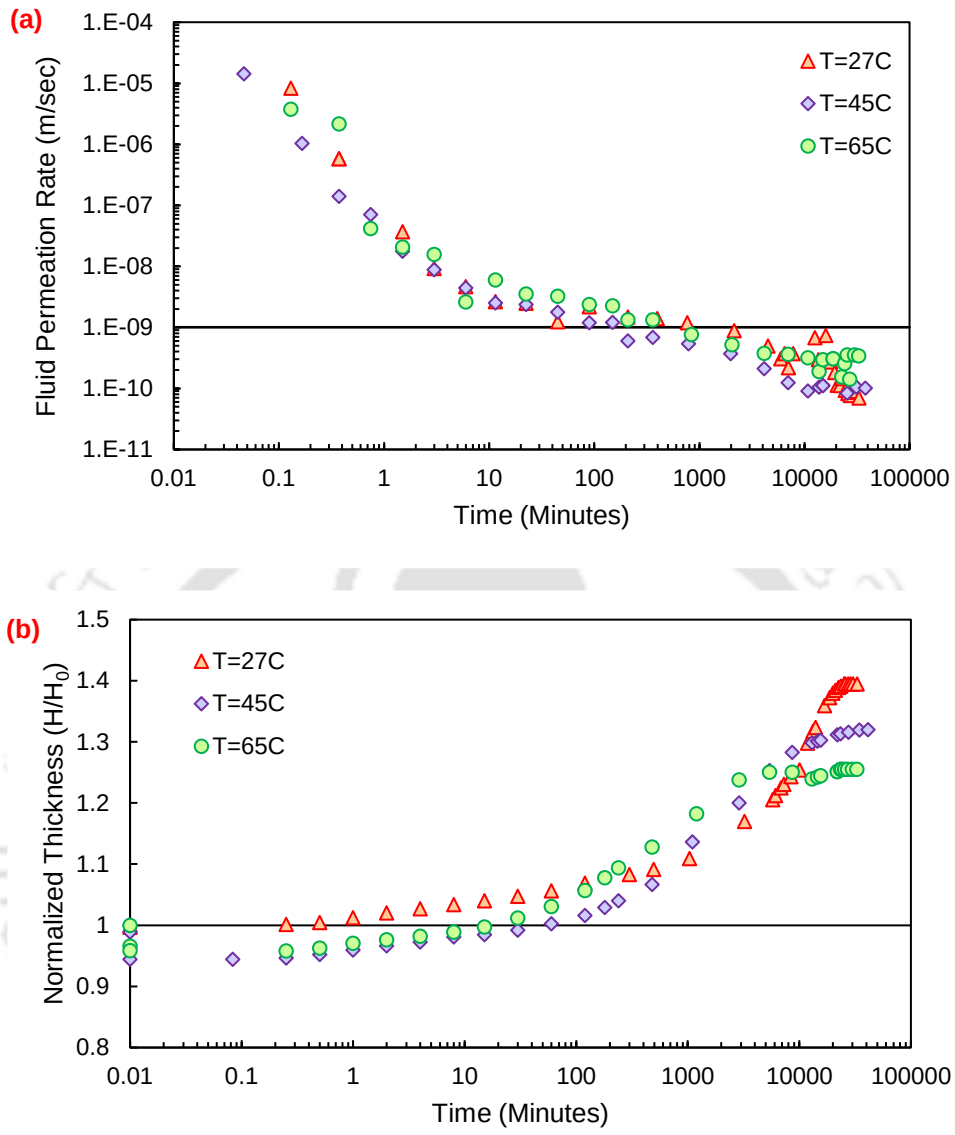

Figure 5.19: Temporal variations of (a) fluid permeation rates; (b) normalized thicknesses of GB under different temperatures with distilled water as pore-fluid under 20 kPa mechanical loading.

Temporal variations of the volume change in terms of normalized thicknesses for GB samples at different temperatures with distilled water as pore-fluid under 20 kPa mechanical loading were presented in Figure 5.19(b). All the studied samples showed an initial collapse upon application of thermal and mechanical loadings. Samples started swelling upon hydration for all different temperatures, sample at 27°C achieved original volume within one minute from start of the experiment. Moreover, samples at higher temperatures took 15 and 60 minutes to achieve their

original volume. All samples continued to swell and achieved equilibrium normalized thicknesses of 1.39, 1.32, and 1.255 for 27℃, 45℃, and 65℃ temperatures, respectively. Lower swelling of high temperature samples is attributed to the conversion of the adsorbed water to the pore-fluid. Moreover, the evaporation of pore-fluid at higher temperature, and aggregation of the clay particles also contribute to the lower swelling of the GB samples at elevated temperatures.

Temporal variations of fluid permeation rates of GBXG10 samples with distilled water as pore-fluid under 20 kPa mechanical loading for different temperatures were plotted in Figure 5.20(a). Initial fluid permeation rate was found to be in order of 10^{-5} m/sec for all studied temperatures, which reduces upon hydration due to breaking of GB granules. The fluid permeation rates reduced further and achieved the sealing in 50, 300 and 3000 minutes from start of the experiment for 27℃, 45℃, and 65℃ temperatures, respectively. The sealing time increased with the increase in temperature. The fluid permeation rates of GBXG10 samples decreased further and achieved an equilibrium fluid permeation rate of 8×10^{-12}, 5×10^{-11}, and 1×10^{-10} m/sec for 27℃, 45℃, and 65℃ temperatures, respectively. The equilibrium fluid permeation rates of GBXG10 samples increased with increase in temperature. The increase in sealing time and fluid permeation rates upon increase in temperature is due to increased aggregation of clay and poor gel formation of XG at higher temperature. The fluid permeation rate of GBXG10 sample was found to be further lower than the samples having lower percentages of XG at 27℃ and 45℃. Further, the fluid permeation rate did not change upon increase in xanthan gum content for 65℃ samples due to poor gel formation in XG at elevated temperatures.

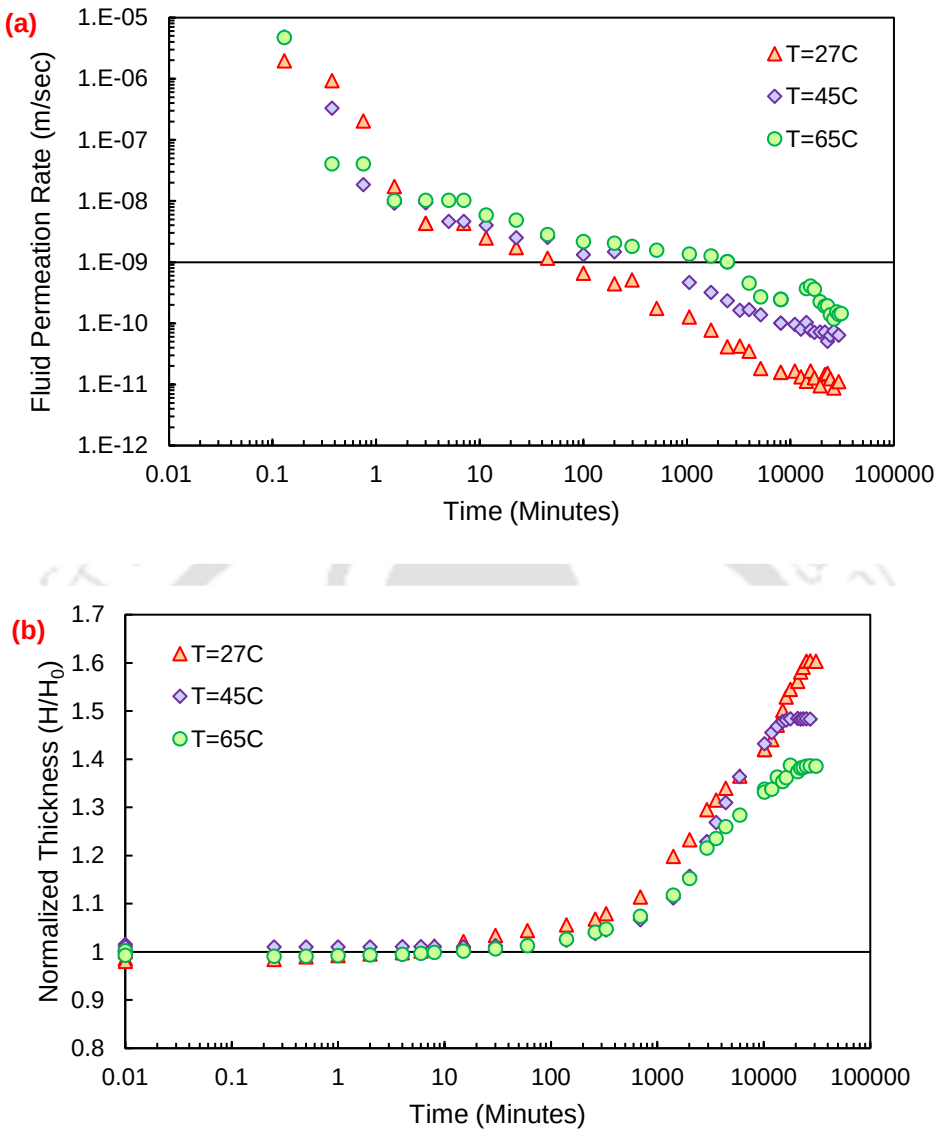

Figure 5.20: Temporal variations of (a) fluid permeation rates; (b) normalized thicknesses of GBXG10 under different temperature with distilled water as pore-fluid under 20 kPa mechanical loading.

The temporal variations of volume change in terms of normalized thicknesses for GBXG10 samples with distilled water as pore-fluid under 20 kPa mechanical loading for different temperatures were plotted in Figure 5.20(b). GBXG10 Samples showed an initial collapse of 1-2 % upon application of thermal and mechanical loadings for 27℃ and 45℃ temperatures. Moreover, sample with 65℃ showed an initial swelling upon heating, the slight swelling upon

heating is due to conversion of adsorbed water into the vapor phase. Further, application of mechanical loading led to the reduction, but overall volume was higher than the initial volume even after application of 20 kPa load. The GBXG10 samples at 27℃ and 45℃ swell and achieved their original volume within 6 and 15 minutes, respectively, from start of the experiments. The GBXG10 samples continued to swell and achieved the equilibrium normalized thickness of 1.61, 1.39, and 1.48 for 27℃, 45℃, and 65℃ temperatures, respectively. The normalized thickness of GBXG10 samples reduced due to conversion of adsorbed water to the pore-fluid and increased aggregation at elevated temperatures. Similarly, the fluid permeation rates and volume change of GBXG2 and GBXG5 under different temperatures have been given in Appendix 1.

Temporal variations of fluid permeation rates of GB samples with 0.5M KCl as pore-fluid under 20 kPa mechanical loading for different temperatures were plotted in Figure 5.21(a). Initial fluid permeation rates were found to be in order of 10^{-4} – 10^{-5} m/sec, which reduce upon hydration due to development of repulsive force. Equilibrium fluid permeation rates of 9×10^{-8}, 2×10^{-7}, and 4×10^{-7} m/sec were found for 27℃, 45℃, and 65℃ temperatures, respectively, with 0.5M KCl as pore-fluid, which is 1-2 orders of magnitude higher than the limiting value. The developed repulsive forces in GB in presence of high KCl environment were not sufficient for complete disintegration of GB granules and hence, GB could not achieve sealing in this environment. Moreover, the permeation rates increased with increase in the temperature, which is attributed to the conversion of adsorbed water to the pore-fluid and aggregation of clay particles at higher temperatures.

The temporal variations of volume change in terms of normalized thickness for GB samples with 0.5M KCl salt solution under 20kPa mechanical loading for different temperatures were plotted in Figure 5.21(b). GB samples showed an initial collapse of 1-3 % upon application of thermal and mechanical loadings. The GB samples started swelling upon permeation with 0.5M KCl salt

solutions and achieved original volume within few minutes from start of the experiment. The samples continued to swell and achieved equilibrium normalized thicknesses of 1.04, 1.05, and 1.04 for 27℃, 45℃, and 65℃ temperatures, respectively. Normalized thicknesses of GB samples did not showed significant changes upon changes in temperatures.

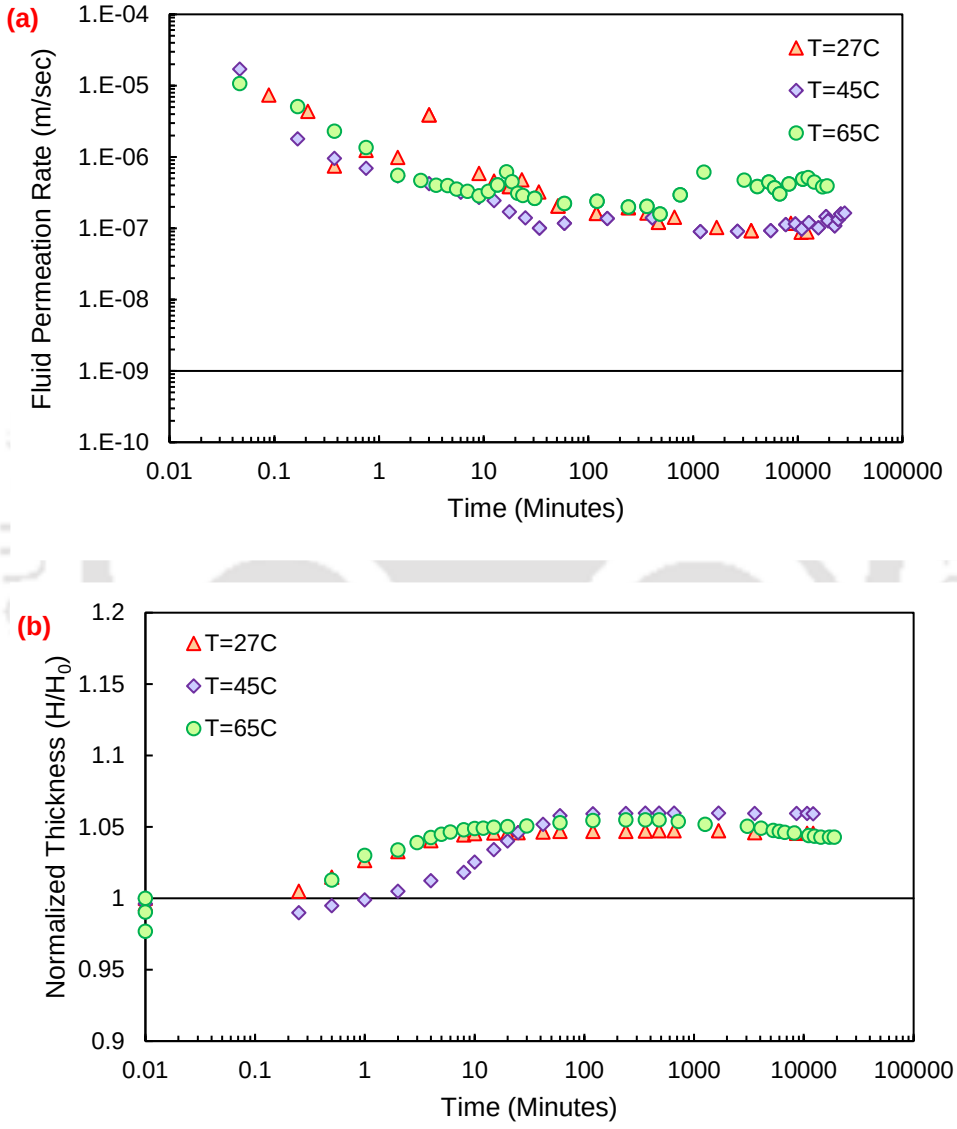

Figure 5.21: Temporal variations of (a) fluid permeation rates; (b) normalized thicknesses of GB for different temperatures with 0.5M KCl as pore-fluid under 20 kPa mechanical loading.

Temporal variations of fluid permeation rates of GBXG10 samples with 0.5M KCl as pore-fluid under 20 kPa mechanical loading for different temperatures were plotted in Figure 5.21(a). Initial

fluid permeation rates were found in order of 10^{-5} m/sec for all studied temperatures, which reduces upon hydration. The breaking of GB granules, and formation of XG are the reasons for reduction in fluid permeation rates. The GBXG10 samples achieved sealing in 30 – 200 minutes from start of the experiment for all studied temperatures. Fluid permeation rates of samples reduced further and achieved an equilibrium permeation rate of 2×10^{-11}, 5×10^{-11}, and 3×10^{-10} m/sec for 27℃, 45℃, and 65℃ temperatures, respectively. The fluid permeation rates of GBXG10 samples were significantly lower than GB and GBXG2 samples in high KCl environment. Moreover, the increase of XG content from 5 to 10 %, did not significantly influenced the fluid permeation rates. The fluid permeation rates of GBXG10 samples were also found to increase with increase in temperature. The decrease in viscosity, increase in aggregation, and conversion of adsorbed water to the pore-fluid are the main reasons for increase in the permeation rates with temperatures. The fluid permeation rates of GBXG10 samples were found to be higher than the GBXG5 sample even after higher percentages of XG due replacement of soil solids with biopolymer.

The temporal variations of volume change in terms of normalized thicknesses for GBXG10 samples with 0.5M KCl salt solution under 20 kPa mechanical loading were plotted in Figure 5.21(b). The GBXG10 samples showed an initial collapse of 1-3% upon application of thermal and mechanical loadings. The samples started swelling upon permeation of pore-fluid and achieved their original volume in 4, and 15 minutes from start of the experiment for 27℃, and 45℃ temperatures, respectively. Moreover, GBXG10 sample with 65℃ continued to collapse and could not achieve its original volume. Moreover, other samples continued to swell and achieved equilibrium normalized thicknesses of 1.11, 1.028, and 0.96 for 27℃, 45℃, and 65℃ temperatures, respectively. The normalized thickness values of GBXG5 samples represent negligible swelling at higher temperatures. Lower swelling at elevated temperatures is also

attributed to the poorly developed repulsive forces in the high salt environment, conversion of adsorbed water to the pore-fluid, and increase in aggregation of bentonite particles. Similarly, the variations of fluid permeation rates and volume changes of GBXG2 and GBXG5 with 0.5M KCl under 20 kPa mechanical loading is given in Appendix 1.

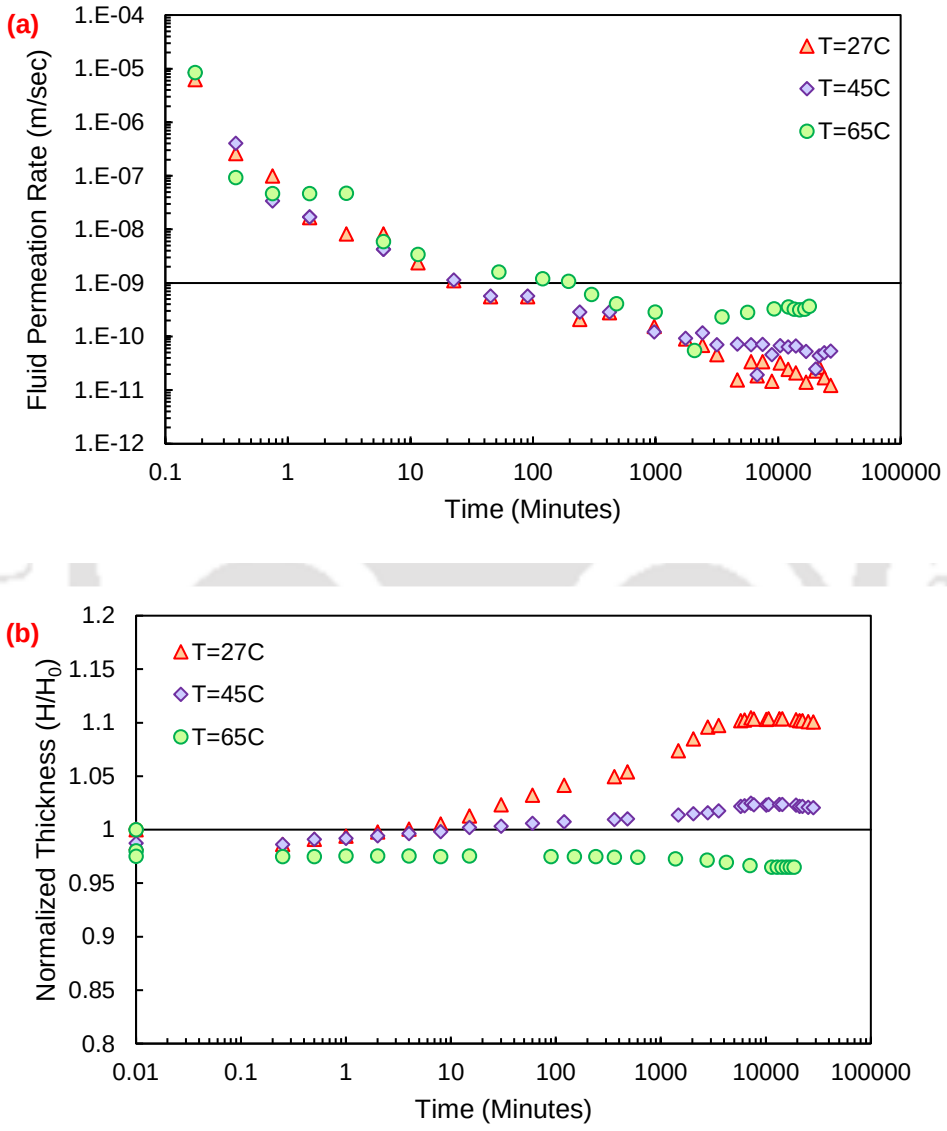

Figure 5.21: Temporal variations of (a) fluid permeation rates; (b) normalized thicknesses of GBXG10 for different temperatures with 0.5M KCl as pore-fluid under 20 kPa mechanical loading.

5.5 Summary

The fluid permeation, self-sealing ability, diffusion, and volume change of the granular bentonite amended with polymer and different biopolymers with NaCl, KCl, and $CaCl_2$ as pore-fluid under 20 and 50 kPa mechanical loadings and different temperatures and the following point were derived:

- The water-adsorbing synthetic polymer amended granular bentonite failed to achieve the sealing in the presence of high concentrations of KCl and $CaCl_2$. Moreover, polymer structure also gets collapse in high ionic environment and led to the formation of hollow channels, which results in high permeation in such situation.
- All four biopolymers used in the study have hydroxyl groups, whereas, XG and AG has carboxyl groups as well. These biopolymers get attached to the GB surfaces by electrostatic forces, hydrogen bonding, and cation bridging mechanisms.
- The XG, GG and AA biopolymers form thick viscous gel; moreover, the AG forms less viscous gel upon hydration. The biopolymer gel forms the coating over the GB upon hydration.
- The GBGG fails to attain sealing with a high concentration of NaCl, and KCl as pore-fluid for the studied mechanical loading. Although it achieved sealing with $CaCl_2$ as pore-fluid for higher mechanical loading, it failed to achieve sealing with lower mechanical loading.
- The GBAG sample failed to achieve sealing with all the high concentrations of the studied pore-fluids under lower mechanical loading. The samples achieved sealing with higher concentrations of the NaCl and $CaCl_2$ under higher mechanical loading (i.e., 50 kPa), but the samples did not achieve sealing with high concentration of KCl as pore-fluid.

- The GBAA samples achieved sealing with all different pore-fluids. It showed fluid permeation in the range of 10^{-9} m/s for KCl and $CaCl_2$. The reason for such behaviour in the GBAA samples is the formation of thick viscous gel of agar-agar upon hydration.

- The XG amended GB (GBXG) achieved the sealing with different studied pore-fluids. The XG gel forms a coating over the GB surface, and clogs the voids present in it. The XG gel entraps the cations from pore-fluid, and increased viscosity of the pore-fluids led to the lower permeation rates. GBXG sample showed low permeation rate with low mechanical loading, which is due to the ease in ability of gel to clog the smaller pores under lower mechanical loading.

- Through-Diffusion test was conducted with two cations for GB and GBXG samples. Since these experiments were conducted in saturated samples, the granules of the GB break into individual particles. Further, the amendment of GB with small percentage of XG did not influence diffusion properties significantly, A small increase in diffusion and retardation coefficient was observed for both K^+ and Ca^{2+}.

- The fluid permeation rates were found to increase with increase in temperature, and volume change of samples were found to decrease with temperature. Such observations are due to decrease in viscosity, increase in aggregation and conversion of adsorbed water to the pore-fluid at elevated temperatures.

- The study observes the sealing ability of different biopolymer-amended GBs. The fluid permeation rate is majorly governed by the biopolymer type, pore-fluid chemistry, mechanical loadings, and temperature.

भारतीय प्रौद्योगिकी संस्थान गुवाहाटी
Indian Institute of Technology Guwahati

Chapter – 6

Sorption of Coronavirus Surrogate with Different Clay Minerals

---

6.1 General

Chapter 5 discussed the applicability of polymer and biopolymer-amended granular bentonite for applications in containment systems. The present work will discuss the role of the mineralogy of clays on the sorption ability of viruses. The present work is divided into two parts. The first part presents the sorption of coronavirus surrogate with commonly available clays bentonite, and kaolin dominant in montmorillonite and kaolinite mineral, respectively. In this study, batch experiments were conducted to understand the sorption of Newcastle disease virus (NDV) as a surrogate to SARS-CoV2 onto the clay mineral's surface. Different natural bentonites and kaolin were used in the study to understand the influence of bentonite quality on the sorption behavior of NDV on the clay. The virus pathogens have a decay rate with time, which has been considered during sorption experiments. The second part of the work presents the sorption of coronavirus surrogate with three clay minerals i.e., illite, sepiolite, and halloysite. The batch sorption experiments were conducted with NDV as a surrogate for coronavirus to understand the role of mineralogy on sorption characteristics.

6.2 Interactions of NDV with bentonite and kaolin clay

This section discusses the sorption of NDV on bentonite and kaolin clay. The NDV contains hemagglutinin-neuraminidase (HN) and Fusion (F) as surface glycoproteins. These surface glycoproteins can potentially be attached to the negatively charged surface of clays (Figure 6.1).

The results from batch sorption experiments will be discussed in detail to understand the clay–virus sorption. The influence of contact time, clay mineral type, and dose of clay were evaluated on the sorption of NDV on clays. Four different bentonites (B1-B4) of different plasticity were considered in the present study to understand the influence of the specific surface area of bentonites. Further, the interaction energy profiles for NDV and coronavirus to the bentonite, and kaolin clay were evaluated based on Derjaguin–Landau–Verwey–Overbeek (DLVO) theory. An understanding of clay – virus sorption based on the results was presented in detail.

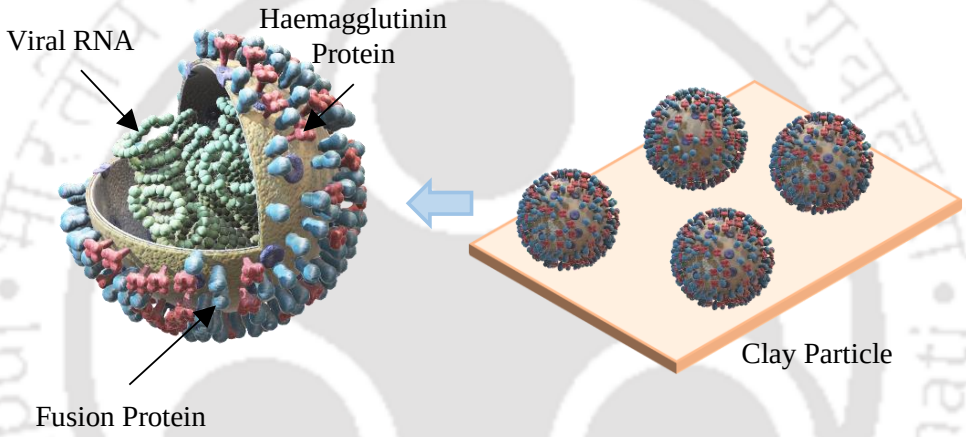

Figure 6.1: Illustration showing the interaction of NDV on clay particle

6.2.1 Sorption kinetics for NDV with bentonite and kaolin

An average initial virus concentration of 12000 PFU/mL was used in the tests and the concentration of bentonite was maintained at 50 mg/mL in these tests. Similarly, an average initial concentration of 2500 PFU/mL was used for kaolin kinetic sorption experiments and two different kaolin concentrations 10 mg/mL and 1 mg/mL were used in the study. The results for different interaction times varying between 5 and 180 minutes were presented. The plaque assay was performed to analyze the presence of the virus in samples after sorption. The same concentration of NDV was also taken as a control to measure its concentration after the same time. The control was taken to consider the biological decay of NDV. The reduction in plaque with respect to control

NDV was represented in terms of percentage plaque reduction or plaque reduction. The sorption kinetic results for NDV on bentonite B3 and kaolin were presented in Figure 6.2(a) and Figure 6.2(b), respectively. Percentage plaque reduction was found to increase with the contact time. The sorption rate was rapid for bentonite, and the equilibrium sorption was reached quickly as percentage removal was over 99% in 15 minutes.

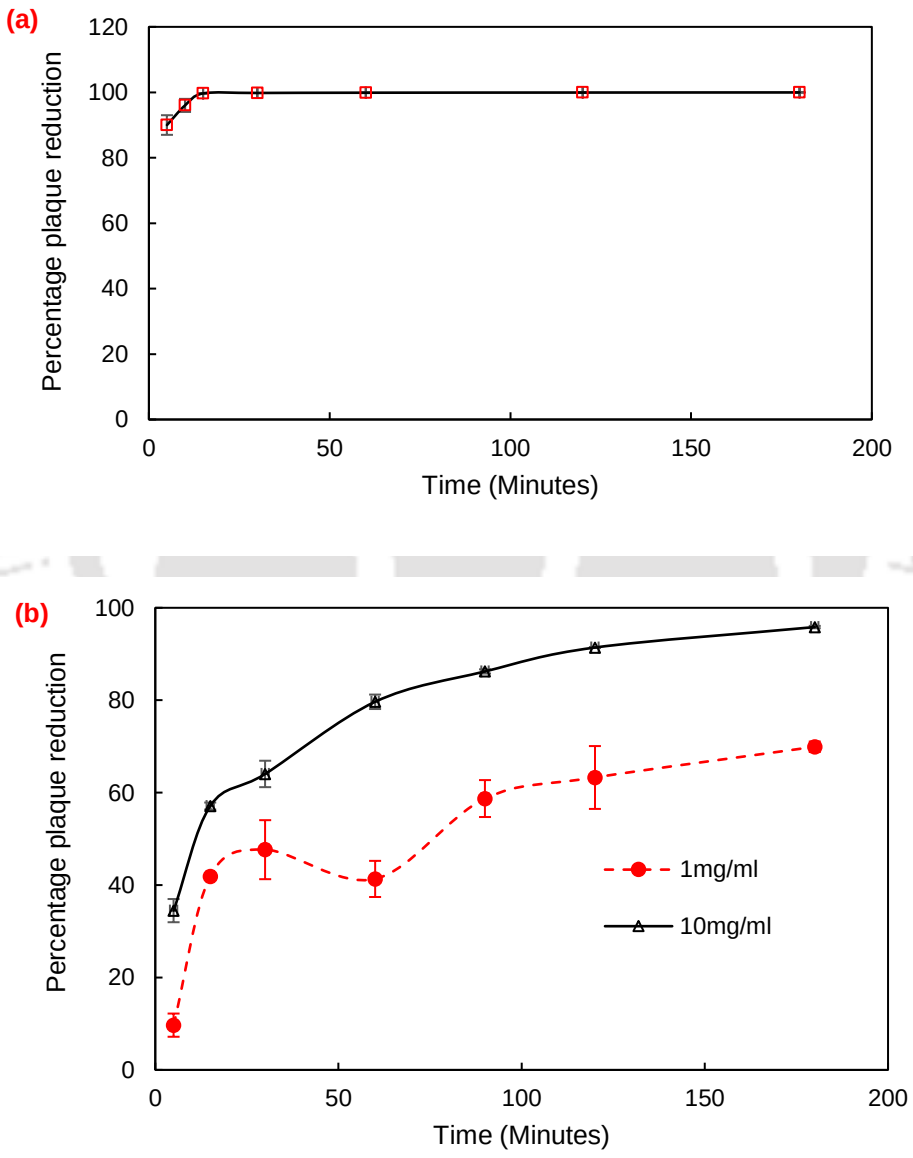

Figure 6.2: Percentage plaque reduction of NDV with time for (a) bentonite with 50 mg/ml concentration; (b) kaolin with 1 mg/mL and 10 mg/mL concentration

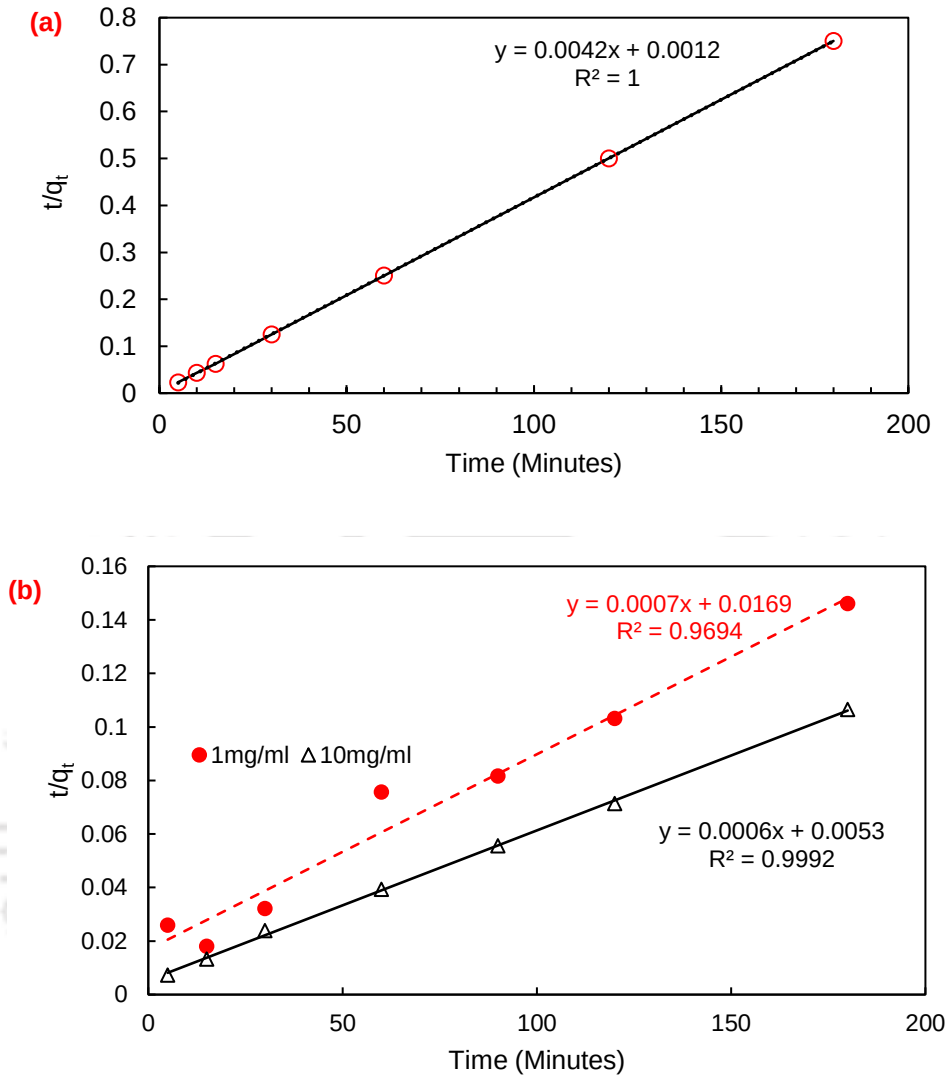

Figure 6.3: Pseudo-second-order kinetics for (a) bentonite; and (b) kaolin.

In contrast, it took 2 hours for kaolin with 10 mg/ml concentration for reaching percentage removal over 90%. The t/q_t data with time (Equation 2) were shown in Figure 6.3(a) and Figure 6.3(b) for determining the second-order sorption rate coefficients based on the data presented in Figure 6.2 (a & b). The data followed a linear relationship with a high value of the coefficient of regression (R^2) indicating the kinetics of adsorption of the virus on bentonite follow second-order kinetics. The adsorption rate constant k_2 was found to be 0.0074 (mg.PFU^{-1}.min^{-1}) for bentonite. The rate constants were found as 4.15×10^{-9} and 9.54×10^{-10} for 1mg/mL and 10 mg/mL concentrations of

kaolin. The high value of k_2 also represents the rapid sorption of NDV with bentonite as compared to kaolin.

6.2.2 Effect of clay concentrations

The percentage plaque reduction of NDV by bentonite B3 and kaolin as a function of clay concentration was shown in Figure 6.4(a) and Figure 6.4(b), respectively. Based on sorption kinetics data, an incubation period of 3 hrs was considered. Due to the presence of charge on the NDV proteins, the charged clay particles bind the surface protein of NDV on its surface.

The NDV particles binded to the clay surface get separated from the solution once clay particles are removed from the mixture by centrifugation and thus do not contribute to a plaque assay. The observed percentage of plaque reduction increased with the increase in the dose of the clay due to an increase in the number of sorption sites. The plaque reduction was over 99 % with the increase in the bentonite concentration to ≥ 5 mg/mL. The plaque reduction was also found to be over 90 for kaolin concentration ≥ 5 mg/mL. Three different virus concentrations were used with kaolin, and results did not vary significantly with virus concentration. For lower concentrations of clay (i.e., < 5 mg/mL), the number of available sites for NDV sorption reduced significantly, subsequently leading to a lower percentage of plaque reduction.

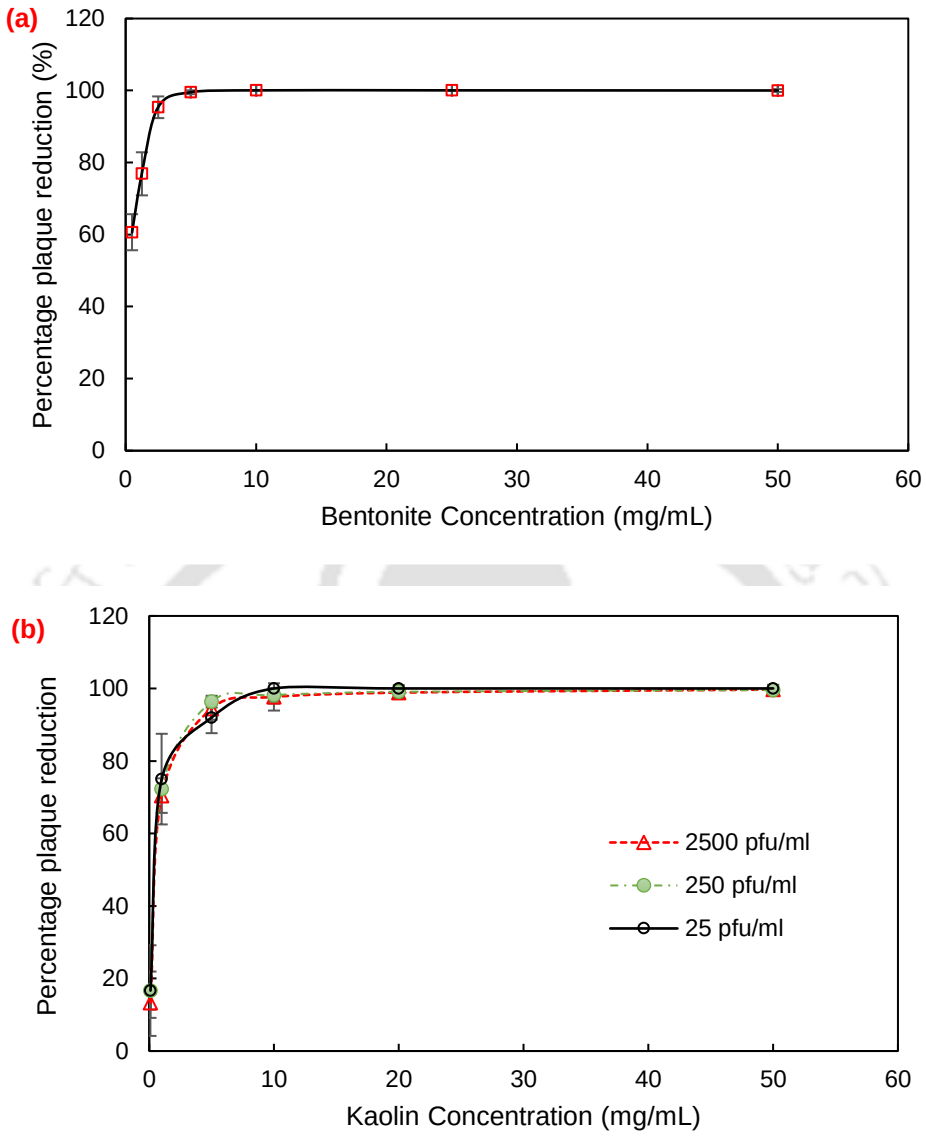

Figure 6.4: Reduction in plaque percentage for NDV with variations in (a) bentonite concentration using 12000 PFU/mL virus concentration; and (b) kaolin concentration using 25, 250, and 2500 PFU/mL virus concentrations

Linear, Langmuir, and Freundlich isotherm models were fitted to the experimental data of bentonite and NDV sorption as shown in Figure 6.5 (a-c). The regression coefficients for NDV sorption with bentonite were found to be 0.95, 0.829, and 0.94 for Linear, Langmuir, and Freundlich isotherm, respectively. The Langmuir isotherm coefficient, b representing sorption energy, was estimated as 0.00302 mL.PFU^{-1} and the maximum sorption capacity was found to be

10,000 PFU.mg^{-1}. A separation factor, R_L, of 0.0268 suggested favorable and close to irreversible sorption of virus particles on the clay surface. The Freundlich isotherm coefficient, K_f was found to be 114.20 PFU^{1-n}.mL^{n}.mg^{-1} and the exponent n was 0.5344, and the predicted coefficient n determines the degree of linearity of the sorption. Although, sorption studies of a few bacteriophages and pathogens are previously available with bentonites, but quality of bentonite material and pathogen type vary significantly, which makes the comparison difficult. The reported values vary in range of 0.00027 – 224.38 for K_f and 0.867 – 1.33 for n values (Vilker et al., 1983; Lispon et al., 1983; Stagg et al., 1977; Park et al., 2015; Syngouna & Chrysikopoulos, 2010; Chrysikopoulos & Syngouna, 2012) for the different bentonite clay with different bacteriophages and pathogens. The values of retardation factors were evaluated from the distribution coefficient, $(K_d)_{Linear}$ and Freundlich coefficient, K_f for linear and Freundlich isotherm, respectively. The retardation factor, R_d, from linear sorption was found to be 5683 and its value from the Freundlich isotherm model was found to be 3316.

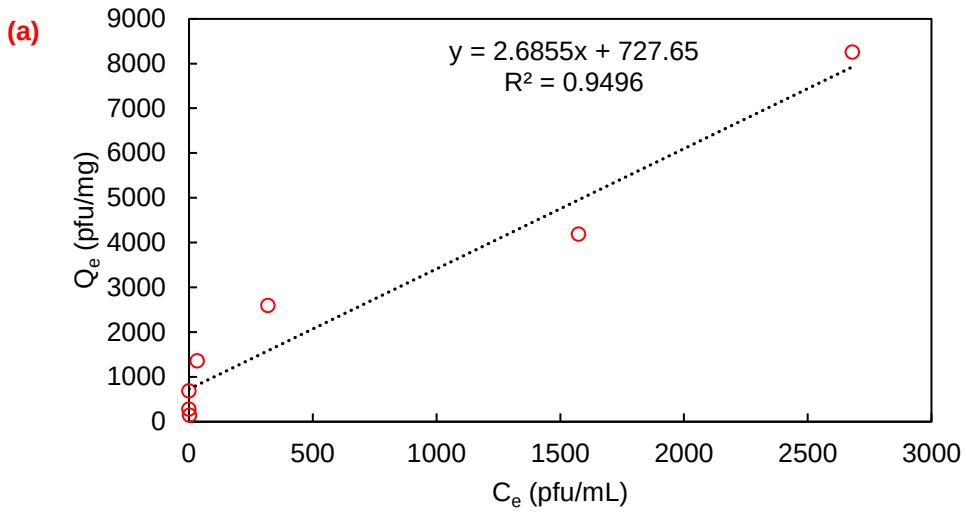

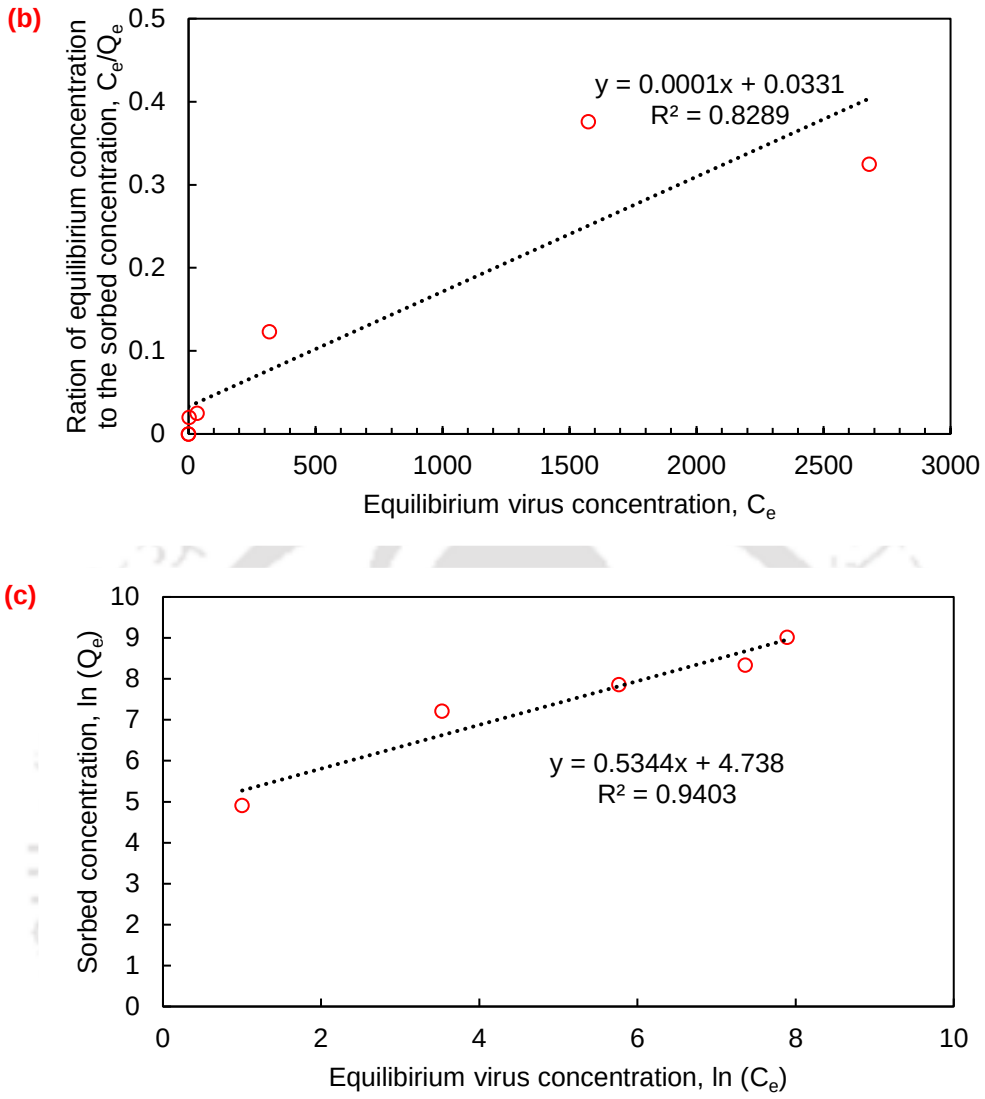

Figure 6.5: Fitting of sorption parameters for (a) Linear sorption isotherm for Bentonite B3; (b) Langmuir sorption isotherm model parameters for bentonite B3; (c) Freundlich sorption isotherm model parameter of bentonite B3

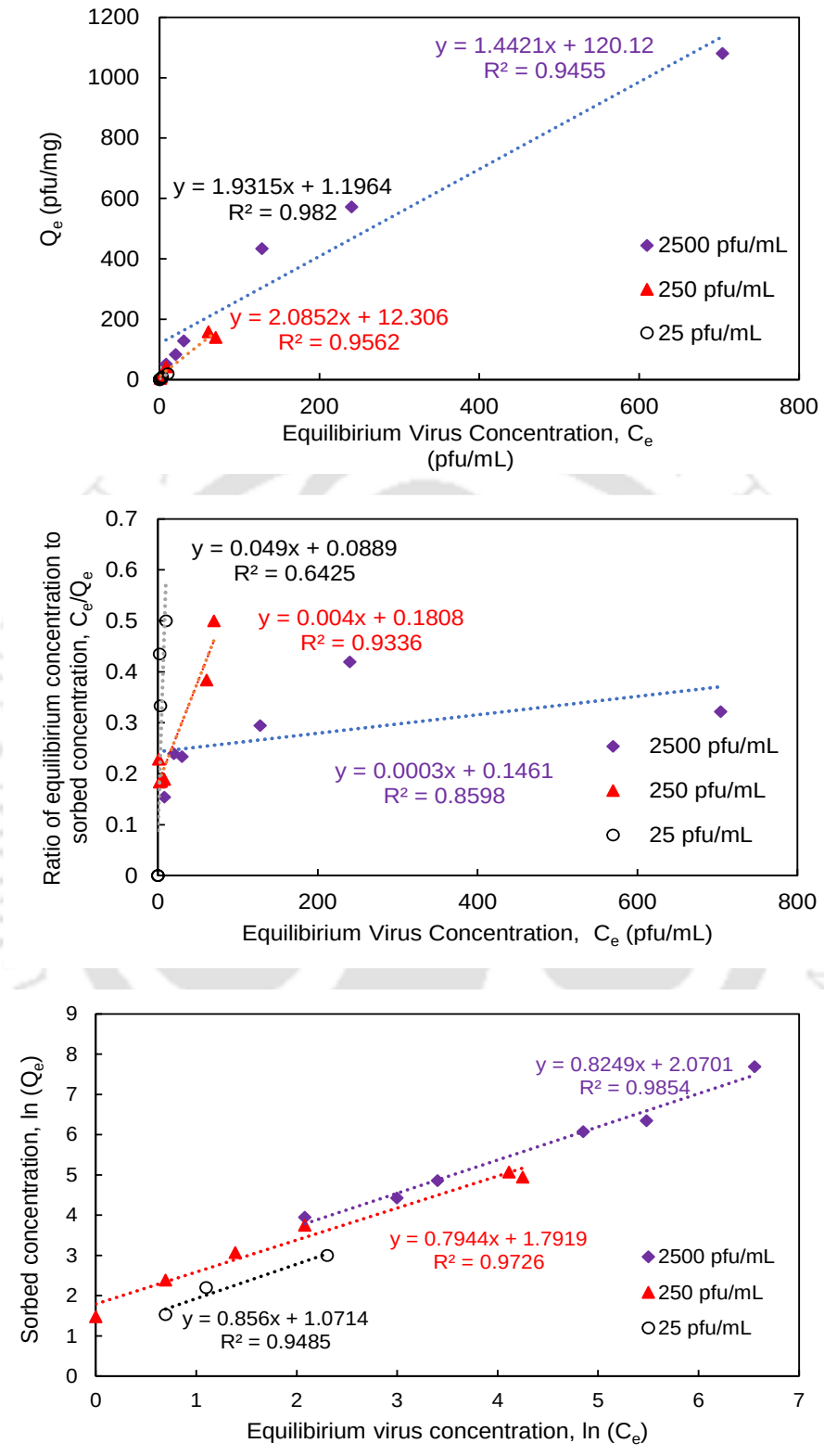

Figure 6.6: Fitting of sorption parameters for (a) Linear sorption isotherm model parameters; (b) Langmuir sorption isotherm model parameters; (c) Freundlich sorption isotherm model; parameters for kaolin with different virus concentration.

Linear, Langmuir, and Freundlich isotherm models were fitted to the experimental data of kaolin and NDV sorption as shown in Figure 6.6 (a-c). The sorption parameters for three different concentrations of NDV with kaolin were evaluated and presented in Table 6.1. The regression coefficients for linear, Langmuir, and Freundlich isotherm for NDV were found mostly higher than 0.9. The Langmuir isotherm coefficient, b representing sorption energy, was estimated as 1.77, 0.022, and 0.002 mL.PFU^{-1} for different virus concentrations. The values of retardation factors were evaluated from the distribution coefficient, $(K_d)_{Linear}$ and Freundlich coefficient, K_f for linear and Freundlich isotherm, respectively. The retardation factor, R_d, from linear sorption was found to be 4240-5686 and these values from the Freundlich isotherm model were found to be 5128-5526 for different concentrations of NDV.

Some studies on the pathogen sorption with kaolin are previously available, but the difference in the quality of kaolin and the type of pathogen used makes the comparison of results difficult. Langmuir isotherm coefficient, b was reported in literature as 0.019 and 0.042 for interactions of *pseudomonas putida* pathogen with two kaolin, namely KGa-1 and KGa-2, respectively (Vasiliadou et al., 2011). A separation factor, R_L, of 0.027-0.163 suggested favourable and close to irreversible sorption of virus particles on the clay surface. The Freundlich isotherm coefficient of the was found to be 2.92 – 7.92 PFU^{1-n}.mL^n.mg^{-1} and exponent *n* was 0.794-0.856 for different concentrations of NDV with kaolin. The values of Freundlich isotherm coefficient, K_f were found to vary over wide range 0.002 - 810027 for interaction of kaolin clay with bacteriophages and pathogens (Lispon et al., 1983; Stagg et al., 1977; Park et al., 2015; Syngouna & Chrysikopoulos, 2010; Chrysikopoulos & Syngouna, 2012; Vasiliadou et al., 2011). Moreover, the values of n were found to vary between 0.117 – 1 for interactions of these pathogens with kaolin. Such high differences in values are due to differences in kaolin quality and pathogen type.

Table 6.1: Linear, Langmuir, and Freundlich equilibrium sorption isotherm model parameters for different concentrations of NDV with kaolin

Sorption Isotherm Model	Parameter	Virus Concentration		
		25 pfu/mL	250 pfu/mL	2500 pfu/mL
Linear	Regression Coefficient, R^2	0.982	0.956	0.94
	Retardation factor, Rd	5340	5686	4240
Langmuir	Regression Coefficient, R^2	0.64	0.934	0.86
	Sorption energy parameter, b	1.778 $mL.PFU^{-1}$	0.022 $mL.PFU^{-1}$	0.002 $mL.PFU^{-1}$
	Max. sorption capacity, q_{max}	20 $PFU.mg^{-1}$	250 $PFU.mg^{-1}$	3,333 $PFU.mg^{-1}$
	Separation factor, RL	0.0274	0.154	0.163
Freundlich	Regression Coefficient, R^2	0.948	0.973	0.985
	Freundlich isotherm coefficient, Kf	2.92 $PFU^{1-n}.mL^n.mg^{-1}$	6.00 $PFU^{1-n}.mL^n.mg^{-1}$	7.925 $PFU^{1-n}.mL^n.mg^{-1}$
	degree of linearity of the sorption, n	0.856	0.794	0.8249
	Retardation factor, Rd	5128	5333	5526

6.2.3 Influence of specific surface area of bentonites

To consider the influence of bentonite surface characteristics on the virus sorption behavior, the NDV sorption was carried out with four different bentonites of different quality. An initial virus concentration of 12000 PFU/mL for three hours of contact time was adopted with 50 mg/ml of each type of bentonite. The equilibrium percentage removal was over 99% for all the studied bentonites as shown in Figure 6.7. The percentage removal of virus increased from B1 – B3, as

more sites were available in bentonite having higher specific surface area. The percentage removal of virus in B4 was slightly lower than in B3, as the specific surface area of B4 is slightly lower than B3, at 7 pH. The surface area of the bentonites showed a good correlation with the sorption ability indicating the sorption mechanism. The increase in the surface area increased the number of available sorption sites.

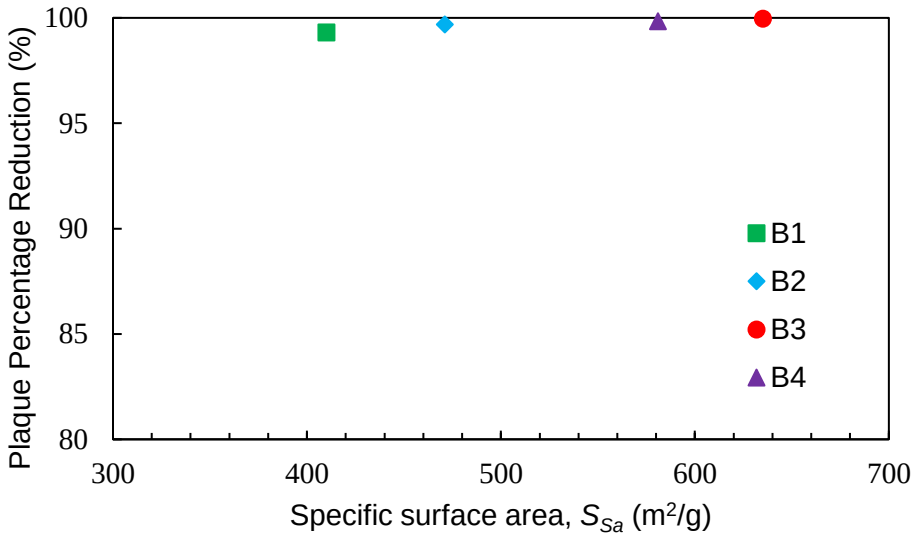

Figure 6.7: Influence of specific surface area of bentonite on percentage plaque reduction at equilibrium with 50 mg/mL of bentonites

6.2.4 Microstructural analysis

The field emission scanning electron microscopy (FESEM) images of bentonite, kaolin, and virus-sorbed clay were taken and shown in Figure 6.8. The virus-sorbed clay micrographs were slightly tricky due to the requirement of a dry sample. Ethanol, which is generally used for sample preparation could not be used here as it would destroy the bound virus particles. Drying at a higher temperature can also destroy the virus structure. So, the following procedure was followed for sample preparation for FESEM. Slurry samples were prepared by mixing the bentonite B3 with distilled water to obtain FESEM micrographs. Similarly, the virus stock was mixed with clay and diluted by adding distilled water. The prepared slurry samples of bentonite, kaolin, and virus-clay

slurries were drop-casted on one side of the double-sided carbon tape. The drop-casted samples were kept overnight for drying at 38˚C in a controlled temperature oven. The samples were then coated with a thin conductive layer of gold. The FESEM micrographs of B3 showed the presence of flaky clay particles in Figure 6.8(a). The FESEM micrographs of bentonite after NDV sorption are presented in Figure 6.8(b). Similarly, the micrograph of alone kaolin and NDV sorbed kaolin were presented in Figure 6.8(c) and Figure 6.8(d), respectively. The sorption of spherical virus particles in groups on the clay surface was visible in the micrographs. FESEM micrographs thus confirmed multi-layer group sorption of virus particles on clay surfaces.

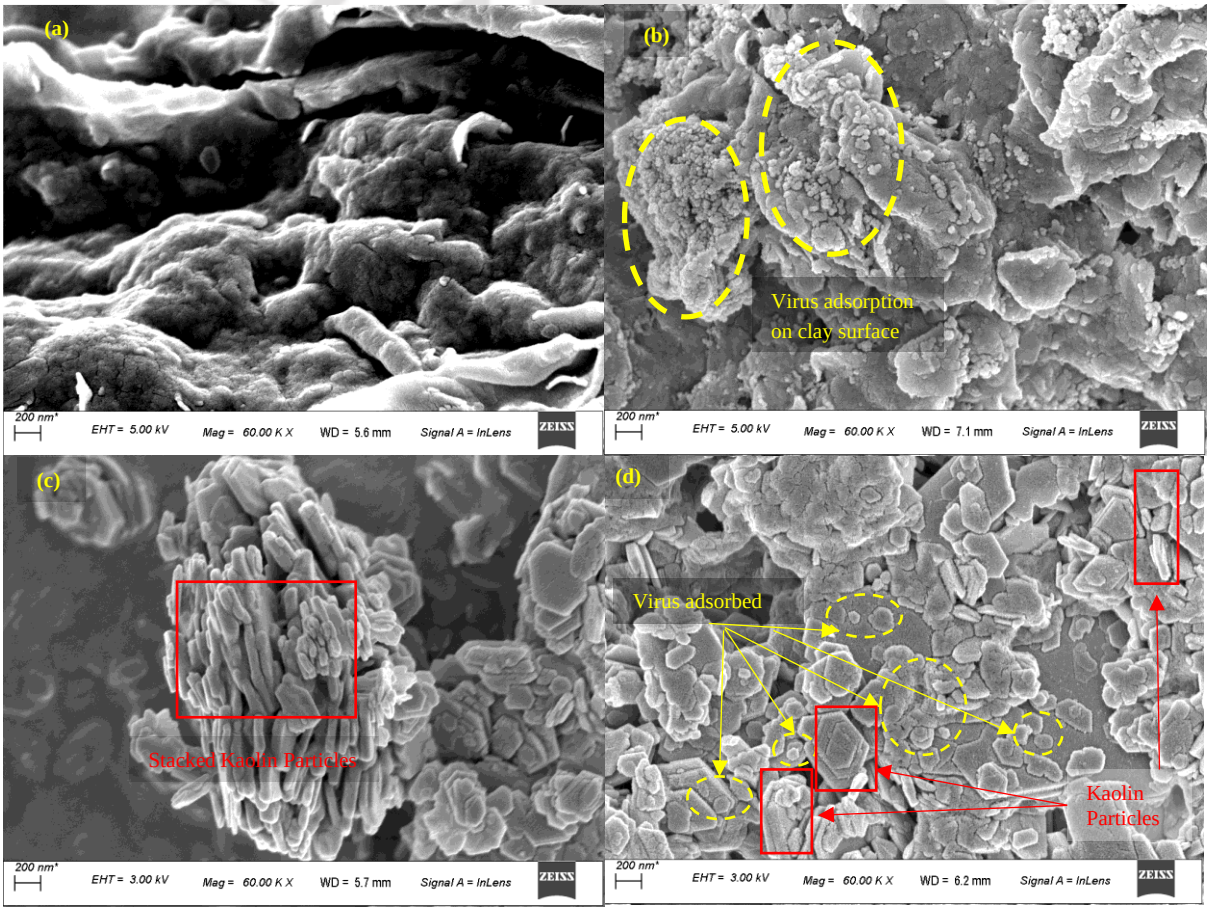

Figure 6.8: Surface morphology by FESEM micrographs for (a) bentonite B3; (b) bentonite after adsorption of Newcastle disease virus (NDV); (c) kaolin; and (d) kaolin after adsorption of NDV.

6.2.5 Interaction energy profiles

The present study evaluates the interaction energy based on Derjaguin–Landau–Verwey–Overbeek (DLVO) theory and assumes the virus particles as spherical and clays as plates. The interaction energy profiles contain the deep well at a very low separation distance and it is also known as the primary minimum, $\phi_{min1.}$ Further, the primary maximum energy level, ϕ_{max1} indicates the energy barrier for attachment and detachment, and the shallow minimum energy well at a relatively higher distance is the secondary minimum, $\phi_{min2.}$ The interaction energy profiles were evaluated for virus–clay interactions by considering sphere plate arrangement.

Table 6.2: Parameter values considered for theoretical evaluations of interaction energies

Parameter	Values	References
Hamaker constant, A_{123}	7.5×10^{-21} J	Murray et al., 1978
Radius of virus, r_p	Coronavirus: 50 nm	Kumar et al., 2021
	NDV: 50 nm	This study
Characteristics wavelength, λ	10^{-7}m	Gregory, 1981
$\epsilon_r = \epsilon/\epsilon_0$ is the relative dielectric constant of liquid	78.4	Chrysikopoulos and Syngouna, 2012
Ionic strength, I_s	0.0001 M	This study
Zeta potential, ζ	Bentonite: - 0.021 V	Chrysikopoulos and Syngouna, 2012
	Kaolin: - 0.026 V	Chrysikopoulos and Syngouna, 2012
	Coronavirus: -0.0256 V	Gatak et al., 2021
	NDV1: -0.00911 V	Shang et al., 2022
	NDV2: -0.0234 V	Shang et al., 2022
Avogadro's number, N_A	6.022×10^{-23} 1/mol	Das et al., 2022
Elementary charge, e	1.6×10^{-19} C	Das et al., 2022
Temperature, T	298 K	This study
Boltzmann's constant, k_B	1.38×10^{-23} J/K	Das et al., 2022
Permittivity of free space, ϵ_0	8.854×10^{-12} $C^2/(J\cdot m)$	Das et al., 2022
Born collision parameter, σ_{Born}	5 Å	Chrysikopoulos and Syngouna, 2012

The energy profiles are shown in Figure 6.9 for experimental conditions for pH = 7 and ionic strength of 10^{-4} mM. The electrokinetic zeta potential values were considered instead of surface potential. The interaction energies of two strains of NDV, namely cHN-P4 (NDV1) and cHN-N3

(NDV2) were considered in the present work. The zeta potentials of these strains at 7 pH for these strains of NDV were found to be - 9.11 mV and – 23.4 mV, respectively. Further, the interaction energies of coronavirus were also evaluated and the zeta potential for the coronavirus was – 25.675 mV at 7 pH (Gatak et al., 2021).

The parameters considered for the evaluation of interaction energies are listed in Table 6.2. The interaction energy profiles of virus kaolin interactions are presented in Figure 6.9(a). The coronavirus and NDV2 strains showed almost similar profiles, whereas, NDV1 showed a lower and slightly shifted towards the right energy peak. Further, the interaction energy profiles for bentonite–virus interactions are shown in Figure 6.9(b). Similarly, coronavirus and NDV2 strains showed similar energy profiles and NDV1 showed the downward and slightly shifted energy peak. As compared to the kaolin–virus peak, the magnitude of energy at the peak was lower for the bentonite – virus peak, which represents better attachment of the virus to bentonite as compared to kaolin.

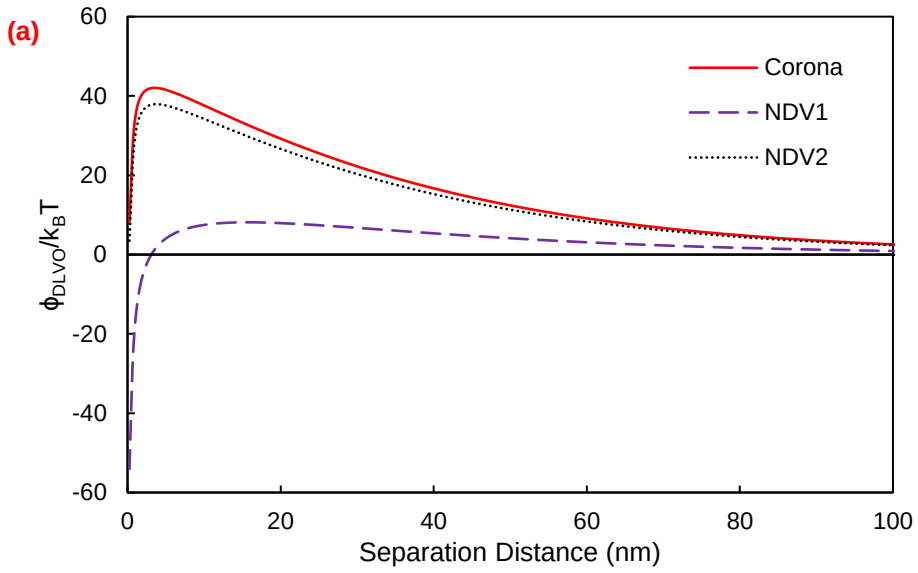

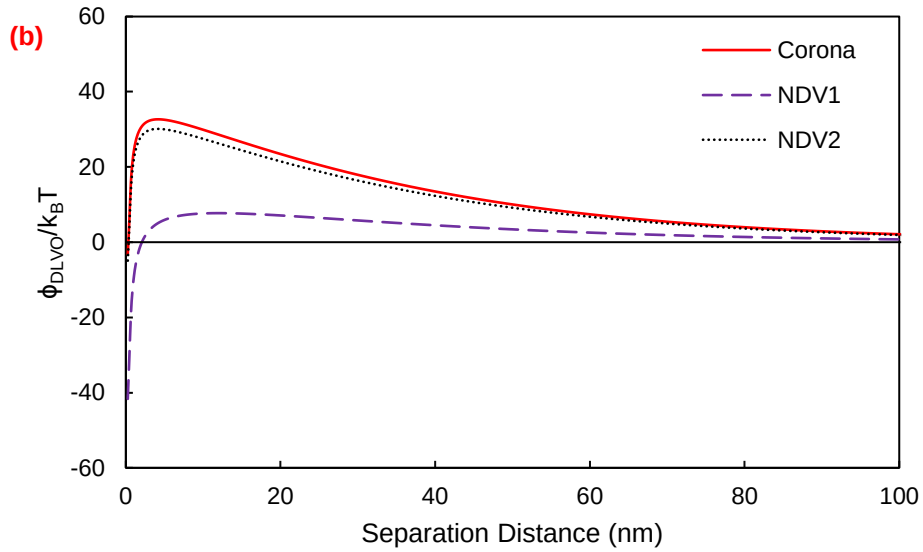

Figure 6.9: Predicted DLVO energy profiles for corona-virus and NDV strains with (a) kaolin; and (b) bentonite

6.3 Sorption of NDV with special clays

This section discusses the sorption of NDV with three special clays, which are found at limited locations and have specific features. The study considered illite (I), halloysite (H), and sepiolite (S) clay minerals for sorption with NDV. The NDV particles have negative charges at neutral pH as discussed in the previous section (6.2.5), it is potentially attached to the positively charged surface cations in different minerals. The results from the sorption of NDV with these clay minerals will be discussed in detail. The role of contact time, clay mineral type, and dose of clays will be covered in this section. An understanding based on results will be discussed in detail.

6.3.1 Sorption kinetics of NDV with clay minerals

An average initial NDV concentration of 280000 PFU/mL was used in sorption kinetics experiments and the concentration of clay minerals was maintained at 2 mg/mL. The interaction period of the study varied between 5 to 60 minutes. The plaque assay was performed to analyze the presence of the virus in samples after sorption as shown in Figure 6.10. The same concentration

of NDV was also taken as a control to measure its concentration after the same time. The control was taken to consider the biological decay of NDV. The reduction in plaque with respect to control NDV was represented in terms of percentage plaque reduction or plaque reduction. The sorption kinetic results for NDV on halloysite, illite, and sepiolite were presented in Figure 6.11. Percentage plaque reduction was found to increase with the contact time. The sorption rate was highest for illite initially, which was overcome by Halloysite with time and Halloysite showed a maximum percentage plaque reduction as compared to the other three clay minerals. The illite showed the minimum percentage plaque reduction. The percentage plaque reduction after 1 hour of interaction period, for illite, sepiolite, and halloysite showed 82, 85, and 92 % plaque reduction, respectively.

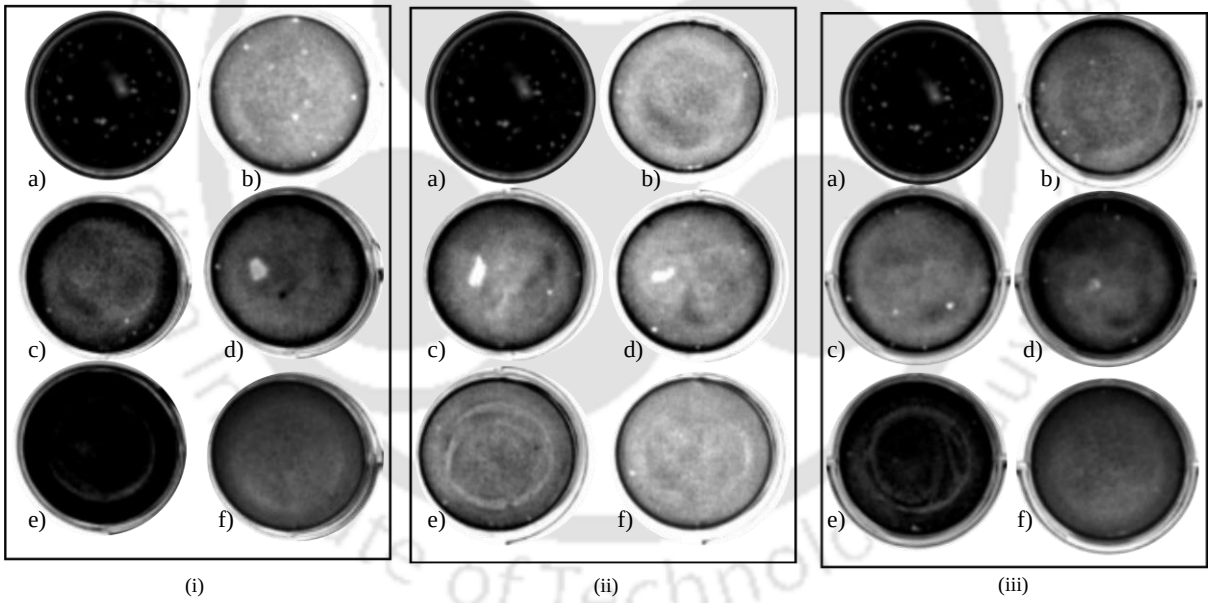

Figure 6.10: NDV replication kinetics for (i) H; (ii) I; (iii) S, in different time points post interaction- (a) 0 min; (b) 5 min; (c) 10 min; (d) 20 min; (e) 40 min; and (f) 60 min.

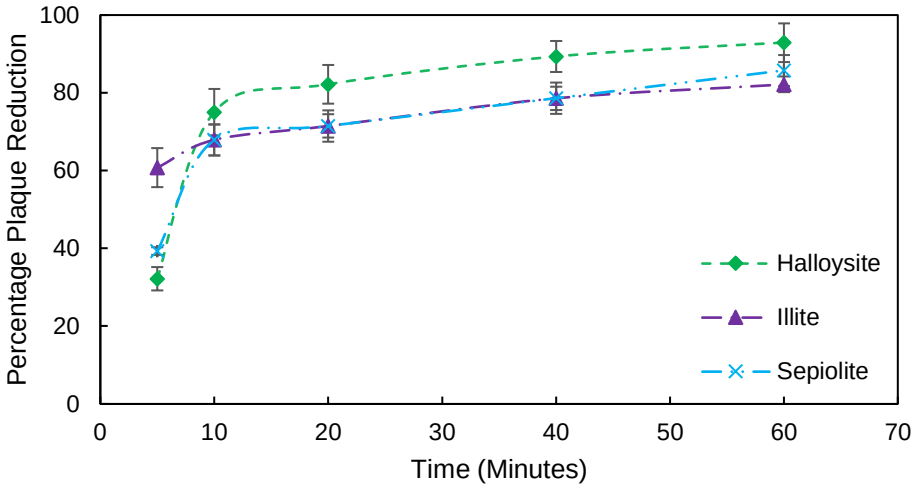

Figure 6.11: Percentage plaque reduction of NDV with time for halloysite, illite, and sepiolite with 2 mg/ml concentration

The sorption kinetics data for all the clay minerals were fitted to pseudo-first-order as well as pseudo-second-order kinetics as shown in Figure 6.12. The sorption data showed a very good fit to the pseudo-first-order as well as the pseudo-second-order kinetics with a coefficient of regression 0.83-0.96 and 0.98-0.999, respectively. The adsorption rate constant k_1 was found to be 0.0346, 0.0136, and 0.0217 (min^{-1}) for H, I, and S respectively. The value of the rate constant represents the rapid adsorption of NDV with H and the slowest with I among the studied clay minerals. Further, the adsorption rate constant k_2 was found to be 2.25×10^{-7}, 8×10^{-7}, and 4×10^{-7} ($mg.PFU^{-1}.min^{-1}$) for H, I, and S, respectively.

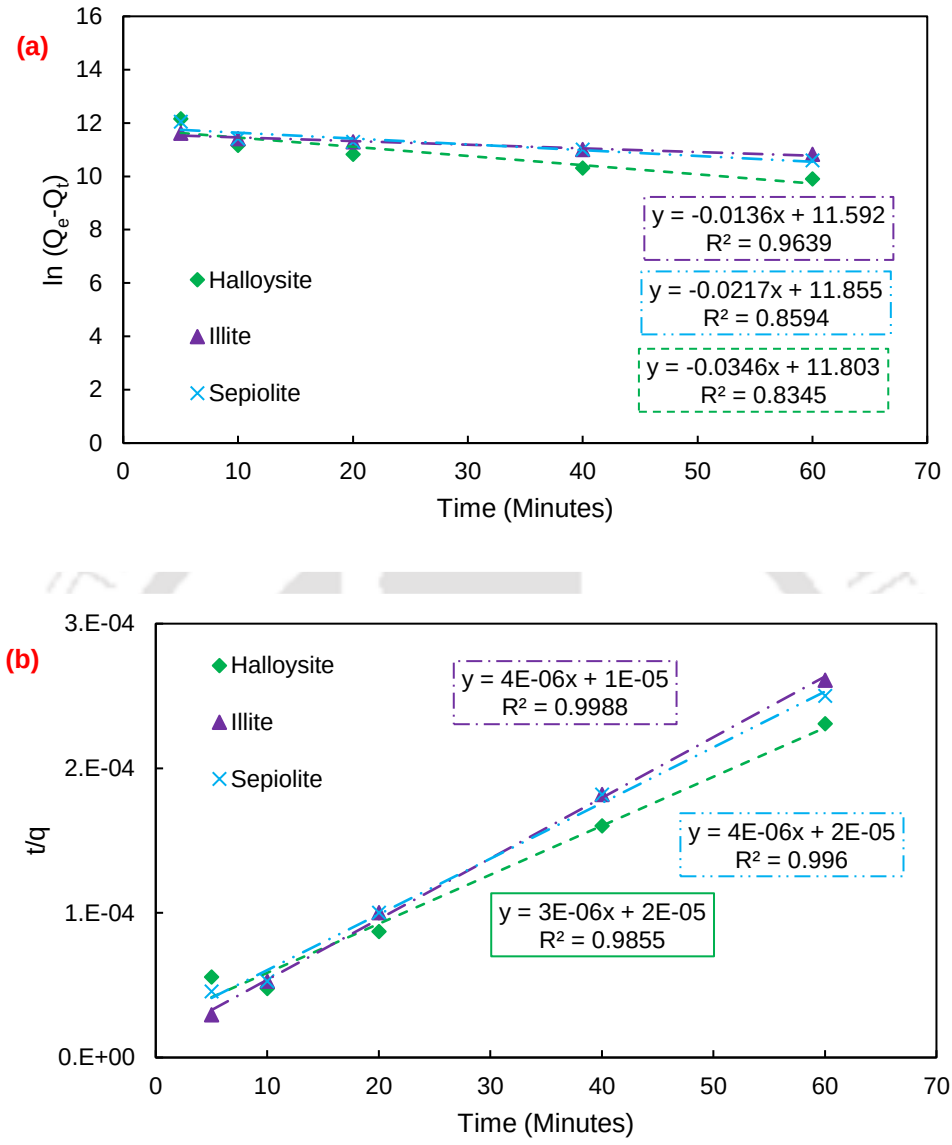

Figure 6.12: (a) Pseudo-first-order kinetics and (b) pseudo-second-order kinetics for NDV sorption with halloysite, illite, and sepiolite

6.3.2 Equilibrium Sorption of NDV with clay minerals

Equilibrium batch sorption experiments of NDV with three clay minerals H, I, and S were conducted with an initial concentration of NDV as 280000 PFU/mL. The concentration of NDV after sorption was measured using plaque assay as shown in Figure 6.13. The percentage plaque reduction of NDV with H, I, and S clay minerals as a function of clay concentration was presented

in Figure 6.14. In this study, the interaction time of 1 hour was considered based on results from the kinetic study. After the sorption experiment, the NDV gets bound to the clay minerals, and bounded NDV gets separated from the solution once the clay mineral particles are removed upon centrifugation and do not contribute to the plaque assay. The observed percentage plaque reduction increased with the increase in the amount of each clay mineral due increase in the number of available sites for the sorption of NDV. The highest percentage plaque reduction was found for the Halloysite at both higher and lower concentrations of the clay mineral. Moreover, the lowest reduction in percentage plaque was found for illite mineral. Due to an increase in the number of available sites for the adsorption of NDV, all clay minerals showed an increased percentage reduction for clay mineral concentration > 10mg/mL.

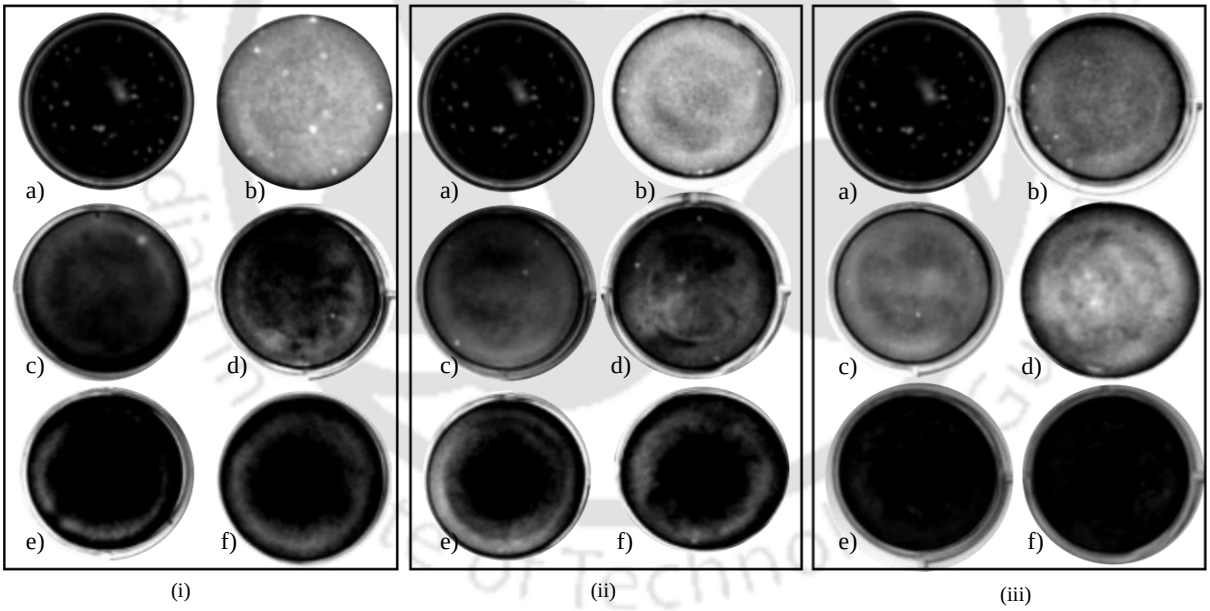

Figure 6.13: NDV sorption with i) H; ii) I; iii) S, at different concentrations -a) Neat virus; b) 1mg/ mL; c) 2mg/mL; d) 5mg/mL; e) 10 mg/mL; f) 20 mg/mL.

The zeta potential/surface charge of the NDV is negative as discussed in the previous section. The adsorption of NDV on Halloysite is attributed to the positively charged termination sites in it. Further, the Halloysite also has a positively charged surface towards the inner side of the hollow

cylindrical surface, so the virus might also attach to the inner side of the Halloysite. The attachment of NDV is with the exchangeable surface cations as well as fixed potassium in the case of illite clay minerals. The availability of potassium in the case of illite is limited, and hence it showed a minimum percentage plaque reduction as compared to other minerals. The sepiolite dominates the hydrogen bonding due to the presence of excess hydroxyl groups, the NDV is getting attached to the water present in channels and tunnels of the sepiolite mineral.

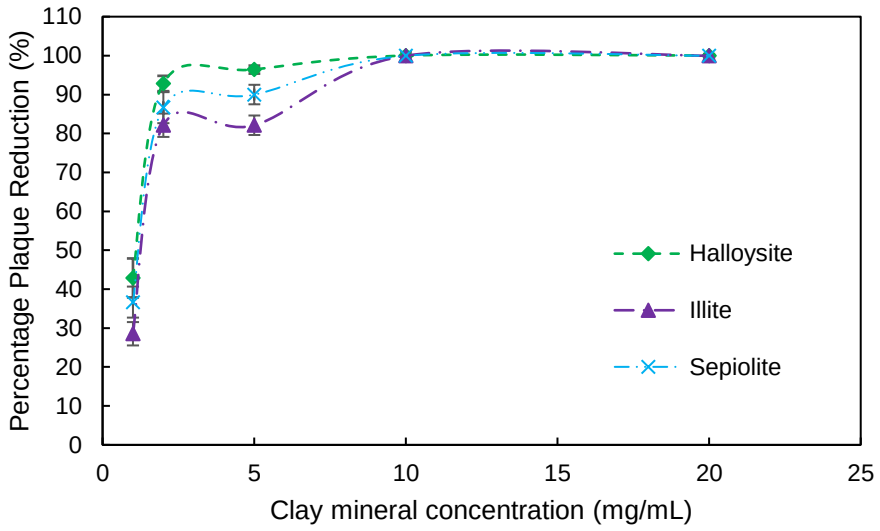

Figure 6.14: Reduction in plaque percentage for NDV with variations in halloysite, illite, and sepiolite concentration using 280000 PFU/mL virus concentration

The linear sorption isotherm model was fitted and plotted in Figure 6.15(a) with the experimental data for H, I, and S minerals. The regression coefficient of NDV sorption on clay minerals was found 0.94, 0.35, and 0.45 for H, I, and S, respectively. Further, the retardation coefficient of these minerals based on the K_d obtained from the linear sorption model was evaluated. The value of R_d was found to be 11820, 700, and 1012 for H, I, and S, respectively. A very high value of retardation factor was found for Halloysite. The sorption data of NDV and clay minerals were also fitted to the Langmuir sorption isotherm model and presented in Figure 6.15(b). The regression coefficients were found to be higher than 0.9 for all studied clay minerals. The Langmuir isotherm coefficient,

b was found to be in the range of 1.022×10^{-4} mL.PFU^{-1} to 2.207×10^{-4} mL.PFU^{-1} for different clay minerals. The separation coefficient, R_L was found to be 0.0159 to 0.022 for different clay minerals. The values of the separation factor suggest close to the irreversible attachment of NDV to the clays. The Freundlich equilibrium sorption isotherm model for NDV with these clay minerals was fitted and shown in Figure 6.15(c). The regression coefficient of NDV with these clay minerals showed a poor fit. The values of retardation factors were found based on Freundlich equilibrium isotherm as 1138, 621, and 973 for H, I, and S, respectively. The detailed sorption parameters for isotherm models have been shown in Table 6.3.

Table 6.3: Linear, Langmuir, and Freundlich equilibrium sorption isotherm model parameters for 280000 PFU/mL concentration of NDV with different clay minerals

Sorption Isotherm Model	**Parameter**	**H**	**I**	**S**
Linear	Regression Coefficient, R^2	0.94	0.35	0.45
	Retardation factor, R_d	11820	700	1012
Langmuir	Regression Coefficient, R^2	0.993	0.95	0.967
	Sorption energy parameter, b	1.55×10^{-4} mL.PFU^{-1}	2.207×10^{-4} mL.PFU^{-1}	2.069×10^{-4} mL.PFU^{-1}
	Max. sorption capacity, q_{max}	1,25,000 PFU.mg^{-1}	1,00,000 PFU.mg^{-1}	1,11,111 PFU.mg^{-1}
	Separation factor, R_L	0.022	0.0159	0.0169
Freundlich	Regression Coefficient, R^2	0.399	0.014	0.220
	Freundlich isotherm coefficient, K_f	10420 PFU^{1-n}.mL^n.mg^{-1}	34578 PFU^{1-n}.mL^n.mg^{-1}	8063 PFU^{1-n}.mL^n.mg^{-1}
	Degree of linearity of the sorption, n	0.2127	0.0687	0.2207
	Retardation factor, R_d	1138	621	973

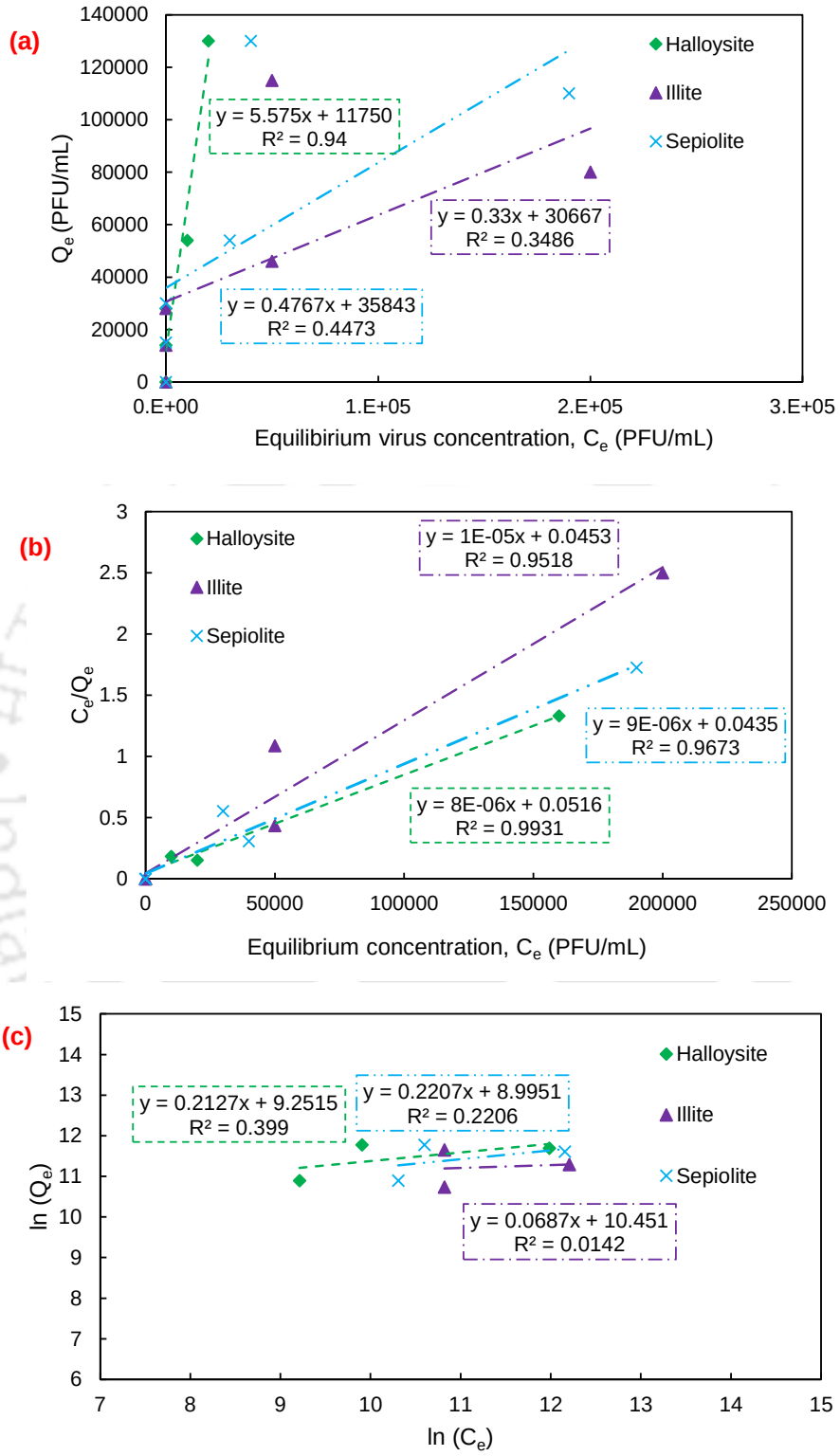

Figure 6.15: Fitting of sorption parameters for (a) Linear sorption isotherm model parameters; (b) Langmuir sorption isotherm model parameters; (c) Freundlich sorption isotherm model; parameters for NDV sorption on different clay minerals.

6.3.3 Microstructural analysis

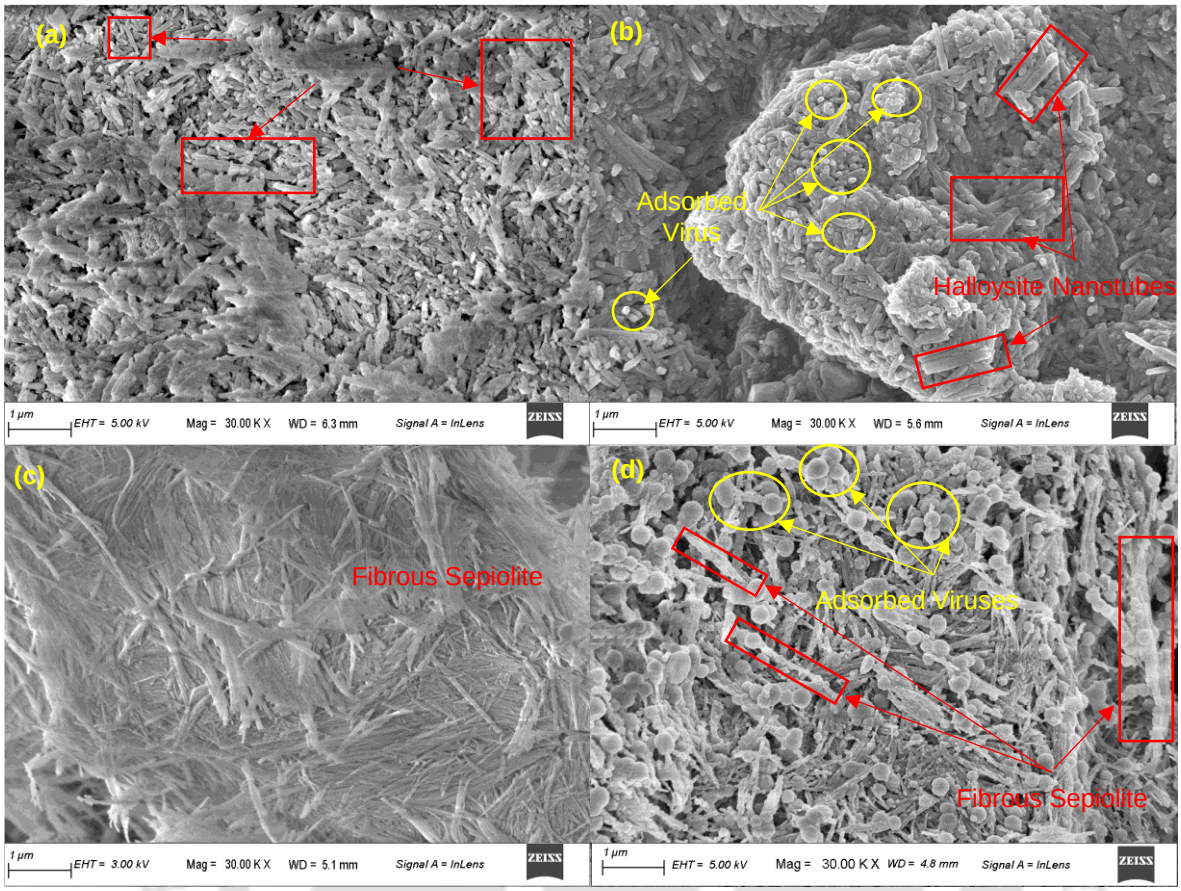

Figure 6.16: Surface morphology by FESEM micrographs for (a) Halloysite; (b) Halloysite after adsorption of Newcastle disease virus (NDV); (c) Sepiolite; and (d) Sepiolite after adsorption of NDV.

The field emission scanning electron microscopy (FESEM) images of Halloysite, sepiolite, and virus-sorbed clays were taken and shown in Figure 6.16. FESEM of virus-sorbed clay minerals was taken by following the same procedure as explained in section 6.2.4. The FESEM micrographs of Halloysite showed the presence of rod-like particles in Figure 6.16(a). The FESEM micrographs of Halloysite after NDV sorption are presented in Figure 6.16(b). Further, the micrograph of alone sepiolite was presented in Figure 6.16(c). The micrograph showed a fibrous structure of the sepiolite mineral. The micrograph of NDV sorbed with sepiolite is presented in Figure 6.16(d), the attachment of the NDV to the sepiolite fibers is visible in the micrograph.

6.4 Summary

The study on the sorption of NDV to the five different clay minerals, namely kaolinite, montmorillonite, Halloysite, illite, and sepiolite clay was conducted and the following points are drawn from the study:

- Sorption of NDV by considering the biological decay on bentonite, kaolin, and halloysite was found to be quick and relatively slower on other clay minerals. The sorption behavior of NDV on bentonite as well as kaolin clay surface followed a second-order kinetic reaction. The additional clay minerals also fitted well with first-order kinetics.
- The removal efficiency (sorption ability) of NDV depends on the mineralogy of the clay. The sorption ability of NDV depends on the quality of bentonite. A removal efficiency of ~100% was found for NDV with the high-quality bentonite of a specific surface area of 635 m^2/g and a concentration higher than 5 mg/mL. A removal efficiency of > 90% was found for NDV with other studied clay minerals at a concentration higher than 10 mg/mL.
- All three sorption isotherms, i.e., Linear, Langmuir, and Freundlich, fitted well on the measured equilibrium sorption data of NDV with bentonite and kaolin with a good regression coefficient. The best fit with Freundlich isotherm-supported multi-layer sorption of virus particles on the bentonite, and kaolin, surfaces. Multi-layer sorption of NDV on clay was also evident from FESEM micrographs. A Langmuir sorption separation factor, R_L = 0.0268 for bentonite, R_L =0.027 to 0.16 for kaolin, R_L = 0.022 for Halloysite, R_L = 0.0159 for illite, and R_L = 0.0169 for sepiolite, suggested a favorable and close to irreversible sorption of virus particles on the studied clay minerals surface.
- Based on the interaction energy profiles NDV2 strain is a good surrogate to the coronavirus and represents almost equal energies at all separation distances. Further, a lower energy

peak in the case of bentonite suggests better binding of virus with bentonite as compared to kaolin, which agrees with the experimental results.

- Exceptionally high values for retardation factors (3000 – 5000) represents good sorption of viral pathogens in clays and both clays (i,e., kaolin and bentonite) are recommended as liners for containment of pathogenic waste in biomedical waste disposal facilities.

Chapter – 7

Mechanism Controlling the Sorption of Coronavirus Surrogate to the Bentonite Clays

---

7.1 General

Chapter 6 discussed the role of the mineralogy of clays on the sorption behavior of Newcastle disease virus (NDV). The bentonite clay containing a high percentage of montmorillonite mineral showed excellent sorption ability. So, further work will be continued with bentonite. The present work will discuss the mechanism governing the adsorption of NDV on bentonite. The bentonite clay has exchangeable surface cations, like sodium, potassium, calcium, magnesium, etc. In natural bentonites, these surface cations are present in different proportions. If the virus particles are directly attached to the negatively charged montmorillonite layer, then the presence of surface cation or type of surface cation does not influence the adsorption ability of the NDV on bentonite. Moreover, if the adsorption ability of the virus on clays is influenced by the type of cations, then these virus particles are not directly bound to the clay surface but to the surface cation. However, there is no study on interactions of NDV with the same clay having different types of cations. The sorption study was conducted on two bentonites in their natural form and six different bentonites prepared after their homo-ionization with sodium, potassium, and calcium ions.

7.2 Sorption of NDV with bentonites

The results from batch sorption experiments for NDV sorption on bentonite clays and homo-ionized bentonite clays were presented in detail in this section. The influence of contact time, clay

dose, and type of surface cations were evaluated for bentonite clays. The understanding of the mechanism governing the sorption of NDV on bentonite based on the results from the study will be discussed in detail.

7.2.1 Sorption kinetics for NDV with bentonites

An initial concentration of 2,80,000 PFU.mL^{-1} of NDV was used for the sorption kinetics studies with two bentonites and six homo-ionized bentonites with sodium, potassium, and calcium while maintaining a bentonite concentration of 2 mg.mL^{-1}. The experiments were conducted for different interaction durations, 5 – 60 minutes. The plaque assay was used to evaluate the NDV concentration in the samples after the sorption experiment as shown in Figure 7.1.

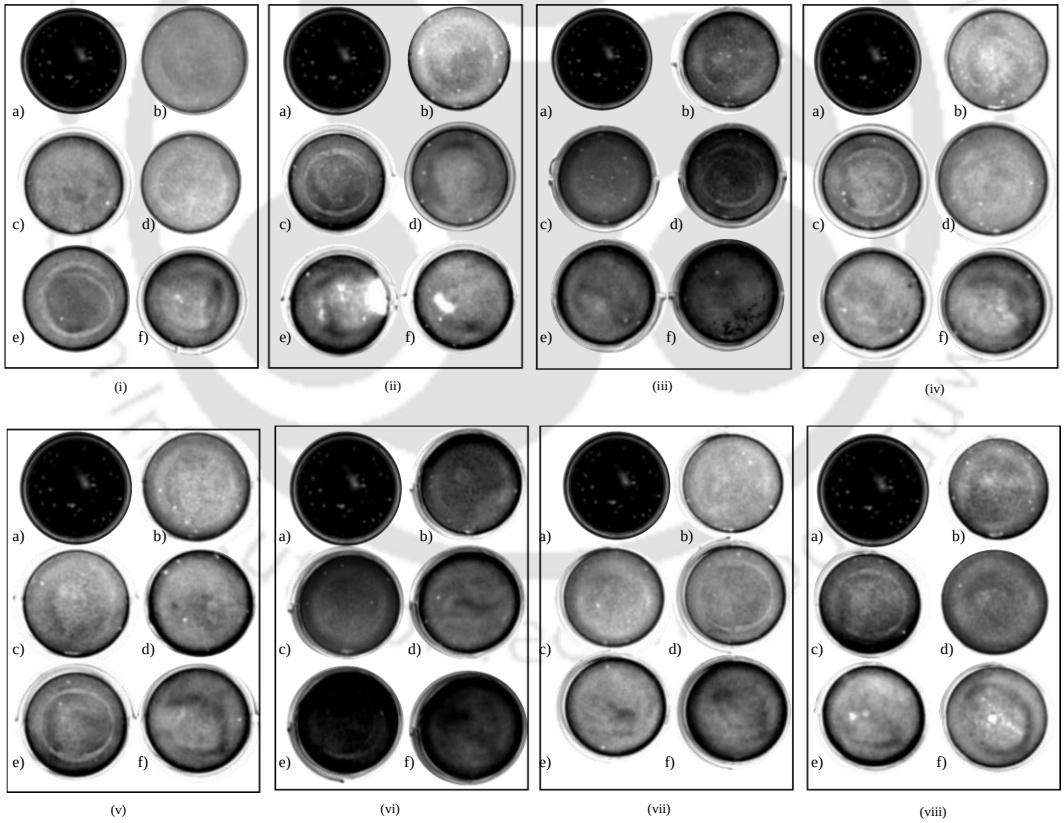

Figure 7.1: NDV sorption kinetics upon interaction with various bentonites at a concentration of 2µg/mL (i) B1; (ii) B1-Ca; (iii) B1-K; (iv) B1-Na; (v) B3; (vi) B3-Ca; (vii) B3-K; and (viii) B3-Na at different time points- (a) neat virus; (b) 5 min; (c) 10 min; (d) 20 min; (e) 40 min; and (f) 60 min.

An NDV control sample of the same concentration was also considered to account for the biological decay of the virus. The NDV plaque percentage reduction with respect to the control experiment with bentonite B1 and its homo-ionized forms was presented for different interaction periods in Figure 7.2 (a). The percentage plaque reduction of bentonite B1 and its homo-ionized forms were found to increase with increased interaction time. The bentonite B1 was found to have lower plaque reduction than homo-ionic B1 bentonite initially. Moreover, it showed more plaque reduction than homo-ionic B1 at equilibrium. The rate of adsorption of NDV on bentonite was found to be dependent on the type of exchangeable cations. The bentonite B1 homo-ionized with calcium (B1-Ca) showed more plaque reduction than B1, which is due to the binding of the virus to the calcium ions.

The percentage plaque reduction with time of NDV with respect to the control experiment with bentonite B3 and its homo-ionized bentonites was presented in Figure 7.2(b). The percentage plaque reduction was found to increase with the increase in interaction periods. Natural and calcium homo-ionized bentonite showed higher reduction as compared to sodium and potassium homo-ionized bentonites. A large reduction in percentage plaque reduction was observed in the case of K-B3. A percentage reduction of 25% was observed for B1 after 5 minutes of interaction period, and it was found to be 45% with B3. The percentage reduction was found to increase with the quality of bentonite during initial interactions.

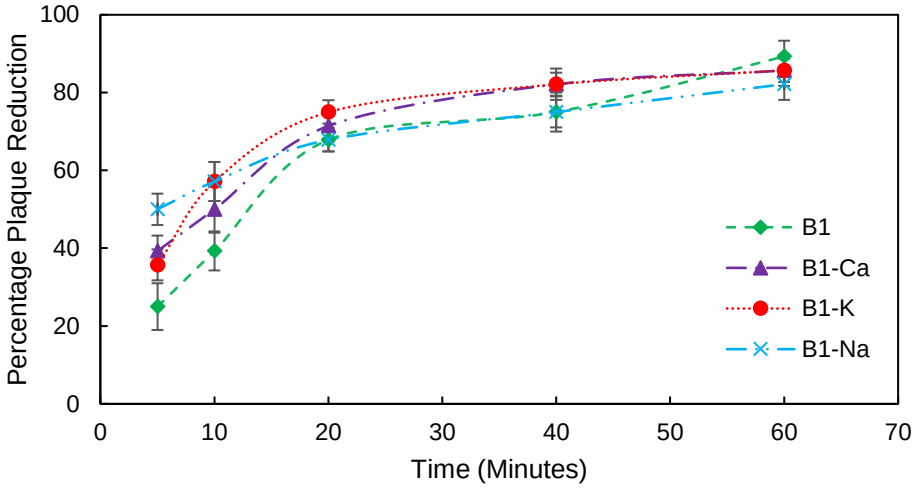

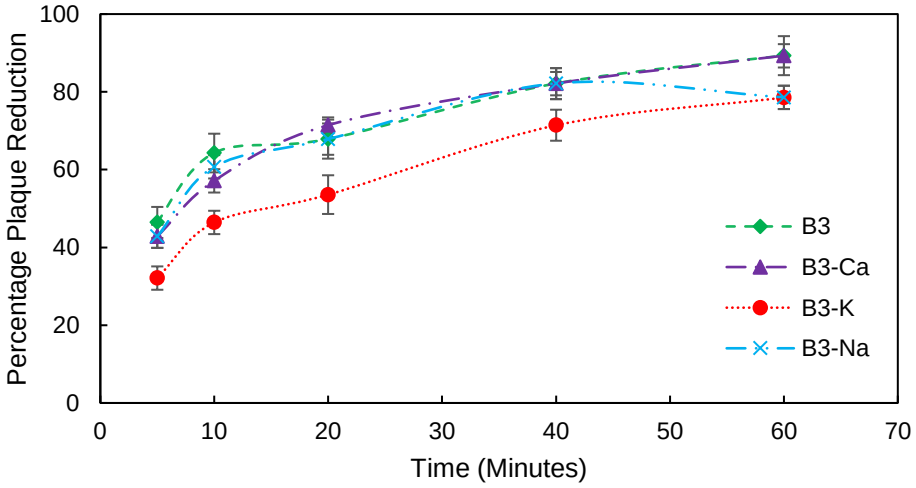

Figure 7.2: Plaque reduction of NDV with time for (a) B1; and (b) B3 bentonites and their homo-ionized form with clay concentration of 2 mg.mL^{-1}

The estimated sorption kinetic data were fitted with both pseudo-first-order as well as pseudo-second-order kinetic models as presented in Figure 7.3. The sorption data showed a high value of the coefficient of regression (R^2) with both pseudo-first-order as well as pseudo-second-order kinetics. The adsorption rate constant k_1 was found to be 0.0332, 0.0265, 0.0254, and 0.0179 (min^{-1}) for B1, B1-Ca, B1-K, and B1-Na, respectively. Moreover, the rate constant (k_1) was found to be 0.0274, 0.0291, 0.0205, and 0.0179 (min^{-1}) for B3, B3-Ca, B3-K, and B3-Na, respectively. The

adsorption of NDV was found to be quickest for Ca homo-ionized and natural bentonites. Further, the adsorption rate constant (k_2) for NDV with bentonite B1 and its homo-ionized forms were found to vary between 9×10^{-8} – 4×10^{-7} (mg.PFU^{-1}.min^{-1}) and it was found to vary between 2×10^{-7} - 4×10^{-7} (mg.PFU^{-1}.min^{-1}) for B3 and its homo-ionized forms.

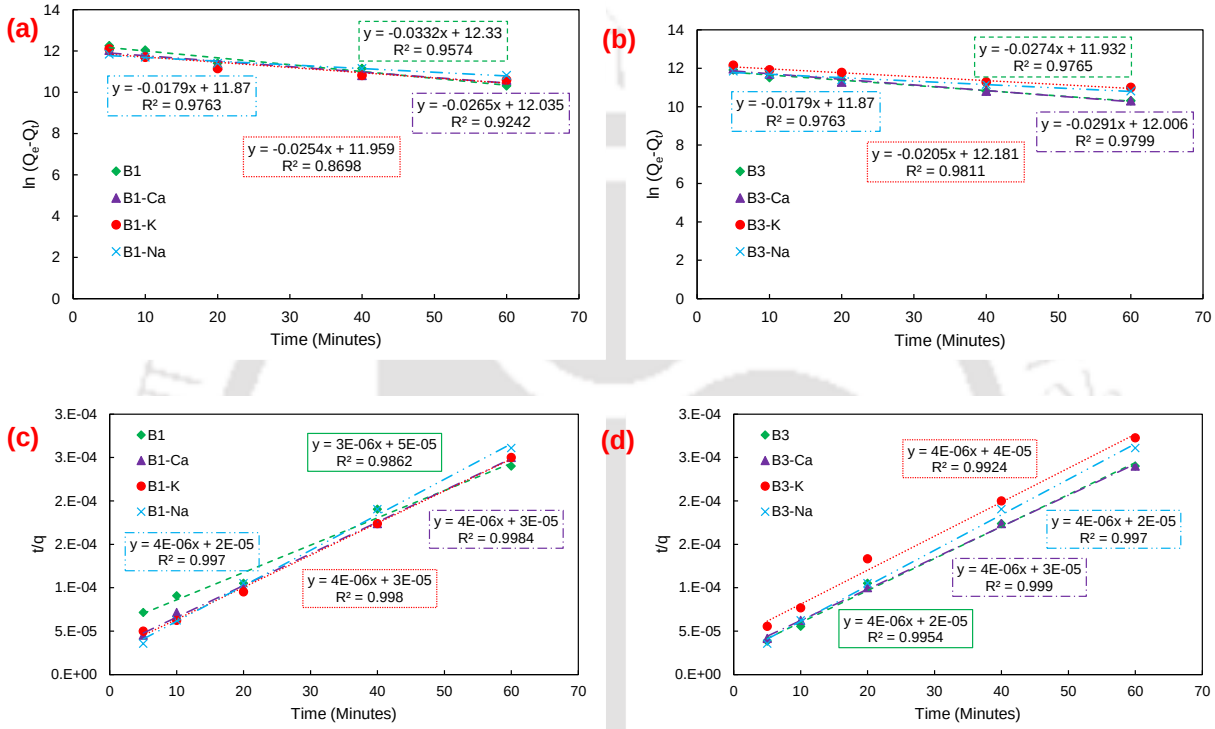

Figure 7.3: Pseudo-first-order kinetics for (a) B1 and homo-ionized B1; (b) B3 and homo-ionized B3; pseudo-second-order kinetics for (c) B1 and homo-ionized B1; and (d) B3 and homo-ionized B3 NDV sorption.

7.2.2 Equilibrium sorption for NDV with bentonites

Equilibrium sorption experiments of NDV with two bentonites and six homo-ionized bentonites obtained after the homo-ionization process were performed and the concentration of virus was measured using plaque assay as shown in Figure 7.4. The percentage plaque reduction of NDV with natural B1 and B1 homo-ionized with calcium, potassium, and sodium as a function of the amount of clay was presented in Figure 7.5(a). In this study, the interaction time of 1 hour was

considered based on results from the kinetic study. After the sorption experiment, the NDV gets bound to the bentonite clay and bounded NDV gets separated from the solution once the clay particles are removed upon centrifugation and do not contribute to the plaque assay. The observed percentage plaque reduction increased with the increase in the amount of the bentonites due increase in the number of available sites for the sorption of NDV. For 1 mg/mL bentonite concentration, the plaque percentage reduction in B1 was found to be higher than other homo-ionized B1. Bentonite B1 homo-ionized with sodium (B1-Na) showed significantly lower plaque reduction as compared to the natural B1 as well as B1-K and B1-Ca. The percentage plaque reduction of NDV with bentonite B3 and its homo-ionized bentonites as a function of bentonite concentration were presented in Figure 7.5(b). Percentage plaque reduction for bentonite B3 and its homo-ionized forms was found to increase with increased concentration of bentonite. At higher bentonite concentrations, the number of available sites for NDV adsorption is significantly high. The percentage plaque reduction was found to be more than 90% for bentonite dose > 10 mg/mL for B3 and its homo-ionized forms.

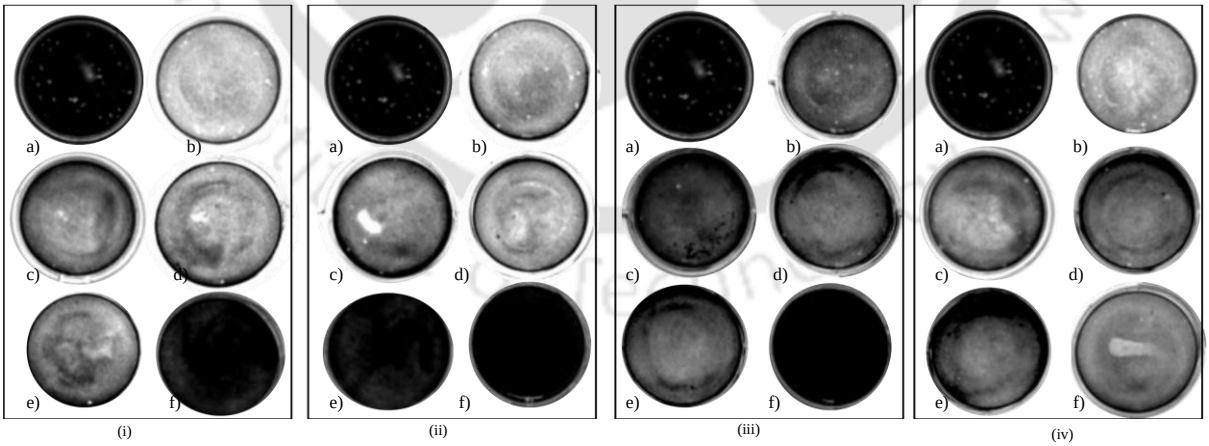

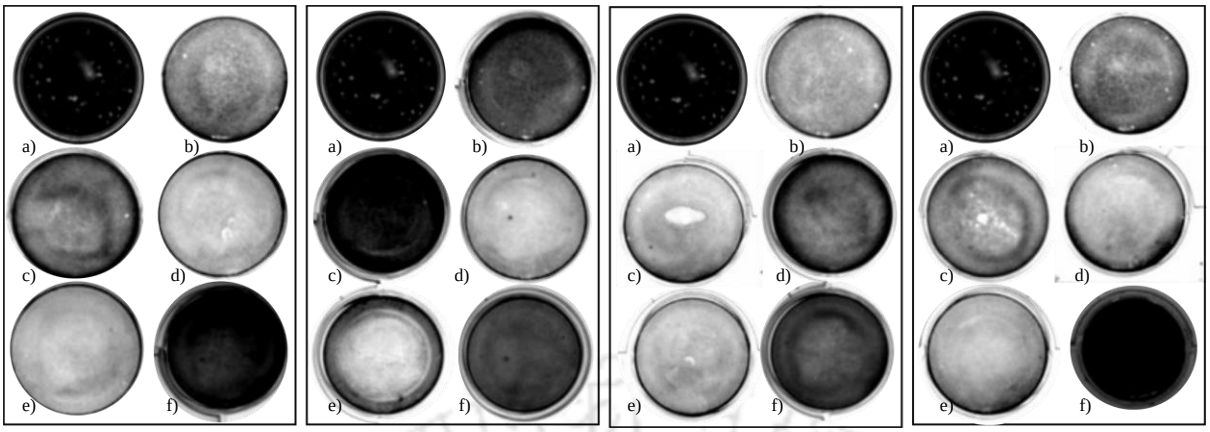

Figure 7.4: NDV equilibrium batch sorption upon interaction with (i)B1; (ii)B1Ca; (iii)B1K; (iv)B1Na; (v)B3; (vi)B3Ca; (vii)B3K; and (viii) B3Na, at different concentration of bentonites (a) Neat virus; (b) 1mg/ mL; (c) 2mg/mL; (d) 5mg/mL; (e) 10 mg/mL; and (f) 20 mg/mL

The B3-Na, bentonite B3 homo-ionized showed minimum percentage plaque reduction as compared to natural B3, B3-K, and B3-Ca similar to the case of B1. The higher reduction in percentage plaque reduction with calcium as an exchangeable cation is due to the divalent nature of the cation. Since the surface potential/zeta potential of the NDV is negative, it does not directly bind to the clay surface. NDV binds to the cations, which further get attached to the negatively charged clay surface and cations act as a bridge between the clay and virus particles. Since, the sorption of NDV showed a dependency on the type of cations, which favors that the virus is not directly attached to the negatively charged clay particle. The higher sorption of NDV to the divalent cation as compared to the monovalent cation, further reinforces the dominance of cation bridging. The sorption behavior of both bentonites (B1 and B3) and their homo-ionic forms favors the cation bridging as the dominant mechanism for sorption of NDV sorption on bentonite clay. The higher reduction in percentage plaque of the bentonite B3 as compared to B1 is attributed to the quality of the bentonite. The bentonite B3 has a higher specific surface area as well as cation exchange capacity as compared to B1, which means a higher number of available sites for adsorption of NDV are available in B3.

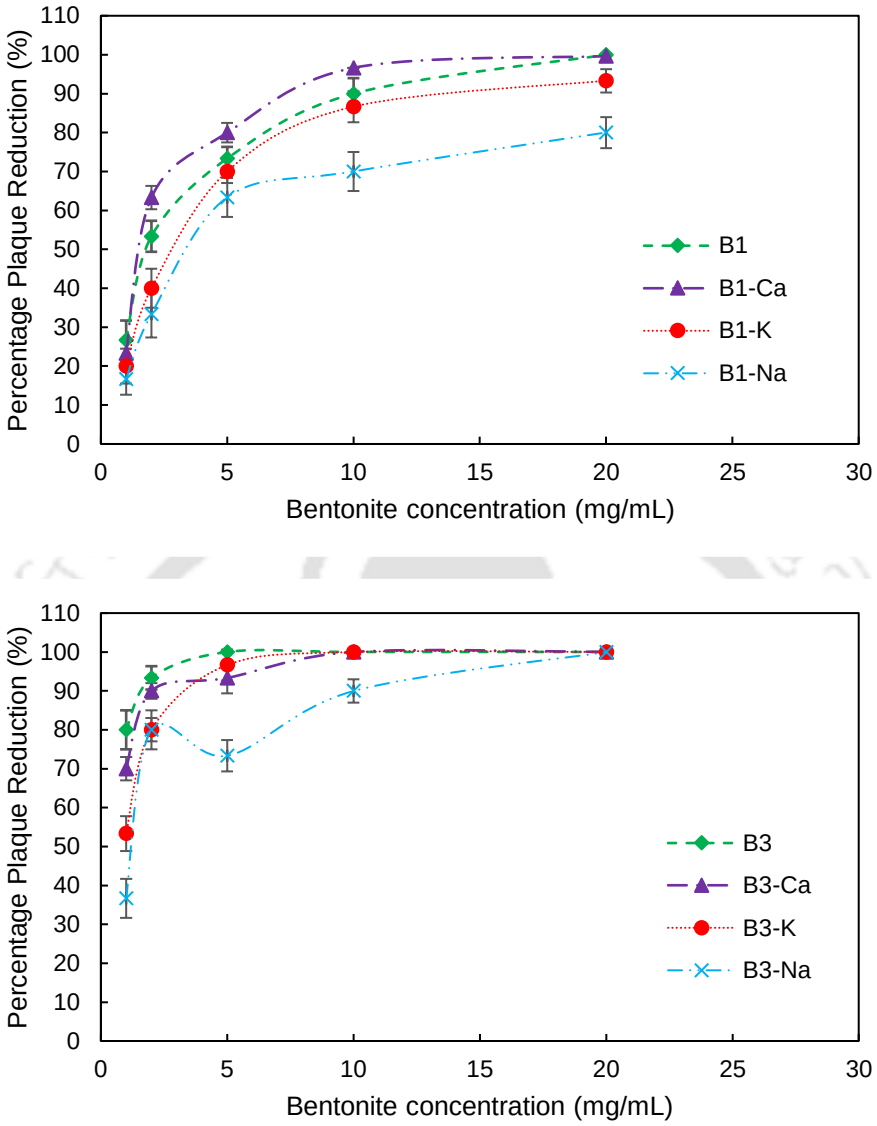

Figure 7.5: Percentage plaque reduction of NDV with different concentrations of (a) B1 and homo-ionized B1; (b) B3 and homo-ionized B3

The linear sorption isotherm model was fitted and plotted in Figure 7.6(a) with the experimental data for B1 and its homo-ionized forms. The regression coefficient of B1 and its homo-ionized forms were found to vary between 0.794 - 0.984, which is quite high. Further, the retardation coefficient of these bentonites based on the K_d obtained from the linear sorption model was evaluated. The value of R_d was found to vary between 419 and 1276. Higher values of retardation factor were found for natural B1 and B1-Ca as compared to B1-K and B1-Na.

Table 7.1: Linear, Langmuir, and Freundlich equilibrium sorption isotherm model parameters for 280000 PFU/mL concentration of NDV with different forms of B1

Sorption Isotherm Model	Parameter	B1	B1-Ca	B1-K	B1-Na
Linear	Regression Coefficient, R^2	0.984	0.964	0.926	0.794
	Retardation factor, R_d	822	1276	462	419
Langmuir	Regression Coefficient, R^2	0.905	0.949	0.932	0.436
	Sorption energy parameter, b	2.4×10^{-5} mL.PFU^{-1}	0.01 mL.PFU^{-1}	2.31×10^{-5} mL.PFU^{-1}	6.32×10^{-6} mL.PFU^{-1}
	Max. sorption capacity, q_{max}	1,00,000 PFU.mg^{-1}	50,000 PFU.mg^{-1}	50,000 PFU.mg^{-1}	50,000 PFU.mg^{-1}
	Separation factor, R_L	0.129	0.00039	0.134	0.36
Freundlich	Regression Coefficient, R^2	0.876	0.846	0.757	0.670
	Freundlich isotherm coefficient, K_f	144.5 PFU^{1-n}.mL^n.mg^{-1}	1964 PFU^{1-n}.mL^n.mg^{-1}	744 PFU^{1-n}.mL^n.mg^{-1}	4.5 PFU^{1-n}.mL^n.mg^{-1}
	Degree of linearity of the sorption, n	0.503	0.2877	0.335	0.733
	Retardation factor, R_d	598	550	380	335

The sorption data of NDV and bentonite B1 were also fitted to the Langmuir sorption isotherm model and presented in Figure 7.6(b). The regression coefficients were found to be higher than 0.9 for all studied B1 bentonites except B1-Na. The Langmuir isotherm coefficient, b was found to be in the range of 6.32×10^{-6} mL.PFU^{-1} to 0.01 mL.PFU^{-1} for different forms of B1 bentonite. The separation coefficient, R_L was found to be 2.4×10^{-5} to 0.13 for different forms of B1, but the value of the separation factor for Na-B1 was found to be 0.36, which is slightly higher. The values of the separation factor suggest close to the irreversible attachment of NDV to the clay. The Freundlich equilibrium sorption isotherm model for NDV with different forms of B1 was fitted

and shown in Figure 7.6(c). The values of retardation factors were found in a range of 335 – 598, the high values of the retardation factors indicated much higher sorption of NDV to different forms of B1. The detailed sorption parameters for isotherm models have been shown in Table 7.1.

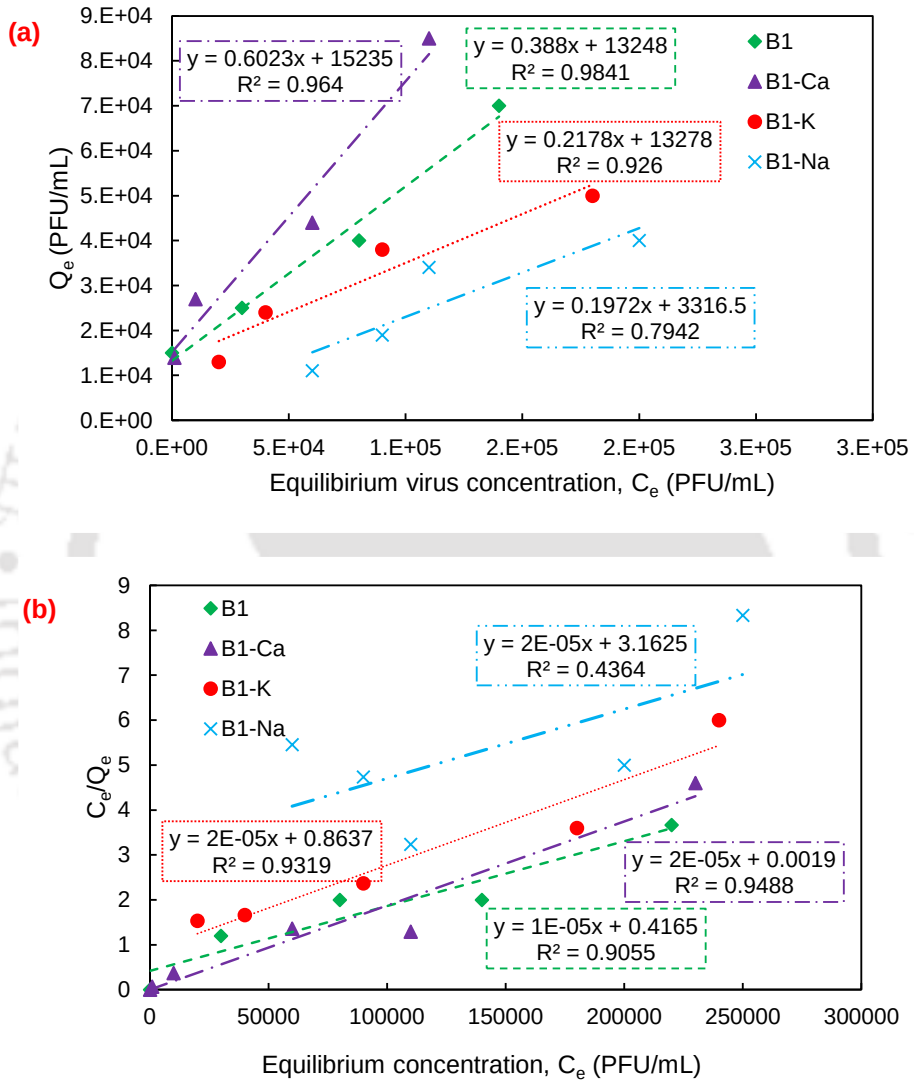

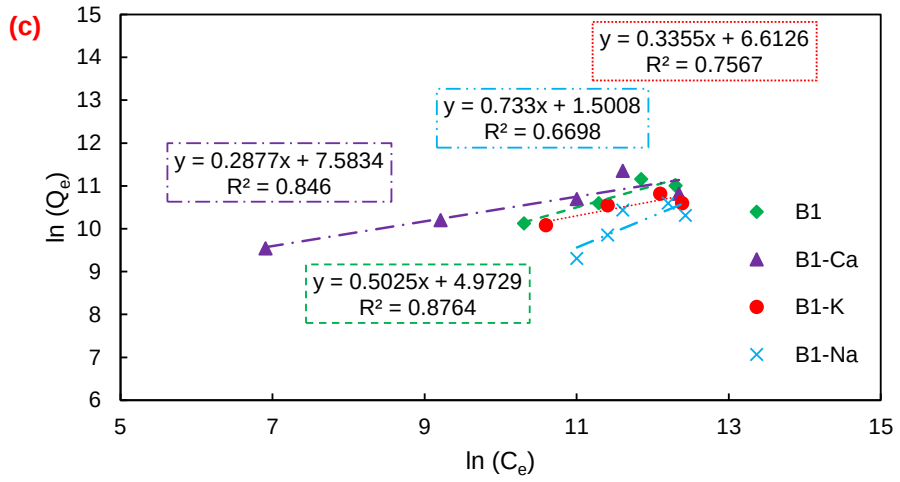

Figure 7.6: Fitting of sorption parameters for (a) the linear sorption isotherm; (b) Langmuir sorption isotherm model parameters; (c) Freundlich sorption isotherm model parameters for different forms of Bentonite B1.

The linear sorption isotherm model was fitted and plotted in Figure 7.7(b) with the experimental data for B3 and its homo-ionized forms. The regression coefficient of B3 and its homo-ionized forms were found to vary between 0.883 - 0.903, except for B3-Na, which has a poor fit with the 0.38 regression coefficient. Further, the retardation coefficient of these bentonites based on the K_d obtained from the linear sorption model was evaluated. The value of R_d was found to vary between 760 – 10283. Higher values of retardation factor were found for natural B3 and B3-Ca as compared to B3-K and B3-Na. The sorption data of NDV and bentonite B3 were also fitted to the Langmuir sorption isotherm model and presented in Figure 7.7(b). The regression coefficients were found to be higher than 0.9 for all studied B3 bentonites except B3-Na. The Langmuir isotherm coefficient, b was found to be in the range of 2.17×10^{-5} mL.PFU^{-1} to 4.5×10^{-4} mL.PFU^{-1} for different forms of B3 bentonites. The separation coefficient, R_L was found to be 0.0078 to 0.14 for different forms of B3. The values of the separation factor suggest close to the irreversible attachment of NDV to the bentonite B3 and its homo-ionized forms. Moreover, lower values of the separation factor suggest

better attachment of the virus with natural and calcium homo-ionized forms of B3. The Freundlich equilibrium sorption isotherm model for NDV with different forms of B3 was fitted and shown in Figure 7.7(c). The values of retardation factors were found in a range of 923 – 3726, the high values of the retardation factors indicated much higher sorption of NDV to different forms of B3. The detailed sorption parameters for isotherm models have been shown in Table 7.2.

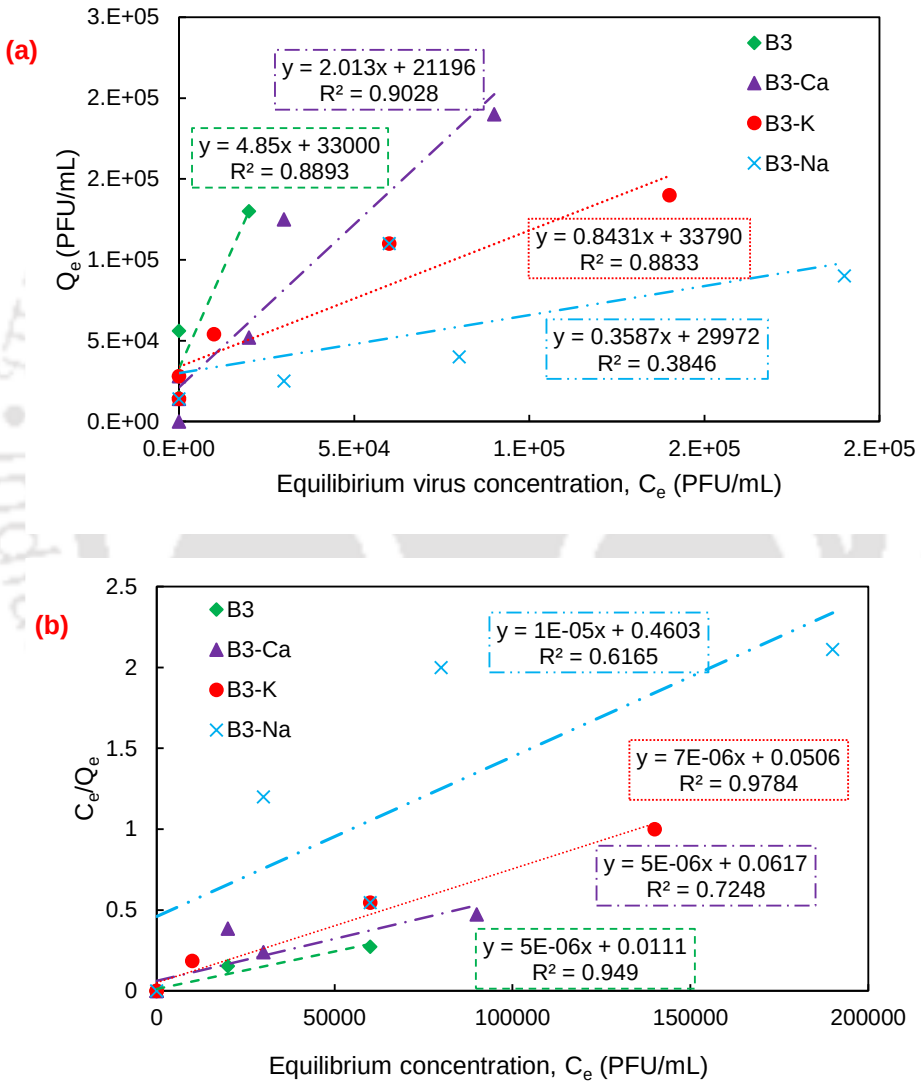

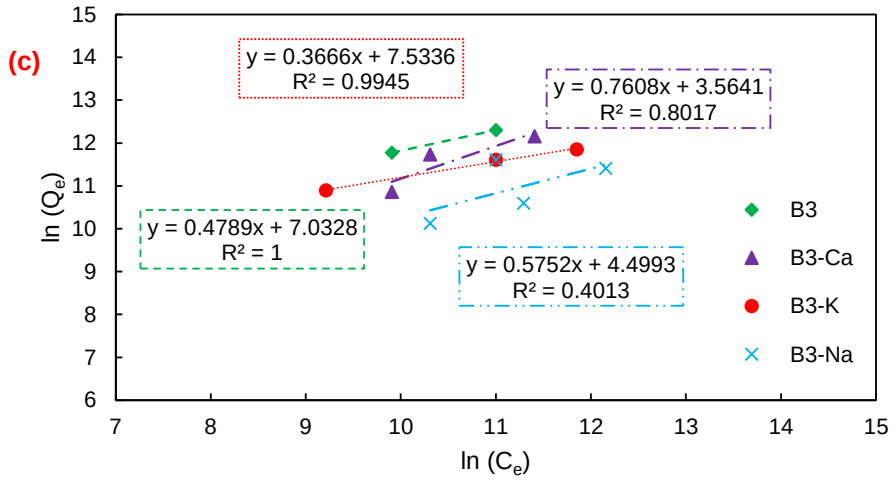

Figure 7.7: Fitting of sorption parameters for (a) the linear sorption isotherm; (b) Langmuir sorption isotherm model parameters; (c) Freundlich sorption isotherm model parameters for different forms of Bentonite B3.

Table 7.2: Linear, Langmuir, and Freundlich equilibrium sorption isotherm model parameters for 280000 PFU/mL concentration of NDV with different forms of B3

Sorption Isotherm Model	Parameter	B3	B3-Ca	B3-K	B3-Na
Linear	Regression Coefficient, R^2	0.889	0.903	0.883	0.385
	Retardation factor, R_d	10283	4269	1788	760.5
Langmuir	Regression Coefficient, R^2	0.949	0.725	0.978	0.616
	Sorption energy parameter, b	4.5×10^{-4} mL.PFU^{-1}	8.1×10^{-5} mL.PFU^{-1}	1.38×10^{-4} mL.PFU^{-1}	2.17×10^{-5} mL.PFU^{-1}
	Max. sorption capacity, q_{max}	2,00,000 PFU.mg^{-1}	2,00,000 PFU.mg^{-1}	142857 PFU.mg^{-1}	1,00,000 PFU.mg^{-1}
	Separation factor, R_L	0.0078	0.042	0.025	0.141
Freundlich	Regression Coefficient, R^2	-	0.802	0.995	0.401
	Freundlich isotherm coefficient, K_f	-	35.3 PFU^{1-n}.mL^n.mg^{-1}	1870 PFU^{1-n}.mL^n.mg^{-1}	90 PFU^{1-n}.mL^n.mg^{-1}
	Degree of linearity of the sorption, n	-	0.761	0.367	0.575
	Retardation factor, R_d	-	3726	1406	923

The bentonite sorption parameters clearly showed better binding of the NDV to the bentonite B3 as compared to B1 due to its high quality, higher specific surface area, and higher cation exchange capacity. Further, NDV showed a better binding to the calcium homo-ionized bentonite, followed by potassium, and then sodium homo-ionized bentonites for both B1 and B3. This can be interpreted from percentage plaque reduction at any concentration of specific concentration of bentonite, and higher retardation factors for calcium bentonite also give the same indication. Such behavior of these bentonites favors cation bridging as the dominant mechanism for sorption of NDV to the bentonite. Further, the results from the study showed that the presence of different types of cations plays a significant role, which means the virus particles are not directly attached to the clay surface. The divalent nature of the calcium ion attracts more virus particles as compared to mono-valent potassium as well as sodium ions. Potassium has a smaller hydrated radius as compared to the same charged hydrated radius of sodium ion. The higher surface charge density on the potassium ion leads to more adsorption of virus to potassium as compared to sodium.

7.3 Modification of DLVO Theory

According to the Gouy-Chapman theory, the electrostatic potential of the clay platelet in a diffused layer varies from surface potential, ϕ_0 at the clay surface to zero at an infinite distance. The electrostatic potential variation for clay is described by the non-linear Poisson-Boltzmann distribution as equation 7.1 (Bharat et al., 2013).

$$y = 2\ln\left(\frac{\exp(\kappa x)+\tanh(z)}{\exp(\kappa x)-\tanh(z)}\right) \qquad (7.1)$$

where y is the scaled potential (y = υe'ϕ/KT = υFϕ/RT) at a distance (x) from the clay surface; z is the scaled potential at the clay surface (z = υe'ϕ_0/KT = υFϕ_0/RT), κ is the inverse of Debye length and evaluated as:

$$\kappa = \sqrt{\frac{8\pi e' \nu^2 n}{\varepsilon KT}} \tag{7.2}$$

e' is the elementary charge (4.77×10^{-10} esu); υ is the valence of ions; n is the concentration of ions in pore-fluid; KT is the thermal energy ion; ε is the dielectric constant; F is the Faraday constant; ϕ is the electric potential at distance x; and ϕ_0 is the electric potential at clay surface.

The estimation of the electrostatic potential for a single clay platelet is simple. For a non-interacting system, the non-linear electrostatic distribution varies from ϕ_0 at the clay surface to zero potential at an infinite distance. The cations in the diffused layer are subjected to two opposite forces, firstly the electrostatic attraction between the negatively charged clay and cation and secondly the diffusion of cations due to concentration gradient. The electrostatic potential distribution presented in Eq. 7.1 requires the value of the surface potential, ϕ_0 at the clay surface. The surface potential of clay is dependent on clay properties like cation exchange capacity, $C_{EC,}$ specific surface area, $S_{A,}$ and pore-fluid chemistry. The expression for evaluation of the surface potential (mV) of clay platelet is given as (van Olphen, 1977):

$$\phi_0 = 0.1725\frac{T}{\nu}\sinh^{-1}\left(\frac{1256.81\times P'}{\sqrt{n\varepsilon T}}\right) \tag{7.3}$$

Where P' is the ratio of the C_{EC} (meq/100 g) to the S_A of clay. the scaled potential, z at the clay surface.

$$z = {\nu e'\phi_0}/{KT} = {\nu F\phi_0}/{RT} \tag{7.4}$$

The potential at a distance of x from the clay surface can be evaluated by substituting Eq. 7.4 in Eq. 7.1. The evaluated electrostatic surface potential from Eq. 7.1 was placed in Eq. 2.22 in place of ψ_s to obtain interaction energy due to the diffused layer and the final expression is as follow:

$$\phi_{dl}(x) = \pi \in_r \in_0 \left[2\psi_P y \ln\left(\frac{1+e^{-kx}}{1-e^{-kx}}\right) + \left(\psi_P^2 + y^2\right)\ln\left(1-e^{-2\kappa x}\right)\right] \qquad (7.5)$$

Total interaction energies are the summation of interaction energy due to van der Waal, diffused layer, and Born's repletion. The expression of interaction energy due to van der Waal and Born's repulsion is the same as given in Eq. 2.21 and Eq. 2.24.

7.3.1 Comparison of Interaction Energy from DLVO Theory and Modified DLVO Theory

The electrostatic potential for both bentonites (B1 and B3) for difference concentrations and cation valence were plotted using expressions mentioned in (Eq. 7.1-7.4) and presented in Figure 7.8. The present study evaluated and compared the variations of interaction energies based on the DLVO theory and proposed a modified DLVO theory. The study considered the clay-virus interaction a sphere-plate type of interaction. The modified DLVO theory incorporated the variation in the electrostatic potential in the diffused layer of clays based on the Gouy-Chapman theory. The interaction energy profiles have deep wells at very low separation distances and it is known as the primary minimum, ϕ_{min1}. The energy barrier for attachment and detachment is represented by the maximum energy level, $\phi_{max1,}$ and the shallow lower energy level at a higher distance represents the secondary minimum, ϕ_{min2}.

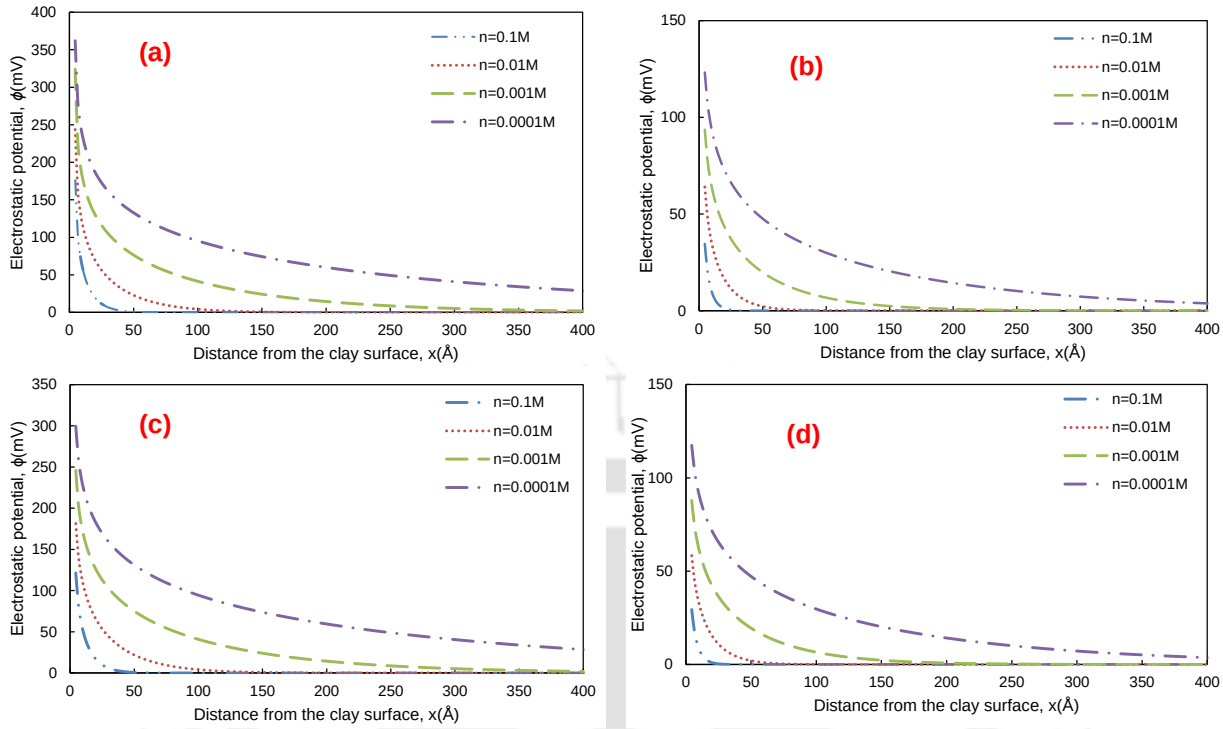

Figure 7.8: Electrostatic potential distribution in DDL from Boltzmann distribution for different concentrations of pore fluid for (a) B1 with monovalent cation; (b) B1 with divalent cation; (c) B3 with monovalent cation; and (d) B3 with divalent cation.

The interaction energy profiles based on DLVO theory and the proposed method were compared in Figure 7.9. The DLVO method utilized the values of the zeta potential as the electrostatic potential for clays, moreover, the values of surface potential were evaluated based on cation exchange capacity and specific surface area of clays for the proposed method. The interaction energy profiles for ϕX-174 bacteriophage interaction with bentonite based on DLVO and modified DLVO are presented in Fig. 7.9(a). Both the energy profiles showed similar patterns, the primary minimum energy level was found to be lower for the proposed method as compared to DLVO theory. The negative value of the energy level represents the attachments of this virus to the clay surface, which is not present in conventional DLVO theory. Hence, the proposed method explains actual behavior better than the DLVO theory. Further, the primary energy barrier was also found to increase in the case of the proposed method as compared to DLVO theory. The increase in the peak value is due to higher potential as compared to the zeta potential towards the clay surface.

Further, the rate of decrease in energy with an increase in separation distance is higher in the case of the proposed method, which is attributed to the decrease in electrostatic potential in the diffused layer. Similarly, the interaction energy profiles of MS2 bacteriophage and NDV were presented in Fig. 7.9(b) and 7.9(c). These viruses also showed similar variations in interaction energies. The values of several parameters utilized in the evaluation of interaction energies are listed in Table 7.3.

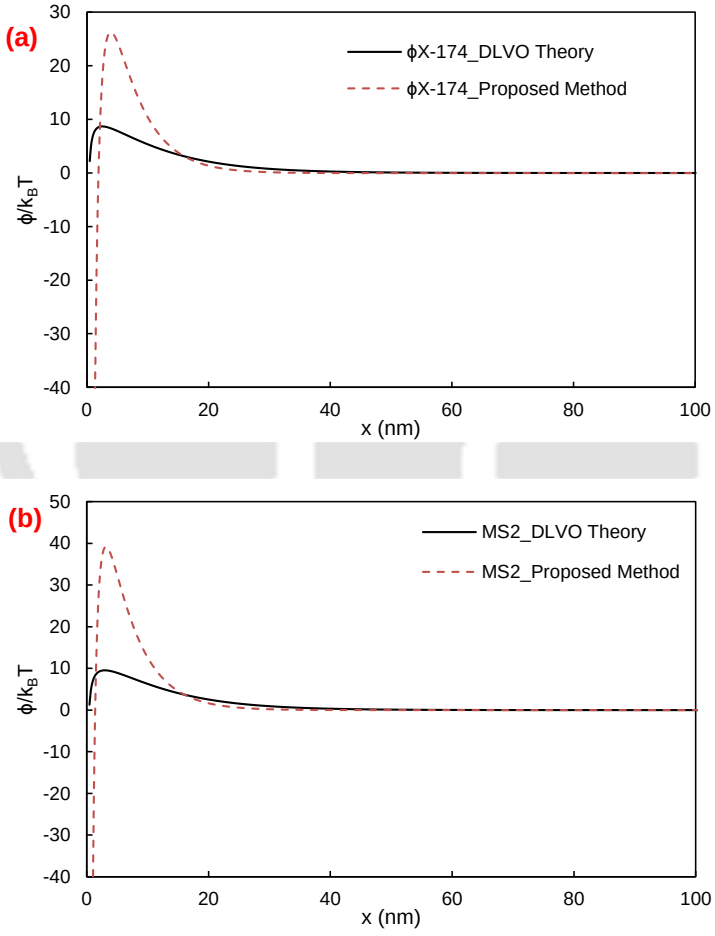

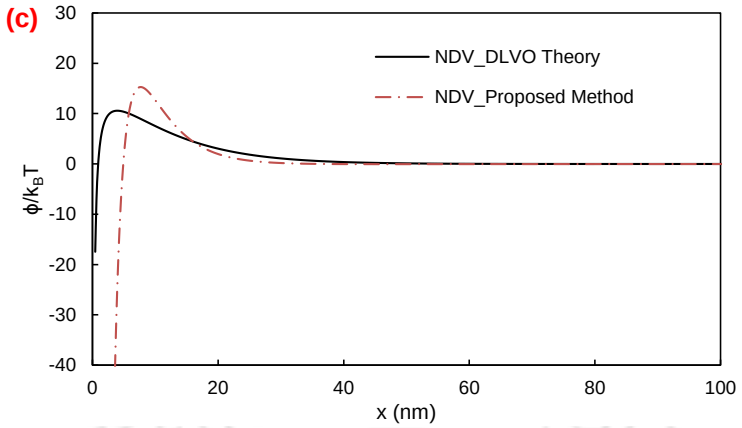

Figure 7.9: Comparision of interaction energy profiles from DLVO theory to the proposed method for montmorillonite with (a) ϕX-174 bacteriophage; (b) MS2 bacteriophage; and (c) Newcastle disease virus (NDV), a coronavirus surrogate.

Table 7.3: Parameter values considered for theoretical evaluations of interaction energies

Parameter	Values	References
Hamaker constant, A_{123}	7.5×10^{-21} J	Murray et al., 1978
The radius of the virus, r_p	MS2: 12.5 nm ϕX-174: 13 nm NDV: 50 nm	Chrysikopoulos and Syngouna, 2012 This study
Characteristics wavelength, λ	10^{-7}m	Gregory, 1981
$\epsilon_r = \epsilon/\epsilon_0$ is the relative dielectric constant of liquid	78.4	Chrysikopoulos and Syngouna, 2012
Ionic strength, n	0.001 M	This study
Zeta potential, ζ	Bentonite: - 0.021 V MS2: -0.040 V ϕX-174: -0.032 V NDV: -0.012 V	Chrysikopoulos and Syngouna, 2012 Neog et al. 2023
Avogadro's number, N_A	6.022×10^{-23} 1/mol	Das et al., 2022
Elementary charge, e	1.6×10^{-19} C	Das et al., 2022
Temperature, T	298 K	This study
Boltzmann's constant, k_B	1.38×10^{-23} J/K	Das et al., 2022
The permittivity of free space, ϵ_0	8.854×10^{-12} $C^2/(J\cdot m)$	Das et al., 2022
Born collision parameter, σ_{Born}	5 Å	Chrysikopoulos and Syngouna, 2012

7.3.2 Role of Valence, Clay Type, and Virus Type on the Interaction Energy Profiles

To understand the role of the valence of the exchangeable cations, the interaction profiles of NDV-bentonite interactions were plotted for both valence 1 and 2. These profiles were presented in Figures 7.10(a) and 7.11(b) for B1 and B3 bentonite. The valence of the cation showed a significant influence on the interaction energy profiles. The interaction energy profile for valence 2 showed a lower energy barrier peak as compared to valence 1, which shows better attachment of the virus to the divalent bentonites. The better attachment of NDV to divalent cations is similar to the experimental findings. As the surface charge density of both bentonites did not change significantly, the interaction energy profiles didn't change significantly with the quality of bentonites. The interaction energy profiles for different bacteriophages (ϕX-174 and MS2) and NDV were compared for bentonite B1 in 0.001M concentration of pore-fluid and presented in Figure 7.10(c). The MS2 showed the highest energy barrier peak and NDV showed the minimum peak, which suggests a better attachment of the NDV to the bentonite as compared to other bacteriophages.

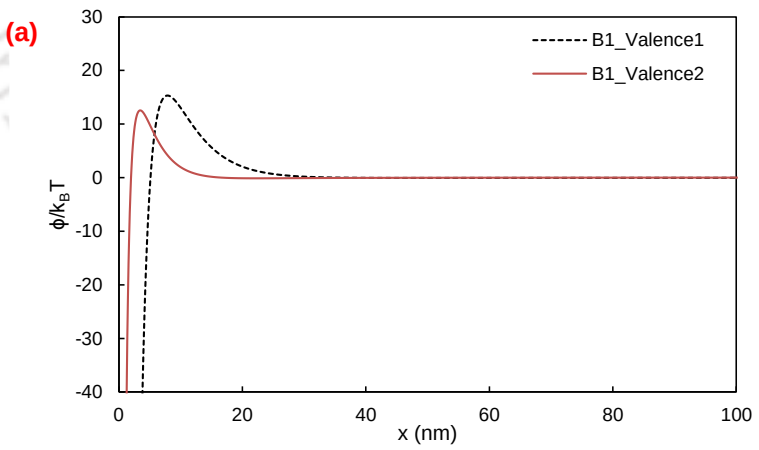

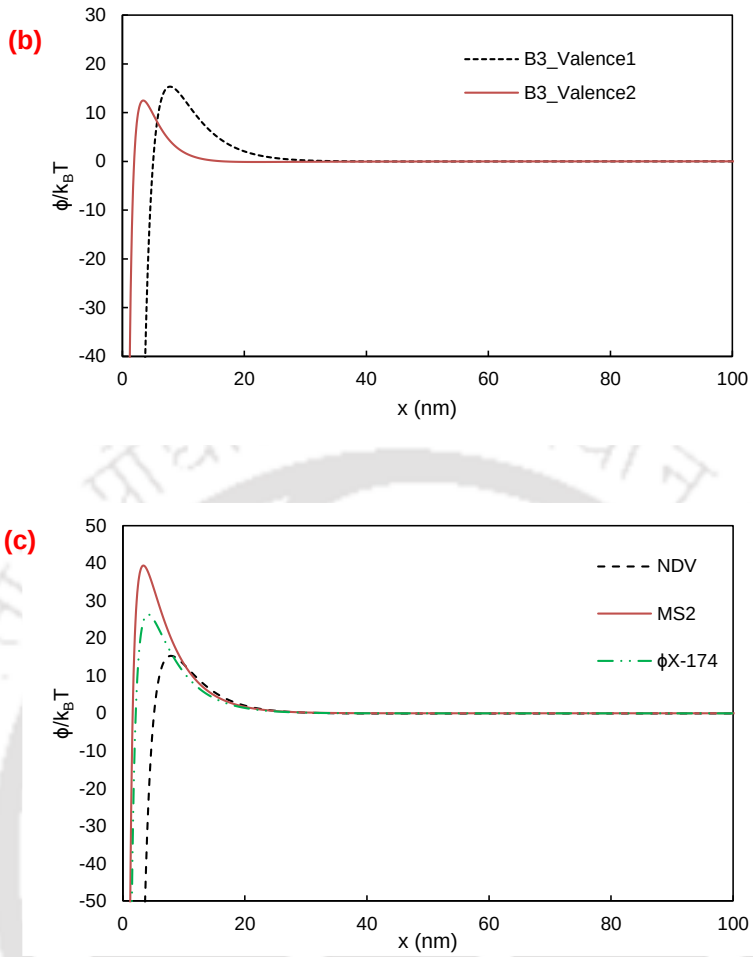

Figure 7.10: Interaction energy profiles from the proposed method for (a) B1 and (b) B3 bentonite for valence 1 and 2 with coronavirus surrogate and (c) comparison of interaction energy profiles of B1 with valence 1 for different viruses. (n=0.001M)

The value of the zeta potential of NDV was – 0.012 V for the studied strain (Neog et al., 2023), which means the studied strain of NDV is negatively charged at the studied pH. Bentonite clay particles are also negatively charged. So, electrostatic forces can not be responsible for the attachment between bentonite and NDV. The contact angle for bentonite surface as 36˚ confirms its hydrophilic nature (Roy and Mishra, 2023). So, hydrophobic interactions cannot be responsible for bentonite NDV interactions. The hydrogen bonding interactions are dominant in kaolinite clay minerals, where the IEP of clay minerals is lesser than the pH of the media. The clay minerals transfer proton from its basal surface to the outer protein of the virus, and these newly acquired

positively charged virus surface gets attached to the clay, but it is not common montmorillonite (Carlson et al., 1968; Schaub and Sagik, 1975; Das, 2021). Further, the pH of the studied bentonite was found to be around 8 and the isoelectric point (IEP) for NDV virus lies in the range of 4-6. For such scenarios, the cation briding is the main mechanism for clay virus interactions, which has also been derived based on experimental and theoretical results in this study.

7.4 Summary

The equilibrium batch sorption and sorption kinetics experiments were conducted with NDV on different quality bentonite in their natural as well as homo-ionized form and the following points were derived:

- The sorption of NDV on bentonite was found to be dependent on its quality. High-quality bentonite (B3) has better sorption ability as compared to B1.
- Sorption of NDV was also found to depend on the type of cation present as an exchangeable cation. The divalent cation (Ca) was found to have a better sorption ability of NDV as compared to potassium and sodium.
- Both Langmuir and Freundlich sorption isotherms fit well on the measured equilibrium sorption data of NDV with a good regression coefficient. The best fit with the Freundlich isotherm supported the multilayer sorption of virus particles on the clay surfaces. A Langmuir sorption separation factor, R_L close to zero for different bentonites, suggested a favorable and close to irreversible sorption of NDV with bentonites. High values of sorption parameters as well as retardation factors advocates the utilization of bentonites as a good adsorbent for viruses.
- The proposed theoretical method predicts the interaction energy profiles of the clay-virus interaction system. The negative values of the primary minimum energy level confirm the

attachment of bacteriophages and NDV to the bentonite, which was not possible to explain with conventional DLVO theory.

- The proposed method incorporates the role of valence in the evaluation of interaction energy profiles. Further, lower energy barrier peaks for divalent bentonite as compared to monovalent bentonite confirm the better attachment of the virus to the bentonite clay, which is also confirmed by the experimental sorption results.
- Cation bridging is the main mechanism behind the adsorption of NDV on bentonite.

भारतीय प्रौद्योगिकी संस्थान गुवाहाटी
Indian Institute of Technology Guwahati

Chapter – 8

Influence of Grain Size of Granular Bentonite on Sorption of Japanese Encephalitis and H1N1 Influenza Viruses

---

8.1 General

Chapter 7 discussed the role of surface cations of bentonites on the sorption behavior of Newcastle disease virus (NDV). The bentonite clay containing a high percentage of montmorillonite mineral showed an excellent sorption ability. The present work will discuss the role of different grain sizes of granular bentonite (GB) on the sorption ability of viruses. The granules of the GB assume different sizes depending on the batch and manufacturer as discussed previously in Chapter 4. The sizes of the GB might play a role in the sorption ability due to changes in the external surface area of the granules. The present work is divided into two parts. The first part presents the sorption ability of JEV with the GBs of different grain sizes in the presence of distilled water. The second part presents the sorption ability of the H1N1 influenza virus with GBs of different grain sizes in the presence of both distilled water and 0.5M KCl solution as pore-fluids. The study was carried out in the presence of high ionic strength KCl solution only with the H1N1 influenza virus due to the survival of virus strain under a high-ionic strength salt environment. Moreover, the studied JEV strain did not survive under a high-ionic strength salt environment. Thus, the sorption studies were carried out only in the distilled water environment.

8.2 Grain sizes of studied GBs

The GB was exhumed from the commercial GCL for the present study. The exhumed GB were separated with different sieves to obtain the GBs with different granulation sizes. The GB finer than 2 mm and 600 µm sieve size was termed GB-A. The portion between 600 – 300 µm was termed as GB-B, and the portion of GB smaller than 300 µm size was termed as GB-C. Further, GB was milled in the laboratory to obtain the finest GB (i.e., GB-D). The grain size of the studied GBs was obtained by the sieve analysis (IS 2720-4; 1985) and was presented in Figure 8.1.

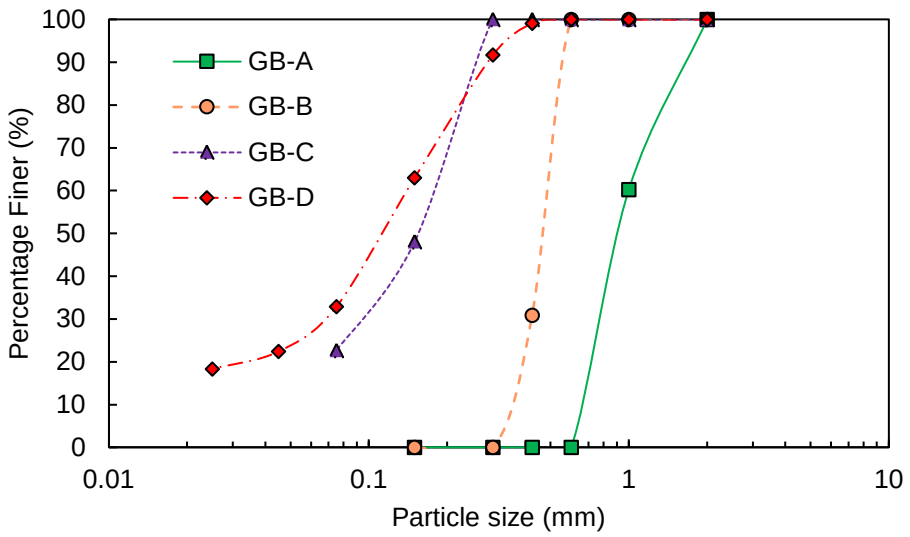

Figure 8.1: Grain size distribution curves of the studied GBs

8.3 Sorption of JEV with different GBs

The JEV consists of a positive sense, single-stranded, and RNA genome. The envelope protein of the JEV is capable of receptor binding. Moreover, the bentonite surface is negatively charged along with positively charged exchangeable surface cations, leading to the binding of JEV (Figure 7.2). Due to the presence of variations in the mean diameter of GB particles in GCLs, the understanding of the sorption characteristics of JEV with different GBs becomes important. In this section, batch

sorption experiments were conducted. The influence of contact time, GB quantity, and size of GB granules were studied.

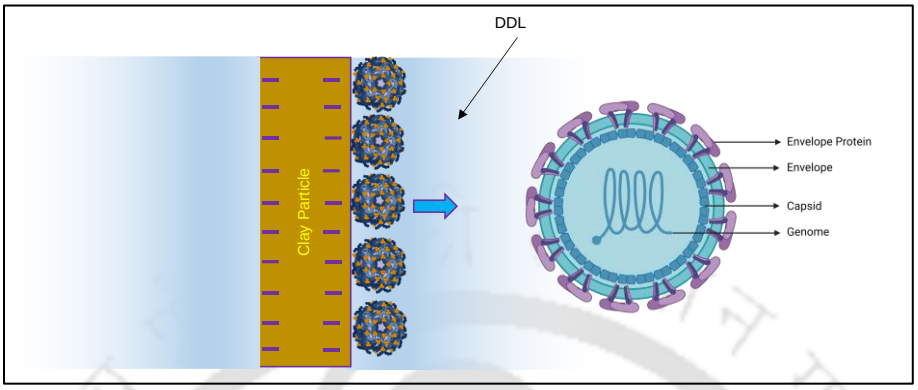

Figure 8.2: Illustration showing interactions of Japanese encephalitis virus to the bentonite clay surface

8.3.1 Sorption kinetics for JEV with different GBs

An initial concentration of 4,00,000 PFU.mL^{-1} of JEV strain was used for the sorption kinetics studies with different GBs while maintaining a GB concentration of 2 mg.mL^{-1}. The experiments were conducted for different interaction durations, 5 – 60 minutes. The plaque assay was used to evaluate the JEV concentration in the samples after the sorption experiment as shown in Figure 8.3.

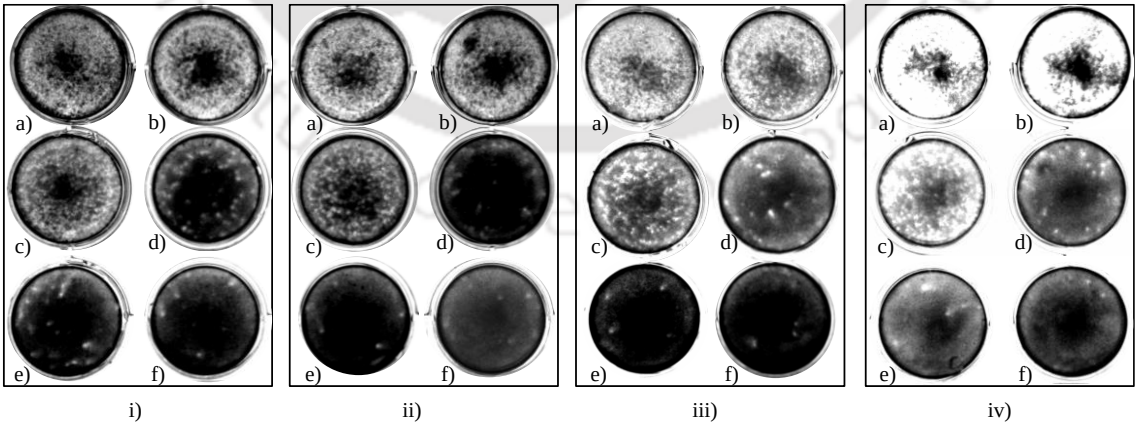

Figure 8.3: JEV sorption kinetics upon interaction with various granular bentonites at a concentration of 2µg/mL (i) GB-A; (ii) GB-B; iii) GB-C; iv) GB-D, at different time points- (a) neat virus; (b) 5 min; (c) 10 min; (d) 20 min; (e) 40 min; and (f) 60 min.

A JEV sample for the control experiment with the same concentration was placed to account for the biological decay of JEV. The JEV plaque percentage reduction with respect to the control experiment with different GBs was presented for different interaction periods in Figure 8.4.

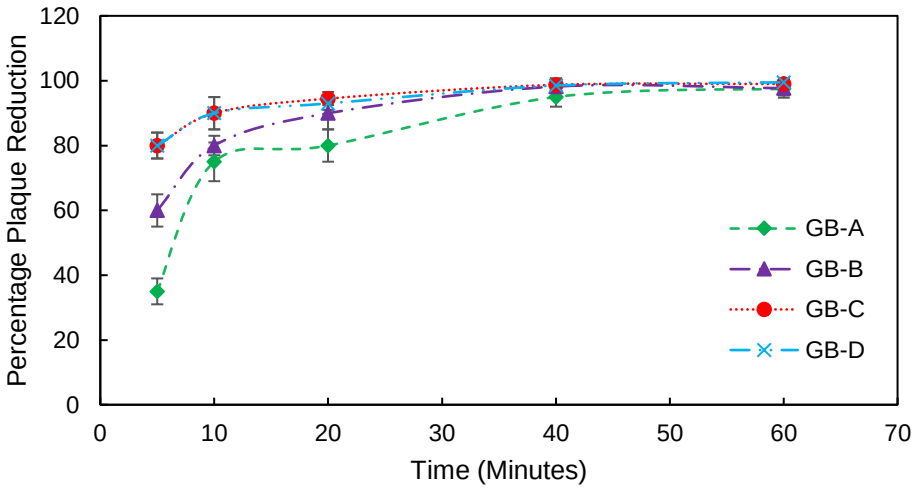

Figure 8.4: Plaque reduction of JEV with time for different GBs with clay concentration of 2 mg.mL^{-1}

The sorption rate was rapid for the finer GBs, whereas the rate slowed down for the coarser GBs. GB-A showed a percentage plaque reduction of 35%, while finer GB, i.e., GB-C and GB-D showed a percentage plaque reduction of 80% with a contact time of 5 minutes. This difference in the percentage plaque reduction is due to a greater number of available sites for the adsorption of the virus in the case of GB-C and GB-D. Finer GBs (GB-C and GB-D) achieved plaque reduction of over 90% within 10 minutes of interaction, while it took 40 minutes for coarser GB (GB-A) to achieve the percentage removal. Moreover, final plaque percentage reduction was found to be similar for both coarser and finer GB, which is due to the time required for the development of repulsive forces leading to the breaking of the granules of GB. The plaque percentage reduction was found to increase with the interaction time for all the studied GBs. A minimum time is required for the attachment of the virus pathogen to the clay surface. The estimated sorption kinetic data

were fitted with both pseudo-first order as well as pseudo-second order kinetic models as presented in Figure 8.5 (a) and 8.5(b), respectively.

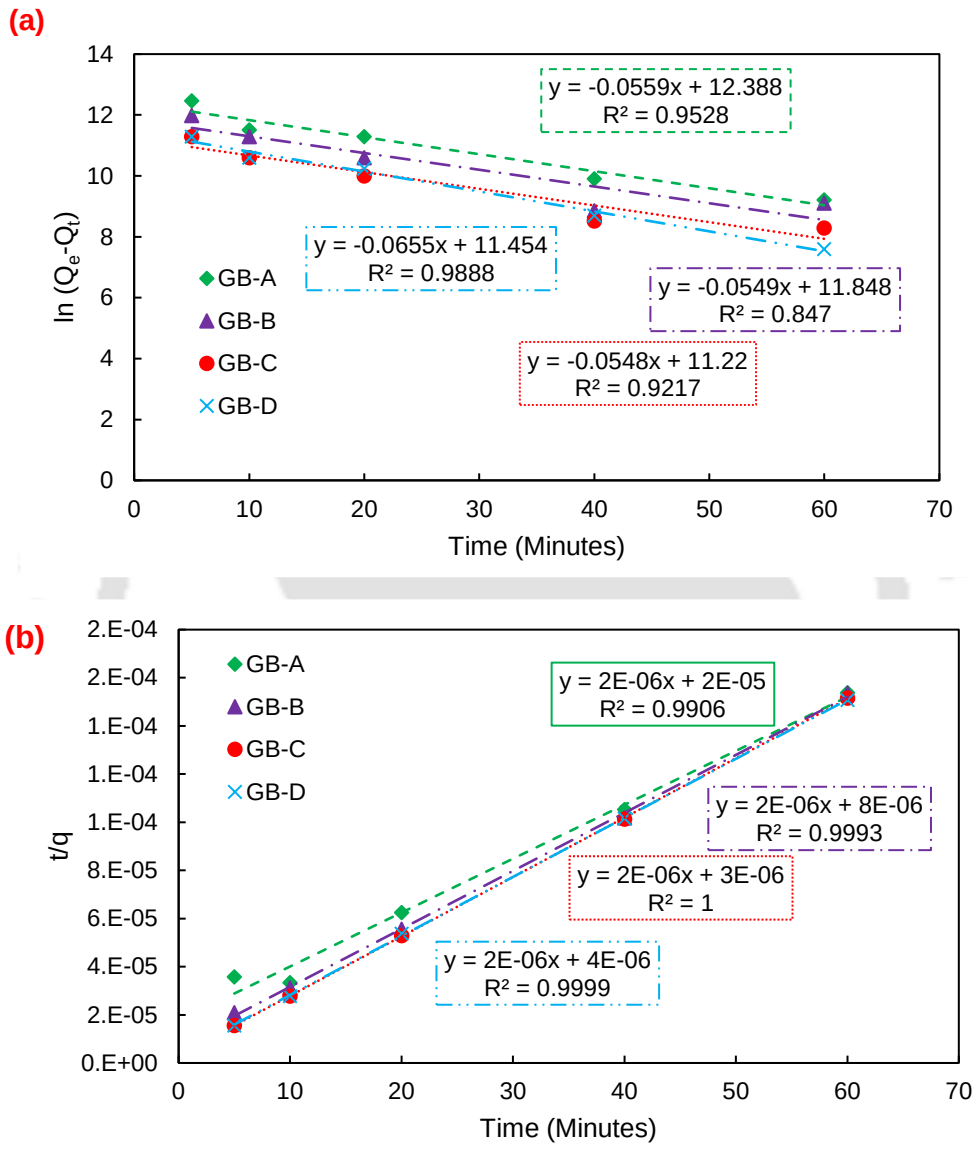

Figure 8.5: (a) pseudo-first-order kinetics; and (b) pseudo-second-order kinetics, for JEV sorption with GBs.

The sorption data showed a high value of the coefficient of regression (R^2) with both pseudo-first-order as well as pseudo-second-order kinetics. The adsorption rate constant k_1 was found to be 0.0559, 0.0549, 0.0548, and 0.0655 (min^{-1}) for GB-A to GB-D, respectively. Further, the

adsorption rate constant (k_2) for JEV with GB was found to vary between 1 – 6.67×10^{-7} ($mg.PFU^{-1}.min^{-1}$) for different GBs. The high value of k_2 for finer GBs represents rapid sorption of JEV with GB.

8.3.2 Equilibrium sorption for JEV with different GBs

Equilibrium sorption experiments of JEV with different GBs were performed and the concentration of the virus was measured using plaque assay as shown in Figure 8.6. The percentage plaque reduction of JEV with different GBs as a function of the amount of GB was presented in Figure 8.7. In this study, the interaction time of 1 hour was considered based on results from the kinetic study. Due to the presence of the charge of protein in JEV, the charged bentonite particles bind the JEV on its surface. The bounded JEV gets separated from the solution once the clay particles are removed upon centrifugation and does not contribute to the plaque assay. The observed percentage plaque reduction increased with the increase in the amount of GBs due increase in the number of available sites for the sorption of JEV. For 1 mg/mL bentonite concentration, the plaque percentage reduction in GB-A was found to be 13%, moreover, it was found to be 76% in the finest GB, i.e. GB-D. The increase in the percentage plaque reduction with an increase in the fineness (from GB-A to GB-D) is attributed to the availability of a greater number of sites for JEV. Although the quality of GBs is the same, except for the granule sizes, the variations in the percentage plaque reduction at lower concentrations indicate the partial breakdown of GB into individual particles due to the presence of salts in cell media utilized for the growth of JEV. The presence of salts in media can lead to the reduction in osmotic potential of GB and hence disintegration of the granules of GB. So, in the case of coarser GB the available number of sorption sites are lower than the finer GBs. With higher bentonite concentration (40 mg/mL), the percentage plaque reduction does not depend on the grain size of GB, which means

all the studied GBs showed more than 97 % plaque reduction. At higher bentonite concentrations, the number of available sites for JEV adsorption is significantly high. The percentage plaque reduction was found to be more than 90% for bentonite dose > 10 mg/mL.

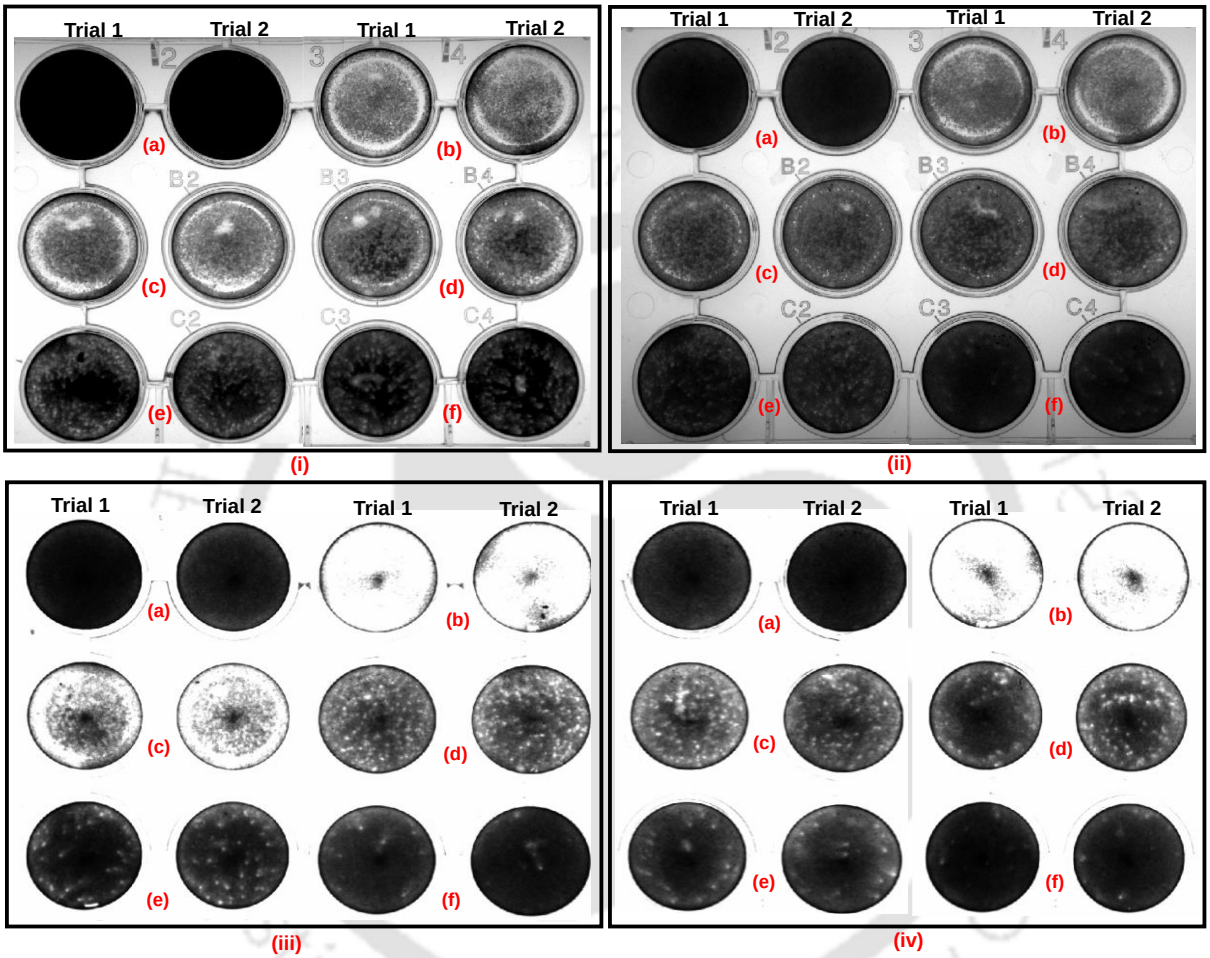

Figure 8.6: Plaque assay for JEV upon interaction with different granular bentonites (i) GB-A; (ii) GB-B; (iii) GB-C; and (iv) GB-D with different concentrations of GBs – (a) negative control; (b) positive control; (c) 1µg/mL; (d) 2µg/mL; (e) 5µg/mL; and (f) 10µg/mL after 1 hour of interaction time.

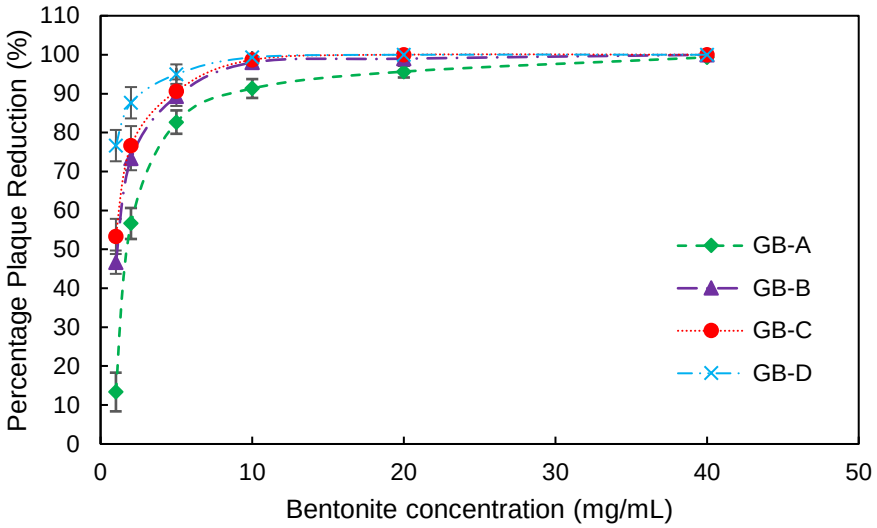

Figure 8.7: Percentage plaque reduction of JEV with different concentrations of GBs having different granule size

Linear sorption isotherm model was fitted with the experimental data for different GBs and plotted in Figure 8.8 (a). The regression coefficient of different GBs was found to be from 0.93 to 0.99. Further, the retardation coefficient of different GBs based on the K_d obtained from the linear sorption model. The value of R_d was found to increase (993-1229) with the decrease in the size of the granule.

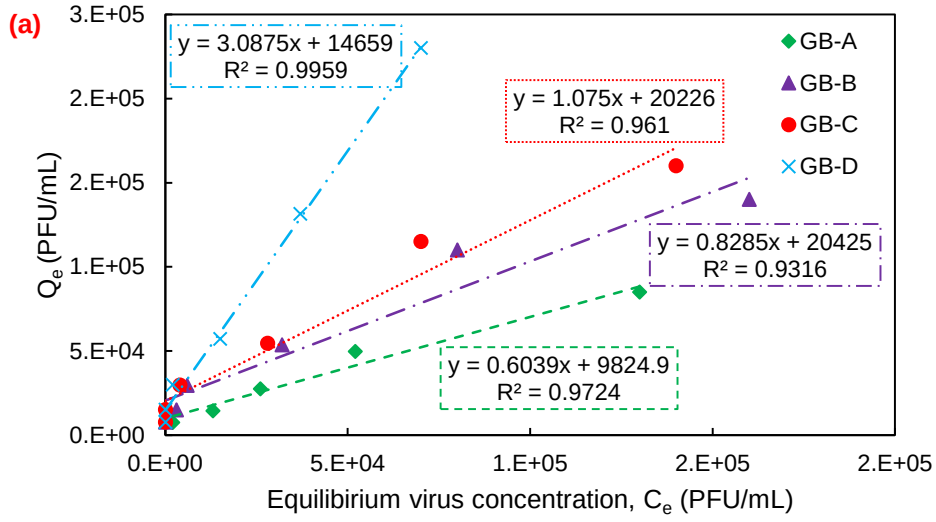

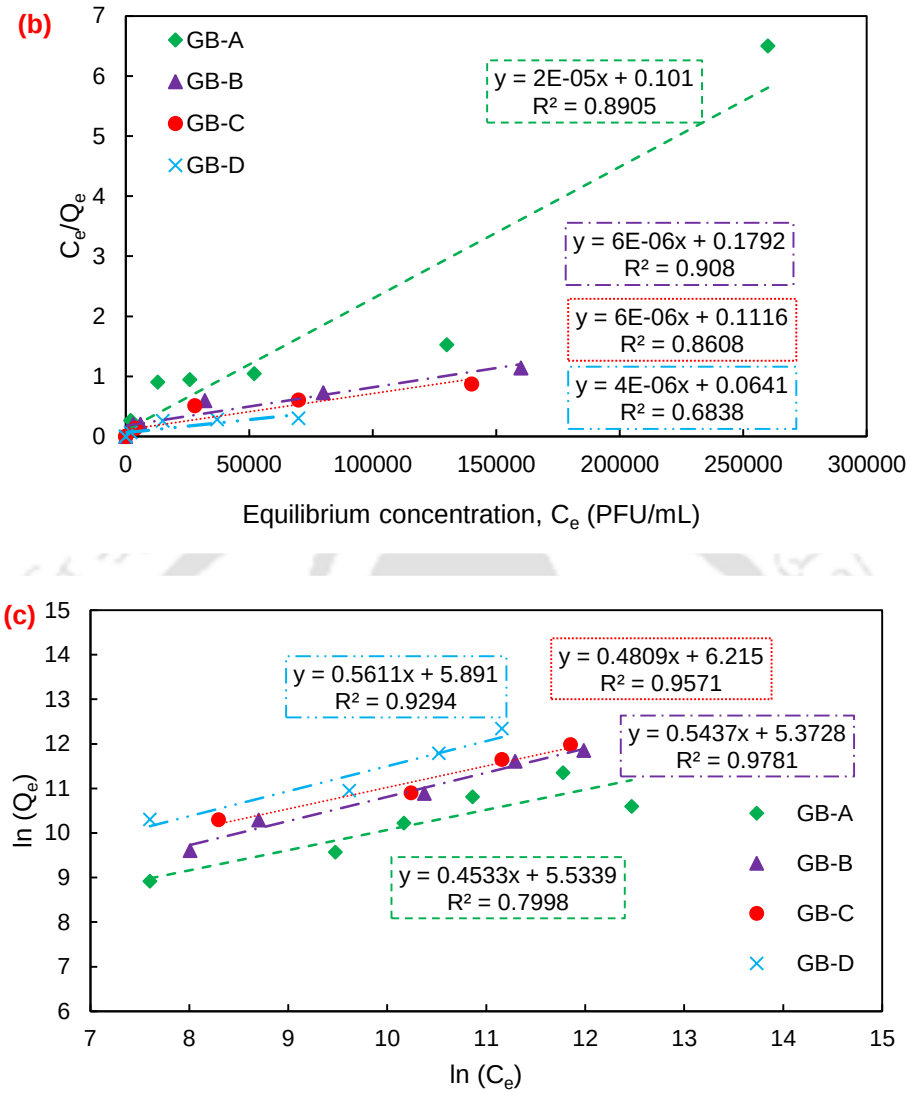

Figure 8.8: Fitting of sorption parameters for (a) the linear sorption isotherm for different GBs; (b) Langmuir sorption isotherm model parameters for different GBs; (c) Freundlich sorption isotherm model parameters for different GBs.

The sorption data of JEV-GBs were fitted to the Langmuir sorption isotherm model and presented in Figure 8.8(b). The Langmuir isotherm coefficient, b was found to be in the range of 1.98×10^{-4} mL.PFU^{-1} to 3.348×10^{-5} mL.PFU^{-1} for different GBs. The separation coefficient, R_L for different GBs was found to be 0.016 to 0.0905, which suggests close to the irreversible attachment of JEV to the clay. The Freundlich equilibrium sorption isotherm model for JEV with different GBs was fitted and shown in Figure 7.8(c). The value of the Freundlich isotherm model was found to vary

between 215.5 to 500.2 $PFU^{1-n}.mL^{n}.mg^{-1}$ for different GBs. The exponent which determines the degree of linearity of the sorption (n), was found to vary from 0.4533 – 0.5611 for different GBs. The values of the retardation factors from the Freundlich isotherm model were found to vary between 542 to 3014 for different GBs. The high values of the retardation factors indicated much higher sorption of JEV to the GBs. The detailed sorption parameters for isotherm models have been shown in Table 8.1.

Table 8.1: Linear, Langmuir, and Freundlich equilibrium sorption isotherm model parameters for 300000 PFU/mL concentration of JEV with different GBs

Sorption Isotherm Model	**Parameter**	**GB-A**	**GB-B**	**GB-C**	**GB-D**
Linear	Regression Coefficient, R^2	0.9724	0.9316	0.961	0.996
	Retardation factor, R_d	993	1191	1053	1229
Langmuir	Regression Coefficient, R^2	0.890	0.908	0.861	0.684
	Sorption energy parameter, b	1.98×10^{-4} $mL.PFU^{-1}$	3.348×10^{-5} $mL.PFU^{-1}$	5.376×10^{-5} $mL.PFU^{-1}$	6.24×10^{-5} $mL.PFU^{-1}$
	Max. sorption capacity, q_{max}	50,000 $PFU.mg^{-1}$	1,66,666 $PFU.mg^{-1}$	1,66,666 $PFU.mg^{-1}$	2,50,000 $PFU.mg^{-1}$
	Separation factor, R_L	0.0165	0.0905	0.05838	0.0507
Freundlich	Regression Coefficient, R^2	0.7998	0.9781	0.9571	0.9294
	Freundlich isotherm coefficient, K_f	253.13 $PFU^{1-n}.mL^{n}.mg^{-1}$	215.46 $PFU^{1-n}.mL^{n}.mg^{-1}$	500.2 $PFU^{1-n}.mL^{n}.mg^{-1}$	361.76 $PFU^{1-n}.mL^{n}.mg^{-1}$
	Degree of linearity of the sorption, n	0.4533	0.5437	0.4809	0.5611
	Retardation factor, R_d	542	1442	1516	3014

8.3.3 Microstructural analysis of JEV with GBs

The field emission scanning electron microscopy (FESEM) images of granular bentonite (GB) and virus-sorbed GB were taken and shown in Figure 8.9. The FESEM micrograph of JEV sorbed GB was slightly tricky due to the requirement of a dry sample. Ethanol, which is generally used for sample preparation could not be used here as it would destroy the bound virus particles. Drying at a higher temperature can also destroy the virus structure. So, the following procedure was followed for sample preparation for FESEM. Slurry samples were prepared by mixing the GB with distilled water to obtain FESEM micrographs. Similarly, the JEV stock was mixed with clay and diluted by adding distilled water. The prepared slurry sample of GB-JEV slurries was drop-casted on one side of the double-sided carbon tape. The drop-casted samples were kept overnight for drying at 38˚C in a controlled temperature oven. The samples were then coated with a thin conductive layer of gold. The FESEM micrographs of GB showed the presence of flaky clay particles in Figure 7.9(a). The FESEM micrographs of GB after JEV sorption were presented in Figure 7.9(b). The sorption of spherical virus particles in groups on the clay surface was visible in the micrographs. FESEM micrographs thus confirmed the sorption of JEV on clay surfaces.

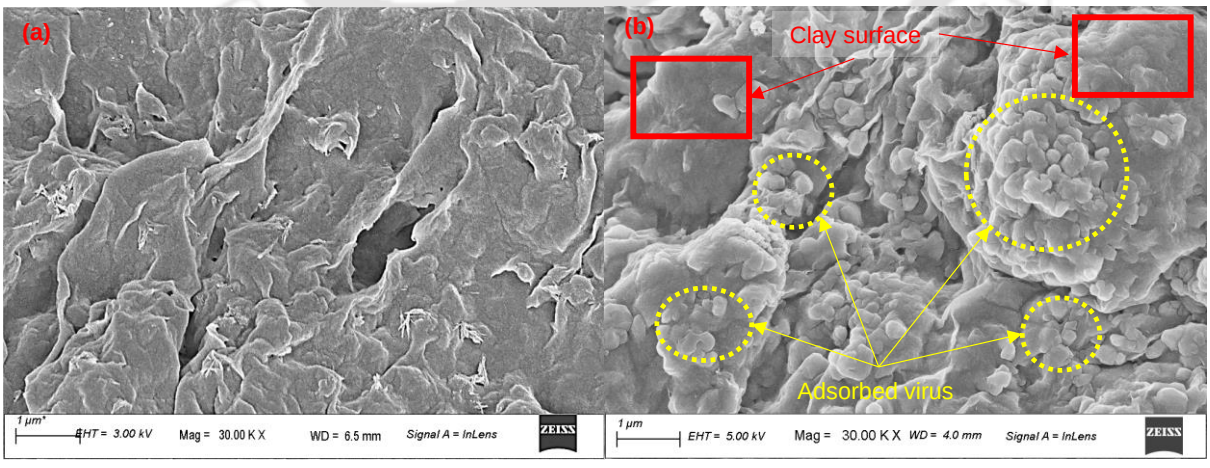

Figure 8.9: Surface morphology by FESEM micrograph for (a) granular bentonite; (b) granular bentonite after adsorption of JEV

8.4 Sorption of H1N1 influenza virus with different GBs

The influenza type A (H1N1 virus) contains hemagglutinin (HA) and neuraminidase (NA) as surface proteins as shown in Figure 8.10. Due to the presence of the charges in these proteins, they potentially get attached to the negatively charged bentonite particles. PR8 strain of the virus was used in the present study. Due to the variations in sizes of GBs available in GCLs, the understanding of sorption characteristics of the H1N1 influenza virus with different GBs is important. Moreover, the presence of the high-concentration salt solution might influence the binding ability of the H1N1 virus to the GB due to loss in the osmotic potential of GB. The loss in osmotic potential of GB may lead to intact GB granules, hence the availability of a smaller surface area for adsorption of the virus. Thus, the sorption studies of the H1N1 virus with GBs in the presence of salt solution also become important. This section presents the results of the sorption of the H1N1 influenza virus with GBs in high concentrations as well as distilled water environments. The influence of contact time, GB quantity, and size of GB granules were studied.

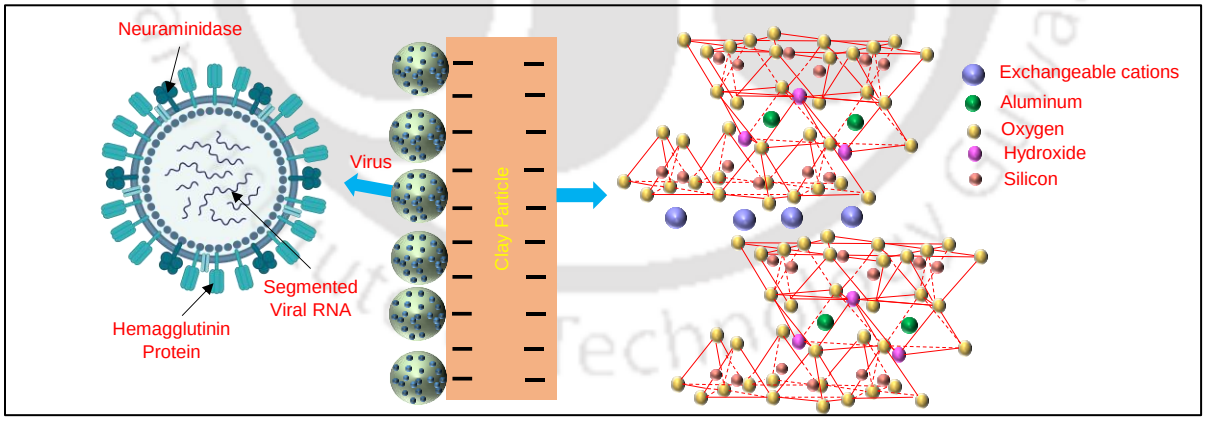

Figure 8.10: Illustration showing the interaction of the H1N1 influenza virus with montmorillonite clay mineral

8.4.1 Equilibrium sorption for H1N1 influenza virus with different GBs

The percentage reduction in the copy number of H1N1 virus with GBs with different sorbent concentrations was plotted in Figure 8.11 (a). Interaction time of 1 hour was considered during the

virus sorption on GBs. Due to the presence of the charges on GB particles, it binds the H1N1 virus on its surface. The virus is separated from the solution once GB particles are removed after centrifugation and does not contribute to the viral copies. The increase in the concentration of the GB contributes to the percentage reduction of viral copies due to an increase in the number of available sorption sites. A percentage reduction of 91% for GB-A and 99.99 % for GB-D was found with a 2 mg/mL bentonite concentration. The increase in percentage copy number reduction with the increase in fineness of GB is due to the number of available sites for attachment of virus on GB surface. Moreover, the percentage reduction also increases with the increase in the concentration of GB due to an increase in the number of available sites for H1N1 adsorption. The percentage reduction of viral copies was found to be higher than 99.9 % for GB concentrations higher than 5 mg/mL. The percentage reduction in copy numbers of the H1N1 virus with powdered bentonite (PB) with different concentrations of bentonite was plotted in Figure 8.11 (b). The incubation period for sorption of PR8 with PB was also kept at 1 hr. The increase in the concentration of the PB resulted in a reduction in the percentage of viral copies. A 2 mg/mL concentration of PB led to a percentage reduction of 57%, while 5 mg/mL of PB reduced the copies by more than 97%. The increase in the percentage reduction of viral copies with an increase in PB concentration is due to an increased greater number of available sites. The higher reduction in viral copies of GB as compared to PB is due to the larger specific surface area of GB as compared to PB.

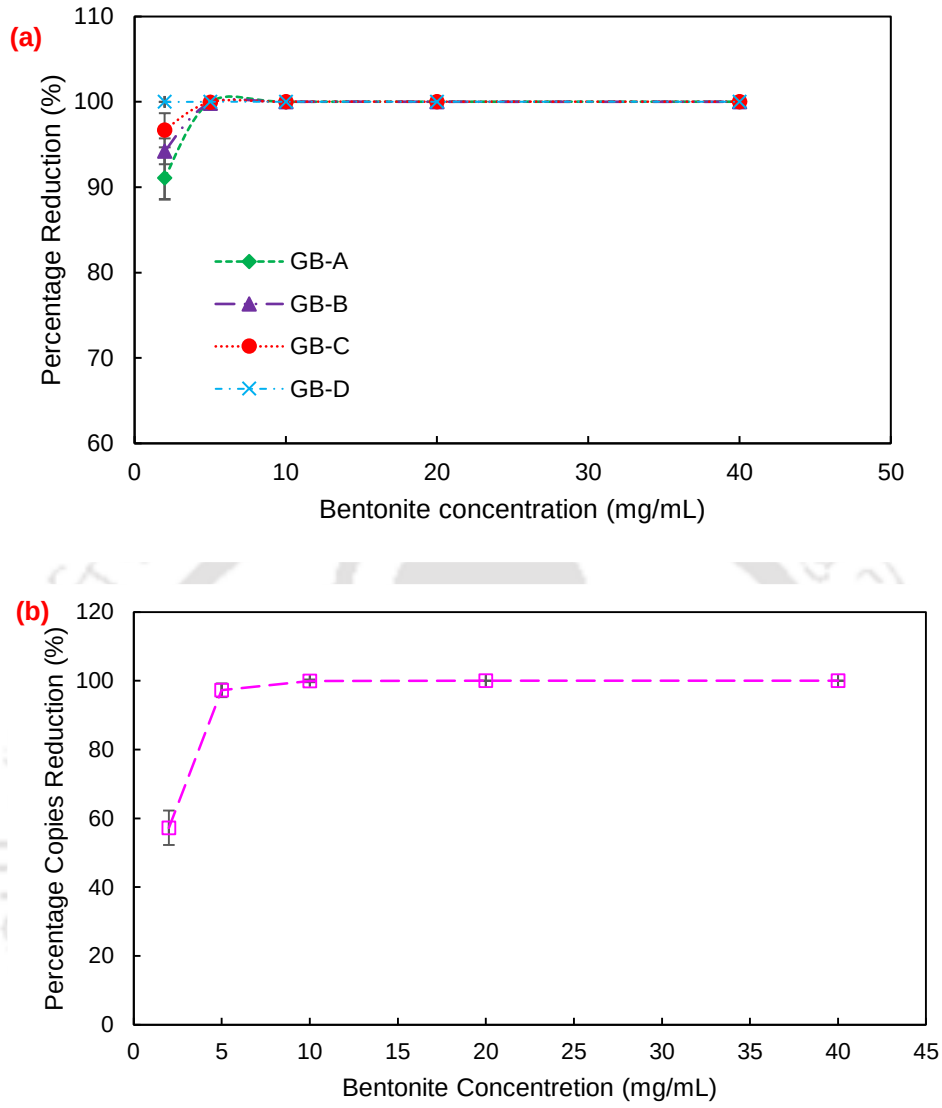

Figure 8.11: Percentage reduction in viral copies for PR8 strain of H1N1 (a) with variations in GB granule size (b) powdered bentonite for different concentrations of bentonites

The sorption data of H1N1-GBs were fitted to the Langmuir sorption isotherm model and presented in Figure 8.12. The data showed a good regression coefficient for different GBs, PB interaction with H1N1. The Langmuir isotherm coefficient, b was found to be in the range of 2.307×10^{-8} mL.copies^{-1} to 7.14×10^{-6} mL.copies^{-1} for different GBs and 2.6×10^{-8} mL.copies^{-1} for PB. The Freundlich equilibrium sorption isotherm model for H1N1 with different GBs was fitted and shown in the same figure. The value of the Freundlich isotherm model was found to vary

between 5.11× 10^6 copies^{1-n}.mL^n.mg^{-1} to 4.535× 10^8 copies^{1-n}.mL^n.mg^{-1} for different GBs and 1.237× 10^8 copies^{1-n}.mL^n.mg^{-1} for PB. The exponent which determines the degree of linearity of the sorption (n), was found to vary from 0.196 – 0.215 for different GBs and 0.148 for PB. The values of the retardation factors from the Freundlich isotherm model were found to vary between 237269 to 384420 for different GBs and 702 for PB. The high values of the retardation factors indicated much higher sorption of the H1N1 virus to the GBs. The detailed sorption parameters for isotherm models have been shown in Table 8.2.

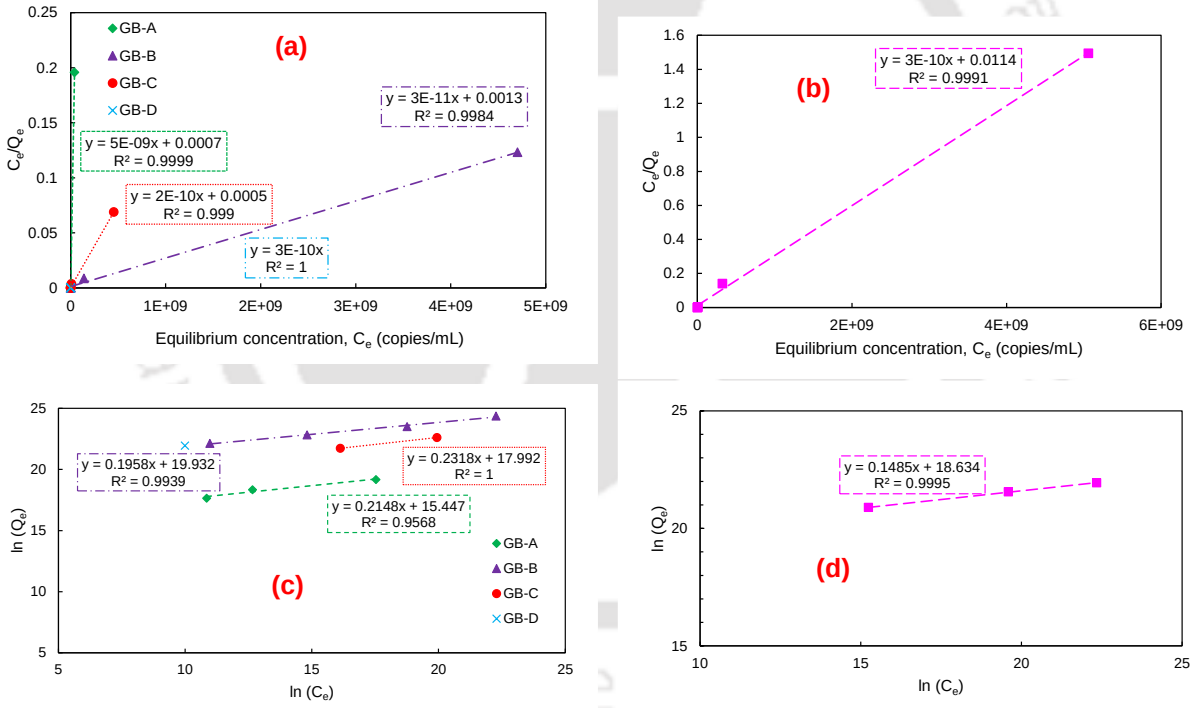

Figure 8.12: Fitting of the sorption parameter for (a) Langmuir sorption isotherm model for different GBs; (b) Langmuir sorption isotherm model for powdered bentonite; (c) Freundlich sorption isotherm model for different GBs; (d) Freundlich sorption isotherm model for powdered bentonite.

Table 8.2: Langmuir, and Freundlich equilibrium sorption isotherm model parameters for 4.55×10^8 copies/mL concentration of H1N1 with different GBs and PB

Sorption Isotherm Model	Parameter	GB-A	GB-B	GB-C	GB-D	PB
Langmuir	Regression Coefficient, R^2	0.999	0.998	0.999	-	0.999
	Sorption energy parameter, b	7.14×10^{-6} mL.copies^{-1}	2.307×10^{-8} mL.copies^{-1}	4×10^{-7} mL.copies^{-1}	-	2.6×10^{-8} mL.copies^{-1}
	Max. sorption capacity, q_{max}	2×10^8 copies.mg^{-1}	3.33×10^{10} copies.mg^{-1}	5×10^9 copies.mg^{-1}	-	3.3×10^9 copies.mg^{-1}
	Separation factor, R_L	0.23	0.34	0.27	-	
Freundlich	Regression Coefficient, R^2	0.957	0.934	-	-	0.999
	Freundlich isotherm coefficient, K_f	5.11×10^6 copies^{1-n}.mL^n.mg^{-1}	4.535×10^8 copies^{1-n}.mL^n.mg^{-1}	-	-	1.237×10^8 copies^{1-n}.mL^n.mg^{-1}
	degree of linearity of the sorption, n	0.2148	0.1958	-	-	0.1485
	Retardation factor, R_d	384420	237269	-	-	702

8.4.2 Equilibrium sorption for H1N1 influenza virus with different GBs in high-concentration salt environment

The percentage reduction in the copy number of the H1N1 virus with different GB concentrations in a 0.5M KCl environment was plotted in Figure 8.13. An interaction time of 1 hour was considered throughout the batch sorption experiments. Due to the presence of the charges on GB particles and the presence of surface cations, clay binds the H1N1 virus on its surface. The virus is separated from the solution once GB particles are removed after centrifugation and does not contribute to the viral copies. The increase in the concentration of the GB contributes to the percentage reduction of viral copies due to an increase in the number of available sorption sites. The percentage reduction of viral copies was found to be higher than 99.9 % for GB concentrations higher than 5mg/mL.

A reduction of 99% of viral copies was observed with 2 mg/mL of GB-A in the presence of a high concentration of KCl, which is higher than the percentage reduction in the same concentration of GB-A (2 mg/mL) without the presence of any salt. In the presence of high-concentration salts, the higher percentage plaque reduction indicates that the virus particles do not directly get attached to the bentonite surface. Moreover, the presence of the cations plays an important role in the attachment of the virus to the clay surface. The zeta potential of the PR8 strain of the H1N1 virus is negative, which also confirms that it cannot directly attach to a negatively charged clay surface. The virus gets attached to the clay surface with cation-bridging mechanisms. The higher removal of the virus in the presence of a high KCl environment also confirms the attachment of the virus to the cation which further gets attached to the negatively charged clay surface by electrostatic forces of attraction.

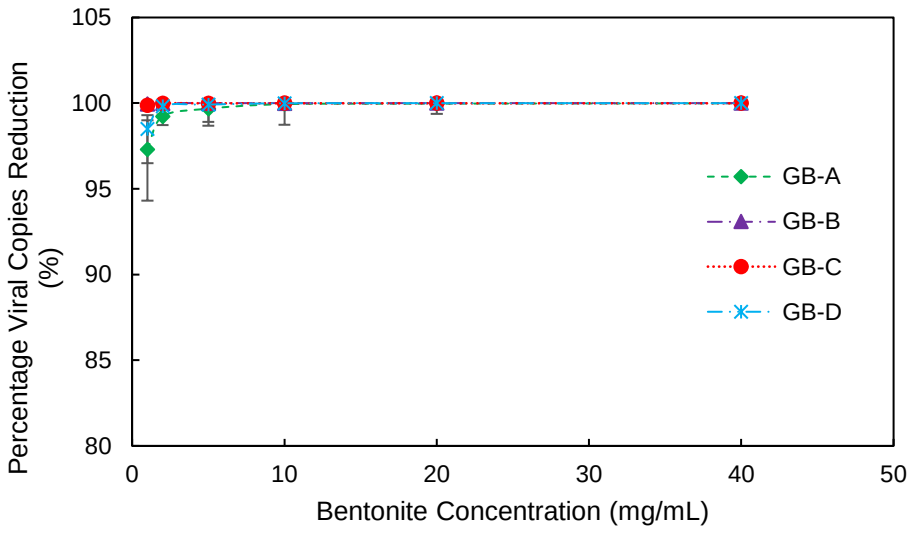

Figure 8.13: Percentage reduction in viral copies for PR8 strain of H1N1 with variations in GB granule size in 0.5M KCl environment

The sorption data of H1N1-GBs in 0.5M KCl environment were fitted to the Langmuir sorption isotherm model and presented in Figure 8.14 (a). The data showed a regression coefficient between 0.82 to 0.99 for different GBs with H1N1 in a high KCl environment. The Langmuir isotherm

coefficient, b was found to be in the range of 1.61×10^{-8} mL.copies^{-1} to 1.43×10^{-5} mL.copies^{-1} for different GBs. The maximum sorption capacity of the H1N1 virus was found to be 1×10^{10} copies.mg^{-1} for all GBs. The separation factor R_L, was found to vary in the range of 8.8×10^{-6} to 7.8×10^{-3}, which is close to zero and represents irreversible adsorption of the H1N1 virus to GBs in the presence of KCl. The Freundlich equilibrium sorption isotherm model for H1N1 with different GBs was fitted and shown in Figure 8.14(b). The value of the Freundlich isotherm model was found to vary between 1.34×10^5 copies^{1-n}.mL^n.mg^{-1} to 3.896×10^7 copies^{1-n}.mL^n.mg^{-1} for different GBs in the presence of KCl. The exponent which determines the degree of linearity of the sorption (n), was found to vary from 0.265 – 0.5662 for different GBs in the presence of 0.5M KCl. The values of the retardation factors from the Freundlich isotherm model were found to vary between 4383 to 117540 for different GBs. The high values of the retardation factors indicated much higher sorption of H1N1 virus in presence of KCl to the GBs. The detailed sorption parameters for isotherm models have been shown in Table 8.2.

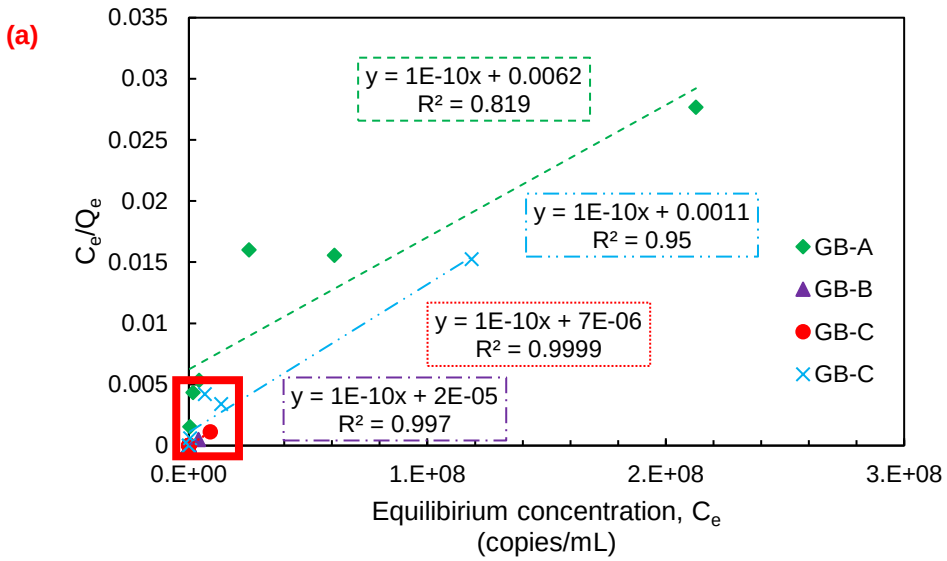

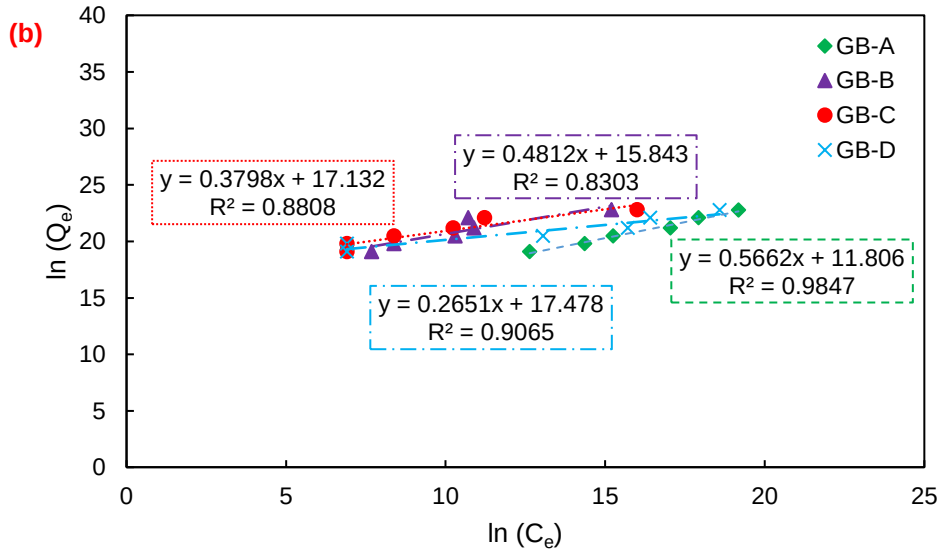

Figure 8.14: Fitting of the sorption parameter for (a) Langmuir sorption isotherm model for different GBs; (b) Freundlich sorption isotherm model for different GBs;

Table 8.3: Langmuir, and Freundlich equilibrium sorption isotherm model parameters for H1N1 with different GBs under high concentration KCl environment

Sorption Isotherm Model	Parameter	GB-A	GB-B	GB-C	GB-D
Langmuir	Regression Coefficient, R^2	0.819	0.997	0.999	0.950
	Sorption energy parameter, b	1.61×10^{-8} mL.copies^{-1}	5×10^{-6} mL.copies^{-1}	1.43×10^{-5} mL.copies^{-1}	9.091×10^{-8} mL.copies^{-1}
	Max. sorption capacity, q_{max}	1×10^{10} copies.mg^{-1}	1×10^{10} copies.mg^{-1}	1×10^{10} copies.mg^{-1}	1×10^{10} copies.mg^{-1}
	Separation factor, R_L	7.787×10^{-3}	2.53×10^{-5}	8.85×10^{-6}	1.39×10^{-3}
Freundlich	Regression Coefficient, R^2	0.9847	0.8303	0.8808	0.9065
	Freundlich isotherm coefficient, K_f	1.34×10^{5} copies^{1-n}.mL^n.mg^{-1}	7.59×10^{6} copies^{1-n}.mL^n.mg^{-1}	2.75×10^{7} copies^{1-n}.mL^n.mg^{-1}	3.896×10^{7} copies^{1-n}.mL^n.mg^{-1}
	degree of linearity of the sorption, n	0.5662	0.4812	0.3798	0.2651
	Retardation factor, R_d	14400	117540	42234	4383

8.4.3 Microstructural analysis

The field emission scanning electron microscopy (FESEM) images of GB, and H1N1 virus sorbed on GB were taken and shown in Figure 8.15. The same procedure as discussed in section 8.3.3 was followed for FESEM of virus-sorbed GB. The FESEM micrographs of GB showed the presence of flaky clay particles in Figure 8.15 (a). The FESEM micrographs of GB after H1N1 sorption were presented in Figure 8.15(b). The sorption of spherical virus particles in groups on the clay surface was visible in the micrographs. FESEM micrographs thus confirmed multi-layer group sorption of virus particles on clay surfaces.

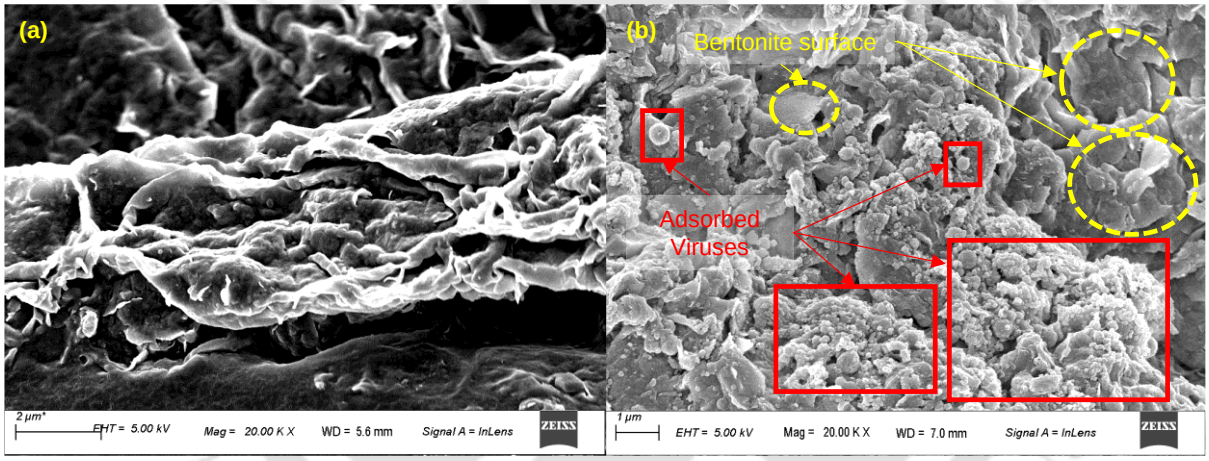

Figure 8.15: Surface morphology by FESEM micrograph for (a) granular bentonite; (b) granular bentonite after adsorption of H1N1 influenza virus

8.5 Summary

The equilibrium batch sorption and sorption kinetics experiments were conducted with JEV, PR8 strain of H1N1 virus with and without salt environment on GBs with different sizes and the following points were derived:

- ❑ The sorption ability of JEV as well as H1N1 virus depends on the size of the granules of the GB. The GB having the finest size showed more sorption ability as compared to

the GB with a large size. A removal efficiency of ~100% was found for the H1N1 influenza virus with studied GB having a specific surface area of 648 m^2/g and a concentration higher than 5 mg/mL.

- Based on the sorption kinetics data, the sorption of JEV was found to be quick on finer GBs (GB-C and GB-D) as compared to coarse GB (GB-A).
- Both Langmuir and Freundlich sorption isotherms fit well on the measured equilibrium sorption data of JEV and H1N1 with a good regression coefficient. The best fit with the Freundlich isotherm supported the multilayer sorption of virus particles on the clay surfaces. A Langmuir sorption separation factor, R_L = 0.0165-0.0905 for JEV with different GBs, $R_L = 8.8\times10^{-6}$ to 7.8×10^{-3} for H1N1 with GBs in the presence of KCl, and R_L =0.23 to 0.34 for GB in the absence of KCl, suggested a favorable and close to irreversible sorption of JEV on GB surfaces and H1N1 in presence of KCl. Moreover, the sorption of the H1N1 influenza virus in its absence was found to be relatively reversible. High values of sorption parameters, as well as retardation factors, advocates the utilization of GB-based GCLs for the containment of biomedical waste from an outbreak of JEV.
- The sorption ability of the H1N1 influenza virus with GB improves in the presence of KCl, even after a reduction in the osmotic potential of GB and poorly developed repulsive force in the presence of high concentration KCl environment. Due to the negative zeta potential of the PR8 strain of the H1N1 influenza virus, the presence of KCl can increase the sorption by providing more cations for cation-bridging. Moreover, the results confirm that cation bridging is the dominant mechanism for H1N1 influenza virus interactions with GB.

भारतीय प्रौद्योगिकी संस्थान गुवाहाटी
Indian Institute of Technology Guwahati

Chapter – 9

Hydraulic and Diffusion Characteristics of Different Viruses with Different Clays

---

9.1 General

Chapter 8 discussed the role of granule sizes of granular bentonite on the sorption of Japanese encephalitis virus and H1N1 influenza virus. The present work discusses the diffusion of coronavirus surrogate, NDV with bentonite and kaolin clay. Further, the present work also discusses the permeation of the H1N1 influenza virus through compacted GBs of different grain sizes and powdered bentonite B3 in salt environments. The virus pathogens have a decay rate with time, which has been considered during through-diffusion experiments and evaluation of diffusion parameters. Present work also indicated the inability of GB-based liners to resist viral pathogenic waste in the presence of a high salt environment. An engineered barrier system for viral pathogens was proposed in this work to limit the secondary infection of the disease.

9.2 Modification of Diffusion Theory for Viral Pathogens to Consider Biological Decay

The major pathogen transport mechanism in the case of compacted clay liners in waste disposal facilities is diffusion. The modified diffusion of virus contaminant involving decay across a 1-D saturated clay plug is governed by Fick's law as mentioned by

$$\frac{\partial c}{\partial t} = \frac{D_e}{R_d}\frac{\partial^2 c}{\partial x^2} - \frac{\lambda c}{R_d} \tag{9.1}$$

where, c is the concentration of the virus *(pfu/mL)*; t is the time (s); x is the distance (m) from the source; λ is the decay coefficient *(/sec)* indicates the half-life of the pathogenic contamination; D_e is the effective diffusion coefficient; R_d is the retardation factor, it is related to the relative movement of contaminants in compacted clay pore with reference to water and attachment of virus with clay surface, and is expressed by

$$R_d = 1 + \frac{\rho (K_d)_{TD}}{\eta} \tag{9.2}$$

where, $(K_d)_{TD}$ is the distribution factor; η is the porosity; ρ is the dry density of clay plug. The initial condition of the diffusion experiment, which represents that the clay sample is free from contamination before the start of the experiment was presented by

$$c(0 < x < L; t = 0) = 0 \tag{9.3}$$

where, L is the length of the clay sample. The boundary conditions at source and collector reservoirs were given in equations (9.4) and (9.5), respectively, for biological contaminants involving decay:

$$c(x = 0, t) = c_0 + \frac{nD_e}{H_s} \int_0^t \left(\frac{\partial c}{\partial t} \right)_{x=0} d\tau - \int_0^t \lambda c(\tau) d\tau \tag{9.4}$$

$$c(x = L, t) = -\frac{nD_e}{H_c} \int_0^t \left(\frac{\partial c}{\partial t} \right)_{x=0} d\tau - \int_0^t \lambda c(\tau) d\tau \tag{9.5}$$

where, c_0 is the initial virus concentration at t = 0; H_s and H_c are the equivalent heights of source and collector reservoirs, respectively. The equations 9.1 – 9.5 were solved numerically using the implicit finite-difference method to obtain theoretical concentration profiles with time. Equation 9.1 was discretized using the forward time central space (FTCS) scheme and represented by

$$c_i^n = c_i^{n+1}\left(1+2\alpha+\frac{\lambda\Delta t}{R_d}\right)-\alpha c_{i-1}^{n+1}-\alpha c_{i+1}^{n+1} \quad (9.6)$$

where, $\alpha = \frac{D_e \Delta t}{R_d \Delta x^2}$; Δt is the time step, and Δx is the mesh size = L/m, L is the length of the sample and m is the number of grid points. The inverse analysis was solved by minimizing the error between the theoretical and measured concentration data in the source and collector reservoir to obtain an effective diffusion coefficient and retardation factor simultaneously.

9.3 Diffusion of the NDV through Kaolin and Bentonite Clay

The pathogenic waste generated from any spread should be handled separately and placed in a separate biomedical waste (BMW) disposal facility. To design such a facility the virus transport parameters across barrier material are required to be estimated. The through-diffusion is a non-destructive technique and can be utilized to get both diffusion and retardation characteristics with the same experiment. The virus concentrations estimated from plaque assay of the source and collector reservoir were presented in terms of relative concentrations (c/c_0). The normalization of measured concentration in terms of plaque-forming units per unit volume (pfu/mL) was done with an initial concentration c_0 = 10000 pfu/mL for the bentonite sample. The initial concentration of 2500 pfu/mL concentration was used in the diffusion experiment with the kaolin sample. The variations of relative concentrations with time are shown in Figure 9.1. The concentration of NDV in the source reservoir decreased with time and the concentration of virus in the collector reservoir was found to be zero throughout the experiments with bentonite as well as kaolin. The test was completed quickly due to the biological decay of the NDV. To consider the influence of biological decay of the NDV, a separate experiment with a single reservoir with the same concentration of NDV was carried out, without any clay plug. The concentrations of the virus were also measured

at the same time to estimate the decay coefficient (λ). The obtained virus concentrations were fitted exponentially and the concentration of virus with time was obtained as

$$c = 10000e^{-0.179t} \tag{9.7}$$

where, t is the time in hours. To evaluate the value of the decay coefficient, the eq. (9.7) was differentiated. The rate of change in NDV concentration was presented as

$$\frac{\partial c}{\partial t} = (-0.179) \times 10000e^{-0.179t} \tag{9.8}$$

The rate of change of concentration of NDV was only due to its decay, which can be represented as

$$\frac{\partial c}{\partial t} = -\lambda c \tag{9.9}$$

After solving the equations (9.7-9.9), the value of the decay coefficient was evaluated. The value of decay coefficient, λ (/sec), for the studied strain of NDV corresponding to bentonite experiment was evaluated as 4.97×10^{-5}/sec. Similarly, the decay coefficient was also evaluated along with diffusion experiment with kaolin, and its value was evaluated as 1.16×10^{-6}/sec. The value of the diffusion coefficient for bentonite B3, and kaolin were 1.67×10^{-9} m^2/s and 3.91×10^{-10} m^2/sec, respectively. The retardation factor was also simultaneously evaluated from the diffusion experiment and was 3572 for bentonite and 2348 for kaolin. The value of the retardation factor from the diffusion experiment was in good agreement with the retardation factor from the batch sorption isotherms. The linear isotherm model showed a good fit with the experimental data. The value of the retardation factor from linear sorption was 5683 for bentonite and 4200-5300 for

kaolin. A slightly higher estimated value of R_d from linear batch sorption isotherm is due to the large number of available sorption sites in the slurry state of bentonite as well as kaolin for NDV.

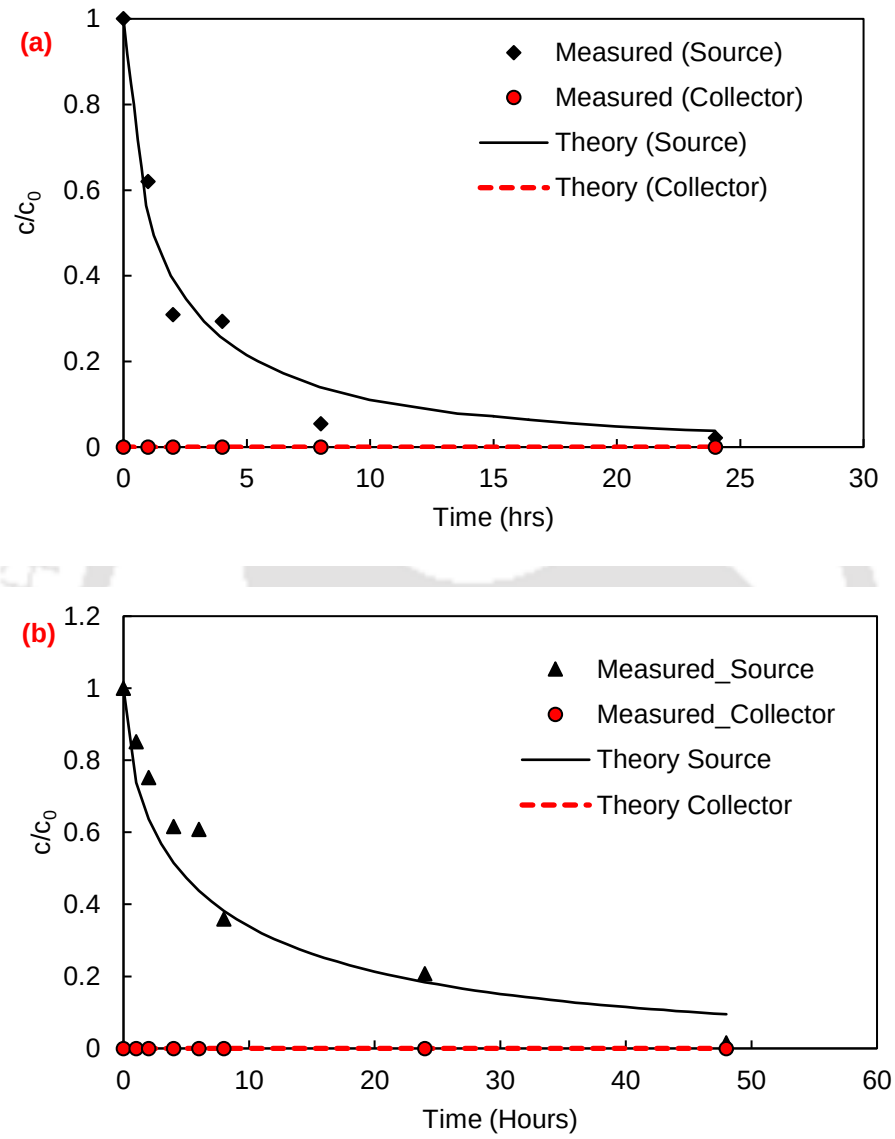

Figure 9.1: Measured concentration data along with theoretical concentration profile for NDV in compacted (a) bentonite clay (b) kaolin clay

The diffusion experiment results showed very low value of diffusion coefficient for both bentonite and kaolin. However, very high value of retardation factor supported the high sorption of virus. Thus, these two studied clays (bentonite and kaolin) were found to be useful in containment of pathogenic waste.

9.4 Hydraulic Permeation Rates of H1N1 Virus in High KCl Environment

The same GBs (GB-A to GB-D) of different grain sizes were used from chapter 8 for hydraulic permeation rates. Hydraulic permeation tests with the H1N1 virus were conducted to evaluate the performance of different GBs and powdered bentonite B3 with 0.5M KCl salt environment. The fluid permeation rates of different GBs and B3 with time were plotted in Figure 9.2. The fluid permeation rates were found to be 1-2 $\times 10^{-5}$ m/sec, 1 $\times 10^{-6}$ m/sec, 1-2 $\times 10^{-8}$ m/sec, 8×10^{-10} m/sec, and 8-9$\times 10^{-10}$ m/sec for GB-A, GB-B, GB-C, GB-D, and B3 respectively. The fluid permeation rates of GB-A, GB-B, and GB-C are significantly higher than the limiting value of fluid permeation (1×10^{-9} m/sec). The fluid permeation rate of the GB-D was found to be lower than the liming value. The high fluid permeation (GB-A – GB-C) in the presence of a high KCl environment is attributed to the insignificant development of the repulsive forces upon hydration. The repulsive forces developed during the hydration of the GB were not sufficient to overcome the van der Waal forces of attraction among the particles. The insignificant breaking of the GB granules was also confirmed by the FESEM analysis of the samples after the permeation experiment. The GB samples after the permeation with H1N1 virus and 0.5M KCl as pore-fluid were lyophilized and FESEM micrographs were captured to measure the size of the granules after permeation. Figure 9.3 shows the GB particle sizes after the permeation experiment and the size of the granules present was found to be 1.042 mm, 510 µm, 71.21 µm, and 10.5 µm for GB-A – GB-D, respectively. Mechanical processing of the GB leads to the breaking of GB granules into individual particles (GB-D). Fluid permeation through processed GB (GB-D) was found to be lower than the limiting values.

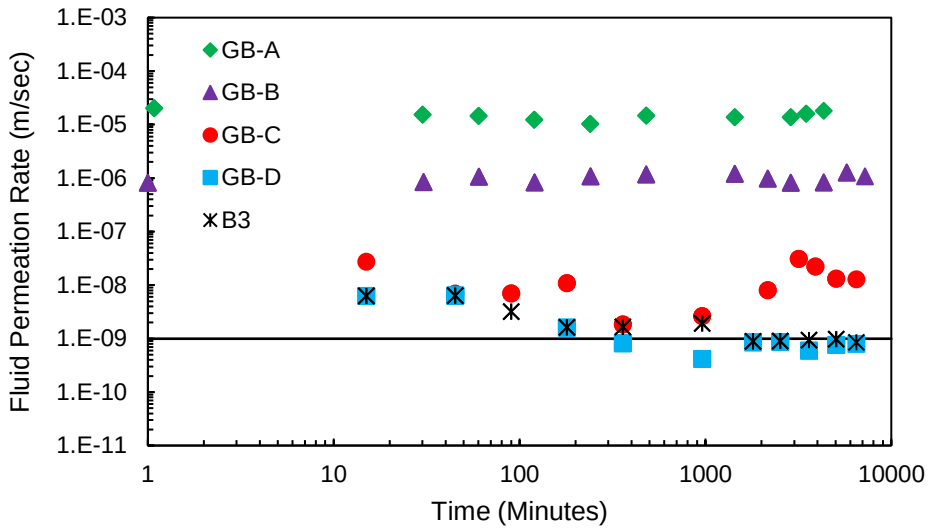

Figure 9.2: Fluid permeation rates of H1N1 virus along with 0.5M KCl salt solution through different GBs and Bentonite B3.

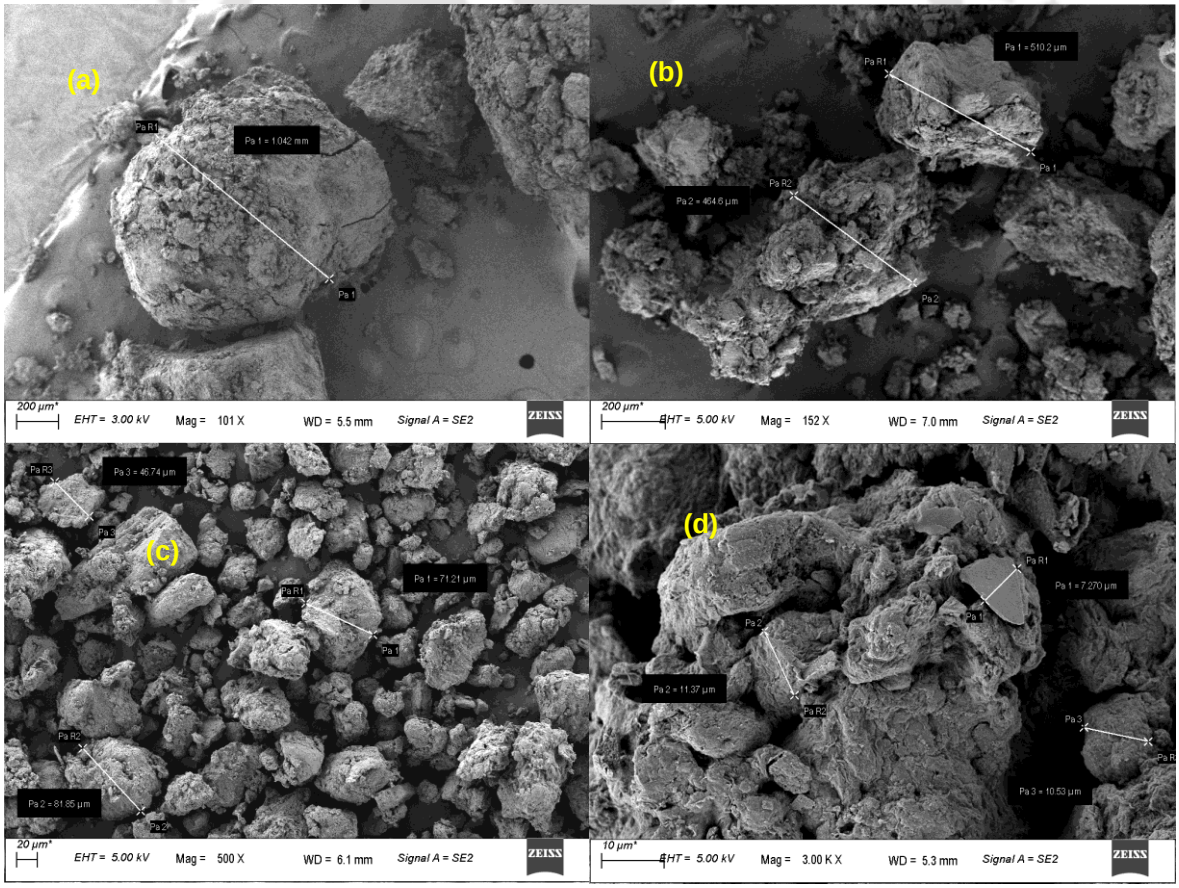

Figure 9.3: Measurement of the sizes of granules after permeation experiment by FESEM micrographs for (a) GB-A; (b) GB-B; (c) GB-C; and (d) GB-D.

9.5 Summary

The following points are drawn from the study:

- The NDV fate and transport parameters in compacted saturated bentonite layer were evaluated. A very low diffusion coefficients of 1.67×10^{-9} m^2/s for bentonite and 3.91×10^{-10} m^2/sec for kaolin and a high retardation factor of 3572 for bentonite and 2348 for kaolin indicated the suitability of these clay for an exclusive pathogenic waste disposal facility for the NDV.
- Fluid permeation rate of H1N1 virus along with 0.5M KCl confirmed the advection-controlled migration of the virus through the compacted GBs in high conc. salt environment. Such behavior of non-sealing of bentonites is due to insignificant repulsive forces in KCl environment.
- The handling protocol at source consists of placing the pathogenic waste in a closed container having the studied powder bentonite/kaolin clays in compacted condition and transferring it to the BMW disposal facility. The results from the present study also support the management of pathogenic waste in exclusive biomedical waste disposal facilities containing the compacted powder bentonite or kaolin as a bottom liner during the disease outbreak.

Chapter – 10

Biopolymers Amended Kaolin as Engineered Barrier for Tailing Disposal Facilities

---

10.1 General

Previous chapters discussed the containment of municipal solid waste, biomedical waste from pandemic using different clay minerals and biopolymer amended clays. The present work discussed the containment of waste from mining activities with biopolymer amended kaolin. These mining wastes are disposed in the form of slurry in engineered disposal facilities behind the dams as shown in Figure 10.1. The work is divided into two parts. First part utilized the containment of inorganic salt waste using xanthan gum amended kaolin (XGK). Second part of the study contains the containment of heavy metals with xanthan gum amended kaolin (XGK) and guar gum amended kaolin (GGK).

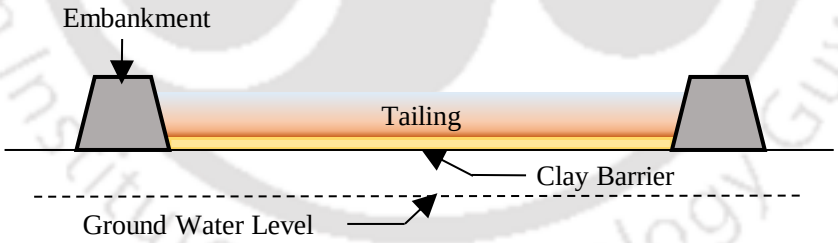

Figure 10.1: Schematic diagram for tailing disposal facility with clay liner

10.2 Xanthan gum amended kaolin as engineered barrier for high concentration inorganic salts

This section discusses the results of hydraulic and volume change characteristics of kaolin and XGK under hydro-chemo-mechanical loading conditions. Study considered the most critical

combinations of chemical and mechanical loadings. Although, mechanical loadings can vary over a wide range from 20 kPa at beginning to 700 kPa at closure of mine tailing facilities, lower mechanical load of 20 kPa was considered as worst-case scenario. The high concentration of salts 0.5M for sodium, potassium, and calcium was taken to consider worst case scenario. Further, through-diffusion experiments were conducted to evaluate the diffusion and retardation characteristics of kaolin and XGK with three different salts.

10.2.1 Hydraulic and Volume Change Behaviour in Salt Environment

A different percentages of biopolymer amendments was explored. A 5% (XGK5) and 10% XG (XGK10) by weight was considered with the kaolin for evaluating the performance. The temporal variations of hydraulic infiltrations for kaolin, XGK5, and XGK10 under 20 kPa mechanical load with 0.5 M KCl as pore-fluid were presented in Figure 10.2(a). The hydraulic infiltration rate of the kaolin sample was found to be higher initially up to 4 minutes, but subsequently reduced from 2×10^{-6} to 4.7×10^{-9} m/s within 10 minutes from the start of the experiment. The hydraulic infiltration rate did not change significantly further with time and could not attain the limiting value of 1×10^{-9} m/s. The initial sudden drop in the hydraulic infiltration rate is due to changes in the fabric of kaolin from dispersed to flocculated upon inundation (Choudhury & Bharat, 2018). The hydraulic infiltration rates of XGK5 and XGK10 were also plotted in the same figure. The hydraulic infiltration rate was found to be 2.53×10^{-6} m/s initially, but subsequently reduced with time. The hydraulic infiltration rate of XGK5 decreased, but it could not achieve the limiting value. Whereas, the hydraulic infiltration rate of the XGK10 decreased gradually and achieved the limiting value of hydraulic infiltration rate in 380 minutes from the start of the experiment, as shown in Figure 10.2(a). The XGK10 sample attained an equilibrium hydraulic infiltration value of 10^{-10} - 10^{-11} m/s after 3000 minutes from the start of the experiment. A reduction of hydraulic

infiltration rate by two to three orders of magnitude was observed due to amendment with the 10% XG. The reason behind the reduction in hydraulic infiltration of XGK is the clogging of pores with xanthan gum gel. The rate of reduction of hydraulic infiltration is quick in kaolin as compared to XGK, because the changes in fabric structure of kaolin does not take much time as compared to the formation of XG gel.

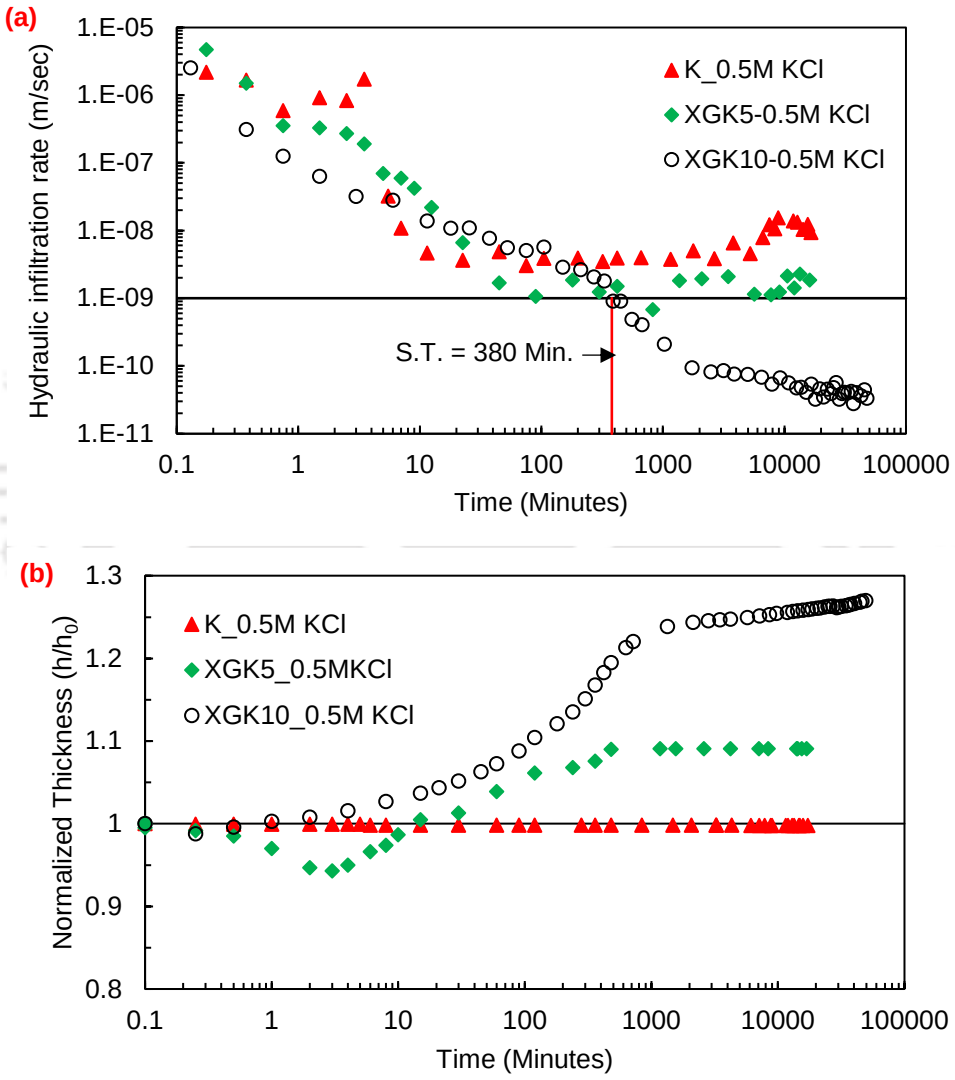

Figure 10.2: *Temporal variations of (a) hydraulic infiltration; (b) normalized thickness for kaolin and XGK with 0.5M KCl under 20 kPa mechanical loading.*

The volume change behavior of kaolin, XGK5, and XGK10 in terms of normalized thickness with 0.5 M KCl as pore–fluid was plotted in Figure 10.2(b) under 20 kPa mechanical load. Normalized

thickness (h/h_0) is defined as the ratio of the present thickness of the sample to the initial thickness. A collapse of the kaolin sample was observed due to the application of the prevailing hydro-mechanical loading conditions. The normalized thickness of the kaolin sample did not increase after the initial collapse, which represents the insignificant development in DDLs of the kaolin sample. The XGK5 sample showed an initial collapse of 5% during the application of chemo-mechanical loading. Further, the XGK5 sample showed swelling and achieved an equilibrium normalized thickness of 1.08, which represents the overall swelling of the sample due to the formation of XG gel. For the XGK10 sample, a slight collapse of approximately 1% was initially observed due to the application of hydro-mechanical load. The sample achieved its original volume within 1 minute of the start of the experiment, and it started further swelling with time due to the complete formation of XG gel. An equilibrium normalized thickness of 1.27 was achieved with XGK10, which represents the overall swelling of the sample. The swelling of XGK samples is taking place due to a higher swelling pressure than the applied stress. The swelling of the sample upon inundation with 0.5 M KCl solution is attributed to the formation of XG gel. The XG gel interacts with potassium ions due to electrostatic interaction between the carboxyl groups of XG and cations. The hydraulic and volume change behaviour of samples were checked with different percentages of the XG. As the lower percentages of the XG are not able to seal the macro-voids in kaolin and resulted in a higher fluid permeation rate than limiting value was observed with 5% XG, higher amount of XG (i.e., 10 %), was only considered for further testing.

The temporal variations of hydraulic infiltration rates for kaolin and XGK10 under 20 kPa mechanical load with distilled water as pore-fluid were presented in Figure 10.3(a). The hydraulic infiltration rate of the kaolin sample was found to be higher at the beginning of the test, but subsequently reduced from 4×10^{-6} to 1.5×10^{-8} m/s within 10 minutes from the start of the

experiment. The hydraulic infiltration rate did not change significantly further with time and could not attain the limiting value of 1×10^{-9} m/s. The initial sudden drop in the hydraulic infiltration rate is due to changes in the fabric of kaolin from dispersed to flocculated upon inundation (Choudhury & Bharat, 2018). The hydraulic infiltration of XGK10 was also plotted in the same figure. The hydraulic infiltration rate was found to be 2.55×10^{-6} m/s at the start of the experiment, which reduced with time. The hydraulic infiltration rate of the XGK decreased gradually and achieved the limiting hydraulic infiltration rate in 510 minutes from the start of the experiment, as shown in Figure 10.3(a). The XGK sample attained an equilibrium hydraulic infiltration value of 3.5×10^{-11} m/s after 8000 minutes from the start of the experiment. A reduction of three orders of magnitude in hydraulic infiltration rate was observed in the values before and after its amendment with XG.

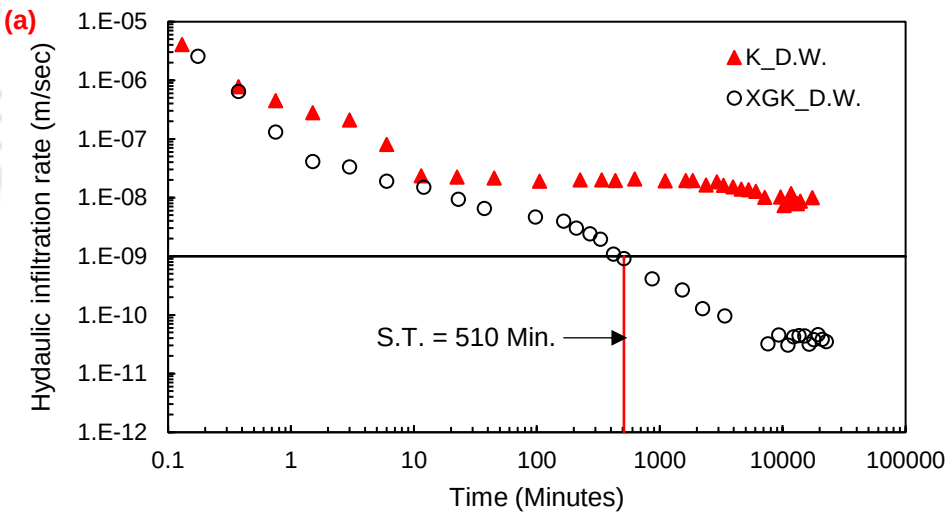

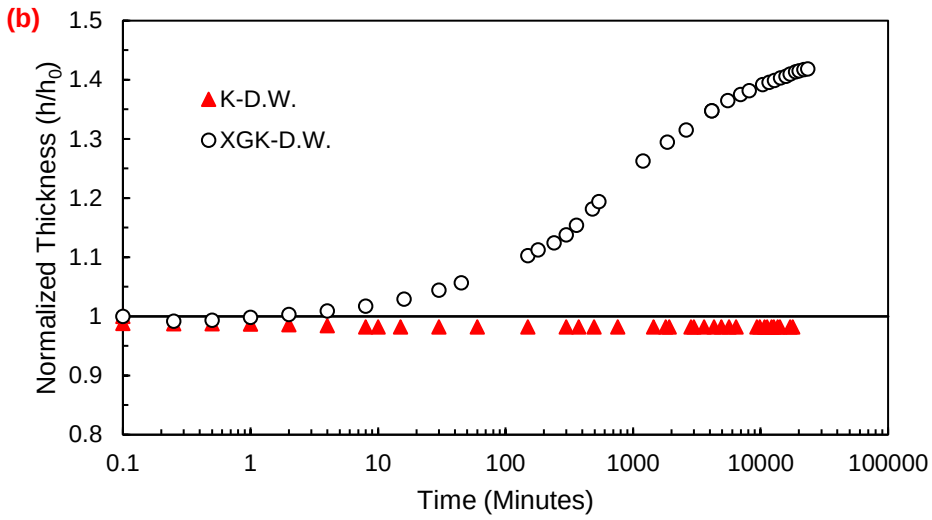

Figure 10.3: *Temporal variations of (a) hydraulic infiltration rate and (b) normalized thickness for kaolin and XGK with D.W. as pore fluid under 20 kPa mechanical loading*

The volume change behavior of kaolin and XGK in terms of normalized thickness with distilled water as pore-fluid was plotted in Figure 10.3(b) under mechanical load. A collapse of the kaolin sample was observed due to the application of prevailing hydro-mechanical loading conditions. Kaolin hydration with distilled water results in the alteration of charges on its edges from positive to negative, which nullifies the coulombic attraction between the edges and faces of kaolin particles (Choudhury & Bharat, 2018; Das & Bharat, 2021). The normalized thickness of the kaolin sample did not increase after the initial collapse, which represents the development of thinner diffused double layers (DDLs) of the kaolin sample (Das & Bharat, 2021; Puppala et al., 2017). For XGK10, a slight collapse of approximately 1% was initially observed due to the application of hydro-mechanical load. The sample achieved its original volume within 2 minutes of the start of the experiment, and it started further swelling with time due to the complete formation of xanthan gum gel. An equilibrium normalized thickness of 1.41, which represents the overall swelling, was achieved with XGK10. The XG in the voids of kaolin sorbs pore-fluid and leads to the swelling of the samples, which was also observed by earlier researchers (Kwon et al., 2023).

The swelling of XGK10 is thus taking place due to a higher osmotic pressure between XG gel than the applied stress.

The dry XG biopolymer is generally found in the coiled structure form (Tian et al., 2019); the presence of the hydroxyl and carboxyl groups on the XG chain attracts water and forms a layer of water around it upon hydration, as shown in Figure 10.4(a). The swelling of the sample upon inundation with water is attributed to the formation of xanthan gum gel, which can absorb water molecules through electrostatic interaction between a water molecule and carboxyl groups present in XG. The formation of the XG gel upon hydration was confirmed with the FESEM micrograph images, as shown in Figures 10.5(a) and 10.5(b). Figure 10.5(a) shows the micrograph of dry XG, which confirms the coiled structure; moreover, Figure 10.5(b) shows the formation of the XG coating. The mechanical force applied is countered by the developed repulsive osmotic forces between the XG-coated kaolin, as shown in Figure 10.4(b). The formation of the XG coating over kaolin particles was also confirmed with atomic force microscopy (AFM). The AFM morphologies of kaolin and XGK were plotted in Figures 10.5(c) and 10.5(d), respectively. The kaolin particles have a thickness of 0.19 µm as shown in Figure 10.5(c), which increased to 0.25 µm for the XGK sample. The increase in the height of kaolin particles is attributed to the formation of an XG gel coating over the kaolin surface. The formation of the coating over the kaolin surface is also confirmed in earlier studies (Kwon et al., 2023).

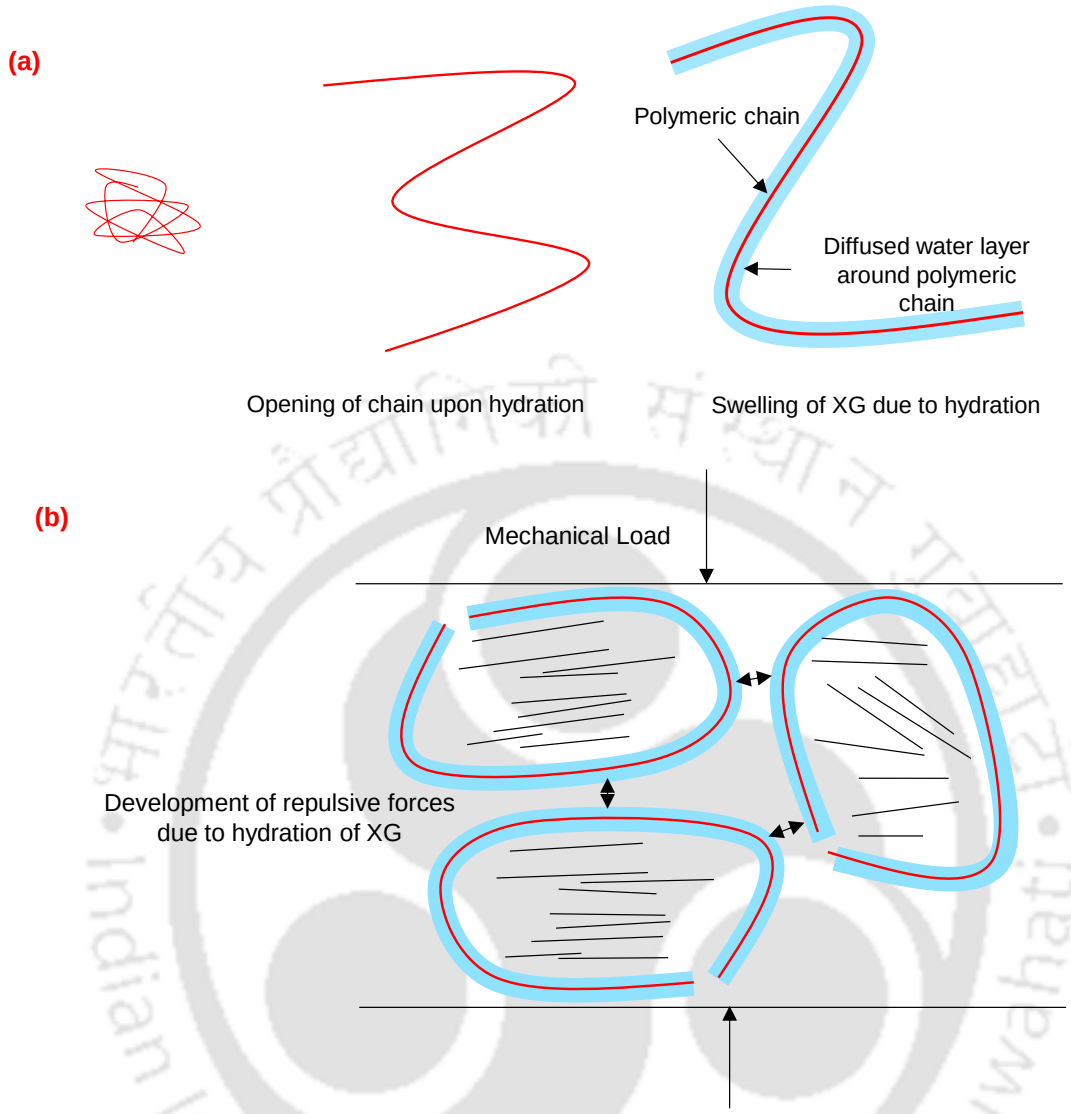

Figure 10.4: *(a) Hydration mechanism of XG; (b) Development of repulsive forces in XGK due to XG gel formation*

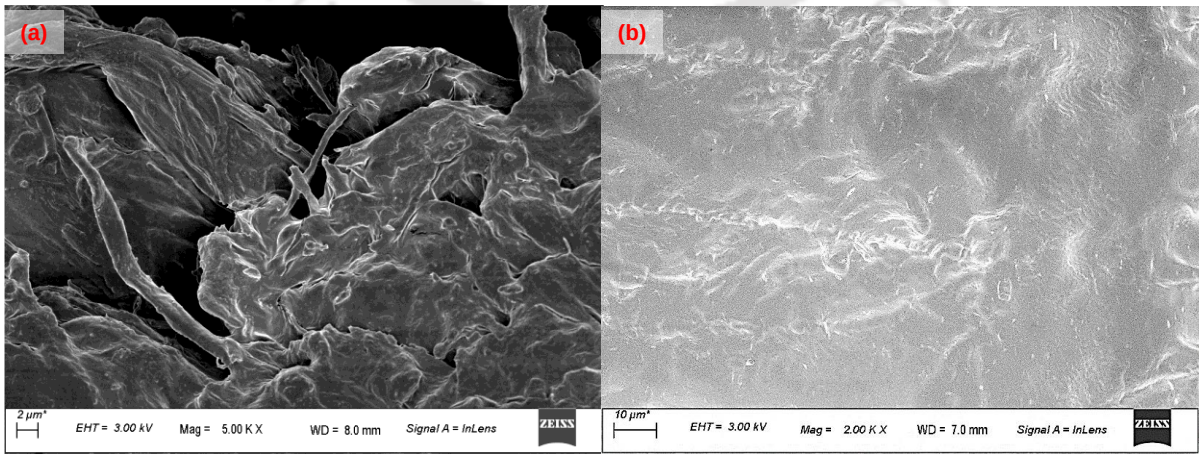

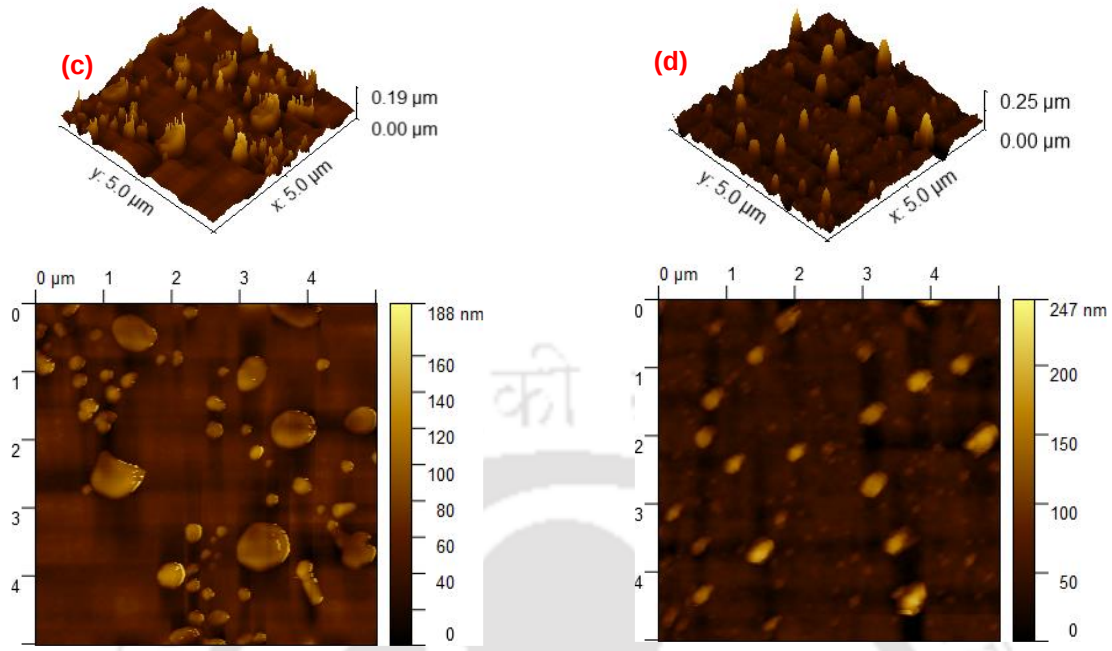

Figure 10.5: *FESEM micrograph of XG in (a) dry powdered state; (b) coating formed after hydration; AFM images of (c) kaolin; and (d) XG amended kaolin*

The FESEM micrographs of kaolin and XGK samples permeated with different pore fluids are presented in Figure 10.6. The FESEMs of kaolin and XGK were performed after permeation with distilled water, as Figures 10.6(a) and 10.6(b), respectively. The saturated samples were collected for FESEM from the middle of the compacted clay samples. The kaolin sample shows various water paths in the sample, which contributes to the higher hydraulic infiltration of the pore-fluid. The XGK sample shows the coating of the xanthan gum layer over the kaolin particles, and the clogging of the pores of kaolin is also visible in Figure 10.6(b). The negatively charged side chains of XG and positively charged edges of kaolin directly interact by hydrogen bonds between carboxyl groups of XG and O in kaolin minerals (Kwon et al., 2023b).

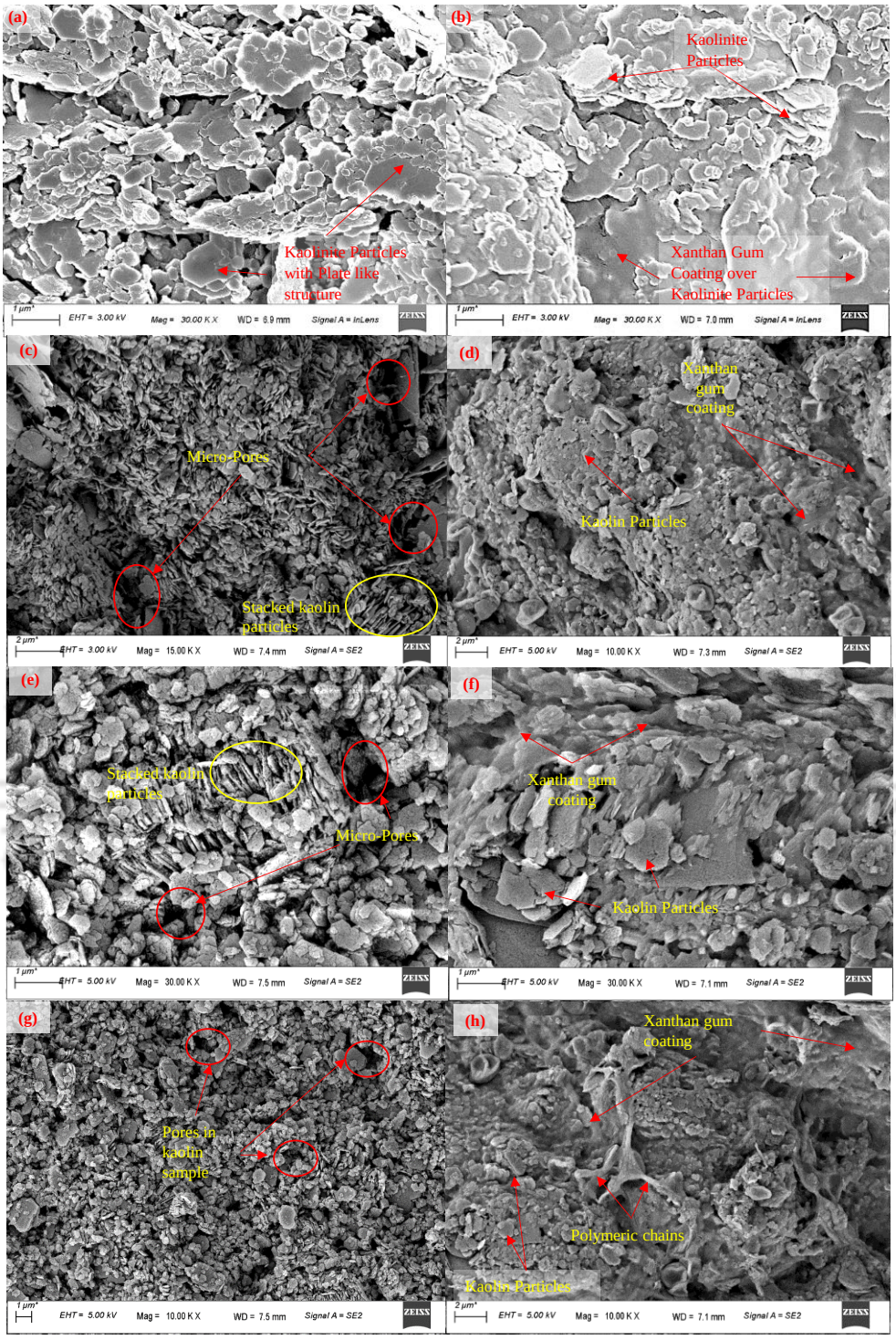

Figure 10.6: *FESEM micrographs of (a) kaolin; (b) XGK after permeation with D.W.; (c) Kaolin; (d) XGK after permeation with 0.5M NaCl; (e) Kaolin; (f) XGK after permeation with 0.5M KCl (g) Kaolin; and (h) XGK after permeation with* $CaCl_2$.

The reason behind the reduction in hydraulic infiltration of XGK is the clogging of pores with xanthan gum gel, as confirmed in Figure 10.6(b). The FESEMs of kaolin and XGK samples were

performed after permeation with 0.5 M NaCl as shown in Figures 10.6(c) and 10.6(d), respectively. The kaolin sample shows various water paths in the sample, which contributes to the higher hydraulic infiltration of the pore-fluid. The XGK sample shows the coating of the xanthan gum layer over the kaolin particles, and the clogging of the pores of kaolin is also visible in Figure 10.6(d). The reason behind the reduction in hydraulic infiltration of XGK is the clogging of pores with xanthan gum gel, as depicted in Figure 10.6(d).The FESEM of the kaolin and XGK after the permeation of 0.5M KCl as pore-fluid were presented in Figures 10.6(e) and 10.6(f), respectively. The kaolin sample showed micro-pores present in it, which contributed to the higher hydraulic infiltration of the pore-fluid. The XGK samples showed the presence of the XG gel, which contributes to the clogging of the pores in the sample as visible in Figure 10.6(f). The FESEMs of kaolin and XGK were performed after permeation with 0.5 M $CaCl_2$ as pore-fluid in Figure 10.6(g) and 10.6(h), respectively. The kaolin sample shows various water paths in the sample, which contributes to the higher hydraulic infiltration of pore-fluid. The XGK sample shows the coating of the xanthan gum layer over the kaolin particles, and the clogging of pores of kaolin is also visible in Figure 10.6(h). The reason behind the reduction in hydraulic infiltration of XGK is the clogging of pores with XG gel. The rate of reduction of hydraulic infiltration is quick in alone kaolin as compared to XGK, because the breaking of the card-house structure does not take much time as compared to the formation of XG gel. This is also a reason for the higher hydraulic infiltration of the XGK sample around 20 minutes after the start of the experiment.

The elemental analysis of samples was performed using energy-dispersive X-ray (EDX) spectroscopy and presented in Figure 10.7. The adsorption potential of the XGK layer for cations was evaluated using EDX. The spectra of pure kaolin and pure XG were presented as Figures

10.7(a) and 10.7(b). Both kaolin and XG sample spectra show the absence of sodium, potassium, and calcium.

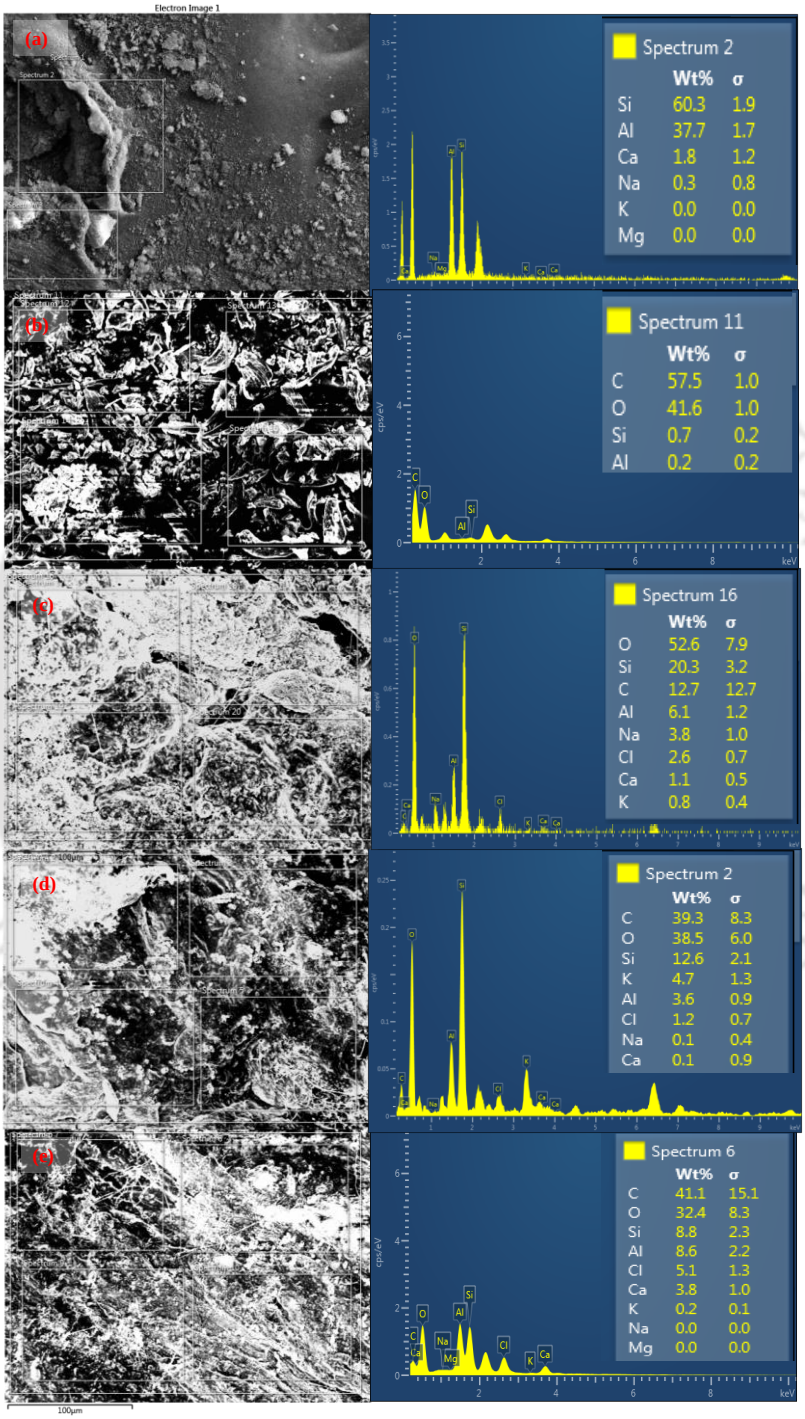

Figure 10.7: *EDX spectra of (a) pure kaolin; (b) pure xanthan gum; and XGK after permeation with (c) NaCl; (d) KCl; (e) $CaCl_2$ as pore-fluid.*

Sodium is present as one of the major elements in the XGK sample permeated with NaCl as shown in Figure 10.7(c). The potassium is found to be present in the XGK sample permeated with KCl as pore-fluid as shown in Figure 10.7(d). Further, the calcium was present in the XGK sample permeated with $CaCl_2$ solution and EDX was presented in Figure 10.7(e). Therefore, the EDX spectra results confirm the adsorption potential of the XGK sample for the different cations upon permeation and its ability to arrest these ions.

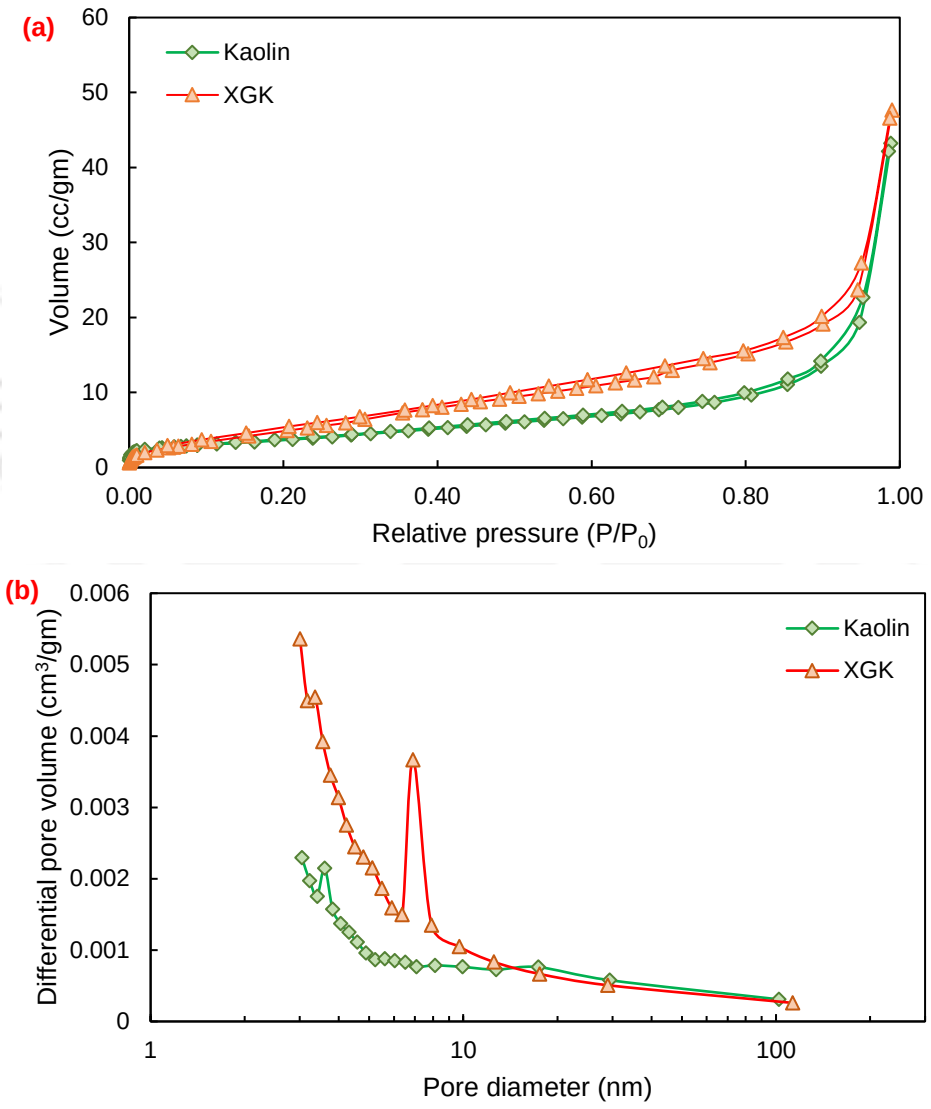

Figure 10.8: *(a) Nitrogen gas adsorption desorption isotherm; and (b) pore size distribution, for kaolin and XGK samples.*

The N_2 gas adsorption and desorption experiments on kaolin and XGK samples were conducted to evaluate the BET surface area and pore size distribution as presented in Figure 10.8 The sorption-desorption isotherms were shown in Figure10.8(a), and highest adsorption was found at a relative pressure (P/P_0) of 0.95-1 (Atinafu et al., 2020; Bordoloi et al., 2022). The surface area of the XGK sample was found to be 18.89 m^2/g, which is quite higher than the surface area of bare kaolin (i.e., 11 m^2/g). The higher specific surface area was found for the XGK sample due to the smaller pore size as compared to kaolin. The smaller pore size of XGK is due to the pore-clogging due to XG gel formation. The pore size distribution of kaolin and XGK sample was presented in Figure 10.8(b). Most of the pores of kaolin and XGK were found to be smaller than 10 nm, while largest pores of 102 and 113 nm were found for kaolin and XGK samples, respectively. More pores of smaller size were dominant in the XGK sample, while kaolin has more pores of larger size.

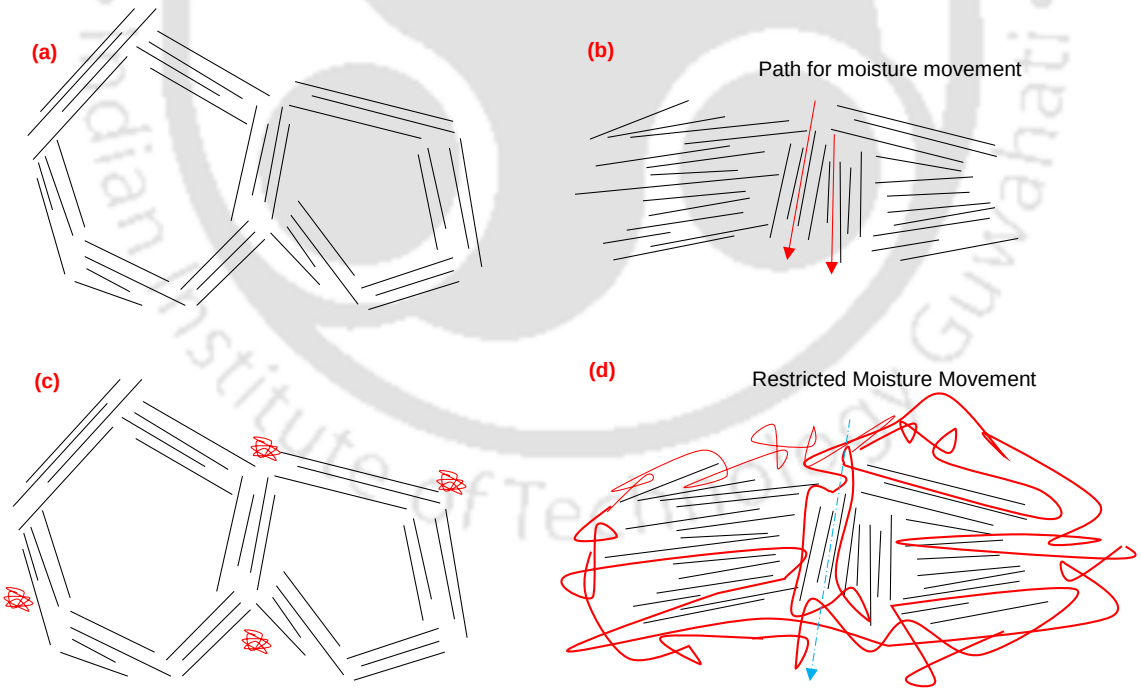

Figure 10.9: *(a) Illustration showing open card-house structure in dry compacted sample; (b) Face – face orientation of kaolin particles after inundation; (c) dry kaolin sample with coiled xanthan gum particles; and (d) xanthan gum gel formation around the kaolin particles with restricted moisture movement*

The kaolin clay compacted in a dry state has an open card-house type structure due to the edge–edge interactions. The hydration of kaolin with water alters the charges on its edges from positive to negative, which further leads to the breaking of the card-house type structure as illustrated in Figs. 10.9(a) and 10.9(b). The observation of a significant reduction in the volume of the kaolin along with hydraulic infiltration is attributed to the same reason. But the alone kaolin at lower density does not have significant development of diffused double layers to achieve the limiting value of hydraulic conductivity ($< 10^{-9}$ m/s). The saturated hydraulic conductivity of the bare kaolin is also governed by the hydrated radius of the cation in pore fluid. The saturated hydraulic infiltration was found to be lowest for the Na^+ ions solution due to the highest hydrated radius of sodium as compared to potassium. The XGK before and after hydration shown in Figs.10.9(c) and 10.9(d) respectively. The macro-voids present in kaolin samples are reduced due to the breaking of card-house structure as well as the clogging of pores with xanthan gum gel. The coating of the XG over kaolin restricts the movement of pore fluid across it. Due to the presence of many carboxyl groups, the XG gel has the potential to the cations. Adsorption of cations on the XG surface and clog formations are the main mechanisms for lower hydraulic infiltration of different pore fluids across the tailing barriers. The sealing time for XGK with distilled water was found to be higher (510 min.) than other pore-fluids, and it was found to be lowest (270 min.) for calcium ions (Ca^{2+}). The sealing time for monovalent cations (i.e., Na^+, and K^+) was found to be almost the same, i.e., (360-380 min.). Calcium ions act as cross-linkers between polymeric chains of XG, which reduces the sealing time. Monovalent cations show a slightly higher sealing time than divalent cations due to a reduction in cross-linking. The highest sealing time of water is attributed to the absence of crosslinking in XG.

10.2.2 Diffusion rates of Salts through Kaolin and XG amended Kaolin

Through-diffusion experiments were conducted for three different salts having a 0.5 M initial concentration in the source reservoir. The saturated kaolin and XGK samples were placed in different diffusion cells, and reservoirs were attached to either end of the diffusion cell. The test was started by placing a 0.5M salt solution on the source side and distilled water on the collector side. The samples were collected and analyzed for the presence of inorganic ions at different time intervals up to 60 days. The temporal variations of relative concentrations of measured source and collector reservoirs for the NaCl diffusion experiment with kaolin were presented in Figure 10.10(a). The temporal variations in relative concentrations of ions in both reservoirs for XGK with 0.5M NaCl solution as an initial concentration in the source reservoir were presented in Figure 10.10(b). The concentrations in the source reservoir decreased with time and increased in the collector reservoir for both kaolin and XGK. A relative concentration of 0.073 and 0.089 was observed after 60 days in the collector reservoir for kaolin and XGK, respectively, with NaCl solution. The diffusion coefficient and retardation factors were evaluated by minimizing the error between measured and theoretical concentration profiles obtained by solving equations (2-6), and optimization [58-59]. The theoretical profiles for source and collector reservoirs were also presented in Figure 10.10(a) and 10.10(b) for kaolin and XGK, respectively. The diffusion coefficient and retardation factor of kaolin with NaCl solution were found to be 1.41×10^{-10} m^2/sec and 18.69, respectively. These values were reduced to 1.09×10^{-10} m^2/sec and 14.05, respectively, for NaCl solution upon amendment of kaolin with XG. The theoretical profiles for kaolin and XGK with NaCl salt solution showed a very good theoretical estimation with a root mean square error (RMSE) value of 0.0199 and 0.0132, respectively. Similarly, the diffusion results for K and XGK with different salts were presented in Appendix 3. The values of the diffusion coefficient and

retardation factor for three different salts through kaolin and XGK were also tabulated in Table 10.1.

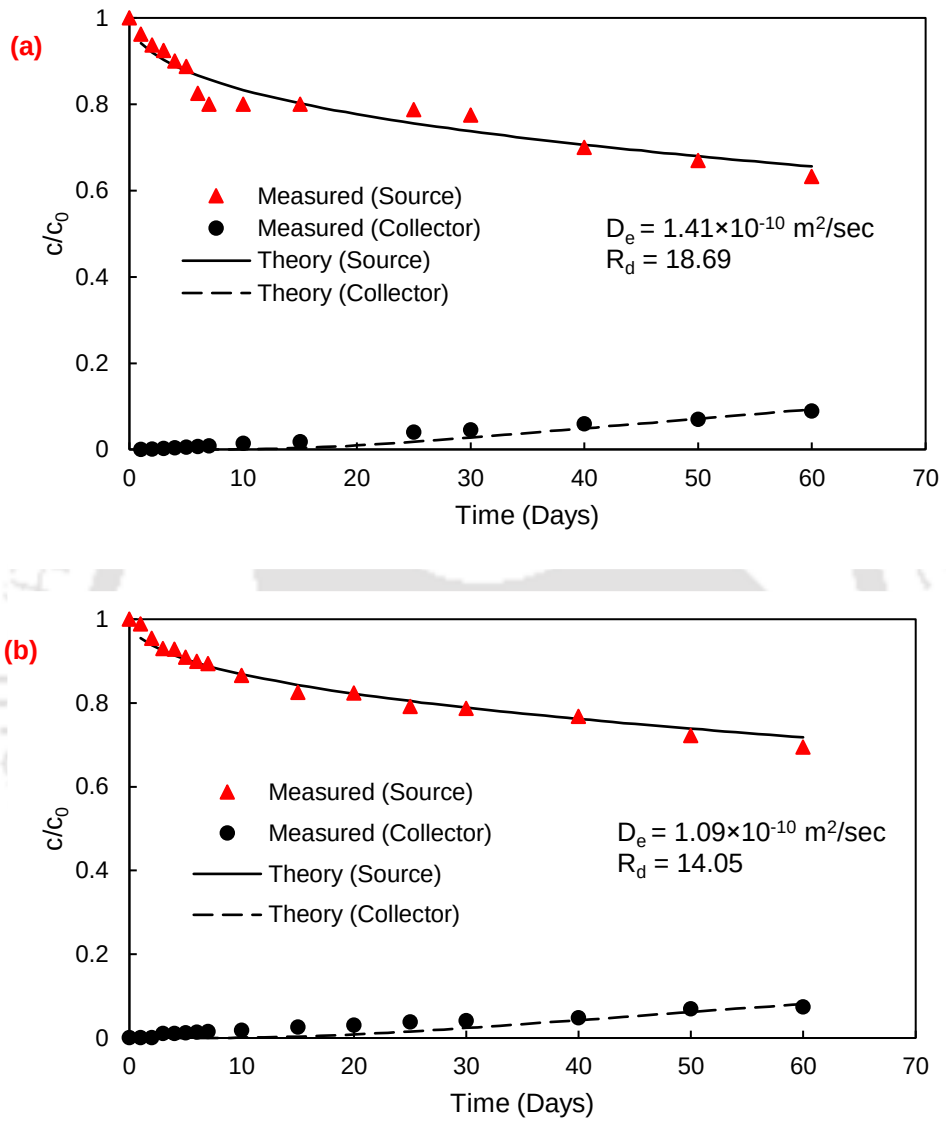

Figure 10.10. *Comparison of experimental measured and theoretical profile at source and collector reservoir for (a) Kaolin; and (b) XGK with 0.5M NaCl.*

The diffusion values obtained in the study were compared to the literature and shown in Table 10.2. The D_e values were found to be similar to the values obtained by [62-63] due to the similar density of the kaolin as in the present work. Moreover, the method used by these researchers is also the same. Whereas, high diffusion and lower R_d as compared to the present work were

observed by [60]. Such differences in the values can be due to the errors involved in destructive technique of In-diffusion techniques. Further, the difference in quality of kaolin can also result in some variation in values. In general, the results obtained in the present study are in good agreement with the literature.

Table 10.1: *The diffusion coefficient and retardation factor for kaolin and XG amended kaolin with different salts*

Material	Pore Fluid	Effective Diffusion Coefficient, D_e	Retardation Factor, R_d	Root mean square error RMSE
Kaolin	0.5M NaCl	1.41×10^{-10} m^2/sec	18.69	0.02
	0.5M KCl	1.61×10^{-10} m^2/sec	9.36	0.0195
	0.5M $CaCl_2$	1.92×10^{-10} m^2/sec	11.62	0.024
XG amended Kaolin	0.5M NaCl	1.09×10^{-10} m^2/sec	14.05	0.013
	0.5M KCl	7.44×10^{-11} m^2/sec	12.82	0.015
	0.5M $CaCl_2$	8.36×10^{-11} m^2/sec	7.69	0.016

Table 10.2: *Comparison of the diffusion coefficient and retardation factor for different contaminant through compacted kaolin*

Contaminant	Density (g/cc)	Porosity	$D_e \times 10^{-10}$ m^2/sec	R_d	Method	Reference
K^+	1.272	0.52	13.9	3.95	In-diffusion for	
Cd^{2+}	1.272	0.52	4.8	2.04	D_e and Batch	[60]
Zn^{2+}	1.272	0.52	9.1	3.15	Sorption for R_d	
^{86}Rb	-	-	2.4*	-	Half-cell method	[61]
Floride	1.1	0.57	3.488-6.976	61-110	Through diffusion test	[62]
K^+	1	0.60	1.55*	-	Solute diffusion test	[63]
	1.2	0.53	1.25*	-		
Cl^-	1	0.60	1.70*	-		
	1.2	0.53	1.10*	-		

K^+	1.7	0.35	8.2	5.8	Through Diffusion Test	[15]
Na^+	1.2	0.54	1.41	18.69	Through Diffusion Test	Present Work
K^+	1.2	0.54	1.61	9.36		
Ca^{2+}	1.2	0.54	1.92	11.62		

* Apparent diffusion coefficient

The difference in the values of the D_e and R_d for similar test conditions with different salts is expected due to the change in the hydrated radius of the cations. The larger hydrated radius of the cations cannot pass through the smaller pores and hence may not significantly contribute to the diffusion process. The same can be said for the lowest value of diffusion coefficient for sodium as compared to potassium and calcium; sodium has the largest hydrated radius as compared to the other cations. Further, the differences in the retardation factor are attributed to the sorption ability of these cations on the kaolin clay. The sorption ability of the kaolin will depend on various physico-chemical forces between the particles. The interactions of the cations with the kaolin show contrast behavior as that of bentonite. The equilibrium sediment volume of kaolin clay shows an order of $K^+ > Ca^{2+} > Na^+$, whereas bentonites show the opposite behavior of $Na^+ > Ca^{2+} > K^+$. Such behavior of kaolin is observed due to the dispersed nature of kaolin in the presence of K^+ as compared to Na^+ [64]. The flocculated structure of kaolin in the presence of the K^+ as compared to Na^+ will dominate positive charges on its termination sites, leading to lower retention of K^+. Moreover, the dispersed structure of the kaolin with the Na^+ will have more negatively charged termination sites as compared to K^+, which leads to higher retention of the Na^+ ion and hence a higher R_d.

10.2.3 Numerical Simulation of Salt Cations through Barriers for Evaluating Design Period

The attenuation ability of the cations is based on the evaluated model parameters (K_s, D_e, and R_d) of the engineered barrier facilities. The contaminant migration through barriers is mainly governed

by the advection-diffusion equation. After evaluating independent advection (saturated hydraulic conductivity) and diffusion (effective diffusion coefficient and retardation factor) characteristics, the transport of contaminants was simulated in a 500 mm-thick kaolin clay layer as well as the XGK layer. The normalized concentration distribution for the studied contaminants was given at different periods in Figure 10.11.

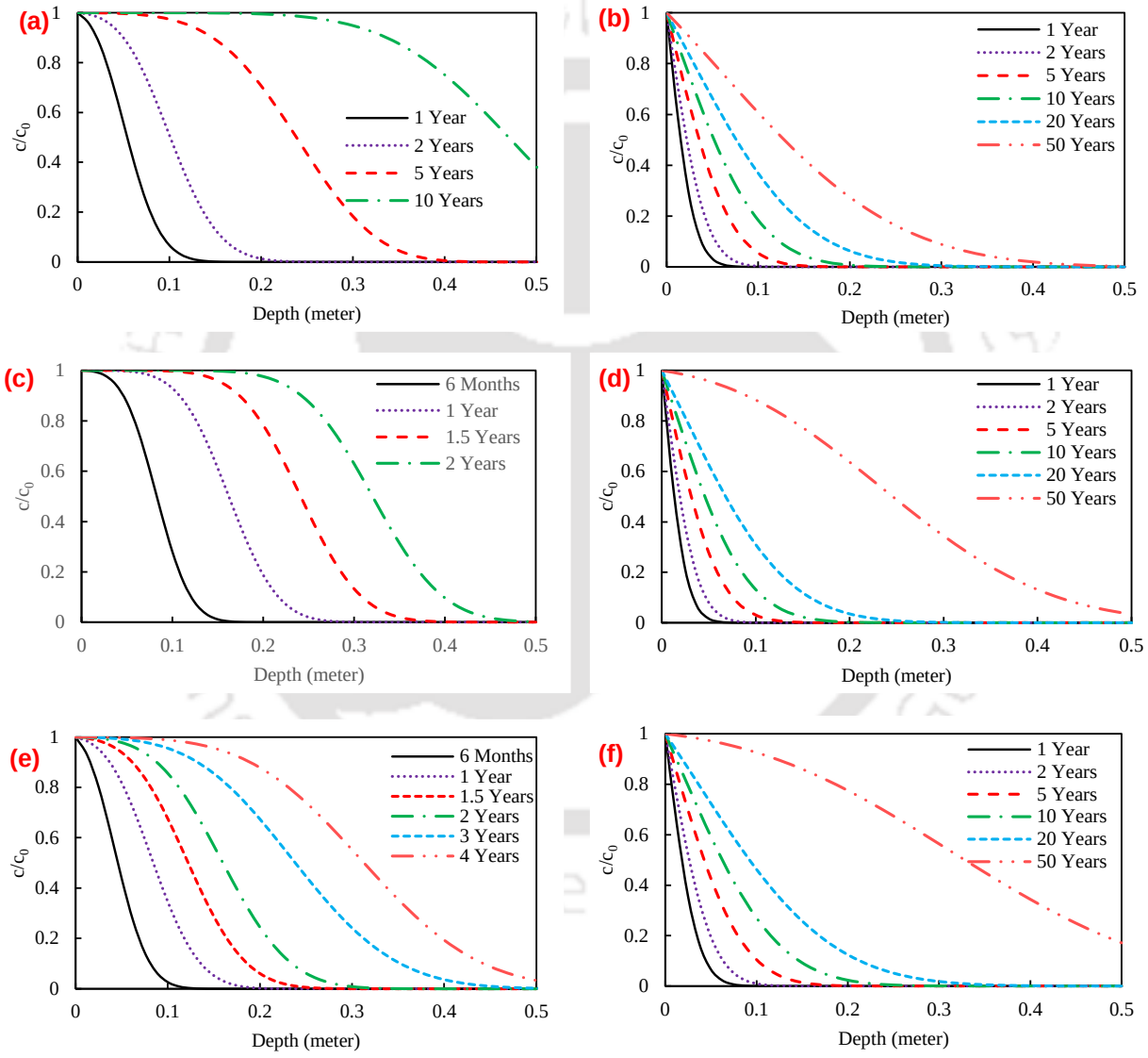

Figure 10.11: Contaminant migration profiles with time for (a) 0.5 M NaCl through kaolin; (b) 0.5 M NaCl through XGK; (c) 0.5 M KCl through kaolin; (d) 0.5M KCl through XGK; (e) 0.5M CaCl2 through kaolin; and (f) 0.5M $CaCl_2$ through XGK.

The hydraulic head of leachate also influences the migration of contaminants through barrier material. The concentration profiles of 0.5M KCl for a 500 mm-thick kaolin layer for different hydraulic heads were plotted in Figure 10.12(a). The plotted profiles showed that the hydraulic head significantly influenced the contaminant profiles. The lowest hydraulic head (i.e., 1 meter) showed a migration of 200 mm in 1 year, while the 10-meter hydraulic head showed the failure of the barrier after 1 year. The concentration profiles of 0.5M $CaCl_2$ for 500 mm-thick kaolin layer for three different hydraulic heads were plotted in Figure 10.10(b). The calcium migration also showed similar results as that of potassium; the barrier system showed very less migration of calcium at the lower head. The barrier system started failing after 1 year and showed rapid migration of calcium at a hydraulic head of 10 meters. The contaminant profiles of three different contaminants for a 500 mm-thick XGK layer with different hydraulic heads for a period of 50 years were plotted in Figure 10.12(c). The migration profiles after 50 years didn't change significantly with hydraulic heads. Moreover, hydraulic heads of 10 meters for all contaminants showed higher migration as compared to lower heads. The calcium ion showed higher migration when compared with the other two cations. For all three contaminants, a 500 mm layer of XGK is sufficient to act as a barrier for more than 50 years. Based on the concentration profiles with different cations for the XGK layer evaluated design time was found to be 50 years.

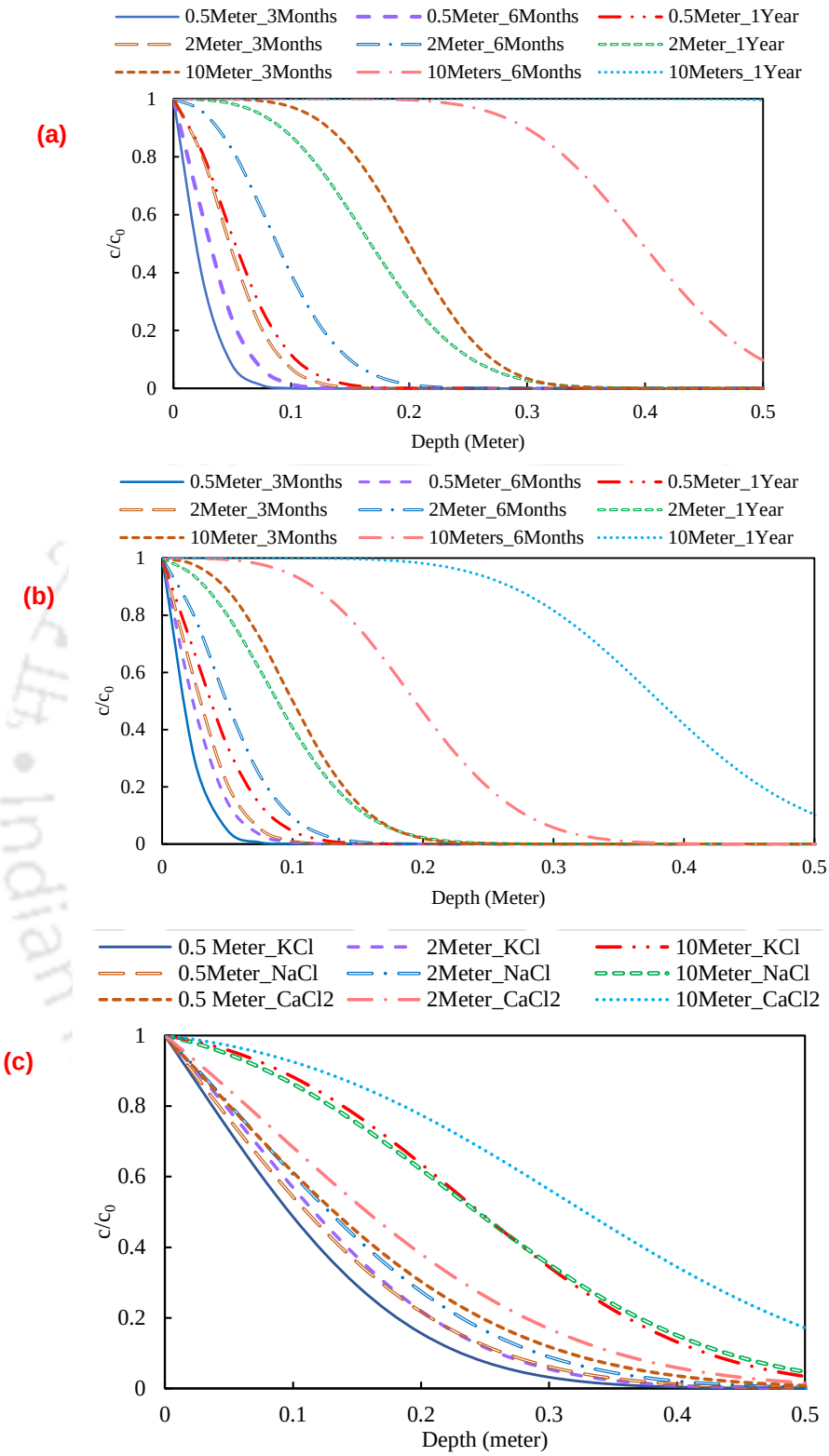

Figure 10.12: Contaminant profiles of different hydraulic heads of leachate for (a) 0.5M KCl through kaolin with time; (b) 0.5M $CaCl_2$ through kaolin with time; (c) XGK with different pore-fluid for 50 years' time duration.

10.3 Biopolymers amended kaolin as engineered barrier for heavy metals

This section discusses the results of hydraulic characteristics of kaolin, XGK, and GGK under constant volume conditions. Different percentages of the biopolymers (XG and GG) were explored for hydraulic performance. The study considered a 1000 ppm concentration of three heavy metals. Further, through-diffusion experiments were conducted to evaluate the diffusion and retardation characteristics of kaolin, XGK, and GGK with three different heavy metals.

10.3.1 Influence of Biopolymer Content on Hydraulic Performance

Temporal variations of fluid permeation rate of kaolin and XG amended kaolin (XGK) with distilled water as pore-fluid for different percentages of XG were shown in Figure 10.13(a). The fluid permeation rate of all samples was found to be in the order of 10^{-6} m/sec initially, which reduces with time upon hydration and achieves equilibrium fluid permeation rates. The bare kaolin sample achieved an equilibrium fluid permeation rate of 4-5 $\times 10^{-9}$ m/sec, which is slightly higher than the limiting value criteria for sealing ability. The lowering of the fluid permeation rate of the kaolin sample upon hydration is due to the breaking of the card-house type structure of the kaolin upon hydration with distilled water as pore-fluid. The XGK samples achieved a fluid permeation rate lower than the limiting value with sealing time (S.T.) of 100 – 1000 minutes for different percentages of the XG. The magnitude of the equilibrium fluid permeation rates was found to be related with the percentage of XG. The higher percentage of XG achieved the lower value of the fluid permeation rates. The lower values of the fluid permeation rates of XGK samples are due to the formation of XG gel upon hydration. These carboxyl groups attract the polar water molecule with the electrostatic forces of attraction and further process of gel formation takes place.

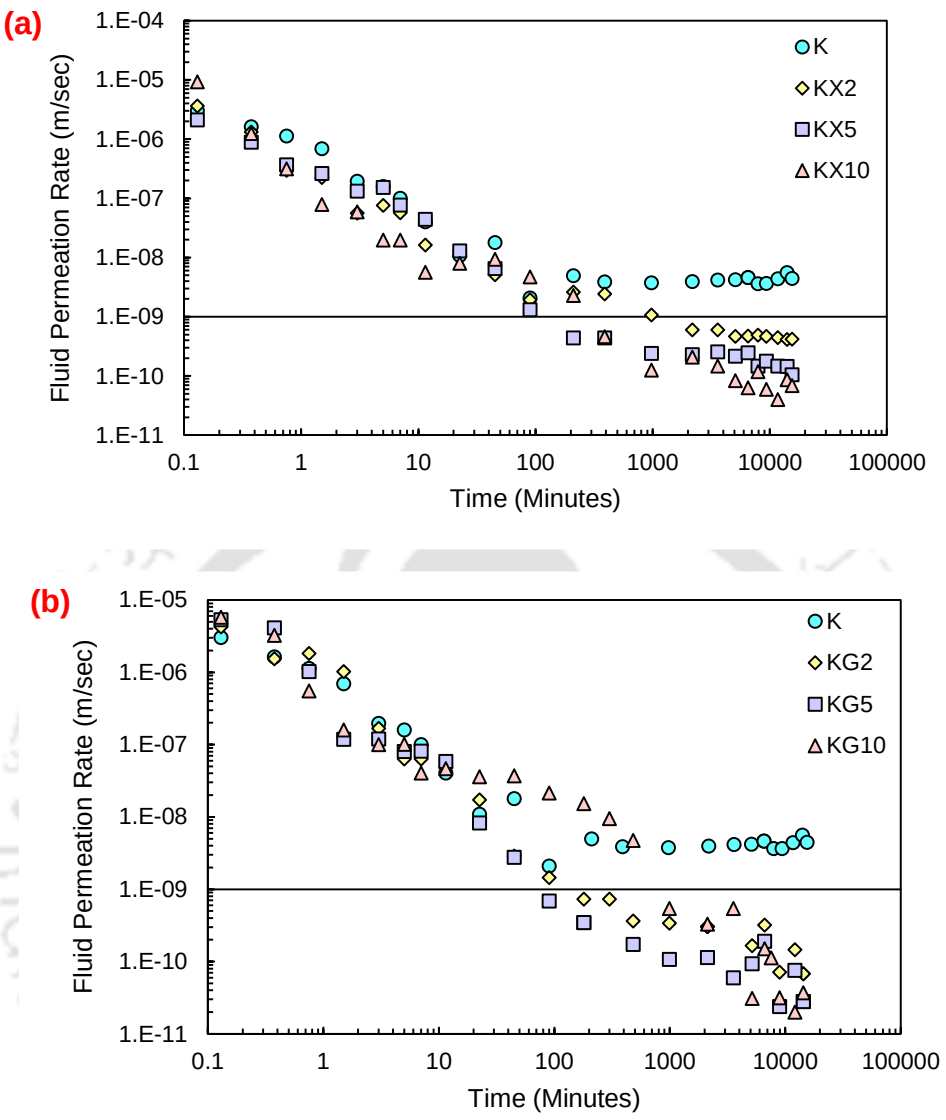

Figure 10.13: Temporal variations of fluid permeation rates with distilled water as pore fluid for (a) xanthan gum amended kaolin; and (b) guar-gum amended kaolin

The temporal variations of the fluid permeation rates of kaolin and guar-gum amended kaolin (GGK) with distilled water as pore-fluid were plotted in Figure 10.13(b). The fluid permeation rates of all samples were found to be higher initially, which reduces with time upon hydration of these samples. The GGK samples achieved a limiting value of fluid permeation rate in sealing time of 100-1000 minutes for different percentages of guar-gum. The GGK samples achieved fluid permeation rate in order of 10^{-10} – 10^{-11} m/sec. The reduction in fluid permeation rates of GGK

samples is due to the formation of guar-gum gel, which took place due to the hydration of guar-gum. The hydration of guar-gum takes place due to the presence of hydroxyl groups in the guar-gum biopolymer.

Temporal variations of fluid permeation for kaolin and XGK samples with 1000 ppm lead solution were presented in Figure 10.14(a). The initial fluid permeation rate was found to be in order of 10^{-6} m/sec, which reduces with time upon hydration except for bare kaolin. The fluid permeation rate with lead solution didn't change significantly with time for alone kaolin can be attributed to flocculated orientation of kaolin. The samples KX2 and KX5 didn't achieved the sealing ability, probably due to requirement of the more XG gel for clogging of the macro-voids of the flocculated kaolin. The KX10 sample achieved the sealing within 300 minutes from the start of the experiment. Samples XG2 and XGK5 achieved an equilibrium fluid permeation of 3×10^{-9} and 1.2×10^{-9} m/sec, respectively. While, XGK10 sample achieved an equilibrium fluid permeation of 3×10^{-11} m/sec with 1000 ppm lead solution. The formation of XG gel upon hydration with Pb solution leads to the formation of thick viscous gel, which clogs the voids present in the kaolin samples. XG also forms coating around the kaolin particle upon hydration which restricts the movement of the pore-fluid.

The temporal variations of fluid permeation of kaolin and GGK samples with 1000 ppm of lead (Pb) solution were presented in Figure 10.14(b). The fluid permeations of the all samples were found to be higher initially, which reduces with time upon hydration with Pb solution. The equilibrium fluid permeation of the kaolin sample was found to be 4×10^{-6} m/sec, which is significantly higher than the limiting value. The fluid permeation rate with Pb solution didn't change significantly with time for alone kaolin can be attributed to flocculated orientation of kaolin. The kaolin sample could not achieve sealing with Pb as pore-fluid. The samples achieved

limiting value of fluid permeation in sealing time of 1000 minutes for KG2 and KG5, and 165 minutes for KG10, respectively. The KG2, KG5, and KG10 samples achieved fluid permeation rate of 2 $\times 10^{-10}$, 2-3 $\times 10^{-10}$, and 5×10^{-11} m/sec, respectively. The reduction in fluid permeation of GGK samples is due to the formation of guar-gum gel, which took place due to hydration of guar-gum. The hydration of guar-gum takes places due to presence of hydroxyl groups in guar-gum biopolymer. The fluid permeation rates of the kaolin sample with 1000 ppm of lead solution were found to be significantly higher, which is attributed to the low pH of the lead nitrate solution.

The pH of 1000 ppm lead nitrated was found to be 4.2, which is lower than the IEP_{Edge} of studied kaolin i.e., 5.3 (Choudhury & Bharat, 2018). Since the pH of the studied pore-fluid is lower than the IEP_{Edge} of the kaolin, it will remain in a card-house-type structure due to positively charged termination sites. Hence, the fluid permeation rate of kaolin with 1000 ppm lead solution didn't reduce with time and remained almost similar to the initial fluid permeation rate. The carboxyl groups of xanthan gum get partially protonated below pH 4.5 and completely deprotonated above 6, which means the IEP of xanthan gum lies between pH of 4.5-6 (Bueno et al., 2014; Brunchi et al., 2016). Further, the guar gum has an IEP of around 3.7 – 4, which is lower than the pH of the lead solution (Hamza et al., 2021). The lower pH of the solution than the IEP of XG led to higher fluid permeation rates in small percentages of XGK (i.e., XGK2, and XGK5). However, guar gum has a lower IEP than the pH of pore-fluid, which contributed to the effective gel formation and lower fluid permeation rates even in low percentages of GGK (i.e., GGK2 and GGK5).

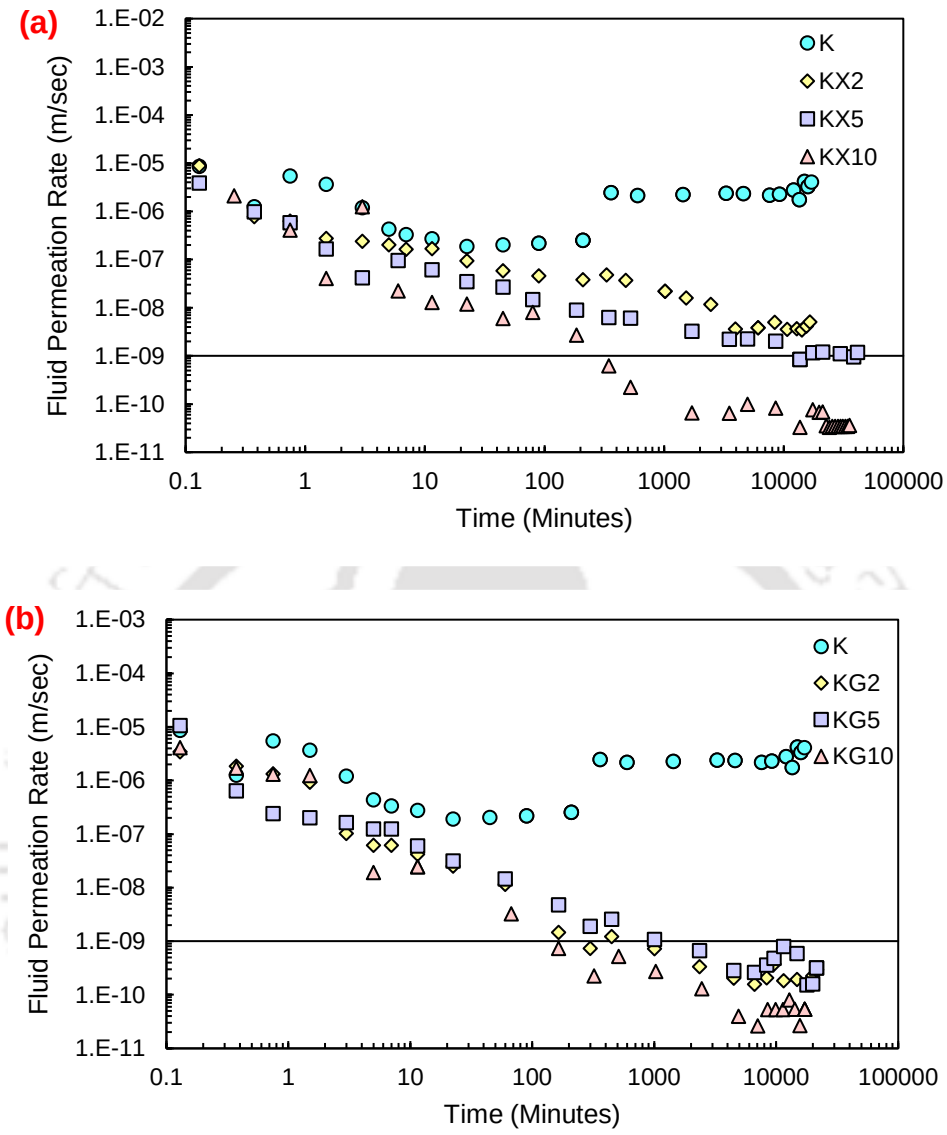

Figure 10.14: Temporal variations of fluid permeation rates with lead solution as pore-fluid for kaolin amended with (a) xanthan gum; and (b) guar-gum

Similarly, the pH of the 1000 ppm of zinc nitrate solution was around 5.7, which is higher than the IEP_{Edge} of the studied kaolin (i.e., 5.3). Since the pH of the studied pore-fluid is higher than the IEP of the kaolin edge, the termination sites of kaolin will be negatively charged. The negatively charged termination sites lead to the breaking of the card-house structure of kaolin in this environment. Low fluid permeation rates have been observed for kaolin when permeated with zinc as compared to lead. Further, the pH of pore-fluid lies in the protonation and deprotonation pH

range of the XG (i.e., 4.5-6), hence protonation of the XG leads to higher permeation rates with XG as compared to the GG similar to the lead. Similarly, the fluid permeation rates of XGK and GGK with chromium and zinc were plotted in Annexure 3.

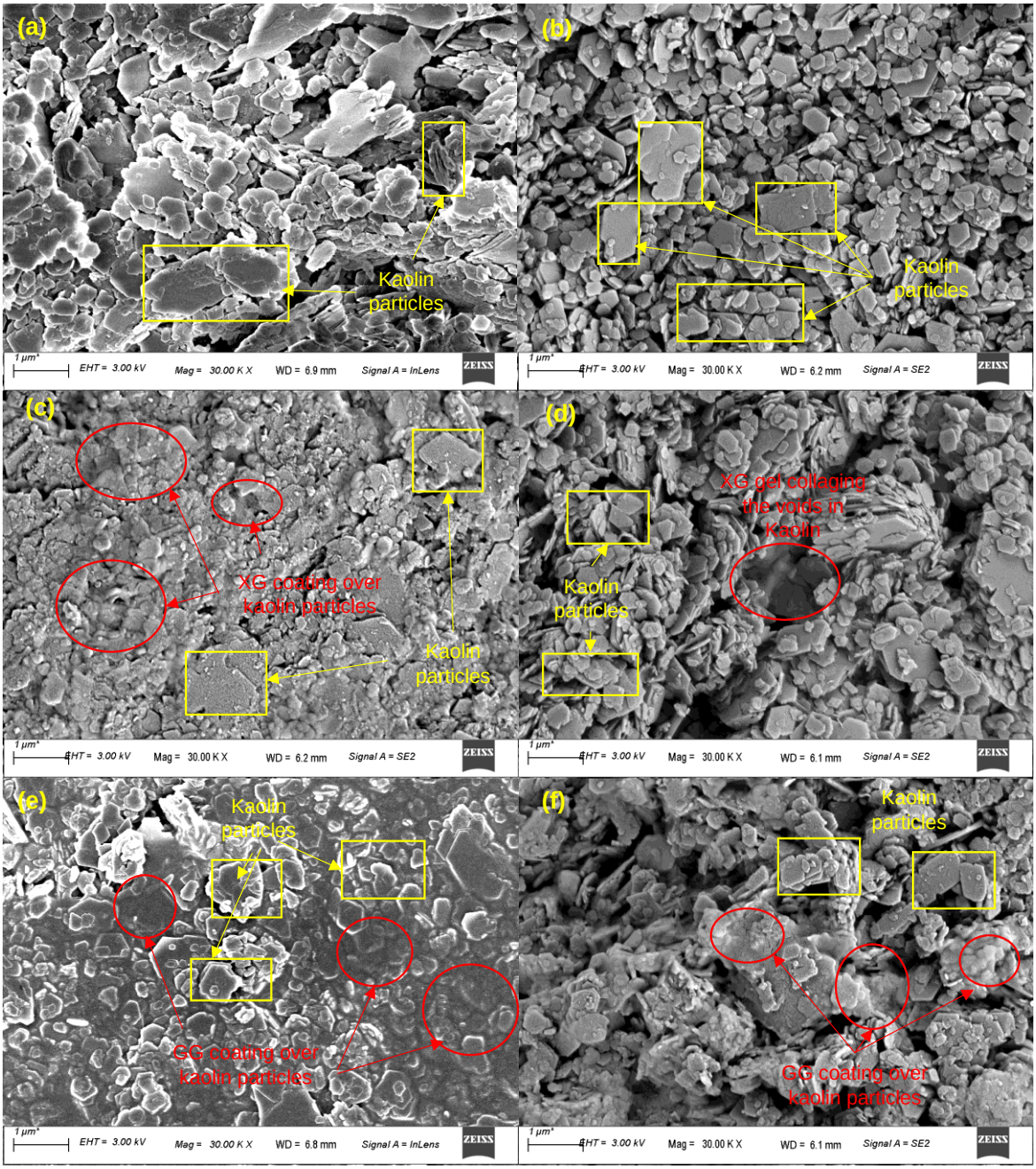

Figure 10.15: FESEM micrographs of (a) kaolin permeated with distilled water; (b) kaolin permeated with chromium solution; (c) XGK permeated with distilled water; (d) XGK permeated with chromium solution; (e) GGK permeated with distilled water; and (f) GGK permeated with chromium solution.

The micrographs obtained from FESEM are presented in Figure 10.15. The micrograph of the kaolin sample permeated with distilled water and 1000 ppm chromium solution were presented in Figure 10.15(a) and 10.15(b), respectively. Micrographs of both the samples have the kaolin particles, and both the samples have the presence of micro-voids among the kaolin particles. The micrographs of XGK samples permeated with distilled water and 1000 ppm chromium solution were presented in Figures 10.15(c) and 10.15(d), respectively. Both samples showed the formation of XG gel and the coating of XG gel over the kaolin particles.

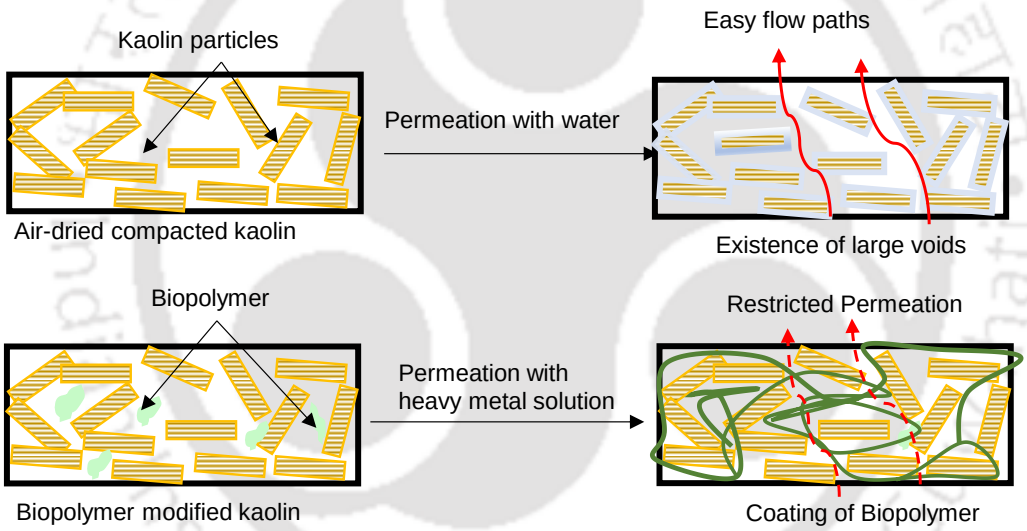

Figure 10.16: Mechanism controlling the fluid permeation through kaolin and biopolymer amended kaolin

The XGK sample permeated with distilled water showed the formation of more XG gel as compared to the sample permeated with chromium solution, this is due to the reduction in gel formation in the presence of chromium solution. The micrograph of GGK samples permeated with distilled water and 1000 ppm chromium solution were presented in Figure 10.15(e) and 10.15(f), respectively. The micrographs showed the presence of the gel over the kaolin particles and the clogging of pores with GG gel in both cases as shown in Figure 16. The GGK sample permeated

with distilled water showed the formation of more GG gel as compared to the sample permeated with chromium solution, this is due to reduction in gel formation in the presence of chromium solution.

10.3.2 Diffusion rates of heavy metals through Kaolin, XGK, and GGK

The through-diffusion experiments were conducted for three different heavy metals solutions with 1000 ppm initial concentration in the source reservoir. The samples were saturated as previously mentioned in the methodology sections and experiment was started by placing 1000 ppm solution of the desired heavy metal on the source side and distilled water on collector side. The liquid samples from both sides were collected for analysis for the concentration of heavy metals at different time intervals up to 60 days. The temporal variations of relative concentrations of measured source and collector reservoirs for the Cr^{6+} diffusion experiment with kaolin, XGK, and GGK were presented in Fig. 10.17(a), 10.17(b), and 10.17(c), respectively. The concentrations in the source reservoir decreased with time and increased in the collector reservoir for all kaolin, XGK, and GGK samples. A relative concentration of 0.148, 0.0041, and 0.0696 was observed after 60 days in the collector reservoir for kaolin, XGK, and GGK respectively, with chromium solution. The diffusion coefficient and retardation factors were evaluated by minimizing the error between measured and theoretical concentration profiles obtained by solving equations (2-6), and optimization (Bharat et al., 2009; Bharat, 2013). The theoretical profiles for source and collector reservoirs were also presented in Figure 10.17 (a), Figure 10.17(b), and Figure 10.17(c) for kaolin, XGK, and GGK respectively. The diffusion coefficient and retardation factor of kaolin with 1000 ppm Cr^{6+} solution were found to be 1.93×10^{-10} m^2/sec and 25.97, respectively. These values were reduced to 3.89×10^{-11} m^2/sec and 39.829, respectively, for 1000 ppm Cr^{6+} upon amendment of XGK. Further, these values were reduced to 1.14×10^{-10} m^2/sec and 28.867, respectively, for 1000

ppm Cr^{6+} upon amendment of GGK. The theoretical profiles for kaolin, XGK, and GGK with 1000 ppm Cr^{6+} solution showed a very good theoretical estimation with a root mean square error (RMSE) value of 0.0235, 0.0165, and 0.0296, respectively. Similarly, the diffusion results for zinc and lead were presented in Annexure 3 and summarized in Table 10.3.

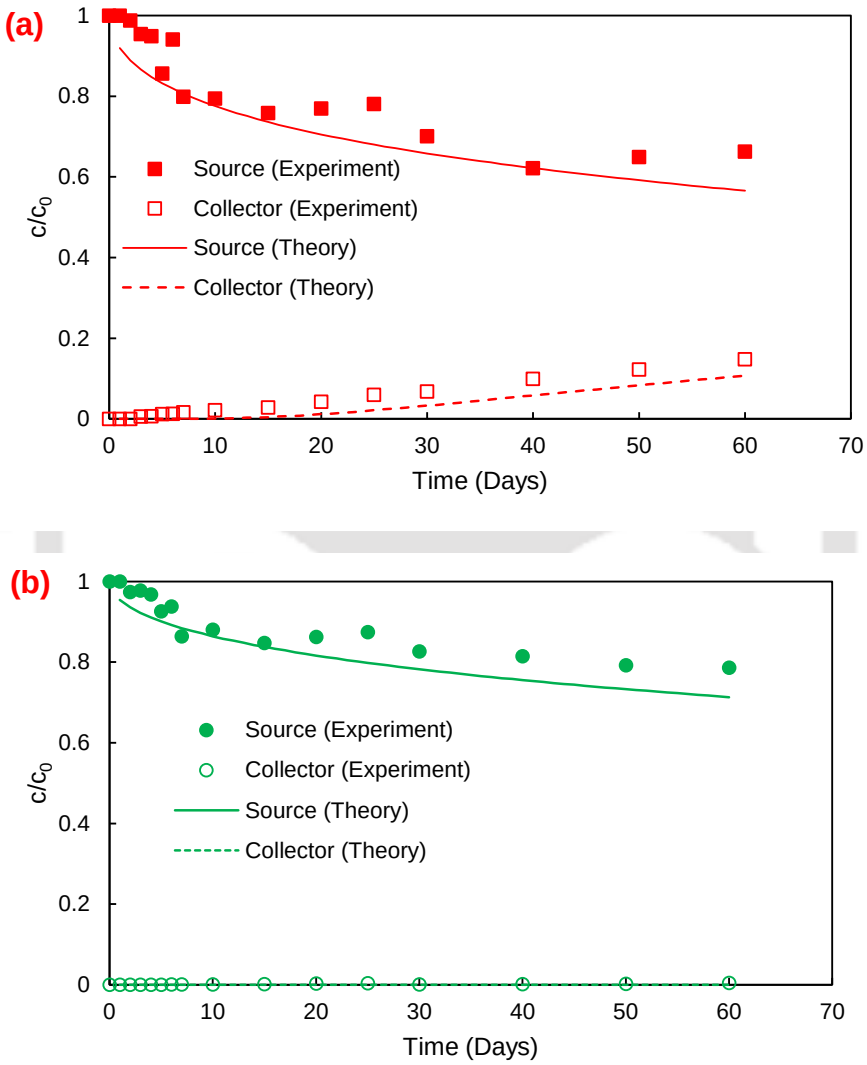

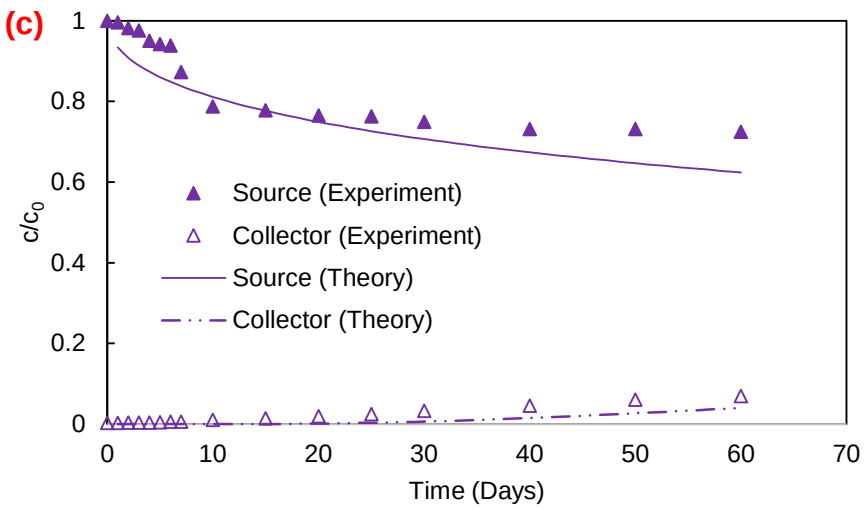

Figure 10.17: Comparison of the experimental and theoretical profile at source and collector reservoir for Cr^{6+} through (a) kaolin; (b) KXG; (c) KGG;

Table 10.3: The diffusion coefficient and retardation factor for kaolin and biopolymer amended kaolin with heavy metals

Material	Pore Fluid	Effective Diffusion Coefficient, D_e	Retardation Factor, R_d	Root mean square error RMSE
Kaolin	1000 ppm Cr^{6+}	1.93×10^{-10} m^2/sec	25.97	0.0235
	1000 ppm Zn^{2+}	1.07×10^{-10} m^2/sec	40.424	0.0447
	1000 ppm Pb^{2+}	1.05×10^{-10} m^2/sec	69.64	0.0482
XG amended Kaolin	1000 ppm Cr^{6+}	3.89×10^{-11} m^2/sec	39.829	0.0165
	1000 ppm Zn^{2+}	6.45×10^{-11} m^2/sec	53.53	0.0394
	1000 ppm Pb^{2+}	5.66×10^{-11} m^2/sec	45.878	0.0165
GG amended Kaolin	1000 ppm Cr^{6+}	1.14×10^{-10} m^2/sec	28.867	0.0296
	1000 ppm Zn^{2+}	5.45×10^{-11} m^2/sec	26.597	0.0292
	1000 ppm Pb^{2+}	2.31×10^{-11} m^2/sec	151.84	0.0154

10.3.3 Numerical simulations of heavy metals through barriers for evaluating the design period

The migration of the contaminants through the engineered barrier is governed by the advection-diffusion equation. After evaluating the individual advection (i.e., hydraulic) and diffusion characteristics (D_e and R_d), the contaminant migration for 3 heavy metals was simulated for a 500 mm thick layer of kaolin, XGK, and GGK. The normalized concentration distribution for chromium was plotted in Figure 10.18 (a-c). The chromium migration was governed by advection in kaolin, whereas it was governed by diffusion in XGK and GGK layers. The kaolin layer of 500 mm thickness attenuated after 2 years with chromium solution. Moreover, the XGK and GGK samples of the same thickness can resist the migration of chromium for more than 50 years as shown in Figure 10.18. Similarly, the contaminant transport profiles for zinc and lead are plotted in Annexure 3.

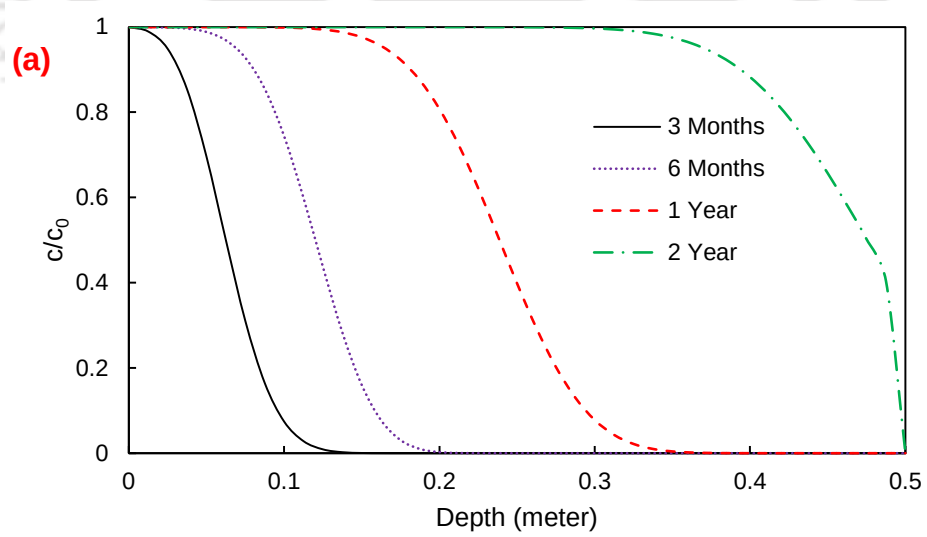

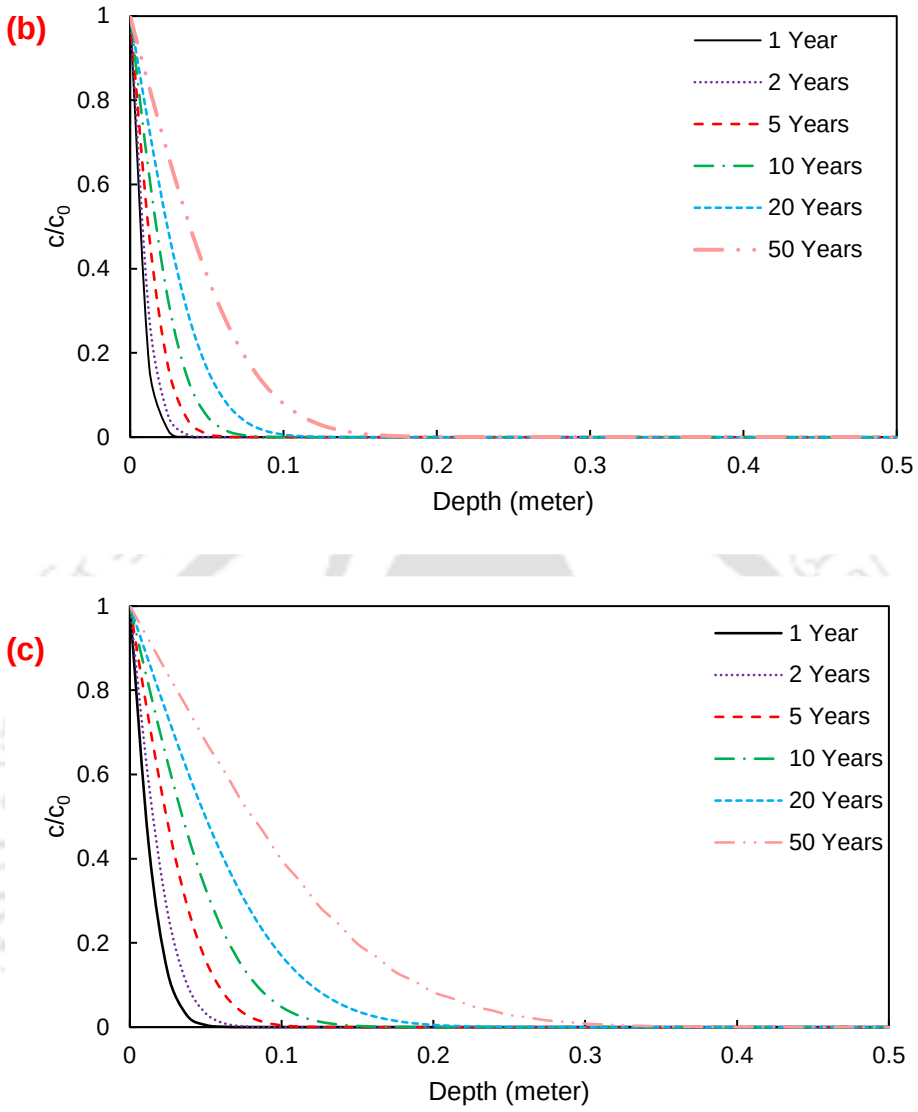

Figure 10.18: Contaminant migration profiles with time for (a) 1000 ppm of chromium solution through (a) kaolin; (b) XGK; and (c) GGK.

10.4 Summary

The study on the engineered barriers for tailing disposal facilities was conducted using salt solutions and heavy metal solutions for permeation experiments and through-diffusion experiments. The following points were drawn from the study:

- ❑ The XG-amended kaolin achieved hydraulic infiltration rates lower than the limiting saturated hydraulic conductivity. The cross-linking of XG chains with positive charge

cations further helped in the reduction in hydraulic infiltration rates, which is evident from the lower sealing time in the presence of divalent cations as compared to the monovalent cations as well as FESEM micrographs.

- The diffusion coefficient of kaolin decreased significantly for all the studied high-ionic-strength salts after amendment with XG and with XG and GG amendment for studied heavy metal solutions due to less availability of the void space with the formation of the gel. The card house structure break-down during initial saturation contributed to much lower D_e and higher R_d.
- The hydraulic head of the tailing disposal facility also plays an important role in contaminant migration through kaolin. The higher hydraulic heads of kaolin were found to be more critical as compared to the lower heads. The hydraulic head did not play a significant role in contaminant migration through XGK, as contaminant migration is governed by the low diffusion mechanism in such cases.
- Even though a recent study (Das & Bharat, 2021) recommended using natural kaolin in addition to GB for barrier applications, the hydraulic performance of kaolin was not found satisfactory at lower compaction densities. An adequate osmotic efficiency was not developed in heavy metals environment at low compaction density.
- The fluid permeation rate of kaolin, XGK, and GGK samples depends on the pH of the medium. Under neutral pH or pH higher than the IEP of the kaolin, the fluid permeation rate decreases upon hydration due to the collapse of the card-house type of structure in kaolin. This behavior was observed with distilled water, chromium, and zinc solution.
- In case of pH of medium lower than the IEP of kaolin, the card-house structure of kaolin does not break, and high fluid permeation rates were observed with lead solution.

- The IEP of biopolymers also plays an important role in fluid permeation rate, the protonation and deprotonation pH of XG was slightly higher than GG. At pH lower than the IEP of the biopolymer, the gel-forming ability reduced significantly and a higher fluid permeation rate for XG was observed as compared to GG with lead solution.
- After amendment with either XG or GG, the diffusion coefficient of kaolin dropped substantially for all the studied heavy metals. This was because the gel developed and less pore space became available. The diffusion setup was initially saturated with distilled water, so the gel formation took place effectively and the card house structure break-down during initial saturation, contributed to much lower D_e and higher R_d. Hence, very low diffusion coefficients were observed for both XGK and GGK
- The XGK was found to be more effective for waste containing chromium, while GGK was found to be more effective for waste containing lead and zinc. Both XGK10 and GGK10 can prevent the migration of chromium, lead, and zinc for 50 years based on contaminant migration profiles.

Chapter – 11

Conclusions and Future Scope

11.1 Conclusions

The GCLs containing GB are utilized as containment to the waste disposal facilities. The performance of GB under harsh leachate condition fails to attain sealing due to loss in swelling potential. The non-sealing of the GCLs can allow the advective flows of the contaminants to the environment. The recent COVID pandemic generated huge quantity of the pathogenic waste, which was forced to disposed to the MSW landfills in absence of proper knowledge on disposal guidelines for such pandemic waste. The present work studied clay minerals to evaluate the attenuation ability of the viral pathogens before their disposal to the either MSW landfill or exclusive BMW disposal facility. The following conclusions were derived from the study:

- The grain sizes of GB in GCLs influence the hydraulic performance in the presence of high-ionic salt solutions. Further, the mechanical processing of GB to achieve finer GB helps in achieving the self-sealing of macro-voids to contain leachate containing high strength salt solutions in landfills.

- Linear anionic high viscous biopolymer, xanthan gum, in small percentages (2%) is found useful to achieve the self-sealing ability of bentonite under adverse conditions. However, cross-linked water adsorbing polymer, linear neutral biopolymer, as well as linear anionic low viscous biopolymer failed to achieve the sealing ability under adverse chemo-hydro-mechanical loading conditions. Further, the lower percentages of the XG also failed to

attain self-sealing at elevated temperatures. A higher percentage (> 5%) is required to attain self-sealing at elevated temperatures.

- The sorption of coronavirus surrogate, Newcastle disease virus (NDV), on six different clays showed almost 100 % sorption at clay concentration over 10 mg/mL. The illite clay mineral showed minimum sorption ability of NDV, while bentonite and Halloysites showed maximum sorption ability at clay concentration lower than 10 mg/mL. Protocols for the disposal of pathogenic waste were proposed using two commonly available clays viz., bentonite and kaolin due to wider availability and economical reasons.

- The sorption of NDV on bentonite is also influenced by the presence and the type of the exchangeable cation. The cation bridging is the main mechanism behind the adsorption of NDV on to the bentonite.

- The sorption ability of the viral pathogens is also influenced by the grain sizes of the GB and virus type. The sorption experiment with H1N1 virus showed better sorption ability a lower influence on the grain size and better sorption ability as compared to JEV. The JEV showed better sorption ability on the finer GB due to a larger exposed surface area.

- The presence of high ionic strength salts in the landfill leachate significantly impact the performance of the liner by permeation of viruses due to GB's inability to break into individual particles. Finer GB (D50 < 0.1 mm granule size) or powdered bentonite could prevent viral contamination even in the presence of high-ionic salts.

- The diffusion coefficient and retardation factor were evaluated for the first time for any virus through compacted clays. The diffusion coefficient of coronavirus surrogate through compacted bentonite was found to be 1.67×10^{-9} m^2/s and 3.91×10^{-10} m^2/sec through

compacted kaolin at 1.2 Mg/m^3 dry density. However, very high value of retardation factor 3572 for bentonite and 2348 for kaolin were found. Moreover, the study also considered the biological decay of the virus in the evaluation of these parameters. The evaluated parameters are helpful in designing the BMW containment facilities.

- Biopolymer-amended kaolin-based barriers were proposed for areas having high availability of kaolin and scarcity of bentonite. The XG-amended kaolin achieved sealing and showed lower diffusion of salts in a high-concentration salt solution environment. Biopolymer-amended kaolin-based barriers were also proposed for the containment of waste having heavy metals.

11.2 Future Scope

The BMW containment facilities is proposed with compacted liner using bentonite and kaolin clay. The present study only considered the clays compacted at 1.2 Mg/m^3. However, the clays can be compacted at higher dry density to improve the performance of the BMW liner systems. So, the role of density in permeation rate as well as diffusion experiments needs to be explored.

The biopolymer as degradable in nature and might degrade in long run. The ability of biopolymer to form the hydrogel can reduce over long period. So, the degradation aspects of the biopolymers important and can be explored in future.

The GCLs are subjected to several atmospheric and environmental conditions, including rainfall and sunlight. These atmospheric conditions lead to the undergo the liner under several wetting-drying cycles. These alternative wetting and drying cycle led to reduction in swelling ability of the bentonites. The understanding on the hydraulic performance of GCLs after exposure to several wetting drying cycles is to be explored.

The present work discussed the hydration of the GCLs high-ionic salt solution directly to the unhydrated GB. Moreover, the permeation of the GCLs with water without any salt can seal the macro-voids present in GB. Prior hydration with water, before exposing it to the chemicals or leachates can be useful. So, the role of pre-hydration on hydraulic performance is required to be studied.

Annexure-1

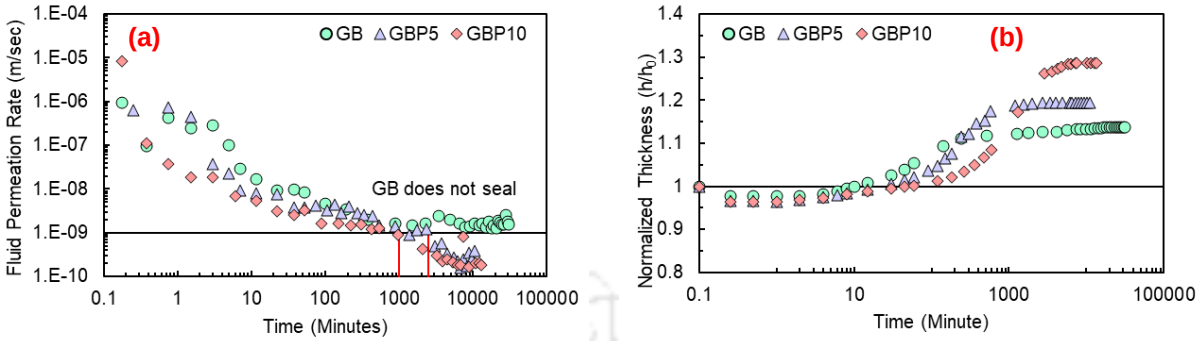

Figure A1.1: Temporal variations of (a) fluid permeation rate; (b) normalized thickness of GB and polymer amended GB with 0.5M NaCl under 50 kPa mechanical loading.

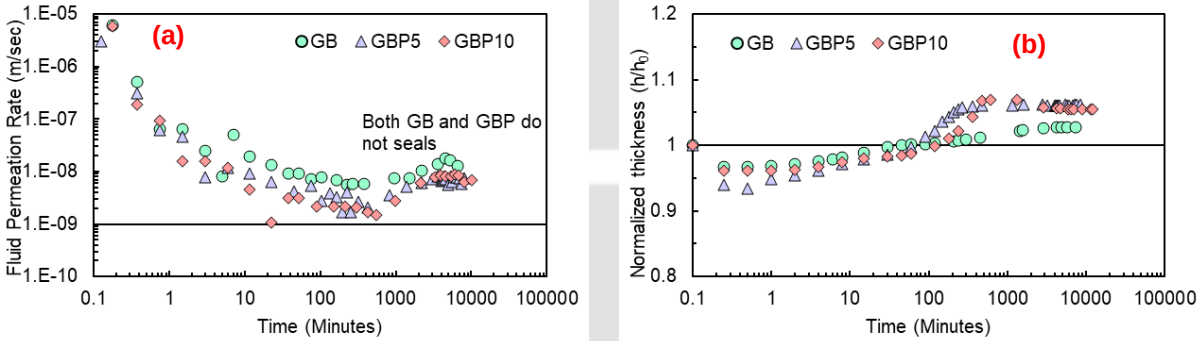

Figure A1.2: Temporal variations of (a) fluid permeation rate; (b) normalized thickness of GB and polymer amended GB with 0.5 M $CaCl_2$ under 50 kPa mechanical loading.

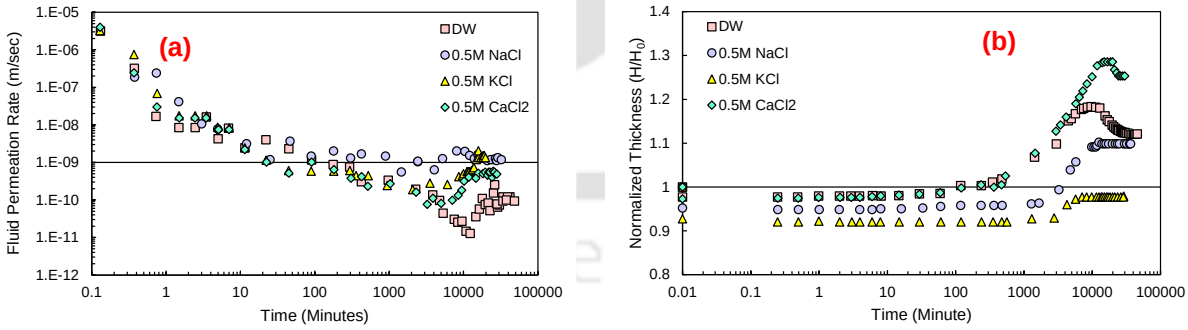

Figure A1.3: Temporal variations of (a) fluid permeation rates; (b) normalized thickness under 50 kPa mechanical loadings for GBGG samples with different pore-fluids

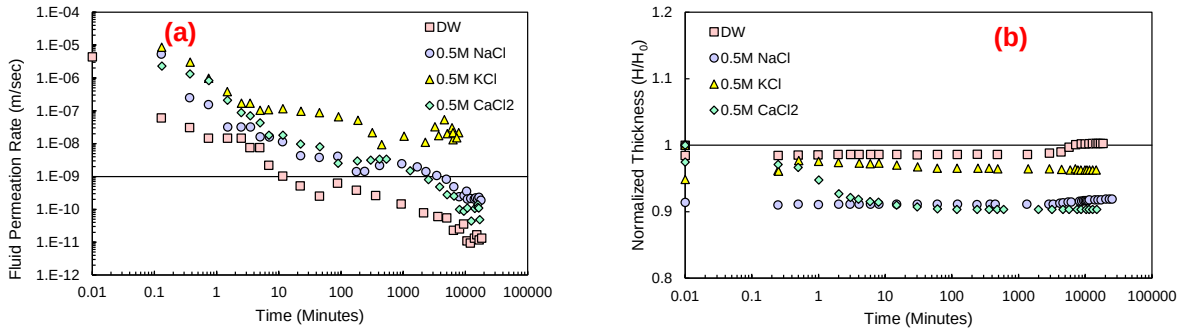

Figure A1.4: Temporal variations of (a) fluid permeation rates; (b) normalized thicknesses under 50 kPa mechanical loadings for GBAG samples with different pore-fluids

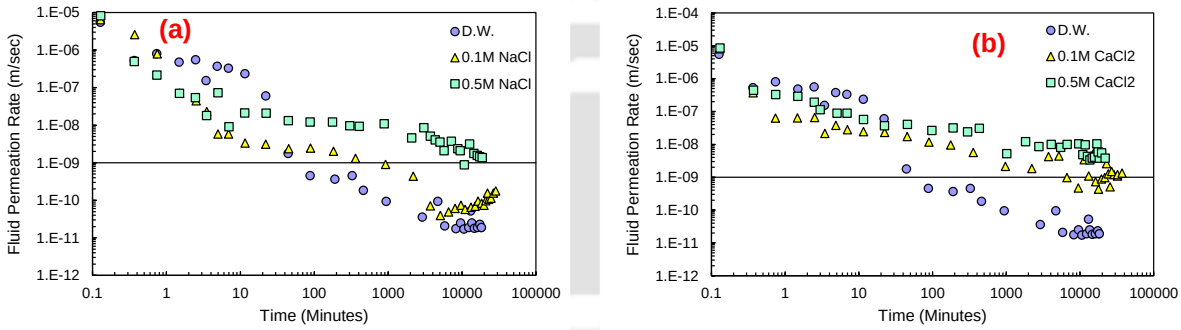

Figure A1.5: Temporal variations of fluid permeation rates with different concentrations of (a) NaCl (b) $CaCl_2$ for GBAG samples under 20 kPa mechanical loading

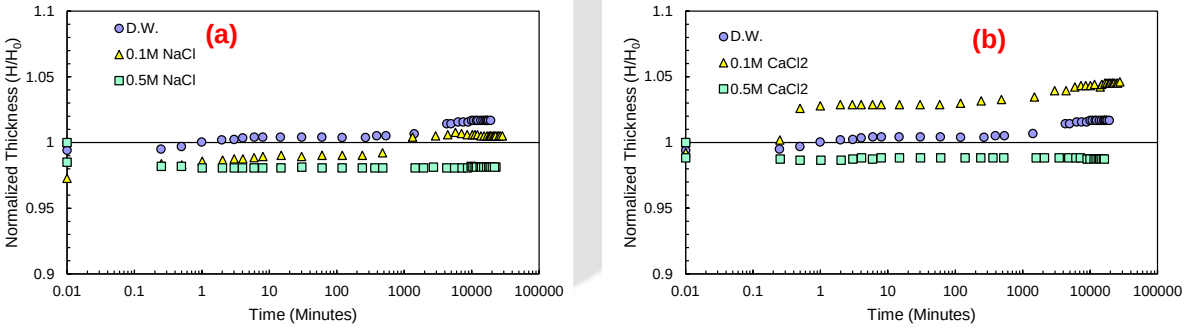

Figure A1.6: Temporal variations of normalized thicknesses with different concentrations of (a) NaCl (b) $CaCl_2$ for GBAG samples under 20 kPa mechanical loading

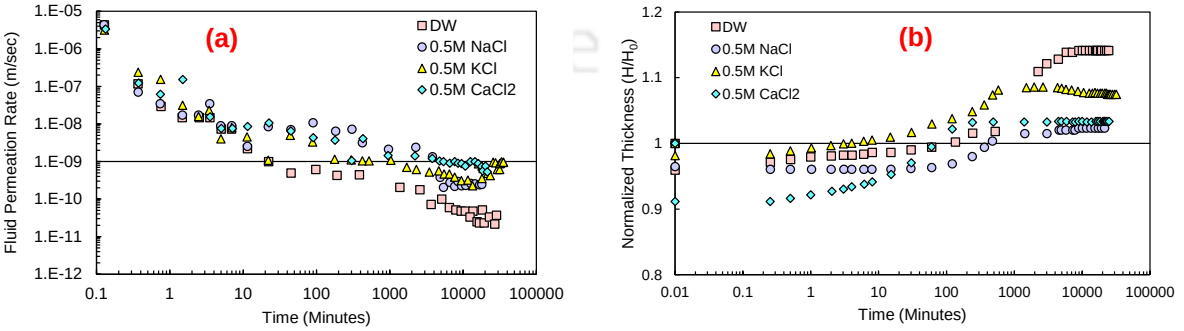

Figure A1.7: Temporal variations of (a) fluid permeation rates; (b)normalized thicknesses under 50 kPa mechanical loadings for GBAA samples with different pore-fluids

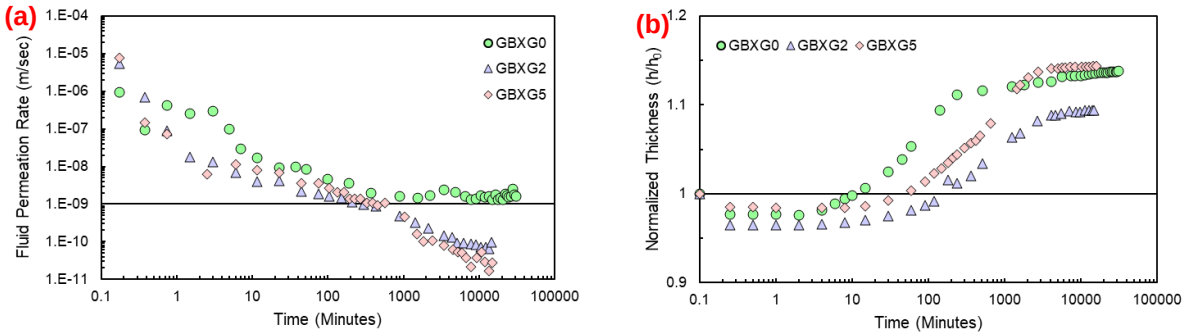

Figure A1.8: Temporal variations of (a) fluid permeation rate; (b) normalized thickness of GB and xanthan gum amended GB with 0.5M NaCl under 50 kPa mechanical loading.

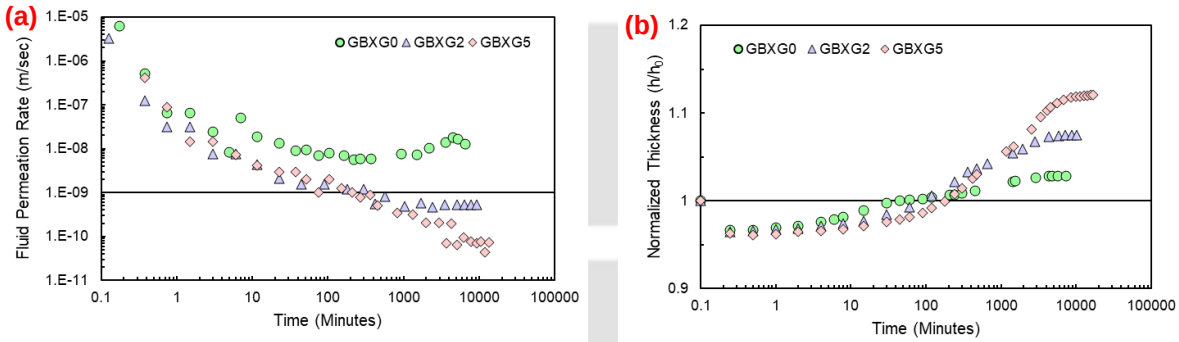

Figure A1.9: Temporal variations of (a) fluid permeation rate; (b) normalized thickness of GB and xanthan gum amended GB with 0.5 M $CaCl_2$ under 50 kPa mechanical loading.

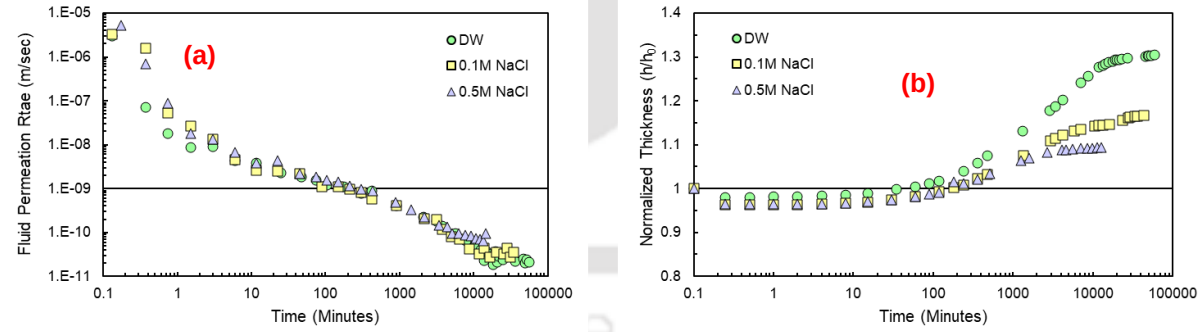

Figure A1.10: Temporal variations of (a) fluid permeation rate; (b) normalized thickness of xanthan gum amended GB (2% XG) with different concentrations of NaCl under 50 kPa mechanical loading.

(a)

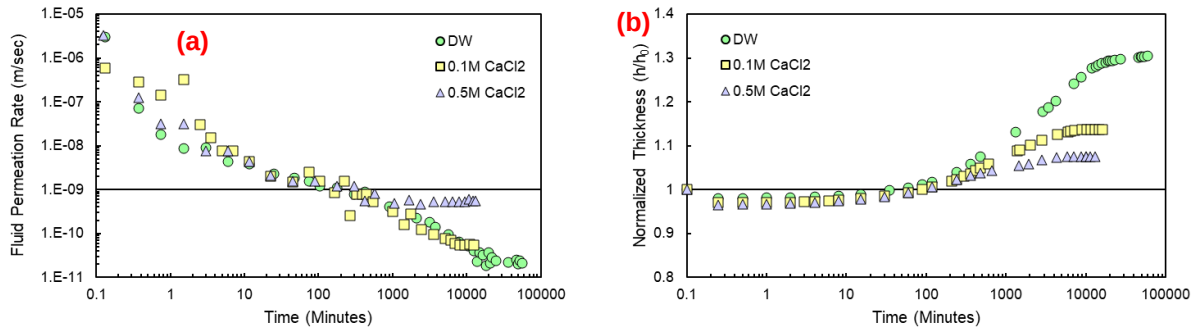

Figure A1.11: Temporal variations of (a) fluid permeation rate; (b) normalized thickness of xanthan gum amended GB (2% XG) with different concentrations of $CaCl_2$ under 50 kPa mechanical loading.

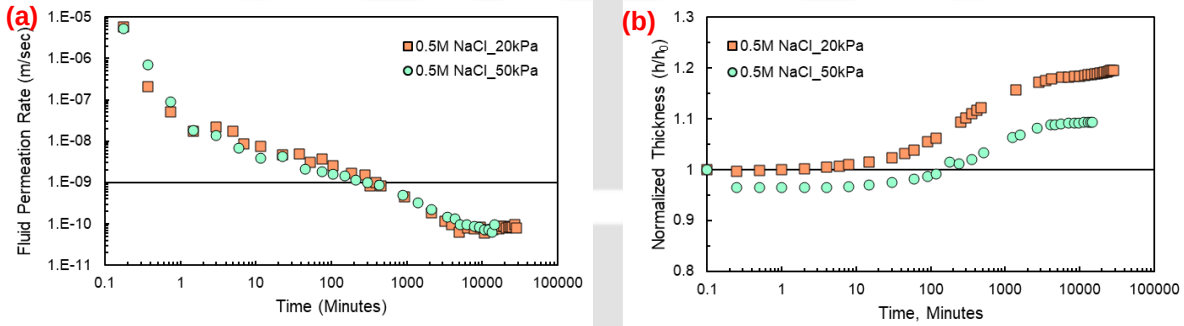

Figure A1.12: Temporal variations of (a) fluid permeation rates; (b) normalized thicknesses of GBXG2 samples under different mechanical loadings for 0.5M NaCl

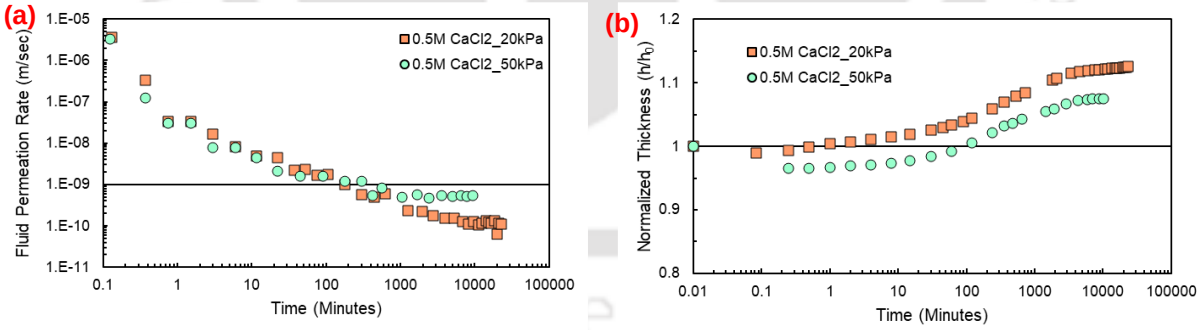

Figure A1.13: Temporal variations of (a) fluid permeation rates; (b) normalized thicknesses of GBXG2 samples under different mechanical loadings for 0.5M $CaCl_2$

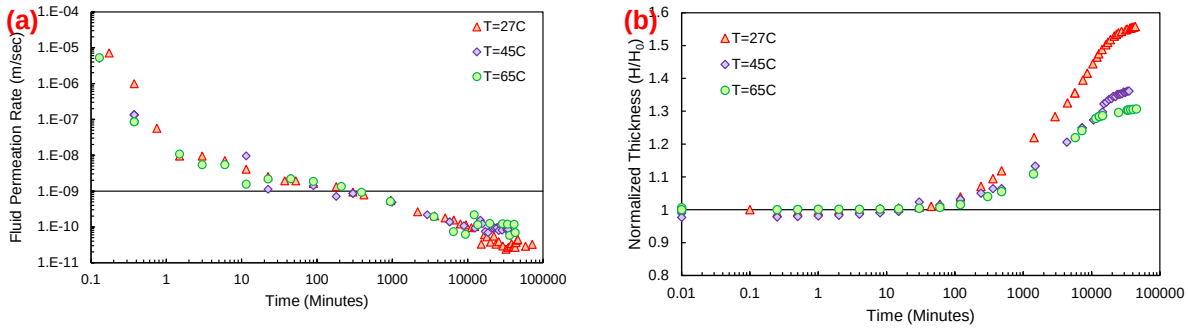

Figure A1.14: Temporal variations of (a) fluid permeation rates; (b) normalized thicknesses of GBXG2 under different temperature with distilled water as pore-fluid under 20 kPa mechanical loading.

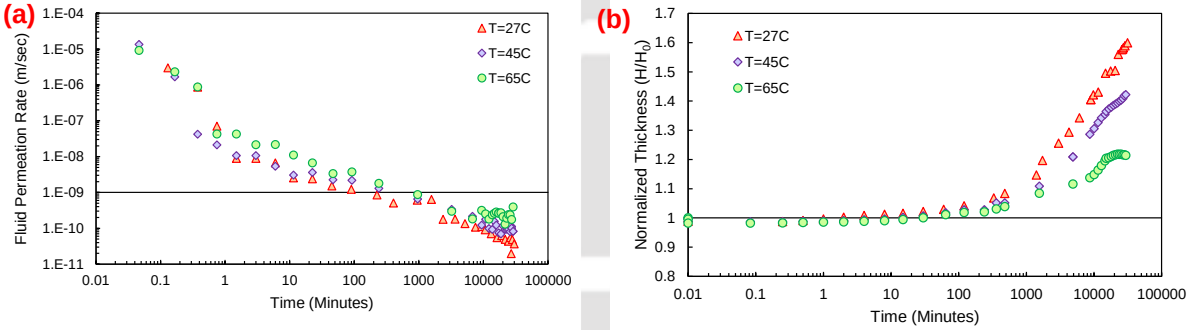

Figure A1.15: Temporal variations of (a) fluid permeation rates; (b) normalized thicknesses of GBXG5 under different temperature with distilled water as pore-fluid under 20 kPa mechanical loading.

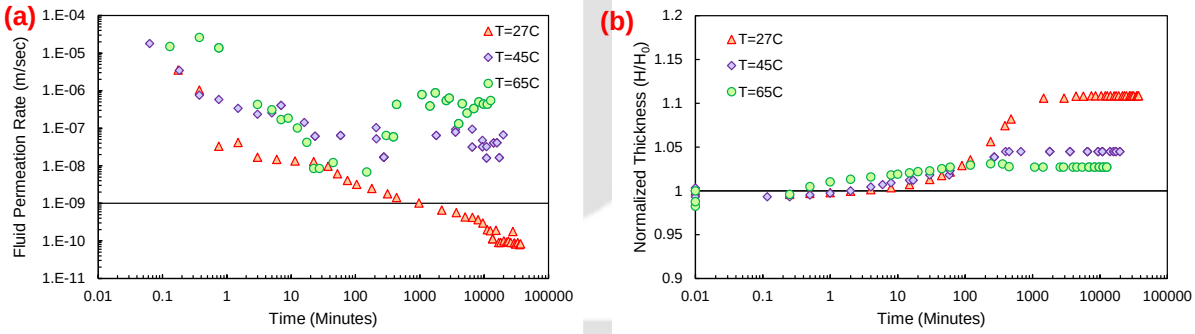

Figure A1.16: Temporal variations of (a) fluid permeation rates; (b) normalized thicknesses of GBXG2 for different temperatures with 0.5M KCl as pore-fluid under 20 kPa mechanical loading.

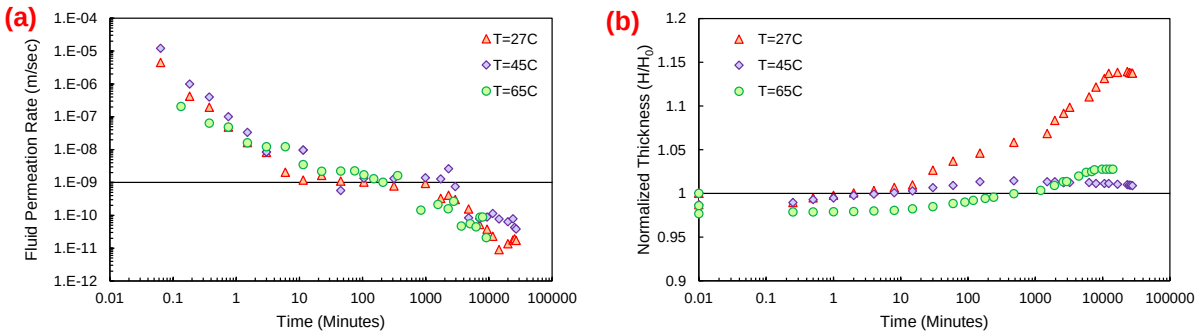

Figure A1.17: Temporal variations of (a) fluid permeation rates; (b) normalized thicknesses of GBXG5 for different temperatures with 0.5M KCl as pore-fluid under 20 kPa mechanical loading.

Annexure 2

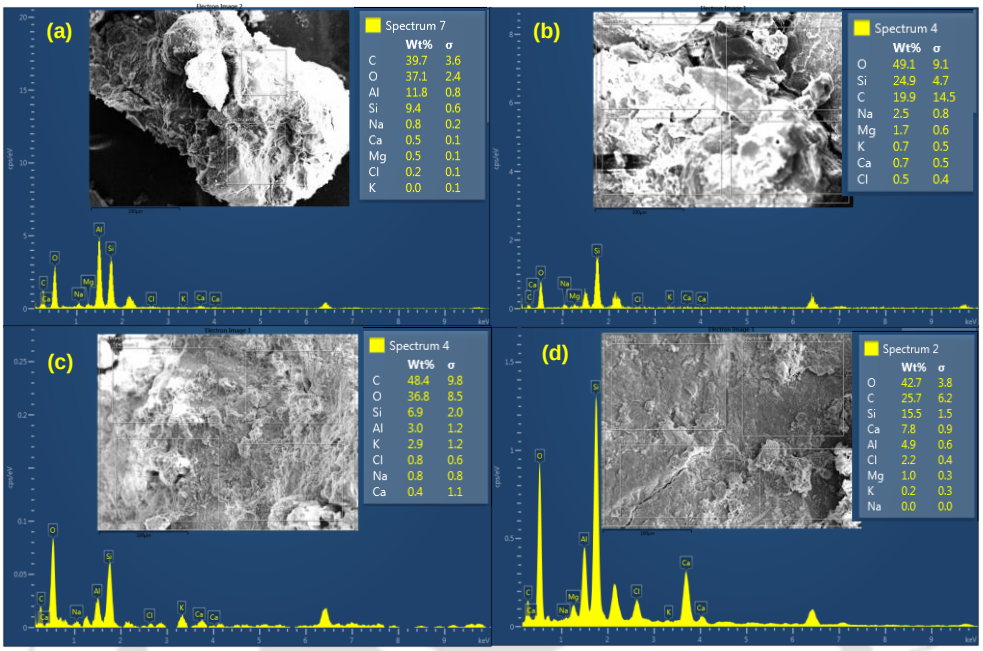

Figure A-2.1: Energy dispersive X-ray spectroscopy spectra for GB samples amended with 10% AG samples after permeation with (a) D.W.; (b) 0.5 M NaCl; (c) 0.5 M KCl; and (d) 0.5 M $CaCl_2$ as pore-fluid under 20kPa mechanical loading

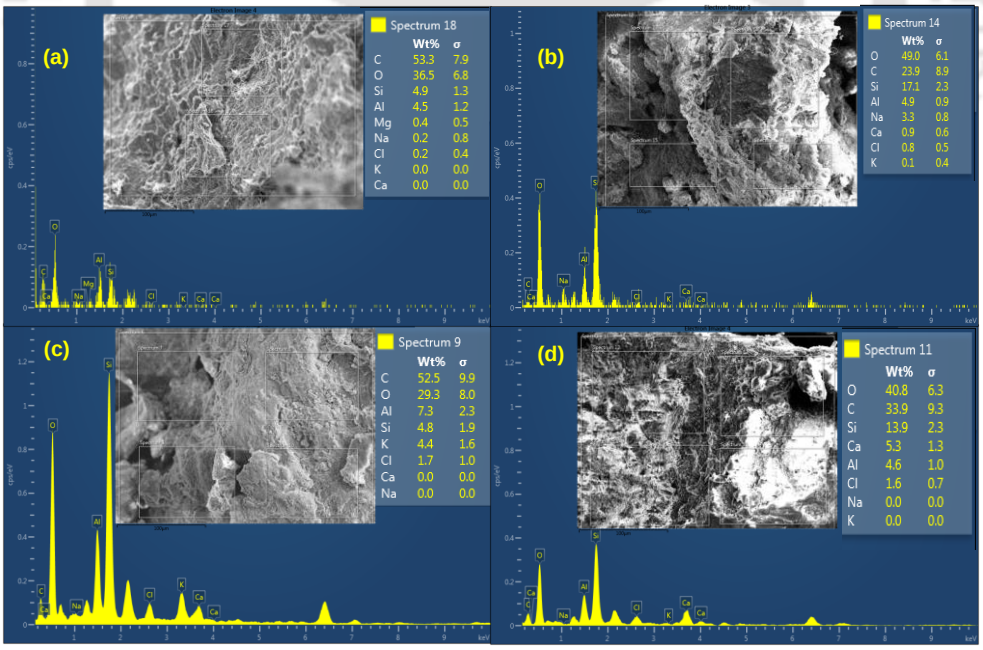

Figure A-2.2: Energy dispersive X-ray spectroscopy spectra for GB samples amended with 10% agar-agar gum after permeation with (a) D.W.; (b) 0.5 M NaCl; (c) 0.5 M KCl; and (d) 0.5 M $CaCl_2$ as pore-fluid under 20kPa mechanical loading

Annexure 3

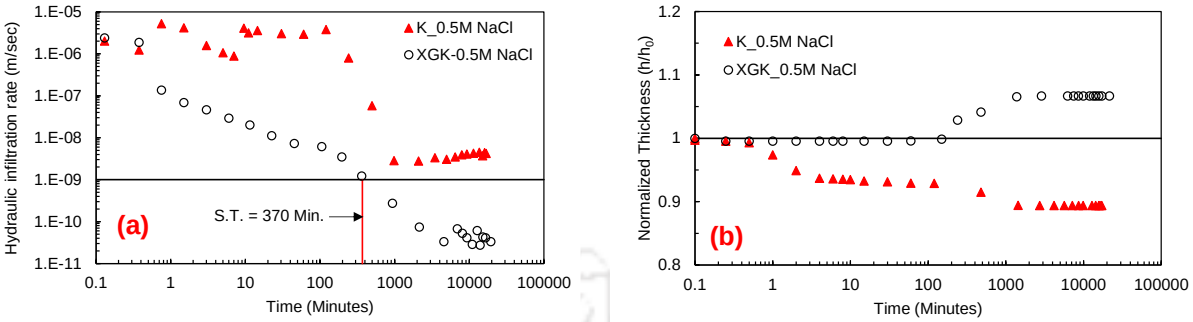

Figure A3.1: *Temporal variations of (a) hydraulic infiltration; (b) normalized thickness for kaolin and XGK with 0.5M NaCl under 20 kPa mechanical loading.*

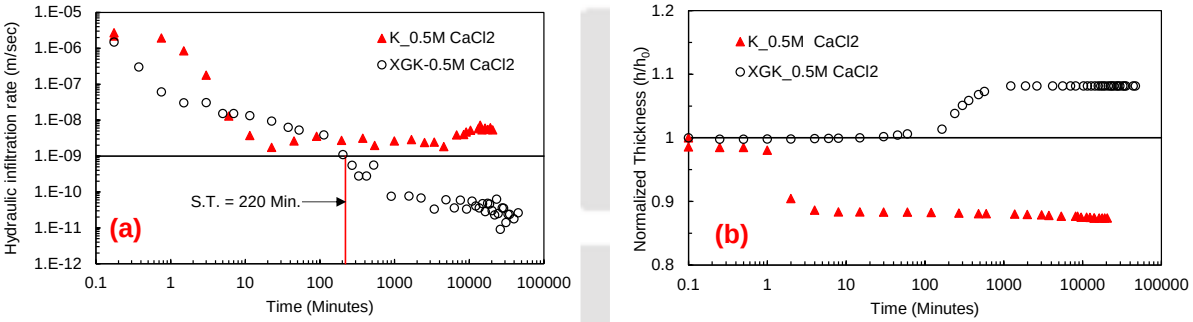

Figure A3.2: *Temporal variations of (a) hydraulic infiltration; (b) normalized thickness for kaolin and XGK with 0.5M $CaCl_2$ under 20 kPa mechanical loading.*

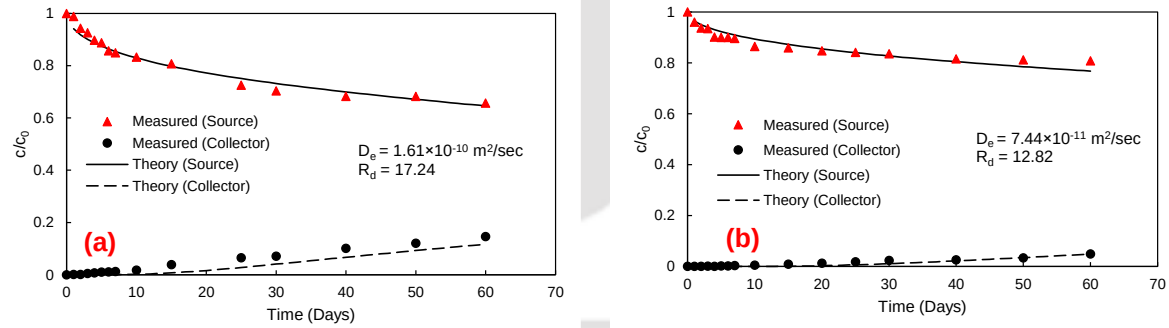

Figure A3.3: *Comparison of experimental measured and theoretical profile at source and collector reservoir for (a) Kaolin; and (b) XGK with 0.5M KCl.*

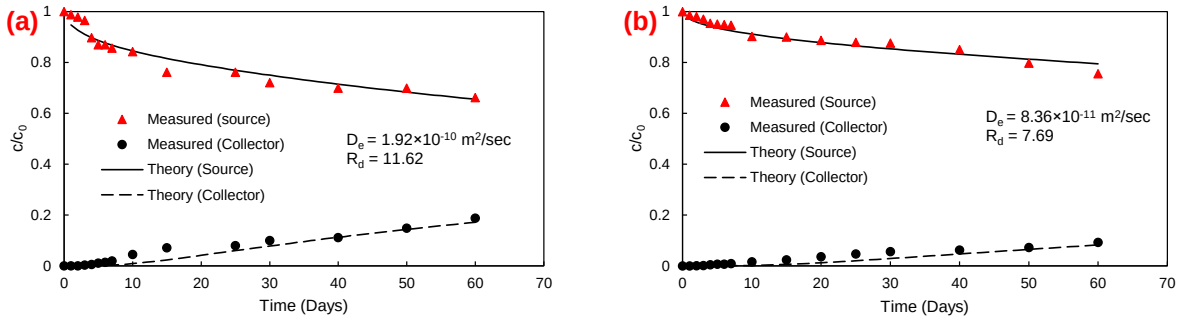

Figure A3.4: *Comparison of experimental measured and theoretical profile at source and collector reservoir for (a) Kaolin; and (b) XGK with 0.5M $CaCl_2$.*

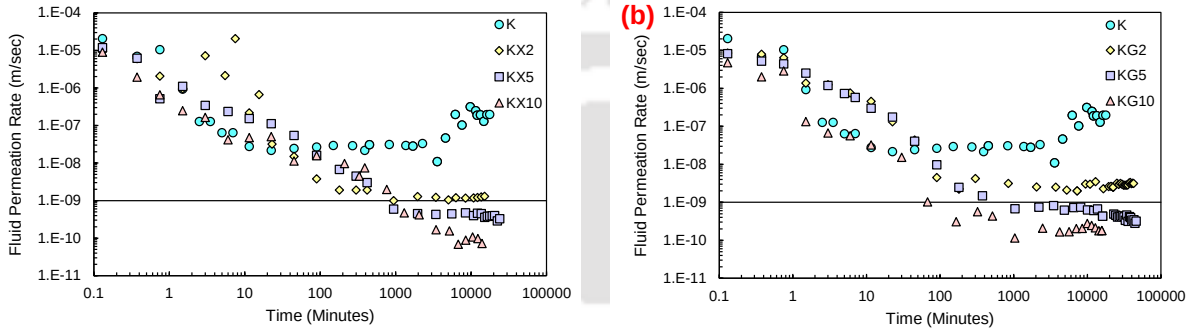

Figure A3.5: Temporal variations of fluid permeation rates with chromium solution as pore-fluid for kaolin amended with (a) xanthan gum; and (b) guar-gum

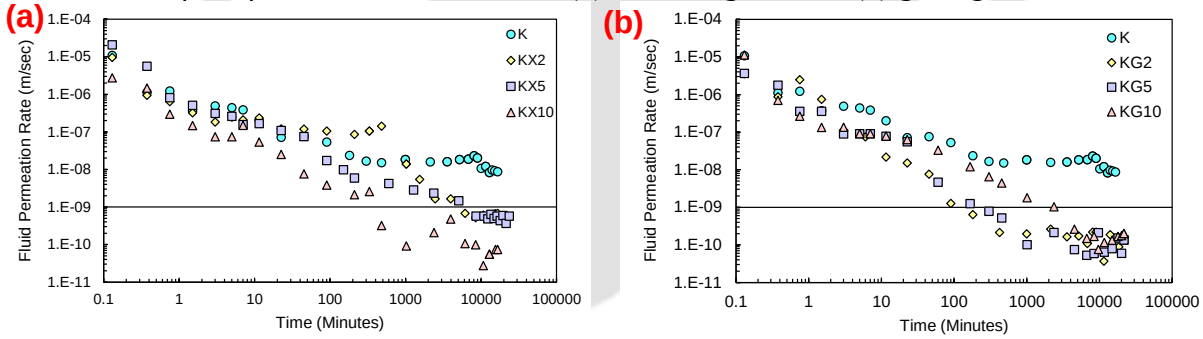

Figure A3.6: Temporal variations of fluid permeation rates with zinc solution as pore-fluid for kaolin amended with (a) xanthan gum; and (b) guar-gum

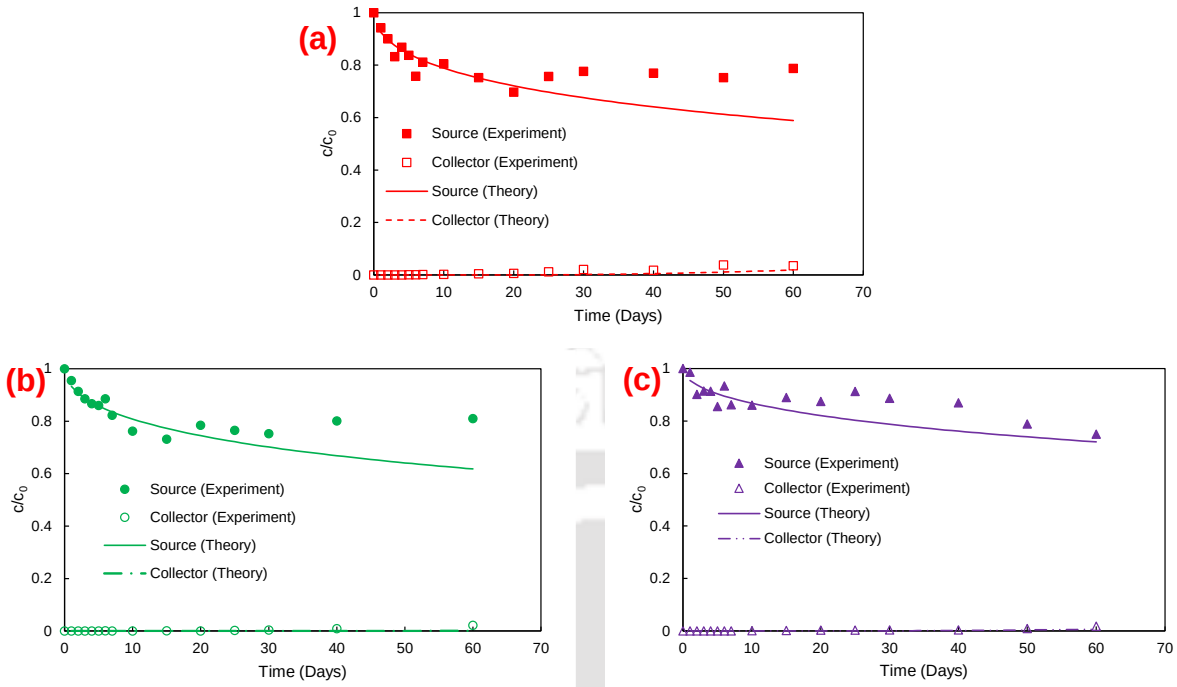

Figure A3.7: Comparison of the experimental and theoretical profile at source and collector reservoir for Zn^{2+} through (a) kaolin; (b) KXG; (c) KGG;

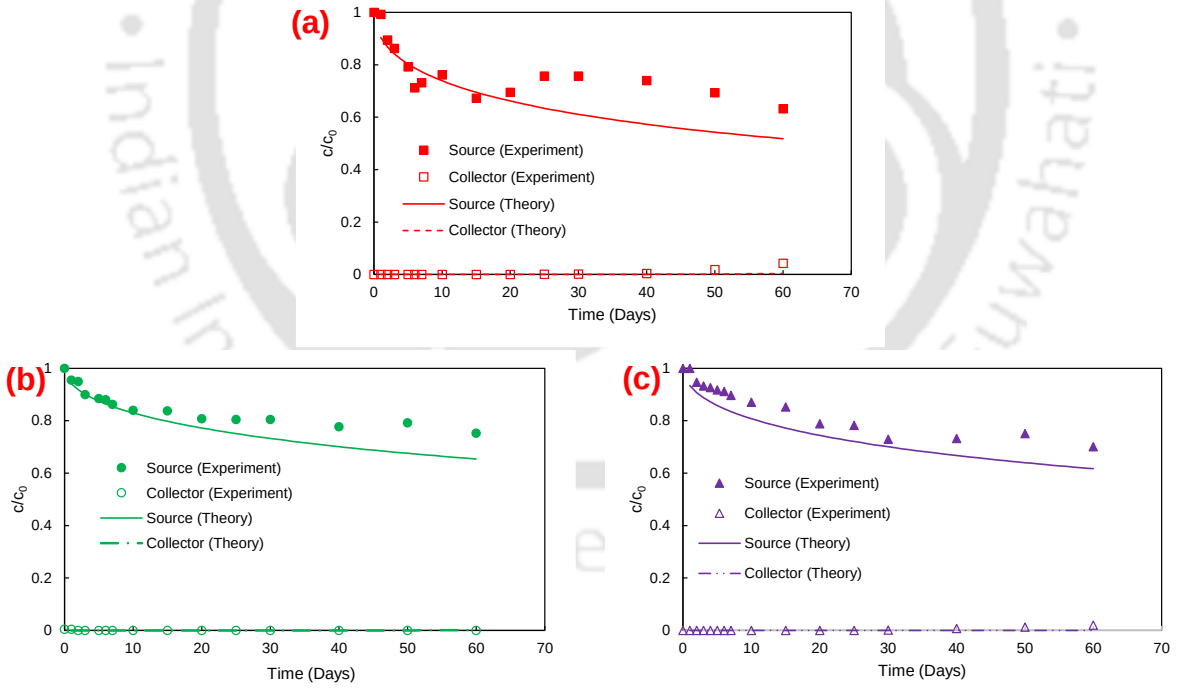

Figure A3.8: Comparison of the experimental and theoretical profile at source and collector reservoir for Pb^{2+} through (a) kaolin; (b) KXG; (c) KGG;

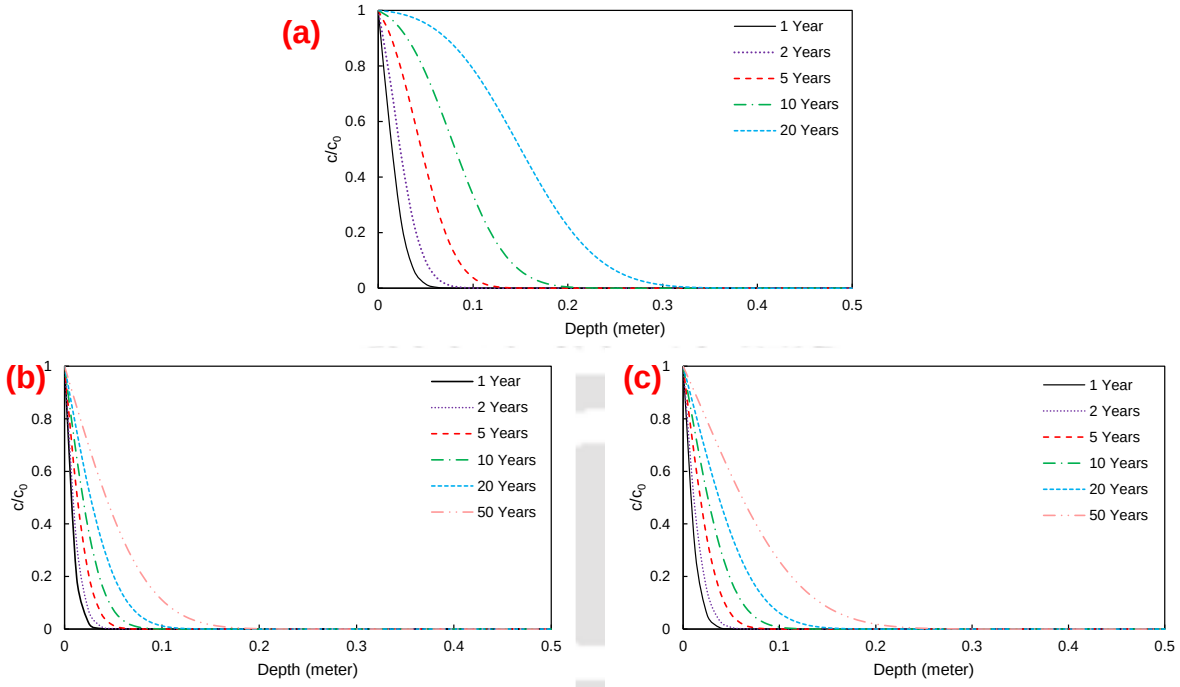

Figure A3.9: Contaminant migration profiles with time for (a) 1000 ppm of zinc solution through (a) kaolin; (b) XGK; and (c) GGK.

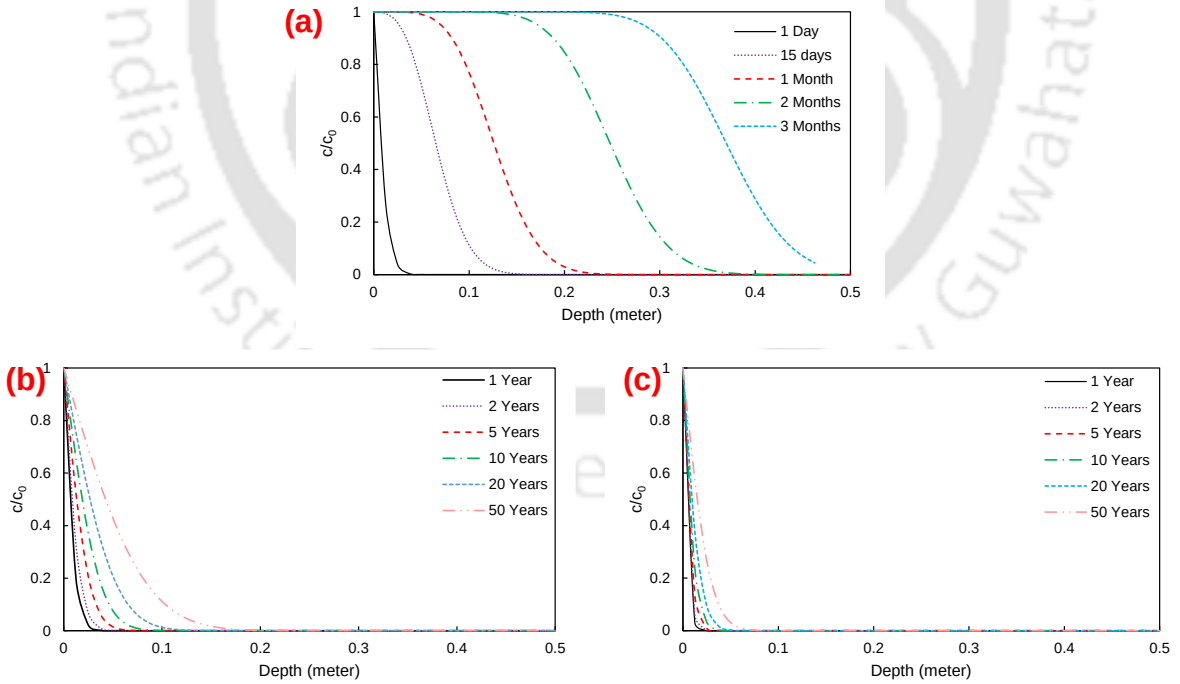

Figure A3.10: Contaminant migration profiles with time for (a) 1000 ppm of lead solution through (a) kaolin; (b) XGK; and (c) GGK.

List of Publications

Journal (From Thesis)

Himanshu Yadav, T.V. Bharat, Shubham Gaurav, and Sachin Kumar 2023. *"Fate and Transport of Coronavirus Surrogate through Compacted Clays for Pathogenic Waste Disposal".* Langmuir, ACS Publications.

Himanshu Yadav and T.V. Bharat 2022. *"The Influence of Mechanical Granulation Process and Plasticity of Granular Bentonite on Self-Sealing and Volume Change Behavior.*" Journal of Hazardous, Toxic and Radioactive Waste. ASCE. (DOI: 10.1061/(ASCE)HZ.2153-5515.0000688).

Himanshu Yadav, T.V. Bharat, and Sachin Kumar. "*Xanthan Gum and Guar Gum Amended Kaolin for Containment of Heavy Metals"* (revision submitted)

Himanshu Yadav and T.V. Bharat. "*Biopolymer amended Kaolin as a Barrier in Tailing Disposal Facilities*." (under review)

Himanshu Yadav, Ajeet Sharma, and T.V. Bharat. "*Biopolymer-amended Granular Bentonite as Engineered Barrier for Municipal Solid Waste Containment Facilities*" (under review).

Himanshu Yadav, and T.V. Bharat. "*Sealing, Volume Change and Diffusion Characteristics of Polymer and Biopolymer amended Granular Bentonite"* (under review)

Himanshu Yadav, Deepa Mehta, T.V. Bharat, Sachin Kumar. Role of Grain Sizes of GB in *Fate and Transport of H1N1 Influenza Virus. (under preparation)*

Himanshu Yadav, Deepa Mehta, T.V. Bharat, Sachin Kumar. *Role of Grain Sizes of GBs in fate and transport of Japanese encephalitis virus. (under preparation)*

Himanshu Yadav, Deepa Mehta, Sahil Kumar, T.V. Bharat, Sachin Kumar. "*Mechanism governing the NDV-bentonite interactions based on experimental and modified DLVO theory." (under preparation)*

Himanshu Yadav, Deepa Mehta, T.V. Bharat, *Sachin Kumar. Role of Mineralogy on NDV-clay interactions (under preparation).*

Himanshu Yadav, T.V. Bharat, *Hydraulic and Volume change of XG amended GB under thermo-chemo-mechanical loadings. (under preparation)*

Journal (Outside Thesis)

T.V. Bharat, **Himanshu Yadav**, J.P. Mahaur and Shriram Kushwaha 2020. *"Effect of Aging time on Consistency Limit Water Contents of Bentonites."* Geotechnical and Geological Engineering. (DOI: doi.org/10.1007/s10706-020-01251-3).

Himanshu Yadav, Deepa Mehta, T.V. Bharat, Sachin Kumar. "A Novel Protocol for Detection and Quantification of Coronavirus-Surrogate Based on Clay-Virus Sedimentation Behavior." (under review)

Himanshu Yadav, Dhanesh Sing Das, T.V. Bharat. *Critical Appraisal of Methods for Determination of Specific Surface Area of Clays (under preparation).*

PATENTS

T.V. Bharat, Sachin Kumar, **Himanshu Yadav**, Subham Gaurav. A device for pathogenic waste disposal and a method thereof. (Status: Filed, Application No. 202331086448).

International Conference

Himanshu Yadav, Deepa Mehta, T. V. Bharat, Sachin Kumar. *"Fate and Transport of Viral Pathogens through Clays"* 61st Clay Mineral Society Meeting, Expanding Clay Science. Honolulu, Hawaii, USA. 3rd – 6th June, 2024.

Himanshu Yadav, T.V. Bharat, Sachin Kumar. "*Viral Pathogenic Waste Containment with Natural Clays*". GeoenvironMeet 2024, 8-11, September, 2024. (Accepted)

Sahil Kumar, **Himanshu Yadav**, and T.V. Bharat. 2024. *"Geo-polymerization of kaolin Amended Black Cotton Soil"* Geo-Congress 2024, Vancouver, Canada, 25th – 28th Feb., 2024

Himanshu Yadav, Ajeet Sharma and T.V. Bharat. 2023. "*Hydraulic and Volume Change Behavior of Guar Gum Amended Granular Bentonite for Containment Applications"* 9th International Conference on Environmental Geotechnics. Chania, Greece, 25th – 28th June, 2023.

Himanshu Yadav, Shubham Gaurav, T.V. Bharat, and Sachin Kumar 2022. *"Sorption Characteristics of Newcastle Disease Virus with Kaolin"* 17th International Clay Conference. Istanbul, Turkey. 25-29 July, 2022.

Himanshu Yadav and T.V. Bharat 2022. *"Bentonite based barriers for protecting offshore monuments from saltwater intrusion."* Third International Symposium of TC301 of ISSMGE Geotechnical Engineering for the Preservation of Monuments and Historic Sites**.** Napoli (Italy) Date: 22-24 June 2022.

Himanshu Yadav and T.V. Bharat 2022. *"Sealing and Volume Change Behaviour of Polymer Amended Granular Bentonite under Extreme Chemical Loading."* Geo-Congress

2022, 20th – 23rd March, Geotechnical Special Publication, GSP – 335. ASCE. pp 199-208.

Himanshu Yadav, Partha Das and T.V. Bharat 2021. *"Influence of Inorganic Salts on the Hydro – Mechanical Behaviour of Compacted Granular Bentonite."* 23rd International Conference on Geoenvironmental Engineering and Applications. Boston, USA on 22nd – 23rd April 2021.

National Conference

Himanshu Yadav, T.V. Bharat (2022). "*Sealing and Volume Change Behaviour of Gellan Gum amended Granular Bentonite under Extreme Chemical Loading for Landfill Applications*" Indian Geotechnical Conference (IGC-2022), Kochi Kerala, India on 15th – 17th December, 2022.

Himanshu Yadav, Ajeet Sharma, and T.V. Bharat (2022). *"Influence of Inorganic Salts on Hydraulic and Volume Change Behaviour of Granular Bentonite under Loading Condition."* NERC IIT Guwahati. 20th – 22nd May, 2022.

Himanshu Yadav and T.V. Bharat (2021). "*Hydraulic and Volume Change Behaviour of Water Absorbing Polymer Amended Granular Bentonite under Chemo – Mechanical Loadings*." Eighth Indian Young Geotechnical Conference at IIT Madras, Chennai, on 17th – 18th September, 2021.

Himanshu Yadav and T. V. Bharat (2019). "*Effect of Heavy Metals Contamination on Diffusion Characteristics of Compacted Clay Liners - A Review.*" Indian Conference on Geotechnical and Geo-environmental engineering at MNNIT Allahabad on 1st – 2nd March, 2019.

REFERENCES

- Abebe, S., Raju, R., Berhanu. G., 2017. Health care solid waste generation and its management in Hawassa Referral Hospital of Hawassa University, Southern, Ethiopia." Int J Innov Res Dev. 2017; 6:126–32.
- Acikel A.S., Gates W.P., Singh R.M., Bouazza A., and Rowe R.K. 2018. Insufficient initial hydration of GCLs from some subgrades: Factors and causes. Geotextiles and Geomembrane 46, 770 – 781.
- Acikel A.S., W.P. Gates, R.M. Singh, A. Bouazza, D.G. Fredlund, and R.K. Rowe. 2018b. "Time-dependent unsaturated behaviour of geosynthetic clay liners." Candian Geotechnical Journal. 55, 1824-1836. dx.doi.org/10.1139/cgj-2017-0646.
- Acikel, A.S., W.P. Gates, R.M. Singh, A. Bouazza, and R.K. Rowe. 2018a. "Insufficient initial hydration of GCLs from some subgrades: Factors and causes." *Geotextiles and Geomembrane* 46, 770 – 781.
- Aguzzi, C., Cerezo, P., Viseras, C., Caramell, C., (2007). Use of clays as drug delivery systems: possibilities and limitations. Applied Clay Science 36, 22–36.
- Ahamed, T.; Hossain, K.M.; Billah, M.M.; Islam, K.M.D.; Ahasan, M.M.; and Islam, M.E.; Adaptation of Newcastle disease virus (NDV) on Vero cell line. *Int. J. Poult. Sci.*, **2004,** 3: 153-156.
- Allen, A., 2001. Containment landfills: the myth of sustainability, Engineering Geology, Volume 60, Issues 1–4,2001,Pages 3-19,ISSN 0013-7952,https://doi.org/10.1016/S0013-7952(00)00084-3.
- Anand, U., X., Li, K., Sunita, S., Lokhandwala, P., Gautam, S., Suresh, ... & G., Jiang. 2022. "SARS-CoV-2 and other pathogens in municipal wastewater, landfill leachate, and solid waste: A review about virus surveillance, infectivity, and inactivation." *Environmental Research*, *203*, 111839.
- Anders, R., & Chrysikopoulos, C. V. (2009). Transport of viruses through saturated and unsaturated columns packed with sand. *Transport in Porous Media*, *76*, 121-138.
- Anderson R., M.T. Rayhani*, R.K. Rowe. 2012. Laboratory Investigation of GCL hydration from clayey sand subsoil. Geotextiles and Geomembranes. 31, 31-38.

- Ashmawy, A., E. Darwish, N. Sotelo, and N. Muhammad. 2002. “Hydraulic performance of untreated and polymer-treated bentonite in inorganic landfill leachates.” Clays Clay Miner. 50 (5): 546–552. https://doi.org/10.1346/000986002320679288.
- ASTM D4318-17e1, 2017. Standard Test Methods for Liquid Limit, Plastic Limit, and Plasticity Index of Soils. ASTM International, West Conshohocken, PA.
- ASTM D5856. (2015) Standard Test Method for Measurement of Hydraulic Conductivity of Porous Material Using a Rigid-Wall, Compaction Mold Permeameter (ASTM International, 2015).
- Badv, K., Abdolalizadeh, R., 2004. A laboratory investigation on the hydraulic trap effect in minimizing chloride migration through silt. Iran J Sci Technol Trans B 28(B1):107–118.
- Barclay, A., & M.T. Rayhani. , M. T. 2013. “Effect of temperature on hydration of geosynthetic clay liners in landfills.” Waste management & research, 31(3), 265-272.
- Barone, F. S., Rowe, R. K., and Quigley, R. M., *1992. A laboratory estimation of diffusion and adsorption coefficients for several volatile organics in a natural clayey soil.* **Journal of Contaminant Hydrology 10***: 225–250.*
- Bates, T. F., Hildebrand, F. A., & Swineford, A. (1950). Morphology and structure of endellite and halloysite. *American Mineralogist: Journal of Earth and Planetary Materials*, *35*(7-8), 463-484.
- Bavi, O., Hosseininia, M., Heydari, M. H., & Bavi, N. (2022). SARS-CoV-2 rate of spread in and across tissue, groundwater and soil: A meshless algorithm for the fractional diffusion equation. *Engineering analysis with boundary elements*, *138*, 108-117.
- Beggs, C. B., & Avital, E. J. (2021). A psychrometric model to assess the biological decay of the SARS-CoV-2 virus in aerosols. *PeerJ*, *9*, e11024.
- Benkhaya, S., S., M'rabet, & A. El Harfi. 2020. „A review on classifications, recent synthesis and applications of textile dyes.” *Inorganic Chemistry Communications*, *115*, 107891.
- Benson C.H. 2013. “Impact of Subgrade Water Content on Cation Exchange and Hydraulic Conductivity of Geosynthetic clay liners in Composite Barriers” Coupled Phenomena in Environmental Geotechnics. CRC Press (2013), pp. 79-84

- Benson, C. H., H. Zhai, and X. Wang. 1994. Estimating hydraulic conductivity of compacted clay liners. J. Geotech. Eng. 120 (2): 366–387.https://doi.org/10.1061/(ASCE)0733-9410(1994)120:2(366).
- Bharat T. V., Das. D. S. 2017. Physicochemical approach for analyzing equilibrium volume of clay sediments in salt solutions, Applied Clay Science,Volume 136,Pages 164-175,ISSN 0169-1317,https://doi.org/10.1016/j.clay.2016.11.021.
- Bharat, T. V. 2013. Analytical model for 1-D contamination diffusion through clay barriers. **J. Environ. Geotech.** 1 (EG4): 210–221.
- Bharat, T. V., Sivapullaiah, P. V., Allam, M. M. 2009. Swarm intelligence-based solver for parameter estimation of laboratory through-diffusion transport of contaminants. Comp. Geotech., 36(6), 984-992.
- Bharat, T. V., Sivapullaiah, P. V., Allam, M. M. 2012. Robust solver based on modified particle swarm optimization for improved solution of diffusion transport through containment facilities. Expert Systems with Applications, 39(12), 10812-10820.
- Bharat, T.V. and Sridharan, A. (2015a). "Prediction of compressibility data for highly plastic clays using diffuse double-layer theory." Clay. Clay. Miner., 63, 30-42.
- Biondi, E., Branciamore, B., Fusi, L., Gago, S., Gallori, E., 2007. Catalytic activity ofhammerhead ribozymes in a clay mineral environment: implications for the RNAworld. Gene 389, 10–18.
- Boopathy, R. et al. 2013. "Characterisation and recovery of sodium chloride from salt-laden solid waste generated from leather industry." *Clean. Techn. Environ. Policy* 15, 117–124.
- Bouazza, A., J.J., Bowders Jr. 2009. "Geosynthetic Clay Liners for Waste Containment Facilities." CRC Press.
- Bouazza, A., W.P. Gates, H. Abuel-Naga. 2006. "Factors impacting liquid and gas flow through geosynthetic clay liners," *Geosynth.–Recent Dev.*, 119–146, Indian International Geosynthetics Society, New Delhi
- Brigatti, M. F., Galan, E., & Theng, B. K. G. (2013). Structure and mineralogy of clay minerals. In *Developments in clay science* (Vol. 5, pp. 21-81). Elsevier.

- Brindley, G., Lailach, G.E., Thompson, T.D., Thompson, T.D.W., 1968. Adsorption of pyrimidines, purines and nucleosides by Li-, Na-, Mg-, and Ca montmorillonite (clay-organic studies XII). Clays and Clay Minerals 16, 285–293.
- Brown K.W., Donnelly., 1988. An estimation of the risk associated with the organic constituents of hazardous and municipal waste landfill leachates. Hazard. Waste Hazard. Mater., 5, pp. 1-30.
- Burnet, F.M., 1943. Human infection with the virus of Newcastle disease of fowls. Med J. Australia 2: 313 – 314.
- Busch J., Ahrens L., Sturm R., Ebinghaus., 2010. Polyfluoroalkyl compounds in landfill leachates. Environmental Pollution, 158. pp. 1467-1471.
- Buszka, P.M., Yeskis, D.J., Kolpin, D.W. et al. 2009. Waste-Indicator and Pharmaceutical Compounds in Landfill-Leachate-Affected Ground Water near Elkhart, Indiana, 2000-2002. Bull Environ Contam Toxicol 82, 653-659. http://doi.org/10.1007/s00128-009-9702-z.
- Cai, P., Huang, Q.Y., Li, M., Liang, W., 2008. Binding and degradation of DNA on montmorillonite coated by hydroxyl aluminum species. Colloids and Surfaces. B, Biointerfaces62, 299–306.
- Campbell, G. L., Hills, S. L., Fischer, M., Jacobson, J. A., Hoke, C. H., Hombach, J. M., ... & Ginsburg, A. S. (2011). Estimated global incidence of Japanese encephalitis: a systematic review. *Bulletin of the World Health Organization*, *89*(10), 766-774.
- Castro-Smirnov, F. A., Piétrement, O., Aranda, P., Bertrand, J. R., Ayache, J., Le Cam, E., ... & Lopez, B. S. (2016). Physical interactions between DNA and sepiolite nanofibers, and potential application for DNA transfer into mammalian cells. *Scientific reports*, *6*(1), 36341.
- Celik, M.S. (2004). Electrokinetic behavior of clay surfaces. Interface Sci. Technol. 1: 57–89. doi:10.1016/S1573-4285(04)80037-1.
- Chen J, Salihoglu H, Benson CH, Likos WJ, Edil TB (2019). Hydraulic conductivity of Bentonite – Polymer Composite Geosynthetic Clay Liners Permeated with Coal Combustion Product Leachates. Journal of Geotechnical and Geoenvironmental Engineering. 145(9): 04019038.

- Chen J.N., Benson C.H., Edil T.B. (2018). Hydraulic conductivity of geosynthetic clay liners with sodium bentonite to coal combustion product leachates. J. Geotech. Geoenviron. Eng., 2018, 144(3): 04018008. https://doi.org/10.1061/(ASCE)GT.1943-5606.0001844.
- Chen J.N., C.H. Benson, T.B. Edil. 2018. "Hydraulic conductivity of geosynthetic clay liners with sodium bentonite to coal combustion product leachates." *J. Geotech. Geoenviron. Eng.*, 144(3): 04018008. https://doi.org/10.1061/(ASCE)GT.1943-5606.0001844.
- Chen, L.; Ruan, F.; Sun, Y.; Chen, H.; Liu, M.; Zhou, J.; et al. Establishment of sandwich ELISA for detecting the H7 subtype in*f*luenza A virus. ***J. Med. Virol.* 2019,** 91, 1168–1171. doi:10.1002/jmv.25408
- Chen, S., Hao, H., Wang, X., Du, E., Liu, H., Yang, T., Liu, Y., Fu, X., Zhang, P., Yang, Z., 2013. Genomic characterisation of a lentogenic Newcastle disease virus strain HX01 isolated from sick pigs in China. Virus Genes 46 (2), 264–270.
- Chen, S.J., Hsieh, L.T., Chiu, S.C., 2003. Emission of polycyclic aromatic hydrocarbons from animal carcass incinerators. Sci. Total Environ. 313, 61–76
- Chen, S.J., Hung, M.C., Huang, K.L., Hwang, W.I., 2004. Emission of heavy metals from animal carcass incinerators in Taiwan. Chemosphere 55, 1197–1205.
- Chen, Y.G., Zhu, C.M., Ye, W.M., Cui, Y.J., Chen, B. 2016. Effects of solution concentration and vertical stress on the swelling behavior of compacted GMZ01 bentonite. Appl. Clay Sci., 124 pp. 11-20.
- Choi, K.S., Kye, S.J., Kim, J.Y., To, T.L., Nguyen, D.T., Lee, Y.J., Choi, J.G., Kang, H.M., Kim,K.I., Song, B.M., Lee, H.S., 2014. Molecular epidemiology of Newcastle diseaseviruses in Vietnam. Trop. Anim. Health Prod. 46 (1), 271–277.
- Choudhury, C., & Bharat, T.V. (2018). Wetting-induced collapse behavior of kaolinite: Influence of fabric and inundation pressure. Can. Geotech. J. 55(7), 956–967.
- Choy JH, Choi SJ, Oh JM, Park T. (2007). Clay minerals and layered double hydroxides for novel biological applications. Appl Clay Sci, 36:122–32.
- Christensen TH, Kjeldsen P (1989). Basic biochemical processes in landfills. In: Sanitary landfilling: process, technology, and environmental impact/ Academic Press, New York, p 29-49.

- Chumbe, A.; Izquierdo-Lara, R.; Calderón, K. *et al.* Development of a novel Newcastle disease virus (NDV) neutralization test based on recombinant NDV expressing enhanced green fluorescent protein. *Virol J* **2017,** 14, 232. https://doi.org/10.1186/s12985-017-0900-8
- Clark, K.J., Sarr, A.B., Grant, P.G., Phillips, T.D., Woode, G.N., (1998). In vitro studies on the use of clay, clay minerals and charcoal to adsorb bovine rotavirus and bovine coronavirus. Vet. Microbiol. 63, 137–146.
- Colombo, T. E.; Versiani, A. F.; Dutra, K. R.; Rubiato, J. G. D.; Galvão, T. M.; Negri Reis, A. F.; et al. Performance of CDC Trioplex qPCR during a dengue outbreak in Brazil. *J. Clin. Virol.* **2019,** 121, 104208. doi:10.1016/j.jcv.2019.104208
- Corman, V. M. et al. Detection of 2019 novel coronavirus (2019-nCoV) by real-time RT-PCR. *Eurosurveillance* ***2020***, https://doi.org/10.2807/1560-7917.ES.2020.25.3.2000045
- Daniel, D.E. (1993) Geotechnical Practice for Waste Disposal; Springer: Boston, MA,
- Das P., and Bharat T.V. (2021). Kaolin based protective barrier in municipal landfills against adverse chemo – mechanical loadings. Scientific Reports. 11:10354. https://doi.org/10.1038/s41598-021-89787-z.
- Das, D. S., Bharat, T. V., 2021. Speci**fi**c surface area of plastic clays from equilibrium sediment volume under salt environment. **Geotech. Test. J.** 44 (5): 1484–1500. https://doi.org/10.1520/GTJ20200190
- Das, D.S., (2022). "Behavior of Bentonite and Kaolin Clays at different Particle Interactions Under Chemical, Hydraulic, and Mechanical Loadings" Indian Institute of Technology Guwahati.
- Das, P., & Bharat, T. V. (2017). Effect of counter ions on the diffusion characteristics of a compacted bentonite. *Indian Geotechnical Journal*, *47*, 477-484.
- Das, P., Bharat, T.V., 2020. Bentonite Clay: A Potential Natural Sanitizer for Preventing Neurological Disorders. *ACS Chem. Neurosci.* 2020, 11, 20, 3188–3190.
- Das, P., Bharat, T.V., 2022. Assessment of Clay Mineral Attenuation Capacity for Human Viral Pathogens. Journal of Hazardous, Toxic, and Radioactive Waste 26(1):04021040-1 DOI:10.1061/(ASCE)HZ.2153-5515.0000643

- Daughton, C. G. 2003. “Cradle-to-cradle stewardship of drugs for minimizing their environmental disposition while promoting human health. II. Drug disposal, waste reduction, and future directions.” *Environmental Health Perspectives*, *111*(5), 775-785.
- Debalkie, D., Kumie, A., 2017. Healthcare waste management: the current issue in Menellik II Referral Hospital, Ethiopia. Curr World Environ. 2017; 12:42–52.
- Delage P (2010) A microstructure approach of the sensitivity and compressibility of some Eastern Canada sensitive clays. Ge ´otechnique 60(5):353–368.
- Deng, Y., J. Dixon, G. White, R. Loeppert, and A. Juo. 2006. “Bonding between polyacrylamide and smectite.” Colloids Surf. 281 (1): 82–9 https://doi.org/10.1016/j.colsurfa.2006.02.030.
- Derso, S., Taye, G., Getachew, T., Defar, A., Teklie, H., Amenu. K., 2018. Biomedical waste disposal systems of health facilities in Ethiopia. Environ Health Eng Manage J. 5:1–9.
- Di Emidio, G., F., Mazzieri, R., Verastegui-Flores, W., Van Impe, & A., Bezuijen. 2015. “Polymer-treated bentonite clay for chemical resistant geosynthetic clay liners.” *Geosynthetics International*, 22, No. 1, 125–137.
- Di Emidio, G., Van Impe, W. & Mazzieri, F. (2010). A polymer enhanced clay for impermeable geosynthetic clay liners. Proceedings of Sixth International Conference on Environmental Geotechnics, New Delhi, India, ISSMGE, New Delhi, India, pp. 963–967.
- Di Emidio, G., W., Van Impe, & V., Flores. 2011. “Advances in geosynthetic clay liners: polymer enhanced clays.” *GeoFrontiers 2011*. Advances in Geotechnical Engineering, Dallas, TX, USA, American Society of Civil Engineers, Reston, USA, pp. 1931–1940.
- Diel, D.G., Miller, P.J., Wolf, P.C., Mickley, R.M., Musante, A.R., Emanueli, D.C., Shively, K.J., Pedersen, K., Afonso, C.L., 2012. Characterization of Newcastle diseaseviruses isolated from cormorant and gull species in the United States in 2010.Avian Dis. 56 (1), 128–133.
- Doyle, T., 1927. A hitherto unrecorded disease of fowls due to filter passing virus. J.Comp. Pathol. Therap., 144–169.
- EPA (2015). Draft Environmental Guidelines: Solid Waste Landfills, 2nd ed.; US

- Farmaki, S., E., Vorrisi, O.K., Karakasi, & A., Moutsatsou. 2018. "Effect of limestone and dolomite tailings' particle size on potentially toxic elements adsorption." Open Geosci. *10*(1), pp.726-739.
- Fehervari, A., Gates, W., Patti, A., Turney, T., Bouazza, A. & Rowe, R. (2016). Potential hydraulic barrier performance of cyclic organic carbonate modified bentonite complexes against hyper-salinity. Geotextiles and Geomembranes, 44, No. 5, 748–760.
- Franchi, M., Ferris, J.P., Gallori, E., 2003. Cations as mediators of the adsorption of nucleic acids on clay surfaces in prebiotic environments. Origins of Life and Evolution of the Biosphere 33, 1–16.
- Freundlich, H., Heller, W., 1939. The Adsorption of *cis* - and *trans* -Azobenzene. Journal of the American Chemical Society 61, 2228–2230. https://doi.org/10.1021/ja01877a071.
- Ganar, K., Das, M., Sinha S., and Kumar, S., 2014. Newcastle Disease Virus: Current status and our understanding. Virus Research. Vol. 184. 71-81.
- Gapak, Y., Das, G., Yerramshetty, U., Bharat, T.V., 2017. Laboratory Determination of Volumetric Shrinkage Behavior of Bentonites: A Critical Appraisal. **Applied Clay Science** 135 (January): 554-566.https://doi.org/10.1016/j.clay.2016.10.038.
- Ghosh D, Basu A (2009) Japanese Encephalitis—A Pathological and Clinical Perspective. PLoS Negl Trop Dis 3(9): e437. https://doi.org/10.1371/journal.pntd.0000437
- Ghosh D, Basu A (2009) Japanese Encephalitis—A Pathological and Clinical Perspective. PLoS Negl Trop Dis 3(9): e437. https://doi.org/10.1371/journal.pntd.0000437
- Gillham, R. W., Robin, M. J. L., Dytynyshyn, D. J., Johnston, H. M., 1984. Diffusion of nonreactive and reactive solutes through fine-grained barrier materials. Can Geotech J 21(3):541–550
- Glanville, T.D., Richard, T.L., Harmon, J.D., Reynolds, D.L., Ahn, H.K., Akinc, A., 2006. Environmental Impacts and Biosecurity and Composting for Emergency Disposal of Livestock Mortalities. Iowa State University, USA.
- Gomatos, P. J., & Tamm, I. (1963). The secondary structure of reovirus RNA. *Proceedings of the National Academy of Sciences*, *49*(5), 707-714.
- Goodall D.C. and Quigley R.M. (1977). Pollutant migration from two sanitory landfill near

  Sarnia, Ontario. Can. Geotech. Journal Vol. 14, 223-236.

- Góralczyk-Bińkowska, A., A., Długoński, P., Bernat, J., Długoński, & A., Jasińska, 2021. "Environmental and molecular approach to dye industry waste degradation by the ascomycete fungus Nectriella pironii." *Scientific Reports*, *11*(1), 23829.
- Goyal, S. M., Gerba, C. P., 1979. Comparative adsorption of human enteroviruses, simian rotavirus, and selected bacteriophages to soils. Applied and environmental microbiology, 38(2), 241–247.
- Gregory, J. (1981). Approximate expressions for retarded van der Waals interaction. *Journal of colloid and interface science*, *83*(1), 138-145.
- Grim R. E., (1968). Clay mineralogy, 2nd edn. McGraw-Hill, New York
- Grim, R E (1959). "Physico-Chemical Properties of Soils: Clay Minerals." Journal of the Soil Mechanics and Foundation Division, ASCE, Vol. 85, No. SM2, pp. 1-17.
- Gupta, S., Boojh, R., 2006. Report: Biomedical waste management practices at Balrampur Hospital, Lucknow, India. Waste Management & Research 24: 584–591.
- Gwyther C.L., Williams A.P., Golyshin P.N., Jones G.E., Jones D.L. 2011. The environmental and biosecurity charateristics of livestock carcass disposal methods: A review. Waste Management. Vol. 31. 767-778.
- Haarstad, K., & T., Mæhlum. 2008. "Pesticides in Norwegian landfill leachates." *The Open Environmental & Biological Monitoring Journal*, *1*(1).
- Harwood, J.J., & S.R., Koirtyohann. 1987. "Modelling of leachates from dolomitic mine tailings." *Environ Geochem Health*. Mar;9(1):17-22. doi: 10.1007/BF01811112. PMID: 24214146.
- Ho, Y.S., 2003. Removal of Copper Ions from Aqueous Solution by Tree Fern. Water Res., 37, 2323–2330.
- Huang, W. E.; Lim, B.; Hsu, C. C.; Xiong, D.; Wu, W.; Yu, Y.; et al. RTLAMP for rapid diagnosis of coronavirus SARS-CoV-2. *Microb. Biotechnol.* **2020,** 13, 950–961. doi:10.1111/1751-7915.13586
- Israel, D.H., Mohamed, A.D., Biruck, D.Y., Hanibale, A.Z., 2011. Assessing the management of healthcare waste in Hawassa city, Ethiopia. Waste Manag Res. Aug;29(8):854-62. doi: 10.1177/0734242X10379496. Epub 2010 Aug 4. PMID: 20686051.

- Jang, J.; Hong, S.H.; Kim, I.H. **Validation of a Real-Time RT-PCR Method to Quantify Newcastle Disease Virus (NDV) Titer and Comparison with Other Quantifiable Methods**. *J. Microbiol. Biotechnol.* **2011;** 21:100-108. *https://doi.org/10.4014/jmb.1006.06006*
- Jhamnani, B., and Singh, S. (2009) Groundwater contamination due to Bhalaswa landfill site in New Delhi. International Journal of Environmental Sciences and Engineering, 121-125.
- Jo, H.Y., T. Katsumi, C.H. Benson, T.B., Edil. 2001. Hydraulic conductivity and swelling of nonprehydrated GCLs Permeated with single species salt solutions. J. Geotech. Geoenviron. Eng., 2001, 127(7): 557-567.
- Johnson, N. P., & Mueller, J. (2002). Updating the accounts: global mortality of the 1918-1920" Spanish" influenza pandemic. *Bulletin of the History of Medicine*, 105-115.
- Johnson, N. P., & Mueller, J. (2002). Updating the accounts: global mortality of the 1918-1920" Spanish" influenza pandemic. *Bulletin of the History of Medicine*, 105-115.
- Joo, Y., Sim, J. H., Jeon, Y., Lee, S. U., & Sohn, D. (2013). Opening and blocking the inner-pores of halloysite. *Chemical Communications*, *49*(40), 4519-4521.
- Kalbasi, A., Mukhtar, S., Hawkins, S.E., Auvermann, B.W., 2005. Carcass composting for management of farm mortalities: a review. Compost. Sci. Util. 13, 180–193.
- Kaleta, E., Baldauf, C., 1988. Newcastle disease in free-living and pet birds. In: Alexander, D.J. (Ed.), Newcastle Disease. Kluwer Acedemic Press, Boston, MA
- Katsumi, T., H., Ishimori, M., Onikata, & R., Fukagawa. 2008. "Long-term barrier performance of modified bentonite materials against sodium and calcium permeant solutions." *Geotextiles and Geomembranes*, 26, No. 1, 14–30.
- Kau, P. M. H., Binning, P. J., Hitchcock, P. W., Smith, D. W., 1999. Experimental analysis of fluoride diffusion and sorption in clays. J Contam Hydrol 36:131–151
- Kilbourne, E. D. (2006). Influenza pandemics of the 20th century. *Emerging infectious diseases*, *12*(1), 9.
- Killham, K., 1994. Soil Ecology. Cambridge University Press, Cambridge.
- Kim, S., and A. M. Palomino. 2011. "Factors influencing the synthesis of tunable polymer-clay nanocomposites using bentonite and polyacrylamide." Appl. Clay Sci. 51 (4): 491–498. https://doi.org/10.1016/j.clay.2011.01.017.

- Kumar, A., Patra, C., Kumar, S., Narayanasamy, S. Effect of magnetization on the adsorptive removal of an emerging contaminant ciprofloxacin by magnetic acid activated carbon. *Environmental Research* **2022**. *206*, 112604.
- Kumar, A., Patra, C., Rajendran, H. K., Narayanasamy, S. Activated carbon-chitosan based adsorbent for the efficient removal of the emerging contaminant diclofenac: Synthesis, characterization and phytotoxicity studies. *Chemosphere* **2022**. *307*, 135806.
- Kumar, M., Mazumder, P., Mohapatra, S., Thakur, A. K., Dhangar, K., Taki, K., ... & Kuroda, K. (2021). A chronicle of SARS-CoV-2: seasonality, environmental fate, transport, inactivation, and antiviral drug resistance. *Journal of hazardous materials*, *405*, 124043.
- Kusturica, M. P., S., Golocorbin-Kon, T., Ostojic, M., Kresoja, M., Milovic, O., Horvat,... & A., Tomas. 2020. "Consumer willingness to pay for a pharmaceutical disposal program in Serbia: A double hurdle modeling approach." *Waste Management*, *104*, 246-253.
- Kutlić A., G. Bedeković, I. Sobota, 2012. "Bentonite Processing", Rudarsko-Geološko-Naftni Zbornik, Vol. 24, Str. 61-65, Zagreb.
- Langmuir, I. The Adsorption of Gases on Plane Surfaces of Glass, Mica and Platinum. *J. Am. Chem. Soc.***1918**, 40, 1361–1403. https://doi.org/10.1021/ja02242a004.
- Langmuir, I., 1918. The Adsorption of Gases on Plane Surfaces of Glass, Mica and Platinum. Journal of the American Chemical Society 40, 1361–1403. https://doi.org/10.1021/ja02242a004.
- Lee JM, Shackelford CD (2005) Impact of bentonite quality on hydraulic conductivity of geosynthetic clay liners. J Geotech Geoenviron Eng ASCE 131(1):64–77.
- Li, T. K. and R.K. Rowe. 2020. "GCL self-healing: Fully penetrating hole/slit hydrated with RO water and 10 mM Ca solution." *Geosynth. Int.* **27**(1), 34–47.
- Lin, L., T., Katsumi, M., Kamon, C., Benson, M., Onikata, & M., Kondo. 2000. "Evaluation of chemical-resistant bentonite for landfill barrier applications." Annuals of Disaster Prevention Research Institute, No. 43 B-2, 525–533.
- Lindh, E., Ek-Kommonen, C., Vaananen, V.M., Alasaari, J., Vaheri, A., Vapalahti, O., Huovilainen, A., 2012. Molecular epidemiology of outbreak-associated and

wildwaterfowl-derived newcastle disease virus strains in Finland, including a novel class I genotype. J. Clin. Microbiol. 50 (11), 3664–3673.

- Lippmann O. 1952. Human conjunctivitis due to the Newcastle-disease virus of fowls. Am J Ophthalmol. 1952 Jul;35(7):1021-8. doi: 10.1016/0002-9394(52)90568-0. PMID: 14933554.
- Liu, H.H., Shih, T.S., Chen, I.J., Chen, H.L., 2008. Lipid peroxidation and oxidative status compared in workers at a bottom ash recovery plant and fly ash treatment plants. J. Occup. Health 50, 492–497.
- Liu, T., Hsiung, J., Zhao, S. *et al.* Quantification of antibody avidities and accurate detection of SARS-CoV-2 antibodies in serum and saliva on plasmonic substrates. *Nat Biomed Eng* **2020,** 4, 1188–1196. https://doi.org/10.1038/s41551-020-00642-4
- Lotareva, O.V., Prozorov, A.A., 2000. Effect of the clay minerals montmorillonite and kaolinite on the genetic transformation of competent Bacillus subtilis cells. Microbiology69, 571–574
- M. Zhang, Z. Cheng, T. Zhao, M. Liu, M. Hu, J. Li (2014). Synthesis, characterization, and swelling behaviors of salt-sensitive maize bran–poly (acrylic acid) superabsorbent hydrogel. J. Agric. Food Chem., 62, pp. 8867-8874.
- Mackenzie, J. S., Gubler, D. J., & Petersen, L. R. (2004). Emerging flaviviruses: the spread and resurgence of Japanese encephalitis, West Nile and dengue viruses. *Nature medicine*, *10*(Suppl 12), S98-S109.
- Mackenzie, J. S., Gubler, D. J., & Petersen, L. R. (2004). Emerging flaviviruses: the spread and resurgence of Japanese encephalitis, West Nile and dengue viruses. *Nature medicine*, *10*(Suppl 12), S98-S109.
- Mari, M., Nadal, M., Schuhmacher, M., Domingo, J.L., 2008. Monitoring PCDD/Fs, PCBs and metals in the ambient air of an industrial area of Catalonia, Spain. Chemosphere 73, 990–998.
- Matoba, Y.; Abiko, C.; Ikeda, T.; Aoki, Y.; Suzuki, Y.; Yahagi, K.; Matsuzaki, Y.; Itagaki, T.; Katsushima, F., Katsushima, Y., Mizuta, K. Detection of the human coronavirus 229E, HKU1, NL63, and OC43 between 2010 and 2013 in Yamagata, Japan. *Jpn J Infect Dis.*, **2014,** 68:138–41.

- Mazzieri, F., G., Di Emidio, & P., Van Impe, 2010. "Diffusion of calcium chloride in a modified bentonite: impact on osmotic efficiency and hydraulic conductivity." *Clays and Clay Minerals*, 58, No. 3, 351–363.
- Mieszkowski, R., 2003. Diffusion of lead ions trough the Poznan clay (Neogene) and through glacial clay. Geol. Quart., 47 (1). 111-118. Warszawa.
- Miller, P.J., Torchetti, M.K., 2014. Newcastle Disease Virus Detection and Differentiation from Avian Influenza. In: Spackman E. (eds) Animal Influenza Virus. Methods in Molecular Biology (Methods and Protocols), vol 1161.Humana Press, New York, NY. https://doi.org/10.1007/978-1-4939-0758-8_19.
- Möller, W. J. (1964). Determination of diffusion coefficients and molecular weights of ribonucleic acids and viruses. *Proceedings of the National Academy of Sciences*, *51*(3), 501-509.
- Mor S., Ravindra K., Dahiya R.P. and Chandra A. (2006). Leachate characterization and assessment of groundwater pollution near municipal solid waste landfill site. Environmental Monitoring and Assessment 118: 435 – 456. DOI: 10.1007/s10661-006-1505-7
- Na, W.; Nam, D.; Lee, H.; and Shin, S. Rapid molecular diagnosis of infectious viruses in micro*fl*uidics using DNA hydrogel formation. ***Biosens. Bioelectron.*** **2018,** 108, 9–13. doi:10.1016/j.bios.2018.02.040
- Nagarajan R.K., Thirumalaisamy S., and Lakshumanan E. (2012) Impact of leachate on groundwater pollution due to non-engineered municipal solid waste landfill sites of erode city, Tamil Nadu, India. Iranian J Environ Health Sci Eng. 9(1): 35.
- Nelson, C.B., Pomeroy, B.S., Schrall, K., Park, W.E., Lindeman, R.J., 1952. An outbreak of conjunctivitis due to Newcastle disease virus (NDV) occurring in poultry workers. Am J Public Health Nations Health. 1952 Jun;42(6):672-8. doi: 10.2105/ajph.42.6.672. PMID: 14924001; PMCID: PMC1526237.
- Noda, K., Matsuda, K., Yagishita, S. *et al.* A novel highly quantitative and reproducible assay for the detection of anti-SARS-CoV-2 IgG and IgM antibodies. *Sci Rep* 11, **2021,** 5198. https://doi.org/10.1038/s41598-021-84387-3

- Ogata, A. F. *et al*. Ultra-sensitive serial profiling of SARS-CoV-2 antigens and antibodies in plasma to understand disease progression in COVID-19 patients with severe disease. *Clin. Chem.* **2020,** https://doi.org/10.1093/clinchem/hvaa213
- OIE. Newcastle disease. In Manual of diagnostic tests and vaccines for terrestrial animals. OIE, The world organisation for animal health, Paris, France, **2012,** pp. 1-19.
- Öman C., Hynning P.A. 1993. Identification of organic compounds in municipal landfill leachates, Environmental Pollution, Volume 80, Issue 3, Pages 265-271,ISSN 0269-7491,https://doi.org/10.1016/0269-7491(93)90047-R.
- Onikata, M., M. Kondo, and M. Kamon. 1996. "Development and characterization of a multiswellable bentonite." In Environmental geotechnics, 587–590. Rotterdam, Netherlands: Taylor & Francis.
- Onikata, M., M., Kondo, N., Hayashi, & S., Yamanaka. 1999. "Complex formation of cation-exchanged montmorillonites with propylene carbonate: Osmotic swelling in aqueous electrolyte solutions." *Clays and Clay Minerals,* 47, No. 5, 672–677.
- Palomino, A. & Santamarina, J., (2005). "Fabric map for kaolinite: Effects of ph and ionic
- Parastar, F., Hejazi, S. M., Sheikhzadeh, M. & Alirezazadeh, A. A parametric study on hydraulic conductivity and self-healing properties of geotextile clay liners used in landflls. *J. Environ. Manag.* **202**(1), 29–37 (2017).
- Park, J. A., Kim, J. H., Lee, C. G., & Kim, S. B. (2014). Pyrophyllite clay for bacteriophage MS2 removal in the presence of fluoride. Water Science and Technology: Water Supply, 14, 485–492
- Park, J. H.; Shin, H. J.; Kim, M. H.; Kim, J. S.; Kang, N.; Lee, J. Y.; Kim, T. K.; Lee, J. I.; Kim, D. D. Application of montamorillonite in bentonite as a pharmaceutical excipient in drug delivery systems. J. Pharm. Investig. 2016, 46, 363−375
- Park, J.A., Kim, J.H., Lee, C.G., Kim, S.B., 2014. Pyrophyllite clay for bacteriophage MS2 removal in the presence of fluoride. Water Science and Technology: Water Supply, 14, 485–492.
- Parvez, M.K.; and Praveen, S. Evolution and Emergence of Pathogenic Viruses: Past, Present and Future. *Intervirology;* **2017**, 60:1–7 DOI: 10.1159/000478729.
- Patra, C., Medisetti, R.M.N., Pakshirajan, K., et al., 2019. Assessment of raw, acid-modified and chelated biomass for sequestration of hexavalent chromium from aqueous

solution using *SterculiavillosaRoxb.* shells. Environ Sci Pollut Res 26, 23625-23637. https://doi.org/10.1007/s11356-019-05582-4.

- Patra, C.; Shahnaz, T.; Subbiah S. et al. Comparative assessment of raw and acid activated preparations of novel *Pongamiapinnata*shells for adsorption of hexavalent chromium from simulated wastewater. *Environ Sci Pollut Res* **2020**, 27, 14836 – 14851. https://doi.org/10.1007/s11356-020-07979-y.
- Peng, S.H., Wang, R., Yang, L.-Z., He, L., He, X., Liu, X., 2018. Biosorption of copper, zinc, cadmium and chromium ions from aqueous solution by natural foxtail millet shell. Ecotoxicology and Environmental Safety 165, 61–69. https://doi.org/10.1016/j.ecoenv.2018.08.084.
- Petherick, A. Developing antibody tests for SARS-CoV-2. *The Lancet*, **2020**, *395*(10230), 1101-1102.
- Petrov, R.J., & R.K., Rowe. 1997. "Geosynthetic clay liner compatibility by hydraulic conductivity testing: factors impacting performance." *Canadian Geotechnical Journal* 34 (6), 863e885.
- Phillips, R.E., Brown, D.A., 1964. Ion Diffusion: II. Comparision of Apparent Self and Counter Diffusion Coefficients. Soil Science Society Proceedings. 758 – 763.
- Rayhani, M.T., R.K., Rowe, R.W.I., Brachman, W.A., Take, and G., Siemens. 2011. "Factors affecting GCL hydration under isothermal conditions." *Geotextiles and Geomembranes*, *29*(6): 525–533. doi:10.1016/j.geotexmem.2011.06.001.
- Rier, S.E., 2008. Environmental immune disruption: a comorbidity factor for reproduction? Fertil. Steril. 89, e103–e108.
- Robin, M. J. L., Gilliham, R.W., Oscarson, D.W., 1987. Diffusion of strontium and chloride in compacted clay – based materials. Soil Sci. J. Vol. 51. 1102-1108.
- Rong, Z.; Wang, Q.; Sun, N.; Jia, X.; Wang, K.; Xiao, R.; et al. Smartphonebased *fl*uorescent lateral *fl*ow immunoassay platform for highly sensitive pointof-care detection of Zika virus nonstructural protein. ***Anal. Chim. Acta*** **2019,** 1055, 140–147. doi:10.1016/j.aca.2018.12.043
- Rouf, M. A., A. Bouazza, R.M. Singh, W.P. Gates, and R.K. Rowe, 2016. "Water vapour adsorption and desorption in GCLs" Geosynthetics International, 23(2), pp. 86-99.

- Rowe R. K., M.T. Rayhani, W.A. Take, G. Siemens, R.W.I. Brachman. 2011. "GCL hydration under simulated daily thermal cycles." Geosynth. Int., 18 pp. 196-205.
- Rowe R.K. (1988). Contaminant transport through groundwater - the role of modelling in design of barriers. 11th Canadian Geotechnical Colloquium. Canadian Geotechnical Journal,
  25:778 – 798.
- Rowe, R. K. & AbdelRazek, A. Y. Performance of multicomponent GCLs in high salinity impoundment applications. *Geotext. Geomembr.* **49**(2), 358–368 (2020).
- Rowe, R. K. & Li, T.-K. Self-healing of circular and slit defects in GCLs upon hydration from silty sand under applied stress. *Geotext. Geomembr.* **48**(5), 667–683 (2020).
- Rowe, R. K., Booker, J. R., 1985. 1-D pollutant migration in soils of finite depth. J Geotech Eng 111(4):479–499.
- Ruckenstein, E. & Prieve, D.C. (1976). AIChE J. 22, 276.
- Saad Gharaibeh, Kamel Mahmoud. 2013. Decay of maternal antibodies in broiler chickens, Poultry Science, Volume 92, Issue 9, Pages 2333-2336, ISSN 0032-5791, https://doi.org/10.3382/ps.2013-03249.
- Sanabria-Leon, R., 2006. Composting as an alternative method to dispose of slaughterhouse wastes in Puerto Rico. University of Puerto Rico, Gran Canaria.
- Santamarina, J. C., K. A. Klein, Y. H. Wang, and E. Prencke. 2002. "Specific Surface: Determination and Relevance." Canadian Geotechnical Journal 39, no. 1 (February): 233–241. https://doi.org/10.1139/t01-077.
- Santos, N. C., & Castanho, M. A. (1996). Teaching light scattering spectroscopy: the dimension and shape of tobacco mosaic virus. *Biophysical journal*, *71*(3), 1641-1650.
- Sardini, P., Delay, F., Hellmuth, K., Porel, G., Oila, E., 2003. Interpretation of out-diffusion experiments on crystalline rocks usingrandom walk modeling. J Contam Hydrol 61:339–350
- Scalia IV, J., G. L., Bohnhoff, C. D., Shackelford, C. H., Benson, K. M., Sample-Lord, M. A., Malusis, & W. J., Likos, 2018. "Enhanced bentonites for containment of inorganic waste leachates by GCLs." *Geosynthetics International*, *25*(4), 392-411.
- Scalia, J., C. Benson, G. Bohnhoff, T. Edil, and C. Shackelford. 2014. "Long-term hydraulic conductivity of a bentonite-polymer composite permeated with aggressive

inorganic solutions." J. Geotech. Geoenviron. Eng. 140 (3): 04013025. https://doi.org/10.1061/(ASCE)GT.1943-5606.0001040.

- Sciascia, L., Liveri, M.L.T., Merli, M., 2011. Kinetic and equilibrium studies for the adsorption of acid nucleic bases onto K10 montmorillonite. Applied Clay Science 53, 657–668.
- Seiphoori, A., Laloui L., Ferrari A., Hassan M., and Khushefati W.H., (2016). Water retention and swelling behaviour of granular bentonites for application in Geosynthetic Clay Liner (GCL) systems. Soils and Foundations 2016;56(3):449–459. http://dx.doi.org/10.1016/j.sandf.2016.04.011.
- Shackelford C.D. (1991) Laboratory diffusion testing for waste disposal – A review. *J Contam Hydrol* **7**, 177-217.
- Shackelford, C., Daniel, D. E., Liljestrand, H. M., 1989. Diffusion of inorganic chemical species in compacted clay soil. J Contam Hydrol 4(3):241–273.
- Shackelford, C.D., Daniel D.E. 1991. Diffusion in Saturated soil. I: Background. Journal of Geotechnical Engineering. Vol. 117, No. 3, 467-484.
- Sharma, B., Pokhriyal, M., Rai, G.K., Saxena, M., Ratta, B., Chaurasia, M., Yadav, B.S., Sen, A., Mondal, B., 2012. Isolation of Newcastle disease virus from a non-avian host (sheep) and its implications. Arch. Virol. 157 (8), 1565–1567.
- Singh, B. (1996). Why does halloysite roll?—A new model. *Clays and Clay Minerals*, *44*, 191-196.
- Slowing, I. I.; Vivero-Escoto, J. L.; Wu, C. W.; Lin, V. S. Y. Mesoporous silica nanoparticles as controlled release drug delivery and gene transfection carriers. Adv. Drug Delivery Rev. 2008, 60, 1278−1288.
- Slowing, I.I., Vivero-Escoto, J.L., Wu, C.W., Lin, V.S.Y., 2008. Mesoporous silica nanoparticles as controlled release drug delivery and gene transfection carriers. Advanced Drug Delivery Reviews 60, 1278–1288.
- Snoeck, C.J., Owoade, A.A., Couacy-Hymann, E., Alkali, B.R., Okwen, M.P., Adeyanju,A.T., Komoyo, G.F., Nakoune, E., Le Faou, A., Muller, C.P., 2013. High genetic diversity of Newcastle disease virus in poultry in West and Central Africa: cocirculation of genotype XIV and newly defined genotypes XVII and XVIII. J. Clin. Microbiol. 51 (7), 2250–2260.

- Solid Waste Management Rules manual 2016.
- Sun, W.; Leist, S. R.; McCroskery, S.; Liu, Y.; Slamanig, S.; Oliva, J.; Amanat, F.; Schafer, A.; Dinnon, K. H., III; Garcia-Sastre, A.; Krammer, F.; Baric, R. S.; Palese, P. Newcastle disease virus (NDV) expressing the spike protein of SARS-CoV-2 as a live virus vaccine candidate. *EBioMedicine* **2020**, *62*, 103132, DOI: 10.1016/j.ebiom.2020.103132
- Sun, W.; Liu, Y.; Amanat, F.; González-Domínguez, I.; McCroskery, S.; Slamanig, S.; Palese, P. A Newcastle disease virus expressing a stabilized spike protein of SARS-CoV-2 induces protective immune responses. *Nat. Commun.* **2021**, *12* (1), 6197, DOI: 10.1038/s41467-021-26499-y
- Sun, W.; McCroskery, S.; Liu, W. C.; Leist, S. R.; Liu, Y.; Albrecht, R. A.; Palese, P. A Newcastle disease virus (NDV) expressing a membrane-anchored spike as a cost-effective inactivated SARS-CoV-2 vaccine. *Vaccines* **2020**, *8* (4), 771, DOI: 10.3390/vaccines8040771
- Swann, J., W. Bras, P. Topham, J. Howse, and A. Ryan. 2010. "Effect of the Hofmeister anions upon the swelling of a self-assembled pH-responsive hydrogel." Langmuir 26 (12): 10191–10197. https://doi.org/10.1021/la100339f.
- Tadiello, L., Guerra, S., & Giannini, L. (2022). Sepiolite-Based Anisotropic Nanoparticles: A New Player in the Rubber Reinforcement Technology for Tire Application. *Applied Sciences*, *12*(5), 2714.
- Tahamtan, A. & Ardebili, A. Real-time RT-PCR in COVID-19 detection: issues affecting the results. *Expert Rev. Mol. Diagn.* **2020,** 20, 453–454.
- Tallin, J.E., D.E., Pufahl, & S.L., Barbour. 1990. "Waste management schemes of potash mines in Saskatchewan." *Can. J. Civ. Eng.* *17*(4), pp.528-542.
- Tang, F. *et al.* Lack of peripheral memory B cell responses in recovered patients with severe acute respiratory syndrome: A six-year follow-up study. *J. Immunol.* **2011, 186**, 7264–7268 (2011).
- Teo, J. W. P.; Chiang, D.; Jureen, R.; and Lin, R. T. P. Clinical evaluation of a helicase-dependant ampli*f*ication (HDA)-based commercial assay for the simultaneous detection of HSV-1 and HSV-2. ***Diagn. Microbiol. Infect. Dis.*** **2015,** 83, 261–262. doi:10.1016/j.diagmicrobio.2015.07.018

- Tian K, Benson CH, and Likos WJ (2016). Hydraulic conductivity of Geosynthetic Clay Liners to Low-Level Radioactive Waste Leachate. J. Geotech. Geoenviron. Eng., 2016, 142(8): 04016037.
- Tian K, Likos WJ, Benson CH (2019). Polymer Elution and Hydraulic Conductivity of Bentonite – Polymer Composite Geosynthetic Clay Liners. Journal of Geotechnical and Geoenvironmental Engineering. 145(10). 04019071.
- Tian, K., C.H., Benson, W.J., Likos. 2016. "Hydraulic conductivity of geosynthetic clay liners to low-level radioactive waste leachate." *J. Geotech. Geoenviron. Eng.* 142 (8), 04016037.
- Vabret, A., Mouthon, F., Mourez, T., Gouarin, S., Petitijean, J., Freymuth, F., Direct diagnosis of human respiratory coronaviruses 229E and OC43 by the polymerase chain reaction. J Virol Methods. **2001,** 97(2001):59–66.
- Van Loon, L. R., Jakob, A., 2005. Evidence for a second transport porosity for the diffusion of tritiated water (HTO) in a sedimentary rock (Opalinus clay-OPA): application of through- and out-diffusion techniques. Transp Porous Media 61:193–214
- van Olphen, H. 1977. *Introduction to Clay Colloid Chemistry*. New York: Wiley-Interscience.
- van Olphen, H., (1963). An introduction to clay colloid chemistry, 1st edn, John Wiley & Sons,
- Vangpaisal, T., and A. Bouazza. 2004. "Gas permeability of partially hydrated geosynthetic clay liners." J. Geotech. Geoenviron. Eng. 130 (1), 93–102.
- Veerabadran, N. G., Price, R. R., & Lvov, Y. M. (2007). Clay nanotubes for encapsulation and sustained release of drugs. *Nano*, *2*(02), 115-120.
- Vilker VL, Meronek GC, Butler PC. (1983). Interactions of poliovirus with montmorillonite clay in phosphate-buffered saline. Environ Sci Technol. 1983 Oct 1;17(10):631-4. doi: 10.1021/es00116a014. PMID: 22288711.
- Wilkinson, K.G., 2007. The biosecurity of on-farm mortality composting. J. Appl. Microbiol. 102, 609–618.
- World Health Organization, Water, sanitation, hygiene, and waste management for the COVID-19 virus: Interim guidance **2020**.

- Xi, Y.; Xu, C. Z.; Xie, Z. Z.; Zhu, D. L.; Dong, J. M.; and Xiao, G. Development of a reverse transcription recombinase polymerase ampli*f*ication assay for rapid detection of human respiratory syncytial virus. ***Mol. Cell. Probes*** **2019,** 45, 8–13. doi:10.1016/j.mcp.2019.03.005
- Xie, Z., Xie, L., Chen, A., Liu, J., Pang, Y., Deng, X., and Fan, Q. Complete genome sequence analysis of a Newcastle disease virus isolated from a wild egret. *J. Virol.* **2012,** 86(24), pp. 13854-13855.
- Xu, S.W., Hao, X.Y., Stanford, K., McAllister, T., Larney, F.J., Wang, J.G., 2007. Greenhouse gas emissions during co-composting of cattle mortalities with manure. Nutr. Cycl. Agroecosys. 78, 177–187.
- Xue, M.; Caryn, L. H. Adsorption of a non-enveloped mammalian virus to functionalized nanofibers, *Colloids Surf. B: Biointerfaces* **2014**, Volume 121, Pages 319-324, ISSN 0927-7765. https://doi.org/10.1016/j.colsurfb.2014.06.007.
- Yan, J.H., Xu, M.X., Lu, S.Y., Li, X.D., Chen, T., Ni, M.J., Dai, H.F., Cen, K.F., 2008. PCDD/F concentrations of agricultural soil in the vicinity of fluidized bed incinerators of co-firing MSW with coal in Hangzhou, China. J. Hazard Mater. 151, 522–530.
- Yesudhas, D., Srivastava, A., & Gromiha, M. M. COVID-19 outbreak: history, mechanism, transmission, structural studies and therapeutics. *Infection*, **2021**, *49*, 199-213.
- Yu W.H., Li N., Tong D.S., Zhou C.H., Lin C.X., Xu C.Y., 2013. Adsorptions of protiens and nucleic acid on clay minerals and their interactions: A review, Applied Clay Science, vol. 80; 443-452. http://dx.doi.org/10.1016/j.clay.2013.06.003.
- Yuan, P., Tan, D., & Annabi-Bergaya, F. (2015). Properties and applications of halloysite nanotubes: recent research advances and future prospects. *Applied Clay Science*, *112*, 75-93.
- Yusof N., Haraguchi A., Hassan M.A., Othman M.R., Wakisaka M., and Shirai Y. (2009). Measuring organic carbon, nutrients and heavy metals in rivers receiving leachate from controlled and uncontrolled municipal solid waste (MSW) landfills. Waste Management. 29: 2666 – 2680.
- Zafar M., & Alappat B.J. (2004) Landfill surface runoff and its effect on water quality on river Yamuna. Journal of Environmental Science and Health, Part A, 39:2, 375-384, DOI: 10.1081/ESE-120027529

- Zand, A.D., & Heir, A.V., 2020. “Emerging challenges in urban waste management in Tehran, Iran during the COVID-19 pandemic.” *Resour. Conserv. Recycl.* 162, 105051.
- Zhang, L.; Du, X.; Chen, C.; Chen, Z.; Zhang, L.; Han, Q.; et al., Development and characterization of double-antibody sandwich ELISA for detection of Zika virus infection. *Viruses* ***2018,*** 10, 634. doi:10.3390/v10110634.
- Zhang, X.; Yao, M.; Tang, Z. *et al.* Development and application of a triplex real-time PCR assay for simultaneous detection of avian influenza virus, Newcastle disease virus, and duck Tembusu virus. *BMC Vet Res* **2020,** 16, 203. https://doi.org/10.1186/s12917-020-02399-z